Het hydrodynamisch modelleren van de stroming van zelfverdichtend beton in bekistingen

Hydrodynamic Modelling of the Flow of Self-Compacting Concrete in Formworks

Serge Tichko

Promotoren: prof. dr. ir. G. De Schutter, prof. dr. ir. P. Troch
Proefschrift ingediend tot het behalen van de graad van
Doctor in de ingenieurswetenschappen

Vakgroep Bouwkundige Constructies
Voorzitter: prof. dr. ir. L. Taerwe

Vakgroep Civiele Techniek
Voorzitter: prof. dr. ir. P. Troch

Faculteit Ingenieurswetenschappen en Architectuur
Academiejaar 2015 - 2016

UNIVERSITEIT GENT

ISBN 978-90-8578-917-8
NUR 955, 956
Wettelijk depot: D/2016/10.500/49

Supervisors:

Prof. Dr. Ir. Geert De Schutter
Prof. Dr. Ir. Peter Troch

Research Institutes:

Magnel Laboratory for Concrete Research
Department of Civil Engineering
Ghent University
Technologiepark - Zwijnaarde 904
B-9052 Zwijnaarde
Belgium

Financial support:

Research Foundation - Flanders (FWO)

Dankwoord

In augustus 2009 solliciteerde ik aan de Universiteit Gent met de vraag of ik met een doctoraatstudie zou mogen starten in het domein van de numerieke stromingsberekeningen. Ik had een vacature op de webstek van CFD Online ontdekt waarin de vakgroep Bouwkundige Constructies, gehuisvest in het Magnel Laboratorium voor Betononderzoek te Zwijnaarde, zocht naar een kandidaat om het stromingsgedrag van zelfverdichtend beton in bekistingen te onderzoeken.

Als werktuigkundig ingenieur, toen al reeds zestien jaren werkzaam in de industrie, had ik reeds behoorlijk wat mechanische vraagstukken en een flink aantal stromingsproblemen opgelost, maar mijn kennis in beton en meer bepaald zelfverdichtend beton was onbestaand. Verder zat ik ook met de bedenking in mijn hoofd dat ze deze niet al te jonge persoon waarschijnlijk niet zouden aannemen voor deze job, met al het jong geweld dat jaarlijks aan de universiteit afstudeert. En toch, één week na het sollicitatiegesprek kreeg ik van Prof. De Schutter te horen dat ik geselecteerd was voor de voorliggende onderzoeksfunctie.

Daarom zou ik vooreerst vier mensen willen bedanken, welke mij de kans hebben gegeven om dit onderzoek te mogen verrichten, maar die er ook altijd waren om mij hierbij raad te geven en te steunen. Prof. De Schutter, Prof. Toch, Prof. Vierendeels en Prof. Verhoeven (Geert, Peter, Jan en Ronny voor de vele onderzoekers onder hun vleugels), ongelooflijk hartelijk bedankt hiervoor en tevens voor de aangename sociale activiteiten aan het Labo Magnel en het Labo voor Hydraulica. Eveneens bedankt voor het vele leeswerk, niet alleen van het huidig manuscript maar ook van de ingediende artikels tijdens het onderzoek.

Het is misschien een cliché, maar daarom zeker niet minder gemeend, een hele grote dank te betuigen aan de vele “techniekers” van de beide labo’s. Zonder jullie mateloze inzet en input was het onmogelijk geweest om dit onderzoek te verrichten en tot een goed einde te brengen. Dieter, Jan, Marc, Marcel, Martin, Nathan, Nicolas, Peter, Peter, Stefaan, Davy, Stefan en Tom, hartelijk bedankt voor jullie geweldige hulp. Beste Tommy, bedankt om mijn proeven telkens weer te willen en kunnen inplannen, wetende dat die planning altijd goed vol stond. Brenda, Pieter en Karel eveneens een dikke merci voor de uitvoering van de vele betonproeven en reometermetingen. Marijke, Christel en Viviane, jullie wisten mij altijd snel en met de glimlach uit de nood te helpen met allerlei administratieve beslommeringen, een dikke merci hiervoor.

Ook de vele andere mede-onderzoekers aan de beide labo’s mogen niet vergeten worden en in het bijzonder Sieglien, Kevin, Dieter, Pieter, Geoffrey, Bart, Emmanuel, Jeroen en Ruben. Bedankt om deze “ouwe” in jullie jonge midden te willen opnemen en aanvaarden. De BBQ’s op Labo Magnel, de kookmomenten op het Labo voor Hydraulica, de verschillende recepties, discussies in de keuken, de sportnamiddagen en after-sport avonden zullen niet snel vergeten worden.

In dit project heb ik ook de hulp gehad van twee zeer gemotiveerde thesisstudenten. Jens Van De Maele en Niels Vanmassenhove, hartelijk bedankt voor jullie inzet en voor de wetenschappelijke input in dit onderzoek.

Verder ook een woordje van dank aan diegenen die tijdens mijn onderzoek niet aan de UGent verbonden waren: Karel Lesage (KUL) voor de hulp bij het gebruik van de BML reometer van de KUL en Niki Cauberg (WTCB) voor het mogen gebruik maken van de elektronische druksensoren van het WTCB. Betoncentrale OBC-Ottevaere uit Oudenaarde voor de leveringen van de voor de vulproeven noodzakelijke beton-hoeveelheden. Pompfirma Dejonghe uit Zonnebeke, en in het bijzonder Chris voor zijn expertise en raad.

Tevens bedankt aan de vele vrienden uit de diverse kringen, aan sommige vroegere werkcollega's en aan mijn huidige werkmakkers op de firma Promat. Jullie hebben me blijven steunen tijdens mijn lange tocht. Vooral de geregelde vraag van, "hoe ver staat het met jouw onderzoek?", en het daaropvolgend antwoord van mij met een kleine slik in de keel, "Euh, het vordert, maar er is nog veel werk en het lijkt nooit af te geraken", heeft me telkens weer de moed gegeven om te blijven doorgaan.

Bedankt aan mijn mama en mijn papa, om mij de mogelijkheid te geven om te kunnen studeren, om mij niets in de weg te leggen om mezelf te ontplooien en voor de vele steun in de moeilijkere momenten. Papa, jammer dat je dit moment in mijn leven niet meer mocht meemaken. Je bent in ieder geval in mijn gedachten altijd aanwezig! Verder ook bedankt aan mijn broer, mijn familie en schoonfamilie voor de gebeurlijke schouderklop, als het soms niet zo lekker ging.

Verder denk ik dat ik ondertussen stilaan aan rond ben. Ik ben echter nog een heel belangrijke groep mensen vergeten. Het zijn de leden van mijn gezinnetje: mijn vrouwtje Lieve, mijn dochter Anoesjka en mijn zoon Sasja. Jullie hebben mij heel erg vaak moeten missen toen ik voor de zoveelste keer in mijn boeken en papieren verzonken was of toen ik weeral zat te stressen achter mijn computer tijdens het schrijven van deze en andere proza. Ik kan niet genoeg woorden vinden om jullie te bedanken, om mij de kans gegeven te hebben aan deze avontuurlijke tocht te mogen beginnen, en voor het vele geduld dat jullie telkens weer hebben moeten tonen. Een dikke zoen van deze vaak in gedachte (en soms in den lijve) afwezige echtgenoot en papa!!

Serge

Deurne, 12 juli 2016.

Table of contents

List of Symbols

σ	=	Normal force per unit area or axial stress (Pa)
τ	=	Shear force per unit area or shear stress (Pa)
ε	=	Relative length change or axial strain (-)
γ	=	Angle of deformation (-)
E	=	Elastic modulus or modulus of elasticity (Pa)
G	=	Shear modulus (Pa)
η	=	Newtonian viscosity (Pa.s)
$\dot{\gamma}$	=	Rate of straining or shear rate (s^{-1})
τ_o	=	Yield stress (static or dynamic) (Pa)
K	=	Consistency factor ($Pa.s^n$)
N	=	Consistency index (-)
μ_p	=	Plastic viscosity (Pa.s)
Re_p	=	Particle Reynolds number (-)
ρ_s	=	Density of the suspending medium ($kg.m^{-3}$)
a	=	Particle radius (m)
E_T	=	Thermal energy (J)
k	=	Boltzmann constant (= $1.38.10^{-23}$ $J.K^{-1}$)
T	=	Absolute temperature (K)
Pe	=	Peclet number (-)
η_{HI}	=	Shear viscosity (Pa.s),
B_3	=	Friction coefficient (N.s)
J_t	=	Total number of reversible junctions per unit of volume (m^{-3}).
n_3	=	Total number of primary particles per unit of volume (m^{-3})
n_t	=	Total number of particles after structural build-up or structural breakdown (m^{-3})
H	=	Coagulation rate constant (s^{-1})
U_0	=	Initial coagulation state (-)
U_3	=	End state coagulation (-)
Γ	=	Memory module for shear (-)
Θ	=	Memory module for coagulation (-)
m_a, m_b	=	Parameters indication how much the past should be remembered (s)
t	=	Time or current time (s)
t'	=	Time varying between the initial time and the current time (s)
μ''	=	Thixotropic counterpart of the plastic viscosity (Pa.s)
τ_0''	=	Thixotropic counterpart of the yield stress (Pa)
a_1, a_2	=	Fitting parameters of the modified Hattori-Izumi model (-)
λ	=	Parameter representing the structural state (-)
λ_0	=	Initial structural state (-)
T	=	Characteristic parameter for structuration (s)
α	=	Characteristic parameter for de-structuration (s)
A_{thix}	=	Flocculation rate of fresh concrete ($Pa.s^{-1}$)
T_i	=	Measured torque at the inner cylinder of a rheometer (N.m)
R_i	=	Radius of the inner cylinder of a rheometer (m)
R_o	=	Radius of the outer cylinder of a rheometer (m)
h	=	Height of the cylinder submerged in the material (m)
Ω_i	=	Rotational velocity at the inner cylinder ($rad.s^{-1}$)
R	=	Slump flow spreading distance (m)
ρ	=	Density of the concrete ($kg.m^{-3}$)
V	=	Volume of the Abrams cone (m^3)
g	=	Gravitational acceleration (= 9.81 $m.s^{-2}$)

G_B	=	Intercept of the Bingham relationship with the *T*-axis for *N* = 0 (N.m)
H_B	=	Inclination of the Bingham relationship between *T* and *N* (N.m.s)
N	=	Rotational velocity (rev.s^{-1})
G_{HB}	=	Intercept of the Herschel-Bulkley relationship with the *T*-axis for *N* = 0 (N.m)
K_{HB}	=	Fitting parameter of the Herschel-Bulkley relationship between *T* and *N* (N.m.s^{-m})
m	=	Fitting parameter of the Herschel-Bulkley relationship between *T* and *N* (-)
$\vec{v}$	=	Velocity vector (m.s^{-1})
p	=	Pressure (Pa)
$\bar{\bar{\tau}}$	=	Stress tensor (Pa)
$\vec{g}$	=	Gravity acceleration vector (m.s^{-2})
$\bar{\bar{D}}$	=	Strain rate tensor (s^{-1})
$II_{\bar{\bar{D}}}$	=	Second invariant of the strain rate tensor (s^{-1})
H	=	Total energy (J)
Δp_L	=	Shear flow losses or hydraulic losses (Pa)
s	=	Flow path distance parameter (m)
L	=	Flow path length (m)
τ_w	=	Shear stress at the wall (Pa)
R	=	Radius of the flow cross-section (m)
r	=	Radial position parameter (m)
r_{plug}	=	Radius of the plug zone (m)
$\dot{\gamma}_r$	=	Shear rate at position r (s^{-1})
τ_r	=	Shear stress at position r (Pa)
v_{plug}	=	Velocity at the plug zone radius (m.s^{-1})
Q	=	Volumetric flow rate (m^3.s^{-1})
p_{max}	=	Maximum lateral pressure on the formwork wall (Pa)
C_w	=	Unit weight coefficient (-)
C_c	=	Chemistry coefficient (-)
R	=	Placement rate or casting speed (m.h^{-1})
h	=	Depth of the fluid or plastic concrete from the top of the placement to the point of consideration in the formwork (m)
T	=	Temperature of the fresh concrete (°C)
D	=	Weight density of the fresh concrete (kN.m^{-3})
C_1	=	Coefficient dependent on the size and shape of the formwork ((m.h)$^{1/2}$)
C_2	=	Coefficient dependent on the constituent materials of the concrete ((m)$^{1/2}$)
H	=	Vertical formwork height (m),
K	=	Temperature coefficient (-)
σ_{hk}	=	Characteristic value of the fresh concrete pressure (kN.m^{-2})
γ_F	=	Partial safety factor (-)
σ_{hd}	=	Design value of the fresh concrete pressure (kN.m^{-2})
K_1	=	Factor for the setting behaviour (-)
K_2	=	Density correction factor (-)
F1 - F6	=	Consistency class of the fresh concrete (-)
p_{hor}	=	Horizontal formwork wall pressure (Pa)
$p_{max,base}$	=	Maximum wall pressure at the base of the formwork (Pa)
ρ_{SCC}	=	Density of the fresh SCC (kg.m^{3})
D_H	=	Hydraulic diameter (m)
R_{eq}	=	Equivalent radius (m)

S	=	Flow cross-section (m^2)
P	=	Wetted perimeter (m)
$\vec{F}_i$	=	Contact force acting on the particle (N)
$\vec{F}_i^n$	=	Normal contact force component (N)
$\vec{F}_i^t$	=	Tangential contact force component (N)
$\vec{M}_i$	=	Resultant moment acting on the particle (N.m)
m	=	Mass of a DEM particle (kg)
I	=	Mass moment of inertia of a DEM particle ($kg.m^2$)
$\vec{x}_i^{(t)}$	=	Position of a DEM particle at time t (m)
$\vec{\dot{x}}_i^{(t+\frac{\Delta t}{2})}$	=	Translational velocity of a DEM particle at time $t+\Delta t/2$ ($m.s^{-1}$)
$\vec{\ddot{x}}_i^{(t)}$	=	Translational acceleration of a DEM particle at time t ($m.s^{-2}$)
$\vec{\omega}_i^{(t+\frac{\Delta t}{2})}$	=	Angular velocity of a DEM particle at time $t+\Delta t/2$ ($rad.s^{-1}$)
$\vec{\dot{\omega}}_i^{(t)}$	=	Angular acceleration of a DEM particle at time $t+\Delta t/2$ ($rad.s^{-2}$)
Δt	=	Time step size (s)
k	=	DEM particle size effect correction coefficient (-)
$\vec{r}_i$	=	Position vector of a DPD particle (m)
$\vec{p}_i$	=	Momentum vector of a DPD particle ($kg.m.s^{-1}$)
$\vec{F}_{ij}$	=	Force on a DPD particle i due to particle j (N)
$\vec{F}_{ij}^C$	=	Conservative part of the force on a DPD particle i due to particle j (N)
$\vec{F}_{ij}^D$	=	Dissipative part of the force on a DPD particle i due to particle j (N)
$\vec{F}_{ij}^R$	=	Random part of the force on a DPD particle i due to particle j (N)
$\vec{v}_{ij}$	=	Difference of the velocity of the DPD particles ($m.s^{-1}$)
F_m	=	Conservative DPD parameter ($N.m^{-1}$)
r_{ij}	=	Distance between the DPD particles i and j (m)
$\vec{e}_{ij}$	=	Unit vector pointing from particle j to particle i (-)
w^D, w^R	=	DPD weight functions (-)
ξ_{ij}	=	Randomly fluctuating variable described by Gaussian statistics (-)
γ	=	Strength of the dissipative forces (N)
σ	=	Strength of the random forces ($N.m^{-1}$)
η_r	=	Relative viscosity of a suspension (-)
η_s	=	Viscosity of the suspending fluid (Pa.s)
η	=	Viscosity of the suspension (Pa.s)
φ	=	Volume fraction of the suspended rigid bodies (-)
η_0	=	Intrinsic viscosity of a suspension (-)
K_H	=	Huggins coefficient (-)
f	=	Statistical distribution function (-)
f_a	=	LBM single-particle distribution function (-)
$\vec{e}_i$	=	Lattice velocity ($m.s^{-1}$)
lu	=	Lattice unit (m)
ts	=	LBM time step unit (s)
$\vec{u}$	=	Macroscopic velocity ($m.s^{-1}$)
τ	=	LBM relaxation time (s)
f_a^{eq}	=	LBM equilibrium distribution function (-)
w_a	=	LBM equilibrium distribution function weights (-)
c	=	Basic speed of the lattice ($lu.ts^{-1}$)
ν	=	Kinematic viscosity ($m^2.s^{-1}$)
ν_{pl}	=	Plastic kinematic viscosity ($m^2.s^{-1}$)

V_q = Volume of phase q (m^3)
α_q = Volume fraction of phase q (-)
$\vec{v}_q$ = Velocity of phase q ($m.s^{-1}$)
μ_q = Shear viscosity of phase q (Pa.s)
λ_q = Bulk viscosity of phase q (Pa.s)
$\vec{R}_{pq}$ = Interaction force between phases (N)
$\vec{F}_{lift,q}$ = Lift force on phase q (N)
$\vec{F}_{vm,q}$ = Virtual mass force on phase q (N)
K_{pq} = Interphase momentum exchange coefficient (-)
V = Volume of the FVM control volume (m^3)
$\vec{A}$ = Surface area vector (m^2)
$\emptyset$ = Transported quantity ([Ø])
$\Gamma_\emptyset$ = Diffusion coefficient for Ø ($m^2.s$)
$S_\emptyset$ = Source of Ø per unit volume ([Ø].m^{-3})
N_{faces} = Number of faces enclosing the cell (-)
$\emptyset_f$ = Value of Ø convected through face f ([Ø])
$\dot{m}_{qp}$ = Mass transfer from phase q to phase p ($kg.m^{-3}.s^{-1}$)
$\dot{m}_{pq}$ = Mass transfer from phase p to phase q ($kg.m^{-3}.s^{-1}$)
S_{α_q} = Mass source term for phase q ($kg.m^{-3}.s^{-1}$)
c_0, c_1 = Cell centres (-)
N_f = Number of nodes on face f (-)
δr_i = Vector from the centroid of cell c_0 to cell c_i (m)
$[J]$ = Coefficient matrix (m)
W_{i0}^x, W_{i0}^y, W_{i0}^z = Components of the gradient weights (m^{-1})
$F(\emptyset)$ = Function incorporating any spatial discretization ([Ø].s^{-1})
U_f = Volume flux through face f ($m^3.s^{-1}$)
$\alpha_{q,f}$ = Face value of the q^{th} volume fraction (-)
φ = The level-set (LS) function (-)
$\vec{n}$ = Normal of the interface (-)
κ = Curvature of the interface (m^{-1})
$\vec{u}$ = Underlying velocity of the LS function ($m.s^{-1}$)
σ = Surface tension coefficient ($N.m^{-1}$)
S_i = Porous zone added momentum sink/loss term in the direction i ($N.m^3$)
μ_{app} = Local apparent viscosity (Pa.s)
k_i = Permeability coefficient of the porous zone in the direction i (m^2)
v_i = Darcy's velocity in the direction i ($m.s^{-1}$).
$\dot{\gamma}_{app}$ = Apparent shear rate within the porous medium (s^{-1})
α = Shift factor (-)
φ = Porous medium porosity (-)
B_n = Bingham number value (-)
Δp_{tot} = Pressure loss over the length of the duct (Pa)
$\tau_{0,MB}$ = Yield stress of the modified Bingham model (Pa)
μ_{MB} = Dynamic viscosity of the modified Bingham model (Pa.s)
c_{MB} = Second order parameter of the modified Bingham model ($Pa.s^2$)
$\dot{\gamma}_r$ = Critical shear rate of the two-zone Herschel-Bulkley model in Ansys Fluent@ (s^{-1})
K_{TI} = Lower limit of the permeability for a transverse flow around a cylindrical intrusion (m^2)

K_{Tu} = Upper limit of the permeability for a transverse flow around a cylindrical intrusion (m^2)

K_{Ll} = Lower limit of the permeability for a longitudinal flow around a cylindrical intrusion (m^2)

K_{Lu} = Upper limit of the permeability for a longitudinal flow around a cylindrical intrusion (m^2)

R = Radius of the fluid shell around a cylindrical intrusion (m)

List of Abbreviations

BBRI	=	Belgian Building Research Institute
CFD	=	Computational Fluid Dynamics
CVC	=	Conventional Vibrated Concrete
DEM	=	Discrete Element Method
DPD	=	Dissipative Particle Dynamics Method
DPM	=	Discrete Particle Method
FEM	=	Finite Element Method
FDM	=	Finite Difference Method
FVM	=	Finite Volume Method
GGBFS	=	Ground Granulated Blast Furnace Slag
GUI	=	Graphical User Interface
HPC	=	High Performance Concrete
LBM	=	Lattice Boltzmann Method
LfH	=	Laboratory for Hydraulics
LHPBFC	=	Low Heat Portland Blast Furnace Cement
LHS	=	Left-hand side
LS	=	Level-Set method/function
MLCR	=	Magnel Laboratory for Concrete Research
MLBO	=	Magnel Laboratorium voor Betononderzoek
OPC	=	Ordinary Portland Cement
PBFC	=	Portland Blast Furnace Cement
PCE	=	Polycarboxylether type super-plasticiser
PFA	=	Pulverised Fuel Ash
PLIC	=	Piecewise Linear Interface Construction
PPFAC	=	Portland Pulverised Fuel Ash Cement
PZ	=	Porous Zone
RHPC	=	Rapid Hardening Portland Cement
RHS	=	Right-hand side
SCC	=	Self-Compacting Concrete
SP	=	Super-plasticiser
SRPC	=	Sulphate Resisting Portland Cement
UGent	=	Ghent University in Belgium
VMA	=	Viscosity Modifying Agent
VOF	=	Volume of Fluid method
W/C	=	Water-to-Cement ratio
W/P	=	Water-to-Powder ratio
ZVB	=	Zelfverdichtend beton

List of Figures

List of Tables

Summary

Self-compacting concrete (SCC) enables innovative casting techniques like filling formworks by pumping bottom-up in contrast with the traditional top-filling method. However, fundamental questions remain concerning the occurring formwork pressure when applying this advanced filling procedure. During the present doctoral research, these fundamental issues have been analysed and practical and innovative solutions have been proposed, which will be succinctly described in the following paragraphs of this summary. This doctoral thesis and the related research work is subdivided into seven major chapters.

In chapter 1, the general context of the current research has been clearly described and the research objectives have been formulated. They are listed below:

- Presenting a comprehensive overview of the most relevant formwork design codes and analysing the applicability or limits of validity when casting from the base of a formwork with fresh SCC;
- Performing full-scale formwork base-filling experiments with SCC and:
  - ✓ Measuring the fresh concrete flow at the inlet;
  - ✓ Measuring the wall pressures during the casting process;
  - ✓ Analysing the resulting quality of the cast through visual inspection of drilled samples;
- Presenting a comprehensive overview of the numerical simulation techniques applied in fresh concrete flow modelling;
- Building adequate numerical and analytical models in order to predict the wall pressures during the base-filling experiments, followed by a comparison of the measurements and the simulation results in order to prove the validity and the predicting ability of the presented simulation models and analytical models.

In chapter 2, the rheology and the fresh properties of SCC have been presented. The rheology of fresh SCC has been described throughout a number of rheological models, like the Bingham model and the Herschel-Bulkley model, which relate the shear rate to the shear stress, thereby describing the shear flow behaviour of fresh concrete. Phenomena like shear thickening, thixotropy and segregation, which do influence the flow behaviour of fresh SCC during casting, have been discussed.

Shear thickening has been observed with all the SCC mixtures selected for the casting tests. As such, the Herschel-Bulkley model was selected in the present research. A brief overview of the existing types of rheometers for measuring the rheology of fresh SCC has been given. The two types of rheometers which have been used during our formwork base-filling tests, the Tattersall Mk-II rheometer and the BML Contec-Viscometer 5, have been presented in detail. Based on the practical experience gained during the base-filling tests, we can state that the BML Contec-Viscometer 5 proved to be more accurate and much easier to use when determining the rheology of the chosen fresh SCC mixtures.

In chapter 3, the Navier-Stokes flow equations were presented, describing the conservation of mass and momentum, were presented. The conservation of energy has not been considered, because the density and the viscosity of the fresh concrete are assumed to be independent of the typically very small temperature changes during the pumping and casting process. Based on these flow equations, a new analytical model has been derived, which enables to quickly determine the shear flow losses and the resulting wall pressures when pumping fresh SCC through ducts and in formworks. The Herschel-Bulkley model, presented in chapter2, has been taken into account in the derivation of the analytical model.

Two formwork filling techniques when using SCC are presented: the top-filling and the base-filling method. Top-filling is the most applied formwork filling process and a lot of knowledge and experience about this filling method is already available. The base-filling method is much less applied in casting processes with SCC. Also very little research has been performed so far, resulting in much less knowledge and practical experience. This is also noticeable when studying the available formwork design standards. Not only have these design standards mainly been drafted for casting processes with conventional vibrated concrete (CVC) instead of SCC, they are also only valid for top-filling processes at relatively low casting speeds. This has been the motivation for the present research to focus on the base-filling technique. The newly derived analytical model has been applied on the formwork base-filling process, through the introduction of the hydraulic diameter. This model clearly shows that the formwork wall pressures do exceed the hydrostatic pressure when using the base-filling technique. This is due to the shear flow losses. This fact is not taken into account in any of the available formwork design standards.

Chapter 4 is divided into two main parts. In a first part, an overview is given of the numerical simulation methods which are applied in modelling fresh concrete flow. The principles of these methods and their application domains are discussed, as well as their related advantages and disadvantages. After comparing the pros and cons of each simulation method, the Finite Volume Method (FVM) combined with the Volume of Fluid (VOF) method and the Level-Set (LS) interface tracking technique has been selected for the numerical simulations of the performed base-filling experiments with SCC. This FVM-VOF-LS scheme and the specific settings for the simulation models of our base-filling tests are presented in the second main part of chapter 4, together with a promising modelling technique where the steel rebars are modelled implicitly as a porous zone.

During the present research program, two series of full-scale formwork filling tests have been performed at the Magnel Laboratory for Concrete Research (MLCR) of Ghent University, where in each test the fresh SCC has been pumped from the base of the formwork. These formwork base-filling tests are described in chapter 5. During these casting tests, one large I-beam, ten columns and two walls have been cast. The influence on the formwork pressure of the viscosity of the SCC, the casting speed and the presence of rebars has been studied.

The measured wall pressures revealed that the formwork pressure did indeed exceed the hydrostatic pressure, as predicted by the new analytical model being derived in chapter3. These casting tests also showed that the shear flow losses become more important for high casting rates, small formwork cross-sections (e.g. columns with rebars) or when using a high viscosity SCC.

When pumping SCC from the bottom it was possible to noticeably reduce the casting times by applying high casting rates. However, stronger and stiffer formwork walls were needed to sustain the higher wall pressures. Due to the high casting rates, and as such very short filling times, the effect of thixotropy on the formwork pressure could be disregarded. The quality of the cast concrete was investigated through a visual inspection of a series of drilled concrete samples taken at several relevant locations of the casts. The resulting quality proved to be excellent, considering the very high casting speeds.

In chapter 6, the numerical simulations of the performed pumping and filling tests are described in detail. Also the application of the new analytical model to the base-filling process with rebars is presented. The performed sensitivity analysis revealed that the influence of the consistency factor and the consistency index of the Herschel-Bulkley model on the shear flow losses, and therefore on the wall pressure, is important. As such, it is necessary to accurately determine the rheology of the selected SCC when applying base-filling. The simulation results showed to be in good agreement with the measurements performed during the casting tests, and as such, they confirm that the occurring wall pressures are the sum of the hydrostatic pressure and the flow losses.

The use of the combined FVM-VOF-LS scheme revealed to be stable and relatively fast, however it required a uniform mesh composed of mostly hexahedral cells. This requirement was not easy to fulfil when modelling the performed casting tests, and it will certainly not be straightforward when modelling complex formwork shapes and/or rebar configurations.

For this reason, the combined FVM-VOF-LS scheme has been further expanded with porous zone modelling, where the additional flow losses induced by the presence of the steel rebars are taken into account implicitly by the porous zone parameters. For the standard rebar layout used in our base-filling tests the simulation results obtained with the combined FVM-VOF-LS scheme and the rebars modelled as a porous zone were in very good agreement with the simulation results of the numerical models with rebars modelled explicitly. Based on this observation, the combination of the FVM-VOF-LS scheme and the porous zone analogy for the rebars proves to be very promising, as it drastically reduces the pre-processing time and the computational time, although the determination of the porous zone parameters for complex rebar configurations remains in general a real challenge.

The maximum formwork wall pressures calculated with the newly derived analytical model proved to be in very good agreement with the simulation results from the numerical models. When using the analytical model the calculation time is extremely small, but no information about the local velocities in the flow domain is available.

However, the pressure losses and the maximum wall pressure calculated with the new analytical model allow to quickly determine the required capacity of the concrete supply pump and the necessary strength and stiffness of the formwork wall elements.

Finally, in chapter 7, all the conclusions drawn from the performed research work, which are reported in each individual chapter, are summarized. Also a number of recommendations for further research are presented.

The general conclusions are briefly formulated here:

- When applying base-filling with SCC, in principle hydrostatic formwork pressures can be expected increased with the shear flow losses, which become important for high casting rates, small formwork cross-sections (e.g. columns, dense rebar configurations) or when selecting a high viscosity SCC. The shear flow losses measured during the performed base-filling tests ranged from 7 % up to 16 % of the total wall pressure.
- When pumping SCC from the bottom it is possible to noticeably reduce the casting times by applying high casting rates. However, much stronger and stiffer formwork wall systems will be required to sustain the higher wall pressures.
- When applying high casting rates, the effect of thixotropy on the formwork wall pressure can be disregarded.
- The correct determination of the rheological material parameters of the SCC used in the filling process is important, as these parameters have an influence on the resulting formwork wall pressures, especially the consistency factor and the consistency index of the Herschel-Bulkley model.
- The base-filling process and the related formwork pressures can be accurately simulated applying the FVM-VOF-LS modelling technique. These kind of CFD simulations allow to optimize the formwork filling process.
- If only the maximum formwork pressures are of interest, then a simple and very quick steady state simulation of the completely filled formwork is sufficient. A time-dependent simulation using the combined FVM-VOF-LS scheme is required if a possible occurrence of air voids due to a non-adequate positioning of the supply inlets needs to be detected, or when the required self-levelling properties of a selected SCC mixture need to be assessed.
- For the standard rebar layout used in our filling tests, the simulation results obtained with the FVM-VOF-LS scheme and the rebars modelled as a porous zone were in very good agreement with simulations of the numerical models with rebars modelled explicitly.
- The maximum formwork wall pressures calculated with the new analytical model proved to be in good agreement with the simulation results from the numerical models. These calculations are very fast.

Samenvatting

De uitvinding van zelfverdichtend beton (ZVB) heeft het mogelijk gemaakt om een nieuwe storttechniek toe te passen. Hierbij wordt de verse betonspecie via de basis in de bekisting verpompt, dit in tegenstelling tot de traditionele top-vulmethode. Er rijzen echter een aantal fundamentele vragen op omtrent de optredende bekistingsdrukken bij de toepassing van deze geavanceerde bekistingsvulling. In het kader van het voorliggend onderzoek wordt een aantal van deze vraagstukken behandeld en er worden praktische en innovatieve oplossingen voorgesteld, welke in de volgende paragrafen van deze samenvatting beknopt zullen worden beschreven. Deze thesis en het gerelateerd onderzoek is onderverdeeld in zeven hoofdstukken.

In hoofdstuk 1, is de algemene context van het huidig onderzoek beschreven en zijn de doelstellingen van het voorliggend onderzoek geformuleerd, welk hieronder kort worden opgesomd:

- Een uitgebreid overzicht geven van de meest relevante ontwerpcodes voor bekistingen en het analyseren van de toepasbaarheid of de geldigheidsgrenzen in verband met het vullen van bekistingen met verse ZVB via de basis;
- Het uitvoeren van een reeks grootschalige storttesten met ZVB waarbij de verse betonspecie via de basis wordt toegevoegd, en waarbij:
  - ✓ Het betondebiet aan de inlaat van de bekisting wordt gemeten;
  - ✓ De wanddrukken tijdens het vulproces worden gemeten;
  - ✓ De betonkwaliteit d.m.v. visuele inspecties op boorkernen wordt onderzocht.
- Een uitgebreid overzicht geven van de numerieke simulatietechnieken welke toegepast worden bij het modelleren van betonstromen in de verse toestand;
- Geschikte numerieke en analytische modellen opstellen om de wanddrukken te kunnen voorspellen welke optreden tijdens het vullen van de bekisting via de basis, gevolgd door de validatie van deze modellen via een vergelijking tussen de uitgevoerde metingen en de simulatieresultaten.

In Hoofdstuk 2, worden de reologie en de kenmerkende eigenschappen van ZVB in de verse toestand uiteengezet. Het vloeigedrag van ZVB wordt beschreven door middel van een reologisch model, waaronder het Bingham model en het Herschel-Bulkley model. Een reologisch model beschrijft het verband tussen de afschuifsnelheden en de optredende schuifspanningen. De kenmerkende eigenschappen van ZVB, waaronder shear thickening, thixotropie en segregatie, hebben een duidelijke invloed op het stromingsgedrag van het beton in verse toestand. Shear thickening is bij alle voor de vulproeven geselecteerde ZVB mengsels waargenomen. Om die reden werd het Herschel-Bulkley model voor het huidig onderzoek gekozen. In dit hoofdstuk is tevens een overzicht van de bestaande soorten reometers voor het meten van de reologie van ZVB gegeven. Twee verschillende reometers zijn tijdens de uitgevoerde vulproeven gebruikt geweest, met name de Tattersall Mk-II rheometer en de BML Contec-Viscometer 5. Deze laatste bleek eenvoudiger in gebruik te zijn en de reologische parameters van de verse betonspecie werden ook nauwkeuriger opgemeten.

In Hoofdstuk 3 worden de vergelijkingen van Navier-Stokes besproken, welke het behoud van massa en impuls beschrijven. Het behoud van energie is evenwel niet in rekening genomen geweest, vanwege de aanname dat de dichtheid en de viscositeit van de verse betonspecie onafhankelijk is van de meestal zeer kleine temperatuurs-veranderingen welke tijdens het verpompen en het storten optreden. Op basis van deze stromingsvergelijkingen, is een nieuw analytisch model afgeleid, waarmee de stromingsverliezen en de resulterende wanddrukken tijdens het verpompen van vers beton doorheen leidingen en in bekistingen snel bepaald kan worden. Bij de afleiding van het analytisch model is het Herschel-Bulkley model in rekening genomen.

Twee soorten vultechnieken met ZVB worden besproken: het vullen langs de top van de bekisting en de vulling via de basis van de bekisting. De top-vulling is de meest toegepaste vultechniek gezien de reeds beschikbare kennis en ervaring. Het vullen van de bekisting met ZVB via de basis wordt daarentegen heel wat minder toegepast. Over deze vultechniek is nog maar weinig onderzoek verricht, wat het gebrek aan kennis en praktische ervaring verklaart. Deze trend is ook merkbaar in de beschikbare normen omtrent het ontwerpen van bekistingen. Niet alleen zijn deze normen hoofdzakelijk opgesteld voor vulprocessen met conventioneel beton, ze zijn ook alleen geldig voor top-vulling met relatief lage vulsnelheden. Omwille van het vastgesteld gebrek aan onderzoek, kennis en praktische ervaring, richt dit onderzoek zich volledig op de vultechniek via de basis van de bekisting.

Het analytisch model werd toegepast op het vulproces via de basis van de bekisting, waarbij tevens het concept van de hydraulische diameter werd geïntroduceerd. Het analytisch model toont duidelijk aan dat bij de toepassing van dit vulprocédé de bekistingsdrukken hoger zijn dan de hydrostatische druk. Dit komt door de viskeuze stromingsverliezen. Met dit gegeven wordt in de huidige ontwerpnormen voor bekistingen geen rekening gehouden.

Hoofdstuk 4 is onderverdeeld in twee grote delen. In een eerste deel wordt een overzicht gegeven van de numerieke simulatietechnieken welke reeds aangewend worden voor het simuleren van betonstromen in leidingen en in bekistingen. De werkingsprincipes en het toepassingsgebied van deze simulatietechnieken worden besproken, evenals hun voor- en nadelen. Na evaluatie van de voor- en nadelen van elke simulatiemethode, is de Eindige Volume Methode (EVM) in combinatie met de Volume of Fluid (VOF) methode en de Level-Set (LS) interface tracking techniek gekozen voor de uitwerking van de rekenmodellen van de tijdens dit onderzoek uitgevoerde vulexperimenten. Dit gecombineerd numeriek schema en de bijhorende instellingen worden in een tweede deel van hoofdstuk 4 toegelicht, evenals een veelbelovende simulatietechniek waarbij de wapening impliciet wordt gemodelleerd als een poreuze zone.

In het kader van het huidig onderzoek, werden twee reeksen van grootschalige vulproeven met ZVB uitgevoerd op het Magnel Laboratorium voor Betononderzoek (MLBO) van de Universiteit Gent, waar bij iedere vulproef de verse beton via de basis in de bekisting gepompt werd. Deze grootschalige vulexperimenten zijn beschreven in hoofdstuk 5. Een lange I-ligger, tien kolommen en twee muren werden gestort.

De invloed van de viscositeit van de ZVB, de vulsnelheid en de aanwezigheid van wapening op de bekistingsdruk werd onderzocht. Uit de gemeten wanddrukken bleek duidelijk dat de hydrostatische druk overschreden werd, zoals ook voorspeld door het analytisch model. De vultesten brachten ook aan het licht dat de stromingsverliezen in grootte toenamen wanneer er gevuld werd met een hogere snelheid, er gebruik werd gemaakt van een ZVB met een hogere viscositeit en wanneer de stromings-doorsnede klein werd (zoals bij de kolommen met de wapeningsstaven).

Het vullen van ZVB via de basis van de bekisting laat toe om zeer hoge vulsnelheden toe te passen en aldus een hoog bouwtempo te realiseren. Daarentegen, omwille van de hogere wanddrukken zijn sterkere en stijvere wandelementen evenals sterkere verbindingen noodzakelijk. Door de hogere toegepaste vulsnelheden en de daaruit volgende korte vultijden is het effect van thixotropie te verwaarlozen. De eindkwaliteit van het verharde beton werd via een visuele inspectie van de homogeniteit op geboorde betonstalen onderzocht. Deze betonstalen werden op verschillende plaatsen in het volume van de gestorte betonnen elementen ontnomen. De eindkwaliteit hiervan bleek uitstekend te zijn, en dit ondanks de zeer hoge vul-snelheden.

In hoofdstuk 6 worden de numerieke simulaties van de uitgevoerde pomp- en vulproeven uitgebreid beschreven. Het in hoofdstuk 3 uitgewerkt analytisch model is eveneens op alle uitgevoerde vultesten toegepast geweest. Uit de doorgevoerde gevoeligheidsanalyse blijkt dat de invloed van de consistentiefactor en de consistentieindex van het Herschel-Bulkley model op de stromingsverliezen en de resulterende wanddruk belangrijk is. Daarom is het noodzakelijk om de reologie van het geselecteerde ZVB nauwkeurig te bepalen wanneer het vulproces via de basis van de bekisting toegepast wordt.

De simulatieresultaten zijn in goede overeenstemming met de metingen welke gedurende de vulexperimenten zijn uitgevoerd. De uit het analytisch model resulterende vaststelling, dat de optredende wanddruk de som is van de hydro-statische druk en de stromingsverliezen, wordt hierdoor bevestigd.

Het gekozen numeriek EVM-VOF-LS schema bleek vrij stabiel en relatief snel te zijn, maar dit schema vereist een zeer gelijkmatige vermazing van het rekendomein, preferentieel bestaande uit kubusvormige cellen. Deze eis is in vele gevallen niet eenvoudig te vervullen, zeker niet wanneer men te maken heeft met complexe bekistingsvormen of wapening. Daarom werd het in dit onderzoek aangewende EVM-VOF-LS schema uitgebreid met een numeriek model voor het modelleren van stromingen in poreuze zones. Hierbij wordt de wapening als een poreuze zone beschouwd en als dusdanig niet expliciet gemodelleerd. Alhoewel de bepaling van de parameters van deze poreuze zone voor complexe wapeningsconfiguraties in het algemeen nog een echte uitdaging vormt, voor de in de vulproeven aangewende wapeningsconfiguratie bleek het EVM-VOF-LS schema uitgebreid met een poreus model heel efficiënt te zijn. De hiermee berekende wanddrukken waren in zeer goede overeenstemming met de simulatieresultaten van de numerieke modellen waarbij de wapeningsstaven expliciet gemodelleerd werden.

Op basis hiervan kan men stellen dat het EVM-VOF-LS schema, uitgebreid met het poreus modelleren van de wapening, veelbelovend is. Deze combinatie leidt tot een drastische inkorting van de tijd nodig voor het opbouwen van het numerieke model en de rekentijd.

De maximale wanddrukken berekend met het analytisch model zijn eveneens in zeer goede overeenstemming met de simulatieresultaten van de numerieke modellen. De rekentijd bij het gebruik van het analytisch model is uitermate klein, maar informatie over de lokale snelheden in de bekisting is niet beschikbaar. De via het analytisch model berekende stromingsverliezen en de maximum wanddruk laten toe om heel snel en eenvoudig de benodigde pompcapaciteit evenals de vereiste sterkte en de stijfheid van de bekistingselementen vast te leggen.

Tenslotte worden de in de afzonderlijke hoofdstukken vermelde conclusies nog eens overzichtelijk samengevat in hoofdstuk 7. Tevens wordt een aantal aanbevelingen voor verder onderzoek gepresenteerd.

De in dit onderzoek gevormde conclusies worden hieronder kort weergegeven:

- Bij het verpompen van ZVB via de basis van de bekisting, is de wanddruk de som van de hydrostatische druk en de stromingsverliezen, welke aanzienlijk worden voor hoge vulsnelheiden, kleine secties (bv kolommen met een dichte wapeningsconfiguratie) of bij gebruik van een ZVB met een hoge viscositeit. De tijdens de vulproeven gemeten drukverliezen bedroegen 7% tot 16% van de totale wanddruk.
- De techniek van het vullen van een bekisting met ZVB via de basis laat hoge vulsnelheden toe, waardoor de doorlooptijd van het storten sterk gereduceerd wordt. De hierbij optredende hogere wanddrukken echter maken het gebruik van sterkere en stijvere bekistingselementen en hun verbindingen noodzakelijk.
- Een correcte bepaling van de reologische materiaalparameters van het ZVB mengsel is vereist, aangezien deze parameters een beduidende invloed hebben op de optredende stromingsverliezen en de daarmee gepaard gaande wand-drukken. Vooral de invloed van de consistentiefactor en de consistentieindex van het Herschel-Bulkley model ten aanzien van de stromingsverliezen blijkt niet onbelangrijk te zijn.
- Indien enkel de maximale bekistingsdruk dient bepaald te worden met als doel de bekistingswanden op basis van sterkte en stijfheid oordeelkundig te kunnen selecteren, dan is een eenvoudige en relatief snel uit te voeren stationaire simulatie van het vulproces reeds voldoende. Een tijdsafhankelijke simulatie op basis van het EVM-VOF-LS schema is vereist als men het mogelijk optreden van luchtinsluitsels ten gevolge van een onoordeelkundige keuze van de positie van de betontoevoer wil detecteren of wanneer het zelf-nivellerend vermogen van het gekozen ZVB mengsel moet worden beoordeeld.
- Bij de toepassing van hoge vulsnelheden, is het effect van thixotropie op de resulterende wanddruk te verwaarlozen.

- Voor de wapeningsconfiguratie welke in onze vulexperimenten gebruikt is, zijn de simulatieresultaten verkregen met het model waarbij de wapeningsstaven vervangen worden door een poreuze zone in zeer goede overeenstemming met de resultaten van de numerieke simulaties waarbij de wapeningsstaven expliciet gemodelleerd zijn.
- De geselecteerde EVM-VOF-LS simulatietechniek laat toe om nauwkeurig de wanddrukken te voorspellen welke tijdens een vulproces via de basis van een bekisting optreden. De in dit onderzoek opgestelde numerieke modellen maken het mogelijk om een vulproces op een kostefficiënte manier te optimaliseren.
- Tevens zijn de met het analytisch model bekende maximale bekistingsdrukken in zeer goede overeenstemming met de simulatieresultaten van de numerieke modellen. Deze berekeningen zijn zeer snel en eenvoudig uit te voeren.

Chapter 1: Introduction

"There are books of which the backs and covers are by far the best parts." - Charles Dickens

"There is no book so bad that it is not profitable in some part." - Gaius Plinius

1.1 General context of the doctoral research

1.1.1 Self-compacting concrete (SCC) and concrete structures

As mentioned by De Schutter et al., concrete is without any doubt a truly fascinating building material [1.1]. When cast into moulds or formworks, where the marriage with the steel rebars takes place, any complex building shape can be obtained. There is no other building material that offers this degree of flexibility in a structural design.

Conventional vibrated concrete (CVC) is made out of predefined amounts of coarse and fine aggregates, sand, cement, water and some admixtures, which are all mixed together in a mixing device. In its fresh state, CVC behaves as a very stiff pasty-like material, which needs to be vibrated during the placement in order to become more fluid and thus to be able to fill a formwork completely and push out the entrapped air. The task of compacting CVC by means of vibration is a very labour intensive and therefore expensive activity, but it needs to be carried out very consistently in order to meet the strength and durability requirements of the resulting cast. However during construction, the rules of good casting practice are sometimes not followed due to the very physically demanding work, leading to poor quality casts as reported by De Schutter [1.2]. The lack of finding good workers, willing to carry out the placing and vibration of CVC, has led to many untrained labourers being used to carry out the compaction. An innovative solution to overcome this problem has been provided by the introduction of self-compacting concrete (SCC) in the concrete industry.

The research and development of SCC originally started in Japan in the mid-1980s, when the construction industry together with the academic world found new solutions for difficulties encountered with the durability of concrete structures and with quality assurance of complex structures that were difficult to cast. The solution that was proposed, was to develop a very fluid concrete which compacted itself through the use of gravity alone [1.1].

During the following decade, SCC gradually made its entrance into Europe through the Scandinavian countries and the Netherlands. Although it may still take some time for SCC to replace CVC and become the mainstream concrete for all in-situ placing, within the precast industry this has already happened. In the Scandinavian countries and the Netherlands quite a large part of their entire precast production is based on SCC. In Belgium, some important precast producing companies have also switched to using of SCC. Also some nice examples of in-situ placing in Bredene and Avelgem are to be mentioned.

The development of SCC has led to substantial improvements in the production environment and the working conditions: there is much less energy consumption, no additional vibration for compaction is required and therefore less noise during production, a decreased absence of workers due to sickness to be noted and a higher productivity. The higher material cost of SCC when compared to CVC is outweighed by these substantial improvements.

De Schutter et al. [1.1], Feys [1.3] and Poppe [1.4] defined SCC as a kind of concrete, which needs to possess sufficient fluidity in order to be able to fill a formwork completely (filling ability) without the aid of other forces than gravity, even when having to flow through narrow gaps (passing ability), but also showing a sufficient resistance to segregation, during flow and in stationary conditions (stability). Segregation in fresh concrete occurs when the coarse aggregates start to separate from the mortar paste and gather at the base of the formwork due to gravity, leading to a non-homogeneous concrete cast.

The previously stated definition of SCC may seem quite contradictory: the filling and passing ability require a very fluid (water-like) material, but the stability condition on its turn requires almost quite the opposite. Therefore, producing SCC is finding a compromise between the fluidity and the stability, forming a real challenge for every SCC manufacturer each day. In order to achieve sufficient fluidity in SCC, without increasing the water content, superplasticizers must be applied. As mentioned by De Schutter et al. [1.1] and Feys [1.3], only adding superplasticizers to a traditional concrete is not at all sufficient to create SCC, due to the large amount of coarse aggregates, which can form particle bridges when flowing through the narrow gaps, causing blocking. Therefore, the amount of coarse aggregates is reduced in order to fulfil the passing ability condition. On the other hand, extra amounts of fine materials, like limestone filler, fly ash or silica fume are required in order to increase the stability of the fresh SCC. This illustrates why the material cost is higher with SCC compared to CVC. The combination of all these materials, forming the concrete mix recipe, leads to a very specific flow behaviour or rheology in the fresh state which is quite distinct from the rheology of CVC.

1.1.2 Formworks and formwork pressure

During casting, the fresh concrete is pumped inside a formwork. Two types of filling processes can be observed in practice; filling from the top or filling from the base of the formwork. It is common practice to pour the concrete inside the formwork from the top, certainly when CVC is used. With SCC both filling methods are possible, although top-filling remains the most chosen filling method due to available practical experience.

Whether the concrete is supplied from the top or the base of the formwork, in both cases the concrete will exert a pressure on the formwork walls, and this due to its own weight as well as due to the concrete flow. The formwork walls will have to withstand these pressures and they will have to be strong and stiff enough.

Strong enough in order to prevent the collapsing of the formwork structure during the casting process, and stiff enough in order to guarantee the dimensional accuracy of the final geometry.

At present, quite a few formwork design codes exist for casting from the top with CVC [1.5-1.8], while almost no design codes are available for use with SCC, and certainly not when the base-filling method is used with high casting speeds.

In the present research, the base-filling casting process has been studied more in detail because it is our belief that it has some noticeable advantages compared to the more commonly used top-filling method.

1.1.3 The flow of SCC and numerical modelling

As stated in section 1.1.1, SCC is much more fluid than CVC, and as such it is able to flow easily between the rebars inside the formworks. This flow of fresh SCC during casting can be studied or analysed using computational fluid dynamics (CFD) models, as well as analytical models. These CFD models are based on the equations describing the general conservation laws for fluid flows. For isothermal conditions within a system under study these laws are the conservation of mass and the conservation of momentum (second law of Newton). Both conservation laws are commonly known as the Navier-Stokes equations.

While SCC can be described as a homogeneous material in a flow model, for which a single material behaviour law is valid, it can also be regarded as a true multiphase material, being considered as a suspension of the aggregates in a mortar paste. Regarding the latter approach, the simulation models will not only provide information regarding the flow velocities and the pressures, but also regarding the ability to prevent segregation and blocking from happening during the casting process. As such, these simulation models allow to effectively optimize a casting process, for example to determine the number and position of inlets in order to obtain a good concrete levelling and to avoid air voids, to determine the required strength of the formwork walls and connections or the optimal casting speed.

1.2 Research objectives and outline of the doctoral thesis

1.2.1 Research objectives

Skarendahl et al. truthfully state that due to the introduction of SCC, the shape of a concrete element can be defined with more freedom [1.9]. However, because of a lack of fundamental knowledge concerning the flow of fresh SCC in formworks and regarding the resulting formwork pressures, the designer is hindered in his desire to optimally take advantage of this truly improved form freedom. For the structural engineer and for the building contractor, fundamental questions remain concerning the design of the formwork layout, and regarding the casting or filling process, with or without advanced pumping techniques.

The present research study aims at providing relevant answers to these fundamental questions, as well as to contribute to the build-up of common scientific knowledge and experience regarding base-filling with SCC. Therefore, the research objectives of the present doctoral thesis are:

- Presenting a comprehensive overview of the most relevant formwork design codes and analysing the applicability or limits of validity when casting from the base of a formwork with fresh SCC;
- Performing full-scale formwork base-filling experiments with SCC and:
  - ✓ Measuring the fresh concrete flow at the inlet;
  - ✓ Measuring the wall pressures during the casting process;
  - ✓ Analysing the resulting quality of the cast through visual inspection of drilled samples;
- Presenting a comprehensive overview of the numerical simulation techniques applied in fresh concrete flow modelling;
- Building adequate numerical and analytical models in order to predict the wall pressures during the base-filling experiments, followed by a comparison of the measurements and the simulation results in order to prove the validity and the predicting ability of the presented simulation models and analytical models.

In a previous research program, Feys [1.3] studied the mixture composition and the resulting rheological behaviour of SCC in a very fundamental way, in view of a thorough understanding of pumping of SCC under pressure. The research performed by Feys [1.3] has formed the basis for the numerical and analytical models being developed within the present research [1.13, 1.14 and 1.15].

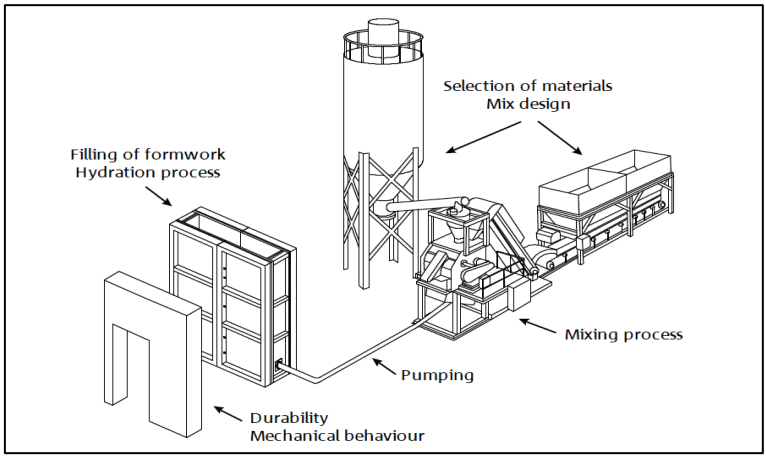

Fig. 1-1: Overview of a casting process [1.16].

The tight interconnection between the current research and the research performed by Feys, both performed at the Magnel Laboratory for Concrete Research (MLCR) of Ghent University (UGent), is illustrated in Fig. 1-1.

The ultimate goal of a future research program is to create a fully automated precast factory, where the required rheology of the fresh SCC is obtained through optimal mixing of the constituents (first stage), followed by the pumping of the fresh SCC mix through ducts (second stage) into multiple formworks (final stage).

1.2.2 Outline of the doctoral thesis

The rheological models describing the shear flow behaviour and the characteristic properties of fresh SCC, like shear thickening, thixotropy and segregation, are presented in chapter 2. This information is of fundamental importance when studying the flow behaviour of SCC through pumps, ducts and formworks. Also a brief review of the currently existing types of rheometers for measuring the rheology of fresh SCC is given. The two types of rheometers which have been used during our formwork base-filling tests, the Tattersall Mk-II rheometer and the BML Contec-Viscometer 5, are explained in detail.

In chapter 3, the general flow equations are presented. Based on these equations, a new analytical model for determining the shear flow losses and the resulting wall pressures when pumping fresh SCC through ducts and in formworks has been derived. Two formwork filling techniques when using SCC are presented: the top-filling and the base-filling method. An overview of the most relevant formwork design codes is given, together with their limits of applicability. Because the base-filling method is much less applied in casting processes with SCC and very little research has been performed so far, the present research work focusses on base-filling.

In chapter 4, a comprehensive overview of the modelling techniques currently applied to fresh concrete flow is given, with the aim to select the most appropriate one when simulating the performed casting experiments with SCC during this research.

The full-scale casting tests and the related simulations are presented in detail in chapter 5 and in chapter 6 respectively. In these two chapters, the wall pressure measurements are compared with the simulated formwork wall pressures, validating the analytical formwork pressure calculation model being presented in chapter 3. During these base-filling tests, the influence of several casting parameters on the formwork pressure is investigated.

In chapter 7, all the conclusions drawn from the performed research work which are reported in each of the individual chapter are summarized, together with a number of propositions towards further research.

Two appendices are appended at the end of the current thesis:

- Appendix A describes the calibration and the transformation procedure for the Tattersall Mk-II rheometer, being used during the first series of casting tests;
- All the measurements performed on the SCC mixtures used in the formwork filling tests are reported in Appendix B.

1.3 References

[1.1] De Schutter G., Bartos P., Domone P., Gibbs J., “Self-Compacting Concrete”, Whittles Publishing, Caithness (2008), 296 pages.

[1.2] De Schutter G., “Damage to Concrete Structures”, CRC Press - Taylor & Francis Group, Boca Raton, Florida (2013), 189 pages.

[1.3] Feys D., “Interactions between Rheological Properties and Pumping of Self-Compacting Concrete”, Ph-D dissertation, Ghent University, Ghent (2009).

[1.4] Poppe A.-M., De Schutter G., Audenaert K., Boel V., “Kennismaking met zelfverdichtend beton (1): samenstelling en reologie”, Bouwkroniek (2002) (in Dutch), pp. 30-34.

[1.5] CIRIA, “CIRIA Report 108 - Concrete pressure on formwork”, Construction Industry Research and Information Association, London (1985).

[1.6] Deutsches Institut für Normung, “DIN 18218 - Frischbetondruck auf lotrechte Schalungen”, Beuth Verlag, Berlin (2008).

[1.7] ACI Committee 347-04, “Guide to Formwork for Concrete”, ACI Standard (2004).

[1.8] Adam M., Bennasr M., Santos Delgado H., “Poussée du béton frais sur les coffrages”, Annales de l’ITBTP, (1965).

[1.9] Skarendahl A., Bilberg P., Beitzel H., Dieryck V., Ghezal A., Khrapo M., Leemann A., De Schutter G., Sonebi M., Österberg T., “Casting of Self-Compacting Concrete”, RILEM (2006), ISBN 2-35158-001-X, 26 pages.

[1.10] Cauberg N., Desmyter J., Piérard J., Parmentier B., “Bekistingsdruk bij zelfverdichtend beton - WTCB dossiers (in Dutch) - Katern 7, nr. 3”, WTCB (2006).

[1.11] Gardner N.J., “Formwork pressure and cement replacement by fly ash”, American Concrete International, Farmington Hills (1984).

[1.12] Billberg P., “Form pressure generated by SCC - Influence of Thixotropy and Structural Behaviour at Rest”, Ph-D dissertation, Royal Institute of Technology, Stockholm (2006).

[1.13] Tichko S., Feys D., De Schutter G., Vierendeels J., Verhoeven R., Troch P., “Numerical modelling of the flow of self-compacting concrete in conveying pipes”, 6th International RILEM Symposium on self-compacting, SCC 2010 Conference Proceedings vol. 2, Montreal (2010), pp. 719-728.

[1.14] Tichko S., Van De Maele J., Vanmassenhove N., De Schutter G., Vierendeels J., Verhoeven R., Troch P., “Numerical simulation of formwork pressure while pumping self-compacting concrete bottom-up”, Eng. Struct., vol. **70**, (2014), pp. 218-233.

[1.15] Tichko S., De Schutter G., Troch P., Vierendeels J., Verhoeven R., Lesage K., Cauberg N., “Influence of the viscosity of self-compacting concrete and the presence of rebars on the formwork pressure while filling bottom-up”, Eng. Struct., vol. **101**, (2015), pp. 698-714.

[1.16] Desnerck, P., “Compressive, Bond and Shear Behaviour of Powder-Type Self-Compacting Concrete”, Ph-D dissertation, Ghent University, Ghent (2011).

Chapter 2: Rheology and fresh properties of SCC

"Real science is discovery, it's not invention. The truths are there, whether we find them or not." - Larry Fleinhardt

2 Overview of this Chapter

Chapter 2 is divided into three main sections. Section 2.1 focuses on the aspects of rheology of fresh SCC which are directly linked to the constitutive relations. These relations express the relation between stresses and strain rates in fluids. Once the appropriate constitutive relations for describing the flow behaviour of fresh SCC have been selected, they are implemented in the Navier-Stokes equations, which will be presented in detail in chapter 3. In section 2.2, the very important topics of shear thickening, thixotropy and segregation, which are characteristic material properties observed in fresh SCC, are introduced and discussed from a theoretical point of view. Last but not least, in section 2.3 the measuring devices used for quantifying the rheological behaviour of fresh SCC are presented. Special attention is given to the two rheometers used in the current research.

2.1 Rheological model for SCC

2.1.1 Introduction

The main purpose here is to cover the aspects of the rheology of SCC which are relevant for the present research work, rather than to explain in full detail all the aspects of rheology of concrete and more specifically the rheology of SCC. This has been extensively done by other authors, like De Schutter et al. [2.1], Feys [2.2], Poppe [2.3], Wallevik [2.4], Heirman [2.5] and Macosko [2.6].

Rheology is generally defined as the study of flow and deformation of matter. When referring to the Greek roots of the word rheology, $\rho\varepsilon o\nu$, it should be defined as the study of flow. In principle, rheology includes everything dealing with flow behaviour: aeronautics, hydraulics, fluid dynamics and even solid mechanics. However, in practice, rheology has usually been restricted to the study of fundamental relations, called constitutive relations, which express the mathematical relation between force and deformation or stresses and strain rates in materials, primarily liquids.

The simplest relation between force and deformation of a perfectly elastic solid, is Hooke's law (1678). It is probably the first constitutive equation, which states that force is proportional to the deformation or,

$$\sigma = E\varepsilon \tag{2.1}$$

$$\tau = G\gamma \tag{2.2}$$

where σ is the normal force per unit area or axial stress (Pa), ε is the relative length change or axial strain (-), τ is the shear force per unit area or shear stress (Pa), γ is the angle of deformation (-), *E* is the elastic modulus (Pa) and *G* is the shear modulus (Pa). Steel is for example a perfectly elastic solid, at least when the deformations are relatively small.

For perfectly viscous fluids, like water, the simplest constitutive equation is Newton's law of viscosity (1687). For a fluid layer being submitted to a shear stress in the x-direction on a plane with the normal vector in the y-direction, it expresses that the shear stress in the fluid layer is proportional to the rate of straining or,

$$\tau = \eta\dot{\gamma} = \eta\frac{\partial v_x}{\partial y} \tag{2.3}$$

where η is the Newtonian viscosity (Pa.s), $\dot{\gamma}$ (= dγ/dt) is the rate of straining or shear rate and $\partial v_x/\partial y$ is the velocity gradient of the x-component of the velocity vector (s^{-1}).

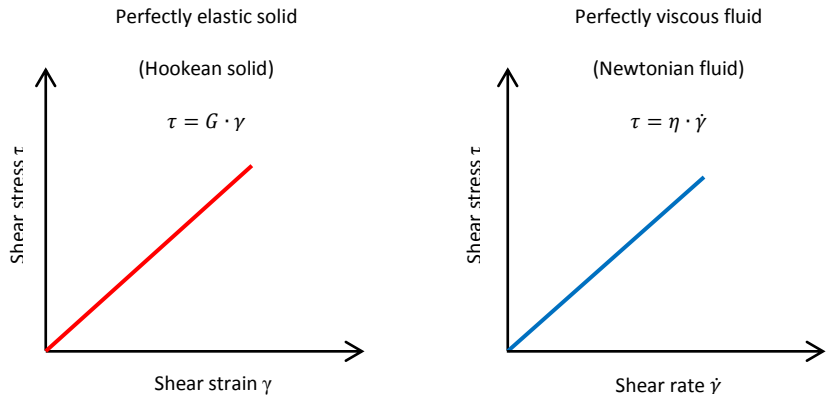

Fig. 2-1: Constitutive equations in case of simple shear for a perfectly elastic solid (left) and a perfectly viscous fluid (right) [2.5].

Although these constitutive equations seem to be quite similar, as shown in Fig. 2-1, they represent a totally different material behaviour. This is further illustrated in Fig. 2-2, where for an applied constant stress, the angle of deformation is constant for the perfectly elastic solid, while the angle of deformation is changing at a constant rate for the perfectly viscous fluid. Once the stress is removed, the elastic solid returns to its original condition, but a viscous fluid stays in its finally achieved shape.

As mentioned by Feys [2.2], Heirman [2.5] and Macosko [2.6], the elastic solid is said to have a perfect shape memory, whereas the viscous fluid does not have any shape memory at all.

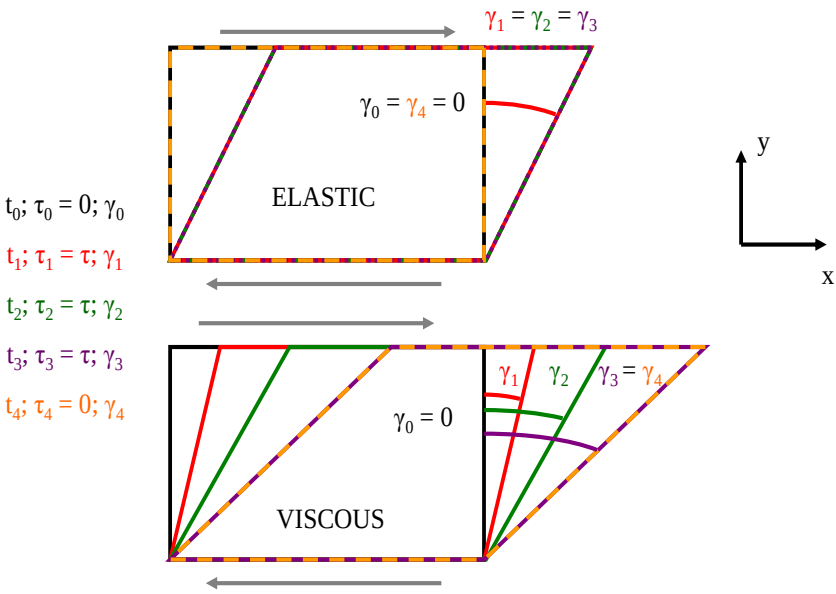

Fig. 2-2: Response of the angle of deformation for an elastic and viscous material to a stepwise stress function [2.2].

2.1.2 Rheological model for SCC in the fresh state

2.1.2.1 Non-linear behaviour

Fluid concrete, and more especially SCC, is not behaving as a perfectly viscous Newtonian fluid in the fresh state. Therefore, other constitutive relations are required to capture properly the flow behaviour of concrete or SCC.

Non-Newtonian flow behaviour can be described mathematically using a non-linear relationship between shear stress and shear rate. In this case, the viscosity is no longer constant for all shear rates. When the viscosity decreases with increasing shear rate, the fluid is said to be shear thinning and the flow curve, representing this non-linear relation between shear stress and shear rate, is bending downward. In the opposite case, when the viscosity is increasing with increasing shear rate, the fluid is revealing shear thickening behaviour and the flow curve is bending upward. Most SCC types in Belgium show varying levels of shear thickening behaviour, as will be further explained in section 2.2.

Eq. (2.4), commonly referred to as the Power-Law model, is able to describe shear thinning and shear thickening behaviour, and is one of the most applied models in rheology:

$$\tau = K\dot{\gamma}^n \quad (2.4)$$

where K is the consistency factor (Pa.s^n) and n is consistency index (-). The shear thinning or shear thickening behaviour is captured by the consistency index n. For $n < 1$, the material is showing shear thinning behaviour while for $n > 1$, shear thickening is expressed. The Power-Law model is also able to represent Newtonian behaviour ($n = 1$).

2.1.2.2 Yield stress

Some materials like fresh SCC, and concrete in general, need a certain stress to be applied before flow initiates, which means that they show a yield stress behaviour. Other known yield stress materials are paint, blood, toothpaste and ketchup. This material behaviour can be modelled mathematically by adding the yield stress to the Newtonian model or the Power-Law model.

When the relationship between shear stress and shear rate remains linear once the yield stress is exceeded, as for CVC, then the flow behaviour of the material can be described by the following equation, better known as the Bingham model:

$$\tau = \tau_0 + \mu_p\dot{\gamma} \quad (2.5)$$

where τ_0 is the yield stress (Pa) and μ_p is the plastic viscosity (Pa.s). In case this relationship between shear stress and shear rate is non-linear once the yield stress is exceeded, as for SCC, then the flow behaviour of the material can be expressed using the Herschel-Bulkley model:

$$\tau = \tau_0 + K\dot{\gamma}^n \quad (2.6)$$

As can be noticed in Eqs. (2.5) and (2.6), the shear rate can only be non-zero when the shear stress exceeds the yield stress.

The Bingham model is a special case of the Herschel-Bulkley model, where the consistency index n equals one. A material obeying the Herschel-Bulkley relation is called shear thinning or shear thickening for the same conditions as mentioned for the Power-Law model.

Fig. 2-3 illustrates the characteristic flow curves for a Newtonian, a shear thinning, a shear thickening and a yield stress material (Bingham).

The SCC mixtures which were used for the pumping and filling experiments of the present research all revealed shear thickening behaviour in the fresh state. This is quite common for the raw materials being used in SCC mixtures in Belgium. The Herschel-Bulkley material model was therefore selected to characterise their flow behaviour.

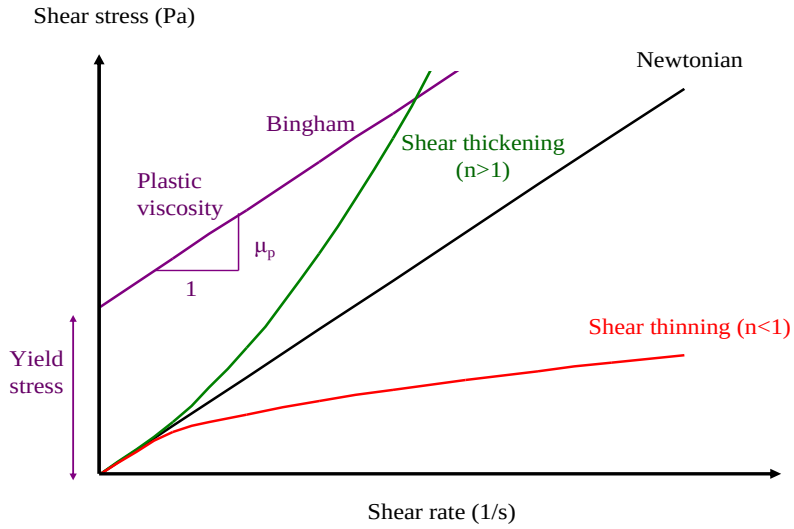

Fig. 2-3: Flow curves for a Newtonian (black), shear thinning (red), shear thickening (green) and Bingham material (purple) [2.2].

2.1.2.3 Time dependency

For some materials, the viscosity can change with time. This is caused by physical or chemical phenomena. Thixotropy and anti-thixotropy are well known time dependent effects. A description of these time effects on concrete will be given in section 2.2.

2.1.2.4 Different definitions of viscosity

Several definitions of viscosity can be found in literature. Some of them will also be used extensively in this work. A clear distinction between these types of viscosities will be made here.

The apparent viscosity at a certain shear rate can be represented by the inclination of a line connecting the flow curve at that specific shear rate with the origin. Therefore it is defined as the ratio between the local shear stress and the corresponding shear rate. Although the apparent viscosity will be used quite often in this study, it is mostly applied in literature dealing with non-concrete rheology.

The tangential viscosity at a certain shear rate is the inclination of the flow curve at that specific shear rate. It can be determined as the first derivative of the flow curve to the shear rate, at that specific shear rate.

The plastic viscosity only has a meaning when the Bingham model is applied. It represents the inclination of the straight line, which equals the tangential viscosity for shear rates larger than zero.

The difference between the apparent viscosity and the tangential viscosity is shown in Fig. 2-4, whereas the plastic viscosity is shown in Fig. 2-3. For a Newtonian liquid, these three different types of viscosity are all equal.

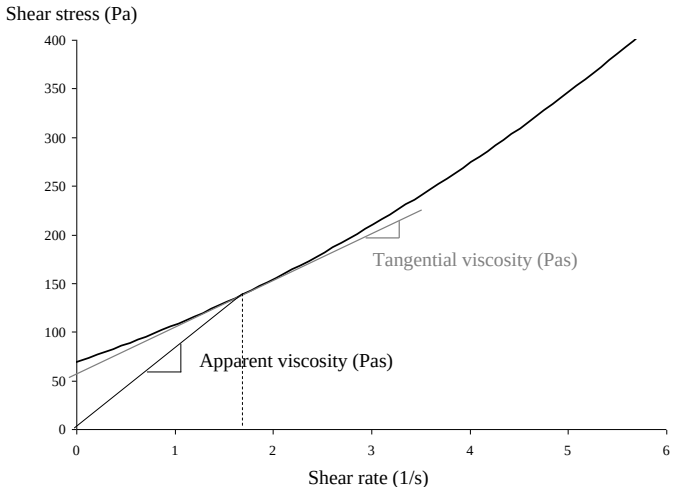

Fig. 2-4: Difference between apparent (black) and tangential viscosity (grey) [2.2].

2.1.2.5 Additional remarks regarding the presented material models

As Macosko clearly mentioned [2.6], all the rheological material models presented in this section should be described by means of 3D tensors with variability in time in order to be theoretically correct. The full 3D equations of the Herschel-Bulkley model, which has been chosen in the present study for characterising the flow behaviour of the tested SCC mixtures, will be presented and further discussed in chapter 3.

2.2 Shear thickening, thixotropy and segregation

2.2.1 Shear thickening

2.2.1.1 Introduction

As already mentioned in section 2.1.2, in Belgium the SCC mixtures in the fresh state do show shear thickening behaviour, which makes the relation between shear stress and shear rate non-linear. Shear thickening is defined as an increase in apparent viscosity with increasing shear rate in a steady shear flow.

Fresh SCC can be regarded as a suspension of some solid particles (the aggregates) in a liquid phase (the cement paste), as mentioned by Feys [2.2], Wallevik O.H. [2.4], Heirman [2.5] and Wallevik J.E. [2.7]. The solid particles represent the suspended phase, whereas the liquid phase is defined as the suspending phase.

Suspensions can be classified as colloidal, non-colloidal or a combination of both. In colloidal suspensions, the solid particles have a typical particle size which is smaller than 1 µm, while in non-colloidal suspensions, the typical particle size varies between 100 µm and a few cm.

Different theories have been derived for explaining shear thickening behaviour in colloidal and non-colloidal suspensions [2.2, 2.6, and 2.8]. Concrete, and SCC in particular, contains both colloidal and non-colloidal particles. Therefore, according to Feys [2.2] it is most probable that the presented theories about shear thickening in colloidal and non-colloidal suspensions have to be combined in order to understand the shear thickening behaviour being observed in SCC in the fresh state.

2.2.1.2 Shear thickening effects in non-colloidal suspensions

2.2.1.2.1 Particle migration

Gadala-Maria and Acrivos [2.9] discovered during their study in 1980 that when shearing a concentrated suspension, a decrease in apparent viscosity with time is observed. Ovarlez et al. [2.10] found out that when a high shear rate distribution is applied to a concentrated suspension, the particles have a tendency to move to regions with lower shear rates, resulting in a flow-induced concentration profile of these particles. They also observed that the phenomenon was independent on the magnitude of the applied shear rate. Both experiments revealed a shear thinning behaviour when highly shearing a concentrated non-colloidal suspension.

Suspensions are submitted to high shear rates during rheometer measurements or when being pumped through ducts. Particle migration can therefore be expected to happen during these two processes. The impact of particle migration on rheometer measurements will be discussed further in section 2.3, while the effect of particle migration during pumping, and more particularly how it influences the shear flow losses, will be presented in chapter 3.

2.2.1.2.2 Shear-induced ordering and disordering

Shear-induced ordering and disordering has been primarily observed in colloidal suspensions (see section 2.2.1.3), but it has also been reported for small, mono-disperse non-colloidal particles by Bertrand et al. [2.11].

At low shear rates, these particles start to organize themselves in different layers. The interstitial layers do contain only the suspending fluid. Due to the absence of particles in these interstitial layers, shearing requires less energy and therefore the viscosity decreases with increasing shear rate.

This shear thinning is not a reversible effect because if no external energy is added to reorganize the suspension into a random packing, the layers continue to exist, even at very low or zero shear rate.

When increasing the shearing, from a certain shear rate or shear stress (also called the critical shear stress) on, the particles quit their layered positions and start forming a random packing again. As a result, viscosity drastically increases with increasing shear rate, and shear thickening is observed.

2.2.1.2.3 Grain inertia

Shear thickening in non-colloidal suspensions is not primarily caused by an order-disorder transition. It can also be triggered by the particles themselves, having some non-negligible amount of inertia which causes particle collisions. This effect has been reported by Bagnold [2.12] when suspending 1 mm wax spheres in a glycerine-water-alcohol mixture. Grain inertia is significant when it has at least an equal order of magnitude as the viscous forces. The importance of grain inertia can be determined by calculating the particle Reynolds number, Re_p, using Eq. (2.7):

$$Re_p = \frac{\rho_s . \dot{\gamma} . a^2}{\eta_s} \tag{2.7}$$

where Re_p is the particle Reynolds number (-), ρ_s is the density of the suspending medium (kg/m³), $\dot{\gamma}$ is the applied shear rate (1/s), a is the particle radius (m) and η_s is the apparent viscosity of the suspending medium (Pa s). This equation quantifies the effect of the inertia forces relative to the viscous forces [2.6]. According to Macosko [2.6], for Re_p much smaller than 0.1, the inertia forces can be neglected.

2.2.1.3 Shear thickening effects in colloidal suspensions

2.2.1.3.1 Brownian motion

Every material is subjected to thermal agitation when the temperature is higher than 0 K. According to Mewis [2.8], the amount of thermal agitation is determined by the thermal energy E_T, quantified by the following equation:

$$E_T = k.T \tag{2.8}$$

where k represents the Boltzmann constant (= $1.38.10^{-23}$ J/K) and T is the absolute temperature (K). For larger particles being suspended, the energy exerted by the temperature is too low when compared to gravity and the viscous drag forces. For particles smaller than 1 µm, the Brownian force (= kT/a) has a similar or even higher order of magnitude than gravity. This Brownian force causes the colloidal particles, or also referred to as the Brownian particles, to move permanently in a random pattern. This Brownian motion becomes more important than the other inter-particle forces when the particle size decreases further.

A lower limit for these Brownian particles is set at 1 nm, below which the size of the molecules becomes significant and the homogeneity of the suspending medium can no longer be assumed.

2.2.1.3.2 Inter-particle forces

2.2.1.3.2.1 Van der Waals attraction forces

The van der Waals forces is a general term which is used to define the attraction of intermolecular forces between molecules. As mentioned by Mewis [2.8] and Geiker et al. [2.13], these forces have three components, of which the London-dispersion force is the most important one. This force induces always an attraction between particles, caused by the interaction between induced dipoles in the neighbouring molecules.

2.2.1.3.2.2 Electrostatic forces

If only the van der Waals forces would be active in a suspension, then all the solid particles present in this suspension would be attracted to each other and a very large agglomeration of particles would be formed. The solid particles in the suspension are electrically charged on their surface. In the suspending medium, the counter-ions, which are ions with opposite charge, are attracted to these electrically charged solid particles.

As mentioned by Mewis [2.8] and Geiker et al. [2.13], this leads to a decreased concentration of the counter-ions with increasing distance from the particle, creating the so-called diffuse double layer. When two particles move towards each other, their diffuse double layers will start to overlap, creating a higher concentration of these counter-ions. Consequently, an osmotic pressure is produced in order to neutralize this over-concentration of counter-ions and the particles are pushed away from each other.

2.2.1.3.2.3 Steric hindrance

Adding a polymer layer to a particle surface can create a physical barrier for other particles. Therefore, two solid particles cannot approach closer than the separation distance created by the polymers. The absolute value of the potential caused by the van der Waals attraction forces and the electrostatic repulsion forces is monotonically decreasing with the inter-particle distance.

Instead, according to Mewis [2.8] and Geiker et al. [2.13] the absolute value of the potential caused by the polymers shows a more abrupt change from its characteristic value near the particle surface, to zero at a particle distance equal to the effective length of these polymers. This repulsion mechanism is called steric hindrance and is a purely geometrical phenomenon.

2.2.1.3.2.4 DLVO theory

Derjaguin and Landau, and Verwey and Overbeek discovered almost simultaneously that the inter-particle potentials may be added in order to calculate the total potential (DLVO theory) [2.14, 2.15]. This is qualitatively illustrated in Fig. 2-5.

It shows the large attraction when the particle separation distance is very low, but also the repulsion “mountain”, which the particles must overcome in order to be attracted to each other. This total potential can be modified by influencing the amount of electrostatic repulsion and/or steric hindrance. Doing so, more attraction or more repulsion can be created, depending on the desired outcome [2.2].

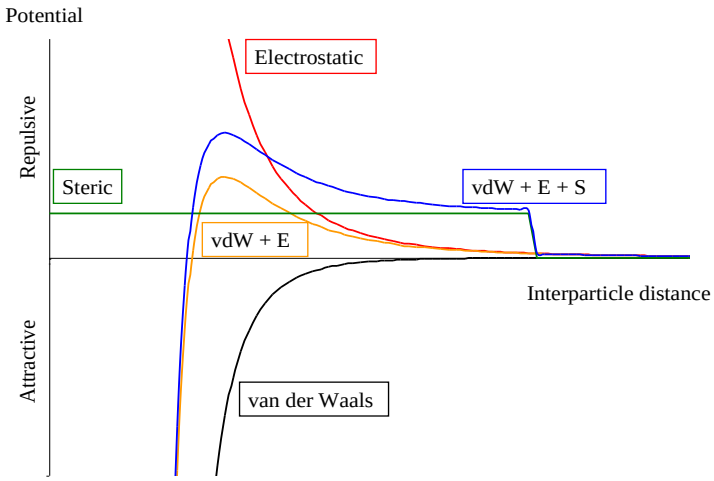

Fig. 2-5: Simplified approach of inter-particle forces: van der Waals attraction (black), electrostatic repulsion (red), steric hindrance (green) [2.2].

2.2.1.3.2.5 The effect of super-plasticers in SCC

Normally, the electrostatic repulsive forces of cement particles in water are not very large. As a result, these cement particles tend to coagulate quite easily. Super-plasticizers can create an additional electrostatic repulsion or a steric hindrance, or both. As a result, fewer particles coagulate, creating more individual particles. The shear stresses are no longer transferred through the agglomerates, but through the suspension and the mixture becomes more fluid. As the hydration reaction within the fresh SCC mixture progresses in time, the super-plasticizers will lose their efficiency, resulting in a loss of workability. More information regarding super-plasticers and their working principle is provided by Feys [2.2] and Flatt et al. [2.21].

2.2.1.3.3 Influence of suspended colloidal particles on viscosity

For colloidal particles submitted to low shear rates, the Brownian motion tends to keep the particles apart and creates a kind of microstructure, which has to be broken or has to be disturbed during shearing. As such, this thermo-dynamically induced microstructure is contributing to some extent to the yield stress behaviour being observed in a colloidal suspension.

At higher shear rates, the hydrodynamic forces on the particles are more important. As mentoned by Feys [2.2], both the thermodynamic and the hydrodynamic effects contribute to the viscosity of a colloidal suspension, and their relative importance is expressed by the Péclet number.

$$\mathrm{Pe} = \frac{\eta_s \cdot \dot{\gamma} \cdot a^3}{\mathrm{k.T}} \tag{2.9}$$

The larger the *Pe*-number is, the more important is the hydrodynamic part. The importance of the thermodynamic forces decreases when the *Pe*-number is larger than 1.

For the Brownian motion, a relaxation time can be defined. It is the time needed to re-arrange a certain colloidal suspension into random order after a disturbing action has been applied. At high shear rates, this Brownian relaxation time is too large, and as a result, re-organisation of the suspension due to the Brownian motion is not possible.

2.2.1.3.4 Shear thinning in colloidal suspensions

As for non-colloidal suspensions, shear induced ordering leading to shear thinning, has also been noticed in colloidal suspensions by Rastogi [2.16, 2.17]. Only in this case the ordering-disordering effect is reversible.

At sufficiently low shear rates, Brownian motion is able to reorganise the distribution of the particles from its shear-induced ordered state into a random state again. The transition from disordered to ordered state, or vice versa, occurs at *Pe* ~ 1.

2.2.1.3.5 Shear thickening in colloidal suspensions - cluster formations

Fig. 2-6 shows from the study of Laun [2.18] how the apparent viscosity of mono-disperse latex particles suspensions, with a particle diameter of 250 nm, changes for increasing shear stresses, and this for different volume fractions of these particles.

At low volume fractions, viscosity does not significantly change with increasing shear stress. When increasing the volume fraction, a clear change in viscosity can be seen, and viscosity becomes dependent on the shear stress.

At low shear stresses, the viscosity decreases with increasing shear stress, indicating shear thinning. At higher shear stresses, the viscosity increases with increasing shear stress, which is defined as shear thickening behaviour.

This shear thinning behaviour at low shear stresses has been explained in the previous section. According to Laun [2.18], shear thickening occurs due to the loss of the ordered state. The high shear stresses do cause an order-disorder transition to occur and consequently, the viscosity has to increase.

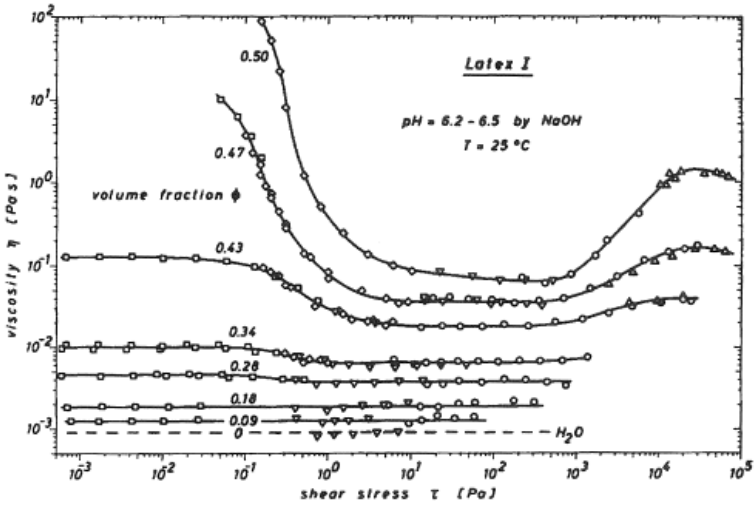

Fig. 2-6: Apparent viscosity as a function of shear stress for mono-disperse latex suspensions [2.18].

But, as mentioned by Feys [2.2], shear thickening does also occur due to large hydrodynamic forces, which are the result of the high shear stresses, acting between the particles in the suspension. These hydrodynamic forces can become larger than the repulsive forces between particles (electrostatic, steric hindrance or Brownian motion), and a temporary assembly of particles is formed.

Shear thickening occurs from a certain value of the applied shear stress on, named as the critical shear stress, at which the hydrodynamic forces equal the repulsive forces. When increasing the shear stress above the critical shear stress, clusters are formed.

When decreasing the shear stress below the critical shear stress, the relaxation time of these repulsive forces is sufficiently small compared to the characteristic time of the hydrodynamic forces and the clusters disappear. The observed shear thickening behaviour in colloidal suspensions is therefore a fully reversible phenomenon.

As mentioned by Cates [2.19], the clusters can only form in the compressive direction of the flow field. Any deviation from this compressive axis causes the clusters to dissolve. Non-spherical particles and particle softness can increase the lifetime of these clusters, due to larger possible deviations in orientation relative to the compressive axis.

The cluster formation is illustrated in Fig. 2-7, where the clusters in the compressive direction are represented by the black particles. The picture in the right shows an ideal situation of the presence of a compressive axis in a shearing flow. The picture in the left represents a more realistic situation, where some particle clusters can

transfer the force from one chain to another, which all have the direction of the compressive axis.

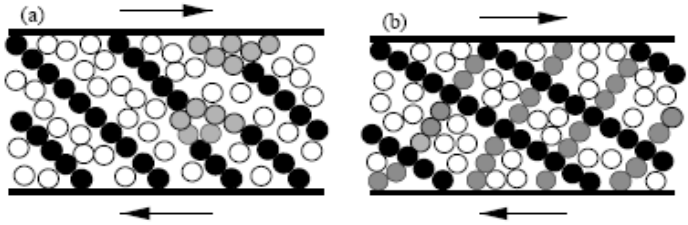

Fig. 2-7: Cluster formation - ideal situation (right), more realistic situation (left) [2.19].

2.2.1.3.6 Some personal thoughts regarding shear thickening and SCC

Most SCC mixtures show shear thickening behaviour. It mainly depends on the mixture composition and the range of shear rates and shear stresses to which the SCC is submitted during the flow process. For low shear rates, and more especially for shear stresses below the critical shear stress, shear thickening behaviour will not be observed. This is typically the case for an SCC flow inside a formwork during a filling process.

On the other hand, when the SCC is pumped through supply ducts, it will experience rather high shear rates and shear stresses. In this situation the SCC will show shear thickening behaviour, which will result in higher shear stress losses and higher pumping pressures. This has been very clearly demonstrated in the research work of Feys [2.2].

2.2.2 Thixotropy

2.2.2.1 Time dependent rheology of SCC

The rheological properties of cement based materials, like SCC, vary in time, as observed by Tattersall et al. [2.20]. The time dependent behaviour of fresh SCC is to be attributed to three specific phenomena: thixotropy, structural breakdown and loss of workability. While they can be distinguished quite easily in theory, in practise these three phenomena are overlapping each other in time, making a separate observation of them not at all obvious.

Thixotropy is defined as a reversible build-up and breakdown of internal structure due to flocculation or coagulation of cement particles, for which the influence of the inter-particle forces is still significant [2.7].

Structural breakdown can be defined as the breaking of existing “chemical” linkages between the cement particles, as mentioned by Wallevik [2.7] and Tattersal et al. [2.20].

These chemical linkages are most probably formed around the time of the first hydration temperature peak observed during the settlement of SCC. In contrast to the thixotropic behaviour, these chemical linkages generally do not build-up so fast. As a result, during the observation time, only the breakdown is seen, and not the build-up process.

Loss of workability is the formation of permanent connections during the hardening process of SCC. As reflected by Flatt [2.21], this is due to the coagulation of cement particles, or the chemical reactions between them, which cannot be broken unless a certain amount of stress is applied.

The influence of structural breakdown and loss of workability on the flow properties of fresh SCC typically becomes important at one hour and more after the start of a formwork filling process.

Traditionally, formworks are filled from the top at relatively low casting speeds (< 7 m/h). For tall concrete elements, this top-filling technique can lead to rather long formwork casting times. In this case, both structural breakdown and loss of workability will influence the filling process.

In the present research, a new promising casting technique with SCC has been studied. Instead of filling formworks from the top, the base-filling technique was applied. As will be presented in detail in chapter 5, this base-filling process allows for much higher casting speeds (> 50 m/h), and therefore drastically reducing the construction lead times.

All the casting experiments performed during this research were carried out within a few seconds up to 30 minutes, due to the high casting rates being applied. During these experiments, the effects of structural breakdown and loss of workability were minimal or to be neglected. For this reason we will be only discussing thixotropy in more detail in the following sections.

2.2.2.2 Fundamental modelling approaches

There are two fundamental approaches to study and to describe thixotropy: a microstructural approach and a macroscopic approach. Describing thixotropy by means of a microstructural model is extremely challenging. This is why thixotropy is mainly described by macroscopic or phenomenological models in literature.

Regarding both approaches, a review of some of the available models for describing thixotropy will be presented hereafter. More detailed information regarding these discussed models can be found in [2.2, 2.4, 2.22 and 2.23]. The aim of the following sections is not to give a complete overview of all existing models about thixotropy, but rather to explain a few selected models and their relation with flow simulations.

2.2.2.3 Microstructural models

This section gives an overview of two of the most relevant microstructural models used to describe thixotropic behaviour of cement based materials, and SCC more specifically.

2.2.2.3.1 Original Hattori-Izumi theory

As already mentioned in section 2.2.1.1, concrete in the fresh state can be regarded as a suspension of coarse aggregates in a fluid cement paste. During flow, the fresh concrete is sheared. Because the coarse aggregates are solid particles which are not sheared during flow, the shearing is concentrated in the cement paste.

The shear viscosity of the fresh concrete is therefore quite strongly dependent on the shear viscosity of the cement paste. Feys [2.2] observed that the presence of the coarse aggregates amplifies the shear viscosity of the suspension.

The transition of the concrete from the fluid stage towards the hardened stage can be understood throughout the formation of junctions between the suspended particles. These junctions can be subdivided into reversible junctions and permanent junctions.

The number of reversible junctions is gradually reducing as time progresses; they change into permanent junctions as the concrete hardens.

Hattori and Izumi [2.24] claim that the shear viscosity η_{HI} is dependent on the total amount of reversible "junctions" or connections between particles:

$$\eta_{HI} = B_3 \cdot J_t^{2/3} \tag{2.10}$$

where η_{HI} is the shear viscosity (Pa.s), B_3 is the friction coefficient (N.s) and J_t is the total number of reversible junctions per unit of volume (m^{-3}).

In order to determine J_t, the total number of primary particles n_3 per unit of volume must be known. This number represents the total number of particles per volume which can undergo reversible coagulation and which are in a completely dispersed state.

When J_t is defined as the total number of reversible junctions, then the total number of particles n_t after structural build-up (coagulation) or breakdown equals the total number of primary particles n_3 minus J_t,, with the assumption that no permanent connections are present and that the connections do not form closed networks but rather a kind of open-chain structure.

When n_t reaches the value of 1, the suspension is in a fully coagulated or structured state. This is visualised in Fig. 2-8.

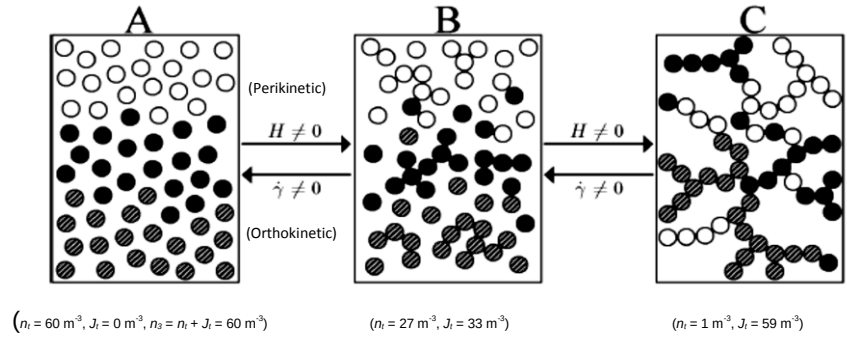

Fig. 2-8: Relationship between n_3, n_t and J_t [2.7].

While developing their theory, Hattori and Izumi also assumed that the number of junctions J_t can only increase when the shear rate equals zero (no stirring - perikinetic), and it can only decrease when shearing (with stirring - orthokinetic). The decrease in the total number of particles n_t, due to coagulation can be determined using the following equation:

$$-\frac{dn_t}{dt} = \frac{H \cdot n_t^2}{n_3} \tag{2.11}$$

where H represents the coagulation rate constant (1/s). When combining thixotropic build-up during rest, which is expressed through the coagulation rate H, and breakdown during shear, the total number of junctions J_t after a certain amount of time equals:

$$J_t = n_3 \cdot U_3 = \frac{n_3 \cdot \left(U_0 \cdot \left(\dot{\gamma} \cdot H \cdot t^2 + 1\right) + H \cdot t\right)}{\left(H \cdot t + 1\right) \cdot \left(\dot{\gamma} \cdot t + 1\right)} \tag{2.12}$$

where $J_0 = n_3 U_0$ and it refers to number of junctions at the initial state at $t = 0$, U_0 and U_3 are the coagulation states at the initial state and at the end state respectively (0 represents the fully dispersed state, while 1 stands for the fully coagulated state) (-).

Permanent junctions between particles are not considered in the original Hattori-Izumi theory. These type of permanent connections are related to loss of workability and the settlement of concrete.

2.2.2.3.2 The Wallevik model for thixotropy- a modified Hattori-Izumi theory

J.E. Wallevik [2.7] suggested three modifications to the original Hattori-Izumi theory, in order to quantify more accurately the thixotropic behaviour of cement based materials.

2.2.2.3.2.1 *Implemented modifications to the Hattori-Izumi model*

Instead of assuming a constant coagulation rate H and a constant shear rate $\dot{\gamma}$, Wallevik introduced the concept of fading memory equations. The idea behind this concept was that a cementitious material can remember the previous process actions (being sheared or not) it had undergone, but that the influence of this process history on the coagulation state would decrease with increasing elapsed time. This proposed modification of the original Hattori-Izumi theory incorporates two more variables m_a and m_b, which define how much the coagulation state should remember the past shear and coagulation respectively. The functions $H \bullet t$ and $\dot{\gamma} \bullet t$ in Eq. (2.12) are replaced by the memory modules Θ and Γ, shown in the following equations:

$$U_3 = \frac{J_t}{n_3} = \frac{U_0 \cdot (\Gamma \cdot \Theta + 1) + \Theta}{(\Theta + 1) \cdot (\Gamma + 1)} \tag{2.13}$$

$$\Gamma(geo,t) = \int_0^t e^{-(t-t')/m_a} \cdot \dot{\gamma}(geo,t') \cdot dt' \tag{2.14}$$

$$\Theta(geo,t) = \int_0^t e^{-(t-t')/m_b} \cdot H(geo,t',\dot{\gamma}) \cdot dt' \tag{2.15}$$

where Γ is the memory module for shear (-), Θ is the memory module for coagulation (-), the index "*geo*" indicates the dependency of a parameter on the surrounding geometry (for example the rheometer), m_a and m_b are the parameters indicating how much the past should be remembered (s), t stands for the current time in the experiment (s) and t' represents the time varying between the initial time and the current time, over which the integration must be taken (s).

2.2.2.3.2.2 *Influence of thixotropy on the yield stress and the plastic viscosity*

The original Hattori-Izumi theory has been further modified in order to determine the increase or decrease in yield stress and plastic viscosity due to thixotropic variations. Wallevik has selected the Bingham model (see section 2.1) for describing the flow behaviour of cement based materials. The influence of thixotropy on the Bingham material parameters, throughout the "modified Hattori-Izumi model", is expressed by:

$$\eta = B + \frac{\sqrt{C_y}}{\dot{\gamma}} \tag{2.16}$$

$$B = \mu + \left(a_1 \cdot B_3 \cdot {n_3}^{2/3}\right) \cdot {U_3}^{2/3} = \mu + \mu'' \tag{2.17}$$

$$\sqrt{C_y} = \tau_0 + \left(a_2 \cdot B_3 \cdot {n_3}^{2/3}\right) \cdot {U_3}^{2/3} = \tau_0 + \tau_0'' \tag{2.18}$$

where η is the shear viscosity (Pa.s), μ is the plastic viscosity when no reversible connections are present (Pa.s), τ_0 is the yield stress when no reversible connections are present (Pa), μ'' and τ_0'' are the thixotropic counterparts of the plastic viscosity and the yield stress (Pa.s and Pa resp.) and a_1 and a_2 are fitting parameters (-). Note that any loss of workability, which is caused by the permanent junctions between the particles must be incorporated in μ and τ_0 themselves. An increase in loss of workability will consequently be reflected by an increase in these two parameters and not in their thixotropic counterparts.

2.2.2.3.2.3 Coagulation Rate

As a last modification, Wallevik proposed a change in the coagulation rate function. The coagulation rate *H*, defined in the original Hattori-Izumi theory, only reflects the increase in the number of junctions due to Brownian motion. Coagulation can also be induced by a certain shear rate, lower than a critical shear rate. On the other hand, for shear rates above this critical shear rate, breakdown becomes dominant. As a result, the coagulation rate *H* has been defined as a function of the applied shear rate relative to a critical shear rate.

2.2.2.4 Macroscopic or phenomenological models

This section presents the thixotropic models proposed by Coussot and Roussel [2.22, 2.23, 2.25], which are both phenomenological models. They aim to quantify the effect of thixotropy from a macroscopic point of view, in contrast with the microstructural models discussed in the previous section.

2.2.2.4.1 The Coussot model for thixotropy

In most cases, the influence of thixotropy on the viscosity has not been considered in practice. Furthermore, the development of the yield stress is much more important, especially when studying the decrease in formwork pressure [3.24], the drawbacks of multi-layer casting [3.22] and even during rheological measurements.

The Coussot model, as formulated by the Eqs. (2.19) and (2.20) [2.22, 2.25], is able to accurately describe thixotropic behaviour observed in fresh cement pastes up to a resting time of one minute:

$$\tau = \eta_0 \cdot \left(1 + \lambda^n\right) \cdot \dot{\gamma} \tag{2.19}$$

$$\frac{d\lambda}{dt} = \frac{1}{T} - \alpha \cdot \lambda \cdot \dot{\gamma} \tag{2.20}$$

where τ is the shear stress (Pa), η_0 is the apparent viscosity at a fully dispersed state (Pa.s).

λ represents the structural state (varying between 0 for a fully dispersed state and ∞ for a fully coagulated state) (-), $\dot{\gamma}$ is the shear rate (1/s), T is the characteristic parameter for the structuration (s) and α is the characteristic parameter for the de-structuration (-).

2.2.2.4.2 The Roussel model for thixotropy

Based on Coussot's model, Roussel has developed a thixotropic model for fluid concretes like SCC [2.23]. This model is mathematically represented by the following equations:

$$\tau = \left(1 + \lambda_0 \cdot e^{-\alpha \cdot \dot{\gamma} \cdot t}\right) \cdot \tau_0 + \mu_p \cdot \dot{\gamma} \tag{2.21}$$

$$\tau = \tau_0 + A_{thix} \cdot t \tag{2.22}$$

where λ_0 is the initial structural state (-), τ_0 is the yield stress at a fully dispersed state (Pa), μ_p is the plastic viscosity of the fresh concrete (Pa.s), t is the time (s), A_{thix} is the flocculation rate of the fresh concrete (Pa/s).

Eq. (2.21) describes the shear stress evolution (decrease) during flow, assuming that the plastic viscosity is not influenced by thixotropy. Eq. (2.22) describes the build-up of (yield) stress during rest. The parameter A_{thix}, which is a material parameter, is a constant, resulting in a linear increase of the static yield stress with time. This has also been observed by Billberg [2.26].

2.2.2.5 Discussion

Two types of models for describing thixotropy have been presented in the previous sections, each having their advantages and disadvantages.

The microstructural models are based on the fundamental study of the interactions between the cement particles in the fresh concrete paste. Despite the fundamental approach, they are not able to accurately model thixotropy. Most probably, some additional physical phenomena which are linked to thixotropy are not taken into account. This explains why these microstructural models still require a lot of tuning parameters that need to be fitted through experiments and simulations, making them very complex and not very practical. On the other hand, the microstructural models are currently the only models describing the influence of thixotropy on the viscosity of cement based materials.

The phenomenological models of Coussot and Roussel form the best compromise between the physics and practice. On the other hand, the influence of the structural parameter λ on the viscosity is not implemented in these models, and therefore further investigations should be carried out. This should result in a simple extension of the current model.

According to Feys [2.2], for each shear rate, larger than a critical shear rate, there exists an equilibrium value of the structure parameter (U_3 or λ), which decreases with increasing shear rate (see Fig. 2-9). As a result, with increasing shear rate, the equilibrium values of the yield stress and the viscosity will decrease and the material becomes more liquid.

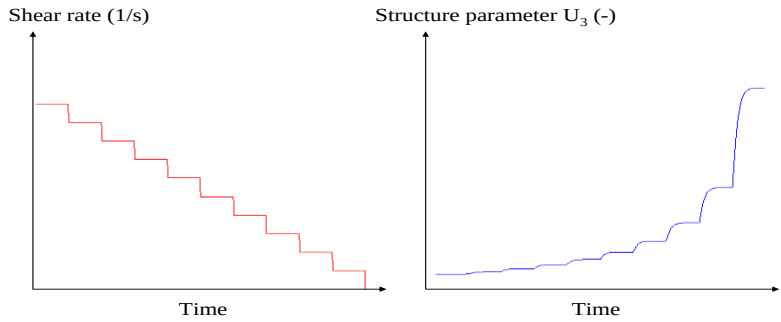

Fig. 2-9: Example of the evolution of the structure parameter with decreasing shear rate, according to the modified Hattori-Izumi theory [2.2].

Currently, the precise relationship between the equilibrium value of the structure parameter and the shear rate is still unknown for cement based materials, but according to the Coussot' model (Eqs. 2.19 and 2.20) [2.25], the equilibrium structure parameter λ at a certain shear rate should scale with the inverse of the shear rate $\dot{\gamma}$. In the modified Hattori-Izumi theory, no relationship between the equilibrium U_3 and the shear rate has been found and the static yield stress model of Roussel does not take this effect into account.

Also, implementing the microstructural model of Wallevik or the phenomenological model of Roussel in a CFD model describing a formwork base-filling process is not straightforward. In order to include such a model into a flow simulation, the thixotropic build-up, whether described by the parameter U_3 or λ, should be represented by a conservation equation of a transported quantity (see also chapter 4 - section 4.1.5). It fully makes sense to do this, as this structural thixotropic build-up is not only related to concrete left at rest in a formwork, but also related to moving concrete which is left unsheared, as being observed in plug flow regions inside a formwork. Unfortunately, none of the three presented models here describing thixotropy are formulated as a transport equation of a conserved property.

Wallevik [2.7] and Roussel [2.23], have chosen to use the Bingham material model to represent the concrete in its fresh state. While Wallevik is convinced that concrete in the fresh state is behaving like a Bingham material, others like de Larrard [2.27] and Feys [2.2] are convinced that fresh concrete is behaving like a true Herschel-Bulkley material. Wallevik attributes a non-linear flow curve during rheometer measurements to particle migration, and thus he states that the non-linear relation would be caused by a measuring artefact.

In the present research we have observed in the rheometer measurements being performed in 2010 and 2012 during the formwork filling tests that for all the selected SCC mixtures a non-linear flow curve was recorded. The rheometer tests that Wallevik performed during his Ph-D research work [2.7], were performed on BML Contec 3 and 4 rheometers, which are Couette-like rheometers. He indeed observed shear induced particle migration, which according to him led to a non-linear flow curve. During our second casting tests, performed in 2012, we used a BML Contec 5 rheometer, which is also a Couette-like rheometer. For this type of rheometer one could argue whether the measured flow curve was prone to particle migration or not, as Wallevik claimed.

However, during the first formwork filling tests in 2010, a Tattersall MK-II rheometer was used. This type of rheometer uses an helical shaped rotor, which is specifically designed by its inventor for preventing plug flow (and particle migration). The helical shape of the rotor induces a continuous mixing flow, preventing to a large extent these two disturbing phenomena to occur during the measurements. The measured flow curves were also highly non-linear, indicating a Herschel-Bulkley material behaviour. More information on rheometry will be presented in section 2.3, while the performed rheometer measurements on the selected SCC mixtures during the two series of casting tests are described in detail in appendix B.

Therefore, we are convinced that the selected SCC mixtures in their fresh state behave as a Herschel-Bulkley material. This has also been indirectly confirmed by the good agreement between the flow simulations and the flow measurements, were a Herschel-Bulkley model was used for characterising the flow behaviour of the tested SCC mixtures.

In section 2.2.1.3.6 we already mentioned that for low shear rate ranges the Bingham model could be used, because in these cases the effect of shear thickening would be minimal. According to Feys [2.2], for flow processes involving large shear rate ranges, like pumping fresh concrete through ducts or rheometry, shear thickening effects will occur and therefore a Herschel-Bulkley model is more suitable.

2.2.3 Segregation

As shown in Fig. 2-10, segregation in concrete occurs when the coarse aggregates start to separate from the mortar paste and gather at the base of the formwork due to gravity, leading to a non-homogenous concrete cast. According to De Schutter et al. [2.1], the segregation resistance can be defined as the ability of a fresh mixture to maintain its original, adequately uniform, distribution of the coarse aggregates during transport, placing (and compaction in the case of CVC).

Designing a good SCC mixture is certainly a challenge: as mentioned in chapter 1, the filling and passing ability of the SCC require it to be a very fluid material, but adequate segregation resistance on its turn requires almost the opposite.

Fig. 2-10: An illustration of segregation of concrete.

Another form of segregation can occur during a flow of fresh concrete near solid walls. During flow the coarse aggregates have a tendency to move away from the solid walls of the flow domain. This phenomenon is called dynamic segregation or shear induced segregation. However, as mentioned by Feys [2.2], dynamic segregation is more likely to occur with CVC instead of SCC.

2.3 Rheometry

In order to determine the rheology of SCC we need to perform measurements using rheometers. This will help us:

- To better understand the interactions between the different constituents in SCC and to improve our knowledge regarding the resulting structure of the concrete in the fresh and hardened state;
- To control the rheological properties of the manufactured SCC mixture and to improve the verification of the required quality of the individual raw materials and the production process.

2.3.1 SCC mixture design and resulting fresh concrete properties

An important step in the design and the optimization of casting processes through numerical simulation is the determination of the required rheology of the concrete in the fresh state. Once these optimal rheological parameters have been determined and selected, it is of great importance to be able to mathematically determine the concrete mixture which will have the required rheology in the fresh state. If not possible, the required rheology will need to be determined experimentally through trial and error mixing tests. This can be a very time consuming and expensive task, which can be reduced to some extent by the experience of the concrete technologist.

De Larrard and co-workers have developed a powerful semi-empirical method for selecting the mixture design of concrete to achieve specified final properties in the fresh and hardened state [2.27]. Its basis is a sound fundamental treatment of the packing of particles of different classes. The various properties are then expressed in terms of packing densities through functions that contain various fitting parameters. The final result of this method tends to show a broad prediction ability for CVC. However, for special concrete types like SCC and high performance concrete (HPC), the prediction of the resulting rheology based on the packing density of particles seems to be less accurate due to the presence of super-plasticisers and viscosity modifying agents (VMA). Further research is therefore necessary for these special concrete types to develop accurate prediction models.

The next sections contain the basic information about how the rheological properties of a certain material subjected to shear are measured. A detailed description of all available measuring devices and their latest, most sophisticated features will not be presented here. The aim is to describe in general terms the available equipment, and how this equipment can be applied to measure some rheological characteristics like viscosity, visco-elasticity, yield stress and thixotropy. Section 2.3.3 focuses on concrete rheometry, and describes in more detail the two rheometers used in this research project: the BML ConTec-Viscometer 5 and the Tattersall Mk-II rheometer.

2.3.2 Rheometer types

Two different types of rheometers [2.2, 2.6], depending on their working principle, are used to determine the properties of a material subjected to shear:

- Drag flow based rheometers: Inside these rheometer types, the concrete sample is subjected to shear due to a difference in motion between its boundaries. As such the tested material is subjected to a drag flow (Fig. 2-11).
- Pressure driven flow rheometers: If the measuring device has no moving parts, but the applied stress is caused by a pressure difference, the material is said to be subjected to a pressure driven flow (Fig. 2-12).

For all geometries shown in Fig. 2-11 and Fig. 2-12, the tested material sample is subjected to a shear stress during the measurement. Furthermore, near the walls of the measuring device, a difference between the velocity of these walls and the velocity of the material can occur, which is called wall slip [2.6]. This wall slip disturbs the measurements and its effect should be eliminated though an optimal design of the rheometer.

In the next sections we will be only focussing on one specific type of the presented drag flow rheometers, more especially the concentric cylinders rheometer. Two industrial models of the concentric cylinders rheometer type, the BML ConTec-Viscometer 5 and the Tattersall Mk-II rheometer, have been used in the present research for determining the rheological behaviour of the SCC mixtures used in our formwork filling experiments.

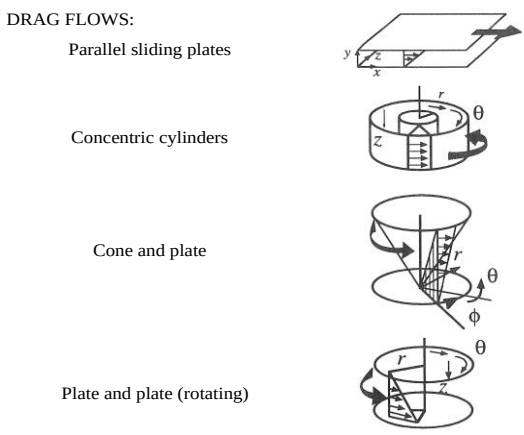

Fig. 2-11: Rheometer designs based on drag flows [2.6].

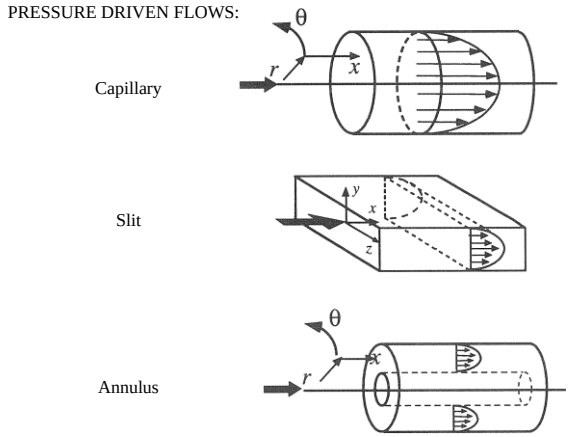

Fig. 2-12: Rheometers in which the flow is driven by pressure [2.6].

2.3.3 Concentric cylinders rheometer - Couette rheometer

2.3.3.1 Theoretical background of the concentric cylinders rheometer

The concentric cylinder rheometer has been originally developed by Maurice Couette in 1890 [2.28], and this type of rheometer has therefore been named according to its inventor: the Couette rheometer. It consists of two concentric cylinders, each having a different rotational velocity. When using Eq. (2.23) to determine the shear stress, and Eq. (2.24) for determining the shear rate, the following assumptions must be fulfilled according to Macosko [2.6]:

- Steady, laminar and isothermal flow,
- No flow in the radial and vertical direction,
- Negligible gravity and end effects,
- No wall slip,
- Symmetry in the tangential direction.

$$\tau = \frac{T_i}{2 \cdot \pi \cdot R_i^2 \cdot h} \tag{2.23}$$

$$\dot{\gamma} = \frac{\Omega_{i.} \cdot \left(R_o + R_i\right)}{2 \cdot \left(R_o - R_i\right)} \tag{2.24}$$

where T_i is the torque measured at the inner cylinder (N.m), R_i is the radius of inner cylinder (m), R_o is the radius of outer cylinder (m), h is the height of the cylinder submerged in the material (m) and Ω_i is the rotational velocity at the inner cylinder (rad/s).

When the gap is small ($R_i/R_o > 0.99$), the shear rate is considered to be constant in the gap. If the gap is not small, the shear rate varies with the radius in the gap, depending on the rheological properties of the material. In this case, Eq. (2.25) must to be applied, rather than Eq. (2.24) [2.2, 2.6].

$$\dot{\gamma}_i = \frac{2 \cdot \Omega_i}{n \cdot \left(1 - \left(R_i / R_0\right)^{2/n}\right)} \tag{2.25}$$

where $n = \dfrac{d \ln\left(T_i\right)}{d \ln\left(\Omega_i\right)}$.

When looking at Eq. (2.25), it is clear that for large gaps the transformation of the measured torque at a corresponding rotational velocity into fundamental rheological parameters (shear stress and shear rate) is not straightforward. Applying Eq. (2.24) for a large gap rheometer, although only valid for a small gap configuration, will result in large measuring errors, and therefore wrongly measured rheological parameters.

2.3.3.2 The BML Contec-Viscometer 5

2.3.3.2.1 The rheometer configuration

One of the previously mentioned assumptions, which is not trivial at all to achieve in reality, is the negligibility of the end effects. At the bottom of the material reservoir, the shear flow is not 1-D, but a rather complex 3-D flow pattern is occurring, seriously disturbing the torque measurement.

Several solutions have been proposed to minimize or to eliminate this 3-D flow pattern. Different bottom geometries have been designed, as reported by Macosko [2.6], and calculations and simulations have been performed by Wallevik [2.7] in order to correct the end effect.

The most effective solution has been to divide the inner cylinder of the rheometer into two parts: an upper part, at which torque is measured, and a lower part, which does not contribute to the measurements.

This solution has been applied in the BML ConTec-Viscometer 5 [2.7] and is shown in Fig. 2-13.a and Fig. 2-13.b.

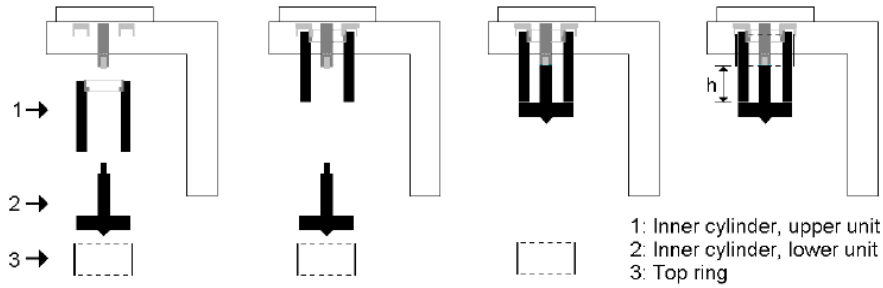

(a)

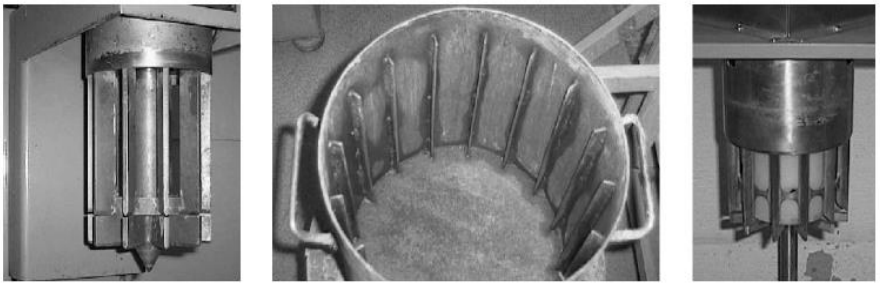

(b)

Fig. 2-13: Measuring configuration of the BML Contec-Viscometer 5 [2.7].

Both cylinders are equipped with vertical ribs in order to prevent wall slip. Several inner and outer cylinders with different heights and diameters are available for measuring different types of concrete with different maximum aggregate sizes.

The BML ConTec-Viscometer 5 (see Fig. 2-14), has an outer cylinder with a radius of 14.5 cm, an inner cylinder with R_i = 10 cm and the height of the inner cylinder, submerged in the concrete measures 12.5 cm.

The total volume of concrete needed for this rheometer is around 12 to 15 litre.

Fig. 2-14: General layout of the BML Contec-Viscometer 5.

2.3.3.2.2 The measurement procedure

This section describes how the rheological properties of SCC can be measured with the BML ConTec-Viscometer 5. Prior to describing the measurement procedure, some important properties like the flow curve, the yield stress and the influence of thixotropy and particle migration will be discussed.

2.3.3.2.2.1 Flow curve

The flow curve of fresh concrete represents a plot of the shear stress versus shear rate. This flow curve can be easily determined by increasing or decreasing the shear rate and measuring the corresponding stress. The obtained flow curve is defined to be reversible if the curve obtained by increasing the shear rate while measuring the shear stress is the same as the curve obtained by decreasing the shear rate. Non-reversibility can be caused by particle alignment without a randomising effect to create anisotropy (see also section 2.2.1.2.2), or it can be due to a time dependent phenomenon in the material like thixotropy (see section 2.2.2). Geiker et al. [2.13] mentioned that when performing measurements in a rheometer, one should be aware of the range of shear rates (or shear stresses) the fresh concrete will undergo during the pumping and formwork filling process.

2.3.3.2.2.2 Yield stress

The yield stress is a very difficult property to determine accurately. Many researchers are still debating whether the yield stress really exists or not [2.29 - 2.33]. Some researchers claim that the yield stress is in fact a Newtonian plateau, with a very high viscosity at very low shear rates.

In fact, they state that the material still flows at these low shear rates, but during the observation time, no flow is measured. Therefore, as this debate is still going on, the yield stress is only defined from a practical point of view as the maximal stress at which no flow is observed during a reasonable time frame [4.9].

Determining the yield stress can be done in three different ways:

- Measuring the stress that needs to be applied in order to initiate flow, using a vane test;
- Extrapolating the flow curve tangentially at zero shear rate;
- Using the correlation between the dynamic yield stress and the slump flow value.

With the first method, the static yield stress is obtained. The vane equipment is based on the principle of the concentric cylinders, but the inner cylinder is imaginary. It is formed by four or six blades which rotate in the fresh concrete, as shown in Fig. 2-15.

The vane test is not suited for measuring flow curves, but it is an accurate measuring device to investigate the static yield stress.

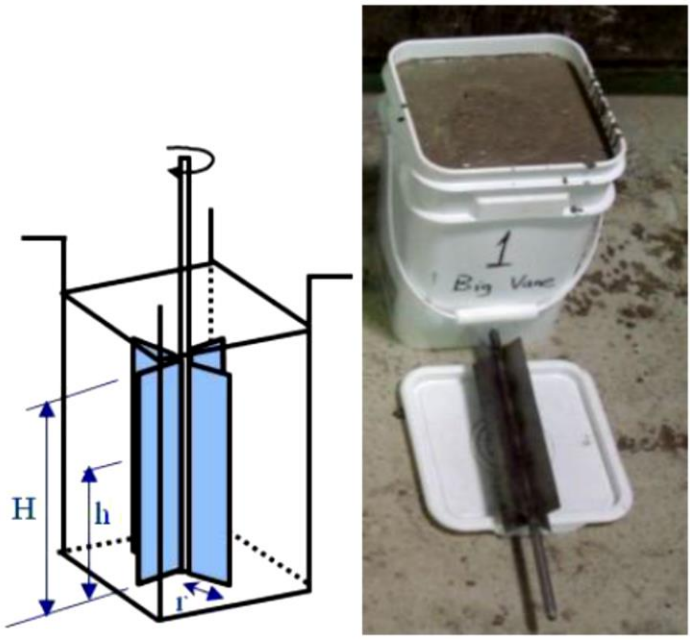

Fig. 2-15: The vane tool measuring equipment [2.34].

During such a vane test, the stress is increased gradually and the strain is measured. When the stress - strain curve shows a plateau or an overshoot (see Fig. 2-16), the material starts flowing and the static yield stress has been determined.

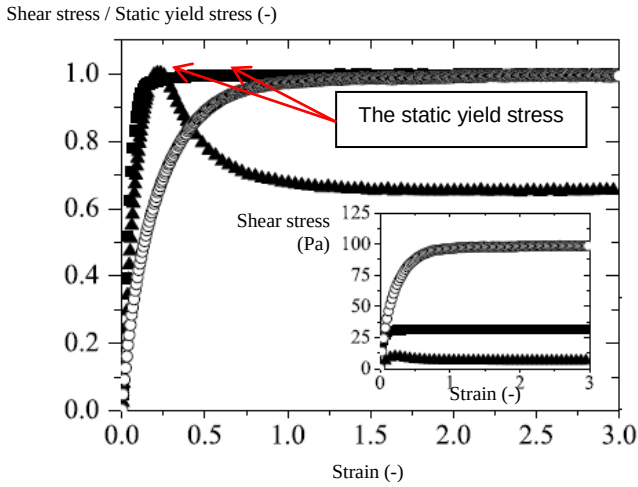

Fig. 2-16: Determination of the static yield stress [2.2].

In the current research, no static yield stress measurements have been performed. Therefore, when the “yield stress” is mentioned, it represents the dynamic yield stress, which is determined by the second method.

The second method determines the dynamic yield stress by finding the intersection of the tangential line of the flow curve with the shear stress axis of the flow curve graph at zero shear rate. Feys [2.2] explains how difficult it is to determine this dynamic yield stress, as this process strongly depends on the choice of the shear rate at which shear rate this tangential line is drawn. This is illustrated in Fig. 2-17.

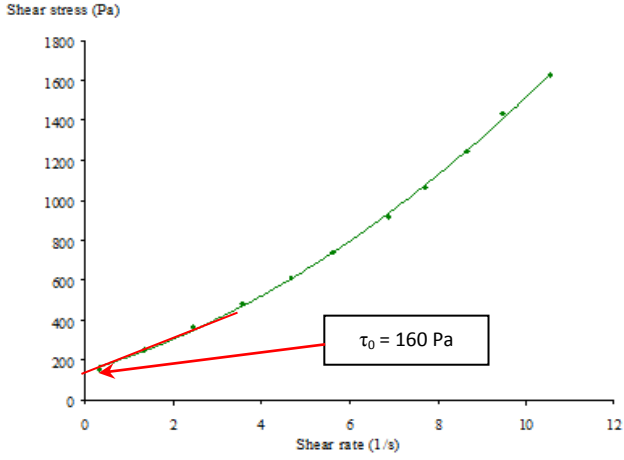

Fig. 2-17: Determination of the dynamic yield stress [2.2].

A third method to determine the dynamic yield stress is by means of a slump flow test [2.35]. Roussel and Coussot have derived an analytical expression describing the relation between the dynamic yield stress, τ_0, and the slump flow spreading distance, R, shown in Eq. (2.26):

$$\tau_0 = \frac{225.\rho.g.V^2}{128.\pi^2.R^5} \quad (2.26)$$

where ρ is the concrete density (kg/m³), g is the gravitational acceleration (= 9.81 m/s²) and V is the volume of the Abrams cone (m³).

The derivation of this equation is based on the fact that when the fresh concrete achieves its final slump flow shape, no shear stress anywhere in the material is larger than the dynamic yield stress.

Heirman [2.5] disputes the validity of this relation. He states that the concrete layer near the end of the flow zone has an insufficient layer thickness: the layer thickness is of the same order of magnitude as the maximum aggregate size (D_{max}), so that homogenous, continuous fluid mechanics equations cannot be used.

2.3.3.2.2.3 Thixotropy

The time dependent phenomenon of thixotropy has been extensively described in section 2.2.2. Although the presented equations describing thixotropy seem very logic, it is not at all evident to determine the different parameters in the equations.

Determining the thixotropic properties of SCC remains a big challenge due to the influence of the shear history of the material, which quite modifies the behaviour of the fresh SCC during the measurements.

For this reason, Roussel suggested to start from a certain reference state (the most de-structured state) in order to investigate thixotropy accurately and to examine the changes after the reference state has been obtained [2.23].

As thixotropy is an error-inducing factor, when determining steady state rheological properties, according to Geiker et al. [2.13] its effect during the measurements can be avoided by pre-shearing the fresh SCC in the rheometer at the maximum shear rate until equilibrium is reached. This is the chosen reference state of the material [2.23].

Once equilibrium is obtained, the shear rate is decreased stepwise. In this way, the down curve is described by the averages of shear stress and shear rate at each step, giving the operator the opportunity to check whether each measured point is determined in equilibrium conditions or not. When the shear stress is still decreasing at constant shear rate, it means that no equilibrium is reached and the data point is rejected for further analysis.

2.3.3.2.2.4 Particle migration

Cement-paste, mortar and concrete contain solid particles of many different sizes. Therefore, the free space to make the material flow in the rheometer must be sufficiently large. As stated by Geiker et al. [2.13], for concrete rheology, the gap size between the inner and outer cylinder in a Couette rheometer must be at least 3 times larger than the size of the coarsest particle. If a smaller gap is applied, then the homogeneity of the material in the measuring device can be questioned and perhaps, some illogical results can be obtained due to the individual influence of the largest particles.

As mentioned in section 2.2.1.2.1, particles can migrate to regions with lower shear rates. As small gap concentric cylinder rheometers are not really of practical use for concrete due to their extreme sizes, no concentric cylinder rheometer suitable for concrete is able to impose a constant shear rate in the sample. As such, particle migration will surely occur and this phenomenon will disturb to some extent the rheological measurements.

Due to the large differences in density between the suspended phase and the suspending medium, not only shear-induced segregation will occur, but also vertical segregation, due to gravity, must be studied [2.7, 2.13]. Some mixer-type concrete rheometers, like the Tattersal Mk-II rheometer, have been developed in order to overcome the gravitational segregation by re-mixing the concrete in the rheometer during the test.

2.3.3.2.2.5 Measurement protocol and settings

Shear is induced in the rheometer due to the rotation of the outer cylinder at a fixed set of rotational velocities. The upper part of the inner cylinder is connected to a torque transducer, registering torque response. The "Freshwin®" software program enables easy working with the device. The flow curve is determined by a stepwise change in rotational velocity. The following measurement settings can be chosen or modified in the software:

- The maximal and minimal rotational velocity;
- The duration of the pre-shearing step;
- The duration of each measuring step at a constant rotational velocity

The measurement data (torque and rotational velocity) is saved in a file at a rate of 25 Hz, and at each time step, the software calculates the average of the five lowest torque values.

Measurements are performed by decreasing the rotational velocity profile stepwise, after a pre-shearing period. As mentioned, the duration of the pre-shearing period, the duration of each velocity step and the number of steps need to be predefined in the software.

At the end of each measurement, the rotational velocity is increased up to 2/3 of the maximal rotational velocity. This point is called the segregation point and if it deviates significantly from the obtained flow curve, it indicates that some changes may have occurred in the fresh concrete during the rheometer test.

2.3.3.2.2.6 Analysis of the measured data

As the software calculates averages of torque and rotational velocity at each time step, a set of discrete points in a torque - rotational velocity diagram is obtained. These points need to be transformed into a flow curve, expressing the relationship between shear stress and shear rate. This can be done with the previously presented equations, Eq. (2.23) and Eq. (2.24) [2.7, 2.13], or according to Reiner [2.36] it can be achieved by applying the Reiner-Riwlin equation. When using the Reiner-Riwlin equation, the transformed values are correct and independent of the concentric cylinder rheometer geometry, but this transformation requires a preliminary choice of a rheological material model. For each selected rheological model, the transformation equations will be different. When applying Eq. (2.23) and Eq. (2.24), no choice of a rheological model is required, but the solution is only approximate, due to the discrete number of data points.

In the "Freshwin®" system software of the BML ConTec-Viscometer 5, the developers have chosen to impose the Bingham model on all results in order to be able to transform the data into the fundamental rheological units. In a first step, the linear relationship of torque versus rotational velocity is determined according to Eq. (2.27).

$$T = G_B + H_B \cdot N \tag{2.27}$$

where T is the torque (N.m), G_B is the intercept of the relationship with the T-axis for N = 0 (N.m), H_B is the inclination of relationship between T and N (N.m.s) and N is the rotational velocity (rev./s). In a second step, the values of G_B and H_B are transformed into yield stress, τ_o, and plastic viscosity, μ_p, using Eq. (2.28) and Eq. (2.29), which are the two parameters of the Bingham model (see Section 2.1.2.2).

$$\tau_0 = \frac{G_B \cdot \left(1/R_i^2 - 1/R_o^2 \right)}{4 \cdot \pi \cdot h \cdot \ln\left(R_o/R_i \right)} \tag{2.28}$$

$$\mu_p = \frac{H_B \cdot \left(1/R_i^2 - 1/R_o^2 \right)}{8 \cdot \pi^2 \cdot h} \tag{2.29}$$

where R_i is the radius of the inner cylinder (m), R_o is the radius of the outer cylinder (m) and h is the height of the inner cylinder being submerged into the material (m).

Eq. (2.28) and Eq. (2.29) are only valid if the fresh concrete between the two cylinders is fully sheared. If the shear stress at a certain radius in the rheometer is lower than the yield stress, the fresh concrete is not sheared and plug flow is observed, resulting in a small modification of Eq. (2.28) and Eq. (2.29) as described by Wallevik [2.7].

When the Herschel-Bulkley model is chosen, a new "Reiner-Riwlin" equation needs to be derived, as presented by Heirman [2.5]. This new relationship holds a third parameter which needs to be determined and transformed. With Eq. (2.31), Eq. (2.32) and Eq. (2.33), the relationship between *T* and *N*, presented in Eq. (2.30), is transformed to a Herschel-Bulkley relationship.

$$T = G_{HB} + K_{HB} \cdot N^m \tag{2.30}$$

$$\tau_0 = \frac{G_{HB}}{4 \cdot \pi \cdot h} \cdot \left(\frac{1}{R_i^2} - \frac{1}{R_o^2} \right) \cdot \frac{1}{\ln\left(R_o / R_i\right)} \tag{2.31}$$

$$K = \frac{K_{HB}}{2^{2n+1} \cdot \pi^{n+1} \cdot h} \cdot n^n \cdot \left(\frac{1}{R_i^{2/n}} - \frac{1}{R_o^{2/n}} \right)^n \tag{2.32}$$

$$n = m \tag{2.33}$$

where G_{HB}, K_{HB}, and m are the parameters of the T - N relationship, and τ_o, K and n are the Herschel-Bulkley parameters of the shear stress - shear rate relationship.

After each rheometer test has been performed with the BML ConTec-Viscometer 5, the raw data is saved in a separate file, being available for a separate analysis if needed. This could be very useful in order to check whether each data point has been obtained in equilibrium conditions, or whether no large fluctuations in the torque measurements have occurred.

2.3.3.2.3 Additional comments

The BML ConTec-Viscometer 5 has been developed with a lot of care and is considered as one of the most useful and practical rheometers for fresh concrete and more especially for SCC. The real flow in the measurement section is very close to the 1-D flow, for which the related rheometer equations have been derived. The software makes the rheometer an easy tool to work with, and creates very stable measurements. By means of the segregation point, a utility is provided to observe particle migration (or material changes in general) during testing and analysis.

Currently, only the Bingham model is implemented in the "Freshwin®" software.

The Herschel-Bulkley parameter conversion, being introduced by Heirman [2.5] and described throughout the Eqs. (2.30) to (2.33), needs to be performed using the raw measurement data and the aid of external software, like for example Matlab®.

The gap between the inner and the outer cylinder equals 4.5 cm in this configuration, resulting in a maximal aggregate size of 16 mm, in order to avoid a significant influence of the coarse particles on the measurements.

2.3.3.3 Tattersall Mk-II

2.3.3.3.1 The rheometer configuration

The Tattersall Mk-II rheometer, shown in Fig 2-18, has been developed by Tattersall [2.37] in order to measure the rheology of fresh concrete with medium to high workability. The design is based on the principle of the concentric cylinders, like the Couette rheometer, but modified in order to avoid gravity-induced segregation of the fresh concrete within the rheometer.

The inner cylinder is equipped with an interrupted helical screw, which constantly remixes the concrete during testing and also enables the fresh concrete to fall back between the blades. The outer cylinder of the rheometer is formed by the steel bucket, which is equipped with ribs in order to prevent wall slip.

The radius of the outer cylinder of Tattersall rheometer measures 12.5 cm, and the distance between the outer edges (of the blades) of the inner cylinder is 16 cm in horizontal direction and 14 cm in vertical direction.

Fig. 2-18: General layout of the Tattersall Mk-II rheometer [2.2].

2.3.3.3.2 The measurement procedure

The shearing in the Tattersall Mk-II rheometer is caused by the rotation of the inner cylinder, while the outer cylinder remains stationary during the test. The torque is measured at the inner cylinder.

The data of torque and rotational velocity are registered at a rate of 5000 Hz by the torque transducer, and the average of 2000 measurements is saved into a data file. As a result, five measuring points are obtained in two seconds time.

The rotational velocity is imposed by controlling the electrical current running through to electromotor. The rotational velocity can be reduced in 11 steps, each time by reducing the electrical current sent to the electromotor. The rotation of the electromotor is transmitted to the inner cylinder by means of a reduction system.

As for the BML ConTec-Viscometer 5, a stepwise decrease in rotational velocity is imposed and the resulting torque is measured. Before the start of each test, the concrete sample is pre-sheared at the maximal rotational velocity, until equilibrium in the resulting torque is achieved.

2.3.3.3.3 Data treatment and transformation

The results of a rheometer test are expressed in torque and rotational velocity. For each step in the test, the torque values at constant rotational velocity are averaged and represent one data point in a T - N diagram.

Due to the complex geometry of the inner cylinder, no formulae are available to transform torque and rotational velocity into fundamental rheological units. As a result, a calibration test has been performed with oil and honey, and a transformation procedure has been worked out by Feys [2.2], which is described in appendix A. Unfortunately, this transformation procedure is rather cumbersome, and the resulting rheological parameters are doubtful for very fluid concrete types like SCC.

Therefore, a new approach has been worked out, using a numerical model to calibrate the Tattersall Mk-II rheometer and to derive the transformation relations based on the obtained results from the performed numerical simulations. Le et al [2.38, 2.40] modelled the geometry of the rheometer, which is shown in Fig. 2-19 together with the resulting numerical mesh.

The results from these simulations reveal that, due to the helical shape of the inner cylinder of the Tattersall Mk-II rheometer, the related rheometer parameters G_{HB}, K_{HB} and m (see Eq. (2.30)) are all dependent on the Herschel-Bulkley parameters τ_o, K and n (see Eq. (2.6)).

After performing a numerical regression on the obtained simulation results, a set of transformation equations are derived, which are summarized in appendix A.

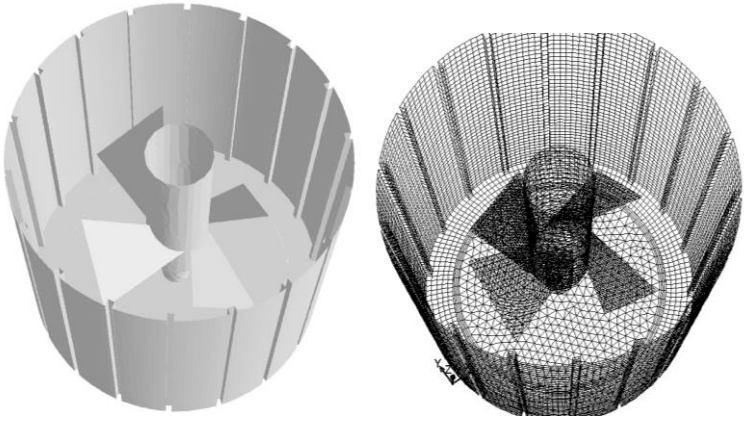

Fig. 2-19: Geometry and mesh of the Tattersall Mk-II rheometer [2.38, 2.40].

These transformation equations, based on the numerical simulation of the Tattersall Mk-II rheometer, turn out to be more accurate and reliable for very fluid concrete types like SCC than the calibration and transformation procedure proposed by Feys [2.2], because the latter procedure is based on the hypothesis that the consistency factor K is only a function of K_{HB} and that the yield stress τ_o is only a function of G_{HB}.

2.3.3.3.4 Additional comments

Due to the interrupted screw, the fresh concrete is less sensitive to segregation, although this design does not inhibit particle migration towards the outer radius. The implemented software is only used for the registration and the visualisation of the measured data. The tests are performed manually, giving the opportunity to the operator to fully adjust some items in the procedure depending on the obtained results, like for example a longer pre-shearing period for very thixotropic mixtures.

2.3.3.4 Comparison of the BML ConTec-Viscometer 5 and the Tattersall Mk-II rheometer

Two international measuring campaigns with predefined concrete mixtures have been performed in order to compare the most standard rheometers [2.39]. The results of both campaigns indicated that all rheometers deliver different results, but they can be divided in some groups delivering similar values for the same fresh concrete batch.

The BML ConTec-Viscometer 5 and the Tattersall Mk-II rheometer both deliver similar values for the measured parameters, as shown in Fig. 2-20. Very similar values for the consistency factor K and the consistency index n have also been measured, indicating rheometer-independence of the shear thickening behaviour. Some differences in the measured yield stress have been observed.

In cases of extremely fluid SCC mixtures, the Tattersall Mk-II rheometer tends to overestimate the shear thickening significantly. Also the transformation procedure for the Tattersall Mk-II is more complex, as already explained in section 2.3.3.3.3.

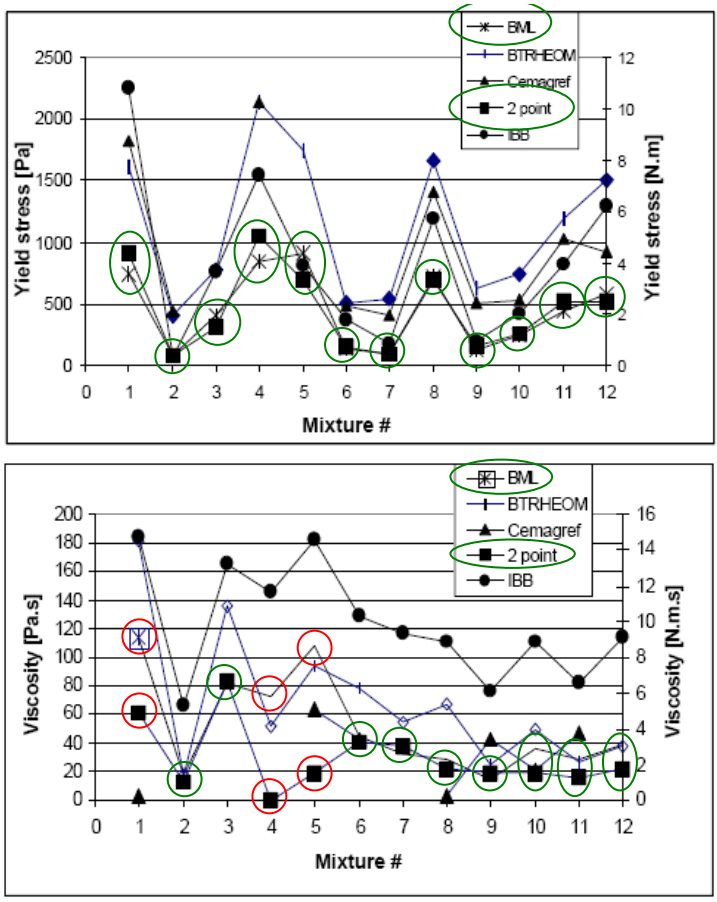

Fig. 2-20: Comparison of several rheometers [2.39].

2.4 References

[2.1] De Schutter G., Bartos P., Domone P., Gibbs J., "Self-Compacting Concrete", Whittles Publishing, Caithness (2008), 296 pages.

[2.2] Feys D., "Interactions between Rheological Properties and Pumping of Self-Compacting Concrete", Ph-D dissertation, Ghent University, Ghent (2009).

[2.3] Poppe A.-M., De Schutter G., Audenaert K., Boel V., "Kennismaking met zelfverdichtend beton (1): samenstelling en reologie", Bouwkroniek (2002) (in Dutch), pp. 30-34.

[2.4] Wallevik O.H., "Introduction to Rheology of Fresh Concrete", ICI Rheocenter Course 17th-18th August, Iceland (2009).

[2.5] Heirman G., "Modelling and quantification of the effect of mineral additions on the rheology of fresh powder type self-compacting concrete", Ph-D dissertation, Catholic University of Leuven, Leuven (2011).

[2.6] Macosko C.W., "Rheology Principles, measurements and applications", Wiley-VCH, New-York (1994), 568 pages.

[2.7] Wallevik J.E., "Rheology of Particle Suspensions - Fresh Concrete, Mortar and Cement Paste with Various Types of Lignosulfonates", Ph-D dissertation, NTNU, Trondheim (2003).

[2.8] Mewis J., Wagner N.J., "Suspension Rheology", short course from the Society of Rheology, Monterey (2008).

[2.9] Gadala-Maria F., Acrivos A., "Shear-Induced Structure in a Concentrated Suspension of Solid Spheres", J. Rheol. **24** (1980), pp. 799-814.

[2.10] Overlez G., Bertrand F., Rodts S., "Local determination of the constitutive law of a dense suspension of non-colloidal particles through MRI", J. Rheol. **50** (2006), pp. 259-292.

[2.11] Bertrand E., Bibette J., Schmitt V., "From shear thickening to shear-induced jamming", Phys. Rev. E. **66** - 060401, (2002).

[2.12] Bagnold R.A., "Experiments on a gravity-free dispersion of large solid spheres in a Newtonian fluid under shear", Proc. Roy. Soc. **225A**, (1954), pp. 49-63.

[2.13] Geiker M.R., Wallevik O.H., "Rheology of cement based materials", DTU-RILEM Doctoral course, Lyngby (2010).

[2.14] Derjaguin B., Landau L., "Theory of the stability of strongly charged lyophobic sols and the adhesion of strongly charged particles in solution of electrolytes", Acta Physicochim. URSS **14** (1941), pp. 633-662.

[2.15] Verwey E.J.W., Overbeek J.T.G., "Theory of the Stability of Lyophobic Colloids", Elsevier, Amsterdam (1948).

[2.16] Rastogi S.R., Wagner N.J., Lustig S.R., "Rheology, self-diffusion, and microstructure of charged colloids under simple shear by massively parallel nonequilibrium Brownian dynamics", J. Chem. Phys. **104:22** (1996), pp. 9234-9248.

[2.17] Rastogi S.R., Wagner N.J., Lustig S.R., "Microstructure and rheology of polydisperse, charged suspensions", J. Chem. Phys. **104:22** (1996), pp. 9249-9258.

[2.18] Laun H.M., "Rheological properties of aqueous polymer dispersion", Angew. Makromol. Chem. **123** (1984), pp. 335-359.

[2.19] Cates M.E., Wittmer J.P., Bouchaud J.-P., Claudin P., "Jamming, Force Chains and Fragile Matter", Phys. Rev. Lett. **81:9** (1998), pp. 1841-1844.

[2.20] Tattersall G.H., Banfill P.F.G., "The rheology of fresh concrete", Pitman, London (1983).

[2.21] Flatt R.J., Houst Y.F., "A simplified view on the chemical effects perturbing the action of superplasticizers", Cem. Conc. Res. **31** (2001), pp. 1169-1176.

[2.22] Roussel N., "Steady and transient flow behaviour of fresh cement pastes", Cem. Conc. Res. **35** (2005), pp. 1656-1664.

[2.23] Roussel N., "A thixotropy model for fresh fluid concretes: Theory, validation and applications", Cem. Conc. Res. **36** (2006), pp. 1797-1806.

[2.24] Hattori K., Izumi K., "A new viscosity equation for non-newtonian suspensions and its application," in "Rheology of Fresh Cement and Concrete", Proc. of the Int. Conf. organized by the British Society of Rheology, Liverpool (1990).

[2.25] Roussel N., Le Roy R., Coussot P., "Thixotropy modelling at local and macroscopic scales", J. non-Newt. Fluid Mech. **117** (2004), pp. 85-95.

[2.26] Billberg P., “Form Pressure generated by Self-Compacting Concrete - Influence of thixotropy and Structural Behaviour at Rest”, Ph-D-dissertation, School of Architecture and Built Environment, Stockholm (2006).
[2.27] De Larrard F., “Concrete Mixture Proportioning - A scientific approach”, E & FN SPON London (1999), ISBN 0-419-23500-0, 421 pages.
[2.28] Couette M.M., “Etudes sur le frottement des 81iquids”, Ann. Chim. Phys. **21** (1890), pp. 433-510.
[2.29] Boger D.V., Walters K., Webster M.F., Williams R.P., “Yield stress”, Proc. Of the XVth Int. Cong. On Rheology, Monterey (2008).
[2.30] Barnes H.A., Walters K., “The yield stress myth?”, Rheol. Acta **24** (1985), pp. 323-326.
[2.31] Barnes H.A., “The yield stress - a review or ‘παντα ρει’ - everything flows?”, J. non-Newt. Fluid Mech. **81** (1999), pp. 133-178.
[2.32] Hartnett J.P., Hu R.Y.Z., “Technical note: The yield stress - An engineering reality”, J. Rheol. **33** (1989), pp. 671-679.
[2.33] Evans I.D., “Letter to the editor: On the nature of the yield stress”, J. Rheol. **36** (1992), pp. 1313-1318.
[2.34] Khajat K.H., Omran A., “State-of-the-Art Review of Form Pressure Exerted by Self-Consolidating Concrete - Executive Summary”, RMC Research & Education Foundation, (2010), pp. 1-25.
[2.35] Roussel N., Coussot P., ““Fifty-cent rheometer” for yield stress measurements: From slump to spreading flow”, J. Rheol. **49**, (2005), pp. 705-718.
[2.36] Reiner M., “Deformation and flow; An elementary Introduction to Theoretical Rheology”, H.K. Lewis & Co. Limited, Great Britain, (1949).
[2.37] Tattersall G.H., Bloomer S.J., “Futher development of the two-point test for workability and extension of its range”, Mag. Conc. Res. **31**, (1979), pp. 202-210.
[2.38] Le H.D., Vierendeels J., Tichko S., Troch P., Kadri E.H., Aggoun S., De Schutter G., “Computational fluid dynamics calibration of Tattersall MK-II type rheometer for concrete”, Applied Rheology **23**, (2013), 12 pages.
[2.39] Ferraris C.F., Brower L.E., Beaupré D., Chapdelaine F., Domone P., Koehler E., Shen L., Sonebi M., Struble L., Tepke D., Wallevik O., Wallevik J.E., “Comparison of concrete rheometers: International tests at MB (Cleveland OH, USA) in May, 2003”, NIST report 7154, Gaithersburg, (2004).
[2.40] Le H.D., “Etude de l'effet de la couche limite sur les profils de vitesses du béton pompé”, Ph-D dissertation, Université de Cergy-Pontoise, Cergy-Pontoise (2014).

Chapter 3: Formwork pressure and formwork design codes

"Life is really simple, but we insist on making it very complicated." - Confucius

3 Overview of this Chapter

Chapter 3 is divided into four main sections. The first section focuses on the general flow equations representing pressure driven concrete flows in ducts and formworks. A new model is presented for determining the shear flow losses with non-Newtonian liquids like fresh SCC based on the Poiseuille equation and the Herschel-Bulkley model. In the second section, two formwork filling techniques are discussed, together with their advantages and disadvantages and some rules of good practice to follow with each technique. In a third section, a summary of available formwork design codes is presented. For each design code, the relevant scope of application is discussed and the equations for determining the resulting formwork pressure based on the occurring loads during casting are presented. Finally, in the last section, the formwork pressures occurring during base-filling with SCC are investigated and the different calculation methods for determining these formwork pressures, whether using an available design code or an analytical model, are compared with each other.

3.1 Pressure driven SCC flow

3.1.1 SCC flow in ducts and formworks

In this section, we present the theory of SCC flow in ducts and formworks. A new theoretical model, mathematically describing these fresh concrete flows, will be derived by applying the same principles as in classical hydraulics for Newtonian fluids. The link between the rheology of SCC and hydraulics will be discussed.

In the next section, the general flow equations, better known as the Navier-Stokes equations, will be formulated. In section 3.1.3, the Bernoulli equation regarding the flow in ducts will be re-derived, based on the Navier-Stokes equations. In section 3.1.4, the Poiseuille formula for Newtonian liquids will be extended for yield stress materials like fresh SCC.

The practical application of the presented equations will be given in section 3.4 and chapter 6, dealing with formwork wall pressures during casting with SCC and pressure losses in ducts while pumping SCC.

The advantage of the presented flow theory is that the pressure losses and wall pressures can be predicted, based on the values of discharge, the rheological properties and the geometry of the duct or the formwork.

3.1.2 The Navier-Stokes equations

As mentioned by Hirsch [3.1], the most general description of a fluid flow is obtained from the conservation laws, more commonly known as the Navier-Stokes equations. They represent mass conservation, conservation of momentum and conservation of energy. The flow conditions observed during pumping and casting with fresh concrete are laminar.

Because the density and the viscosity of the concrete in the fresh state are assumed to be independent of the typically very small temperature changes, the conservation of energy is not taken into account. Therefore for unsteady, isothermal, laminar flows the remaining conservation equations take on the following form:

Conservation of mass:

$$\frac{\partial \rho}{\partial t} + \vec{\nabla}.(\rho \vec{v}) = 0 \tag{3.1}$$

Conservation of momentum:

$$\frac{\partial (\rho \vec{v})}{\partial t} + \vec{\nabla}.(\rho \vec{v} \otimes \vec{v}) = -\vec{\nabla} p + \vec{\nabla}.\bar{\bar{\tau}} + \rho \vec{g} \tag{3.2}$$

where ρ is the density or specific mass of the SCC (kg/m³), $\vec{v}$ is the velocity vector (m/s), p is the static pressure (Pa), $\bar{\bar{\tau}}$ is the shear stress tensor (Pa), $\vec{g}$ is the gravity acceleration vector (m/s²) and $\otimes$ is the tensor product of two vectors.

For SCC, the relation between shear stress and shear rate is described using the Herschel-Bulkley model. The 1-D version of the Herschel-Bulkley model has been presented in chapter 2. For a complex flow, the 3-D form of this model is required.

The strain rate tensor, $\bar{\bar{D}}$, is used to describe the 3-D state of rate of deformation at any point in the fresh concrete. It operates on small displacement vectors around a point in the fresh material to give the time rate of change of the squared length of those vectors. As such, the deformation rate tensor is mathematically defined by the following equation:

$$\bar{\bar{D}} = \overline{\overline{\nabla v}}^T + \overline{\overline{\nabla v}} \tag{3.3}$$

with:

$$\overline{\overline{\nabla v}}^T = \begin{bmatrix} \frac{\partial v_x}{\partial x} & \frac{\partial v_x}{\partial y} & \frac{\partial v_x}{\partial z} \\ \frac{\partial v_y}{\partial x} & \frac{\partial v_y}{\partial y} & \frac{\partial v_y}{\partial z} \\ \frac{\partial v_z}{\partial x} & \frac{\partial v_z}{\partial y} & \frac{\partial v_z}{\partial z} \end{bmatrix} \tag{3.4}$$

The Hershel-Bulkley model formulated in 3-D is then defined as:

$$\bar{\bar{\tau}} = \left(\frac{\tau_0}{|II_{\bar{\bar{D}}}|^{\frac{1}{2}}} + K\left|II_{\bar{\bar{D}}}\right|^{\frac{(n-1)}{2}} \right).\bar{\bar{D}} \tag{3.5}$$

with $II_{\bar{\bar{D}}}$ being the second invariant of the strain rate tensor $\bar{\bar{D}}$. For incompressible fluids, like fresh SCC, the second invariant of the strain rate tensor is defined as:

$$II_{\bar{\bar{D}}} = -\frac{1}{2}\left(tr\left(\bar{\bar{D}}\right)^2\right) \tag{3.6}$$

3.1.3 The Bernoulli equation

In this section, the well-known Bernouilli equation is re-derived, which will be used in section 3.4 to predict the maximum formwork pressure occurring during filling from the base with fresh SCC.

The conservation of momentum equation, Eq. (3.2), is written in divergence form and can be further transformed into the following equation, applying the differentiation rule on the first term and one of the vector calculus identities on the second term of the left-hand side:

$$\rho\frac{\partial\vec{v}}{\partial t} + \vec{v}\frac{\partial\rho}{\partial t} + \rho\vec{v}\vec{\nabla}\vec{v} + \vec{v}\vec{\nabla}.(\rho\vec{v}) = -\vec{\nabla}p + \vec{\nabla}.\bar{\bar{\tau}} + \rho\vec{g} \tag{3.7}$$

After introducing Eq. (3.1) into Eq. (3.7), we obtain:

$$\rho\frac{\partial\vec{v}}{\partial t} + \rho\vec{v}\vec{\nabla}\vec{v} = -\vec{\nabla}p + \vec{\nabla}.\bar{\bar{\tau}} + \rho\vec{g} \tag{3.8}$$

The gravitational force term in Eq. (3.8) can be expressed as:

$$\rho\vec{g} = -\rho g\vec{1}_z = -\vec{\nabla}(gz) \tag{3.9}$$

From vector calculus we also know that:

$$\vec{v}\times\left(\vec{\nabla}\times\vec{v}\right) = \vec{\nabla}\left(\frac{\vec{v}^2}{2}\right) - \vec{v}\vec{\nabla}\vec{v} \tag{3.10}$$

Introducing Eq. (3.9) and Eq. (3.10) into Eq. (3.8), leads to the following equation:

$$\rho\frac{\partial\vec{v}}{\partial t} + \rho\vec{\nabla}\left(\frac{\vec{v}^2}{2} + gz\right) = -\vec{\nabla}p + \rho\left(\vec{v}\times\left(\vec{\nabla}\times\vec{v}\right)\right) + \nabla.\bar{\bar{\tau}} \tag{3.11}$$

Fresh SCC can be regarded as an incompressible fluid with a constant density. This allows us to further rearrange Eq. (3.11) into:

$$\frac{\partial\vec{v}}{\partial t} + \vec{\nabla}\left(\frac{p}{\rho} + \frac{\vec{v}^2}{2} + gz\right) = \vec{v}\times\left(\vec{\nabla}\times\vec{v}\right) + \frac{1}{\rho}\nabla.\bar{\bar{\tau}} \tag{3.12}$$

For stationary flows, Eq. (3.12) becomes:

$$\vec{\nabla}\left(\frac{p}{\rho}+\frac{\vec{v}^2}{2}+gz\right)=\vec{v}\times\left(\vec{\nabla}\times\vec{v}\right)+\frac{1}{\rho}\nabla.\bar{\bar{\tau}} \tag{3.13}$$

Eq. (3.13) represents the Bernoulli equation, describing the stationary flow of an incompressible fluid. The expression between brackets in the left-hand side (lhs) of Eq. (3.13) represents the total energy *H* (in J/kg).

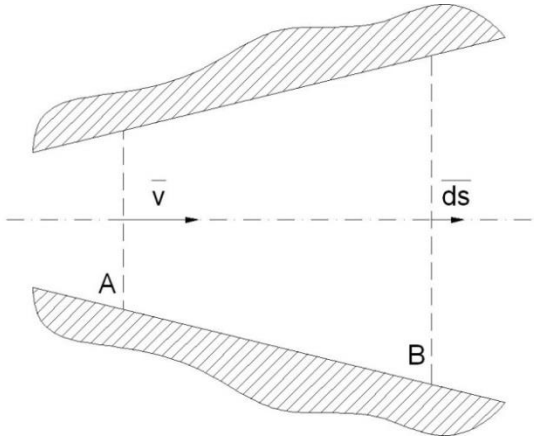

Fig. 3-1: Stationary flow between two cross-sections A and B in a confined space.

Integrating Eq. (3.13) between two cross-section A and B along a flow path *s*, as illustrated in Fig. 3-1, we obtain the following relation:

$$\int_A^B\vec{\nabla}\left(\frac{p}{\rho}+\frac{\vec{v}^2}{2}+gz\right)d\vec{s}=\int_A^B\left(\vec{v}\times\left(\vec{\nabla}\times\vec{v}\right)\right)d\vec{s}+\int_A^B\frac{1}{\rho}\nabla\bar{\bar{\tau}}d\vec{s} \tag{3.14}$$

Working out the first integral of the left-hand side of Eq. (3.14) results into:

$$\int_A^B\vec{\nabla}\left(\frac{p}{\rho}+\frac{\vec{v}^2}{2}+gz\right)d\vec{s}=\left(\frac{p}{\rho}+\frac{\vec{v}^2}{2}+gz\right)_B-\left(\frac{p}{\rho}+\frac{\vec{v}^2}{2}+gz\right)_A \tag{3.15}$$

Working out the first integral of the right-hand side of Eq. (3.14) leads to:

$$\int_A^B\left(\vec{v}\times\left(\vec{\nabla}\times\vec{v}\right)\right)d\vec{s}=\int_A^B\left(\vec{v}\times\left(\vec{\nabla}\times\vec{v}\right)\right).\vec{1}_v ds=0 \tag{3.16}$$

The second integral of the right-hand side of Eq. (3.14) represents the shear flow losses ($-\frac{\Delta p_L}{\rho}$). The resulting form of the Bernoulli equation, along a flow path, states that:

$$\left(\frac{p}{\rho}+\frac{\vec{v}^2}{2}+gz\right)_B=\left(\frac{p}{\rho}+\frac{\vec{v}^2}{2}+gz\right)_A-\frac{\Delta p_L}{\rho} \tag{3.17}$$

3.1.4 The extended Poiseuille formula for non-Newtonian liquids

3.1.4.1 Derivation of the extended Poiseuille formula for Herschel-Bulkley fluids

The original Poiseuille formula was derived in 1839-1840 by Hagen and Poiseuille, assuming the following flow conditions [3.2 - 3.5]:

- The flow must be fully developed, isothermal, steady and laminar;
- The fluid is incompressible and homogeneous;
- The flow is one-dimensional, with no radial or tangential flow component;
- No slippage at the wall is occurring;
- And last but not least, the fluid must be Newtonian.

The original derivation of the Poiseuille equation will be extended here for non-Newtonian fluids, while considering the other assumptions presented above. In order to be able to use the Bernoulli equation presented in the previous section, we need to determine the flow losses. A new analytical model determining the shear flow losses occurring during a flow of an Herschel-Bulkley fluid will be derived. The validity of this analytical model will be checked against known expressions for the flow losses with Bingham fluids and Newtonian fluids.

The shear flow losses, Δp_L, and the shear stress τ_w at the wall are related, as illustrated by the following equation:

$$\Delta p_L \pi R^2 = 2\pi R \tau_w L \tag{3.18}$$

or,

$$\tau_w = \frac{\Delta p_L R}{2L} \tag{3.19}$$

where R is the radius of the flow cross-section (m), τ_w is the wall shear stress (Pa), Δp_L are the shear flow losses (Pa) and L is the flow path length (m). In the flow cross-section, the shear stress τ varies linearly with the radial position parameter r (r = 0 at the centre of the cross-section, $r = R$ at the wall). This is a universal law, meaning it is independent of the rheological properties of the flowing material.

$$\tau_r = \frac{\tau_w r}{R} \tag{3.20}$$

where τ_r is shear stress at position r (Pa). The shear stress at position r must also be in agreement with the Herschel-Bulkley model, formulated in chapter 2 (Eq. (2.6)). The flow of a yield stress material is characterized by a plug flow zone in the centre of the flow cross-section, and a shear flow zone in the remaining part of the flow cross-section. In the plug flow zone, the material is not sheared and moves as rigid plug through the flow domain. As mentioned by Feys [3.6], the size of this plug zone is tightly related with the yield stress. It is defined by the following equation:

$$r_{plug} = \frac{\tau_0 R}{\tau_w} \tag{3.21}$$

Combining Eq. (2.6) (the Herschel-Bulkley model presented in chapter 2) and Eq. (3.20), we obtain the following relations for the shear rate or velocity gradient at position *r*:

For $r \leq r_{plug}$:

$$\dot{\gamma}_r = 0 \tag{3.22a}$$

For $r > r_{plug}$:

$$\dot{\gamma}_r = -\left(\frac{dv}{dr}\right) = \left(\frac{\tau_w \frac{r}{R} - \tau_0}{K}\right)^{\frac{1}{n}} \tag{3.22b}$$

Integrating Eq. (3.22a) and Eq. (3.22b), we obtain an expression for the velocity in the two flow zones.

$$\int_r^R \dot{\gamma}_r \, dr = -\int_{v_r}^{v_{wall}} dv = v_r - v_{wall} \text{ and } v_{wall} = 0, \text{ thus, } v_r = \int_r^R \dot{\gamma}_r dr \tag{3.23}$$

For $r \leq r_{plug}$:

$$v_r = v_{plug} \tag{3.24a}$$

For $r > r_{plug}$:

$$v_r = \int_r^R \left(\frac{\tau_w \frac{r}{R} - \tau_0}{K}\right)^{\frac{1}{n}} dr = -\frac{RKn}{\tau_w(1+n)}\left[\left(\frac{\tau_w r - \tau_0 R}{RK}\right)^{\left(\frac{1+n}{n}\right)} - \left(\frac{\tau_w - \tau_0}{K}\right)^{\left(\frac{1+n}{n}\right)}\right] \tag{3.24b}$$

At $r = r_{plug}$ the flow must be continuous, and therefore the velocity at that radial position must be equal to v_{plug}. The expression for v_{plug} can be obtained by inserting Eq. (3.21) into Eq. (3.24b), leading to:

$$v_{plug} = \frac{RKn}{\tau_w(1+n)}\left(\frac{\tau_w - \tau_0}{K}\right)^{\left(\frac{1+n}{n}\right)} \tag{3.24a-bis}$$

Knowing the velocity in each point of the flow cross-section, Eq. (3.24a-bis) and Eq. (3.24b) can be integrated over the cross-section in order to obtain the following equations for the volumetric flow rate Q_{HB} (m³/s):

For $r \leq r_{plug}$:

$$Q_{HB,1} = \int_0^{r_{plug}} v_{plug} 2\pi r dr = \frac{\pi R^3 Kn \tau_0^2}{\tau_w^3(1+n)}\left(\frac{\tau_w - \tau_0}{K}\right)^{\left(\frac{1+n}{n}\right)} \tag{3.25a}$$

For r > r_{plug}:

$$Q_{HB,2} = \int_{r_{plug}}^{R} v_r 2\pi r dr = -a\frac{R^2}{\tau_w^2}\left(\frac{\tau_w-\tau_0}{K}\right)^b (\tau_w-\tau_0)\left[\frac{\tau_w-\tau_0}{b+2}+\frac{\tau_0}{b+1}-\frac{1}{2}(\tau_w+\tau_0)\right] \quad (3.25b)$$

$$a = \frac{2\pi RK}{\tau_w b} \quad (3.25c)$$

$$b = \frac{1+n}{n} \quad (3.25d)$$

$$Q_{HB} = Q_{HB,1} + Q_{HB,2} = \frac{\pi R^3 K}{\tau_w^3 b}\left(\frac{\tau_w-\tau_0}{K}\right)^b \left\{\tau_0^2 - 2(\tau_w-\tau_0)\left[\frac{\tau_w-\tau_0}{b+2}+\frac{\tau_0}{b+1}-\frac{1}{2}(\tau_w+\tau_0)\right]\right\} \quad (3.25e)$$

Eq. (3.25e) expresses the relation between the flow rate Q_{HB} and the wall shear stress τ_w, and according to Eq. (3.19) also the relation with the shear flow losses Δp_L. Knowing the flow rate Q_{HB}, the rheological parameters of the Herschel-Bulkley model and the flow geometry, the flow path length L and the radius R, then Eq. (3.25e) can be easily solved iteratively to find the occurring shear flow losses Δp_L.

3.1.4.2 Verification of the derived extended Poiseuille formula

In order to verify the validity of the derived equations in the previous subsection, two sets of Herschel-Bulkley parameter values are selected, which represent respectively the Bingham material model and the Newtonian material model.

For the Bingham model, the selected Herschel-Bulkley parameter are:

- The consistency factor K, representing the plastic viscosity μ_p;
- The consistency index n, being equal to 1;
- The yield stress τ_0, having the same meaning as in the Herschel-Bulkley model.

Eq. (3.25.e) then becomes:

$$Q_B = \frac{\pi R^3 \mu_p}{\tau_w^3 2}\left(\frac{\tau_w-\tau_0}{\mu_p}\right)^2 \left\{\tau_0^2 - 2(\tau_w-\tau_0)\left[\frac{\tau_w-\tau_0}{4}+\frac{\tau_0}{3}-\frac{1}{2}(\tau_w+\tau_0)\right]\right\}$$

$$Q_B = \frac{\pi R^3}{\tau_w^3 2\mu_p}(\tau_w^2 - 2\tau_w\tau_0+\tau_0^2)\left\{\tau_0^2 - 2(\tau_w-\tau_0)\left[-\frac{3}{12}\tau_w-\frac{5}{12}\tau_0\right]\right\}$$

$$Q_B = \frac{\pi R^3}{\tau_w^3 2\mu_p}(\tau_w^2 - 2\tau_w\tau_0+\tau_0^2)\frac{2}{12}(3\tau_w^2+2\tau_w\tau_0+\tau_0^2)$$

$$Q_B = \frac{\pi R^3}{12\tau_w^3\mu_p}(3\tau_w^4 - 4\tau_w^3\tau_0+\tau_0^4) \quad (3.26)$$

Introducing Eq. (3.19) into Eq. (3.26) leads to the following equation:

$$Q_B = \frac{\pi}{24}\left(\frac{3\Delta p_L^4 R^4 - 8\Delta p_L^3 R^3\tau_0 + 16L^4\tau_0^4}{\Delta p_L^3 \mu_p L}\right) \quad (3.27)$$

This is the well-known Buckingham-Reiner equation.

For the Newtonian model, the Herschel-Bulkley parameter are translated as follows:

- The consistency factor *K*, representing the dynamic viscosity η;
- The consistency index *n*, also being equal to 1;
- The yield stress, being equal to zero.

We can introduce these parameters again in the extended Poiseuille equation, Eq. (3.25e), and then combine the obtained result with Eq. (3.19), or we can introduce them directly into Eq. (3.27) which then further simplifies to the following equation:

$$Q_N = \frac{\pi}{24}\left(\frac{3\Delta p_L^4 R^4}{\Delta p_L^3 \eta L}\right)$$
$$Q_N = \frac{\pi}{8}\left(\frac{\Delta p_L R^4}{\eta L}\right) \quad (3.28)$$

Both implementations lead to the well-known Poiseuille equation.

The verifications presented above prove the validity of the newly derived extended Poiseuille model for determining the shear flow losses occurring during pumping or casting with an Herschel-Bulkley fluid, like fresh SCC.

3.2 Formwork filling - top- versus base-filling

3.2.1 Introduction

In section 3.1, the flow equations for non-Newtonian fluids like SCC flows were described. A new model for predicting the shear flow losses in ducts and formworks has been derived. Quantifying the shear flow losses will allow us to predict the maximum wall pressures in ducts and formworks during casting, as will be explained in detail in section 3.4. In the current section, two types of casting processes are discussed with totally different concrete flows inside a formwork, therefore leading to different shear flow losses and resulting formwork pressures.

Two types of formwork filling processes are encountered when casting with SCC:

- Filling from the top of a formwork (see Fig. 3-2) and;
- Filling by pumping from the base of a formwork (see Fig. 3-3).

As mentioned by De Schutter et al. [3.9], both filling processes have their advantages and disadvantages, which are summarized here briefly:

a) *Top-filling process*:

Advantages:

- There is no inlet duct intersecting with the formwork wall. Therefore, the surface finish quality is not impaired by the presence of an inlet duct.

- This filling technique, if properly executed, can profit from the thixotropic property of the selected SCC. The maximum formwork pressure is then lower than the full hydrostatic pressure.

Disadvantages:

- In some cases the height of the cast elements can be limited due to necessity of long supply ducts. This is most unfortunate because one of the advantages of using SCC is that it is particularly suited for filling high formworks.
- Filling from the top of a formwork increases the probability of having more air getting entrapped during the filling process, which negatively influences the concrete strength development and the durability.
- Discontinuous filling, due to intermittent deliveries of concrete, leads to weak interfaces between the cast concrete layers. These interfaces, or “pour lines” are only noticed afterwards when the formwork is stripped.
- Due to the fact that the concrete is falling down inside the formwork, the risk of segregation increases. Segregation in fresh concrete occurs when the coarse aggregates gather at the base of the formwork due to gravity, leading to a non-homogenous concrete mixture.

Fig. 3-2: Formwork top-filling process [3.7].

b) Base-filling process:

Advantages:

- The risk of air getting entrapped during the filling process is avoided or limited, thus leading to an improved quality of the cast.

- The occurrence of segregation is counteracted due to the continuous upward movement of the concrete. This also improves the final quality of the cast element.
- There is no need for long supply ducts.
- Due to the continuous pumping of SCC from the base of the formwork, there are no weak interfaces or “pour lines” in the final cast.
- High concrete elements can be cast at high filling rates without any interruption of the filling process, thereby drastically reducing the time needed for casting.

Disadvantages:

- Base-filling requires the use of a shut-off valve, which is mounted at the base of the formwork. This valve prevents the fresh concrete from escaping the formwork, when the supply duct is disconnected after the formwork has been completely filled. It increases the complexity of the formwork.
- Obtaining a good surface finish of the cast element near the inlet valve is a challenge. The design of the shut-off valve is crucial, because the moving part of the valve must perfectly seal the inlet opening and be completely coplanar with the formwork walls, hopefully leaving no surface marks when the formwork is stripped.
- During the filling of the formwork, the SCC remains fluid all the time, thus leading to high formwork wall pressures, especially when casting at high filling rates. These high wall pressures require very strong and stiff formworks, making them more expensive. This fact will in some cases limit the casting height.

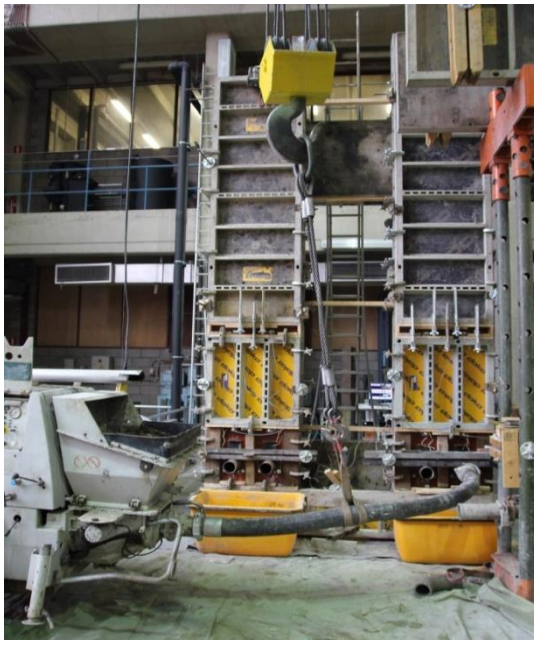

Fig. 3-3: Formwork base-filling process [3.8].

In the next two sections, both formwork filling techniques and their characteristic differences are presented. Some rules of good practice from guides and standards will be formulated and further illustrated.

3.2.2 The top-filling process

3.2.2.1 Description

The top-filling process is historically the most common formwork filling method for CVC and SCC and a lot of practical knowledge and know-how has been gathered so far. The CVC or SCC is poured into the formwork from the top. The concrete can be transported to the top of the formwork using a concrete piston pump (see Fig. 3-4) or using a concrete chute or skip and a crane (see Fig. 3-5).

Fig. 3-4: Top-filling process using a truck mounted concrete pump.

Fig. 3-5: Top-filling process using a skip and a crane [3.10].

Pumping of concrete is a common method for on-site transport and placing. Normally the pumping process is easier with SCC. The high mortar content and high flowability make the fresh SCC generally much more pumpable but higher pumping pressures are needed due to the higher viscosity. The ease of pumping of SCC still permits more efficient pipeline layouts, including splits and bifurcations, which enable much faster placing rates (see Fig. 3-6 and Fig. 3-7).

Fig. 3-6: Bifurcated pipeline increasing the rate of placing fresh SCC [3.11].

Fig. 3-7: Multiple discharge points when casting SCC [3.11].

The transport and placing of fresh concrete on a building site by a skip and a crane can be carried out equally well for CVC as for SCC. Skips used for placing fresh SCC need to have an easily operated and tightly closing opening system, which should enable a slow and controlled discharge of the SCC.

3.2.2.2 *Rules of good practice*

In order to optimise the top-filling process, some rules of good practice need to be followed consistently. The following list summarizes the knowledge gathered so far, and it also highlights the required skills of the operating personnel performing the casting process [3.10 - 3.12]:

- When CVC is used, the lift height (the thickness of the layer cast) is limited by the length of the vibration rods, which are used to compact the fresh concrete layer just being cast. This compaction process is somehow impairing the formwork filling rate (max. 15 m/h). SCC on the other hand does not require any vibration for air removal, thus allowing much faster casting speeds.
- One of the important characteristics of fresh SCC is its filling ability. Depending on the delivery rate, the element and rebar geometry, the lift height as well as the filling ability of the concrete itself, fresh SCC is capable of flowing more than 10 m without segregation. A horizontal flow up to a distance of 5 to 6 m from a single discharge point is achievable, although these limits need to be assessed on a job-by-job basis.

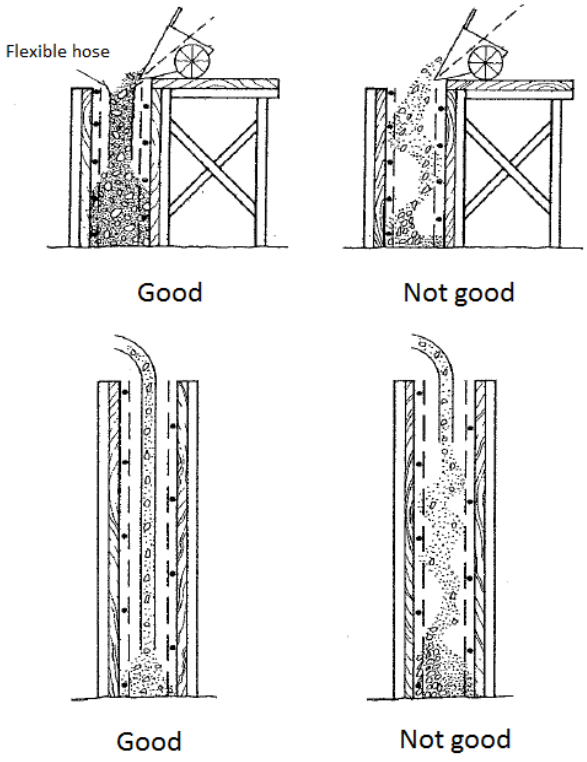

Fig. 3-8: Rules of good practice for formwork top-filling [3.12].

- The free fall height of the CVC or SCC during casting should be limited to less than 1.5 m in order to avoid segregation. In case the free fall height is higher than 1.5 m, a flexible hose is required, as illustrated in Fig. 3-8. The discharge end of the hose needs to be submerged to a depth of approximately 0.30 m in the concrete already placed, in order to avoid air entrainment. This is not always fulfilled in practice, as can be seen in Fig. 3-2!
- It is important that the top-filling process should be as continuous as possible, in order to avoid the occurrence of pour lines, which not only deteriorate the surface finish of the concrete element but also reduce the resulting strength and durability of the cast.
- Concrete placers, as well as on-site managers and foremen, must understand and take into account the importance of each separate element of the execution, and must carry it out effectively. It is essential that the personnel used to place fresh concrete, and more especially SCC, have been trained and instructed in the specific requirements for placing the selected type of concrete.

3.2.3 The base-filling process

3.2.3.1 Description

Placing concrete by pumping into the formwork from below is only possible when SCC is used, as will be illustrated in the following section and also in chapter 5. This base-filling method is not applicable with the much less workable CVC.

3.2.3.2 Rules of good practice

For the base-filling process, also some rules of good practice apply. Most of the guidelines mentioned in section 3.2.2.2 for the top-filling process, also apply for the base-filling technique. Some specific guidelines need to be respected for the base-filling process, which are listed in the following non-exhaustive list [3.10, 3.11]:

- As will be made clear in section 3.3 and also in chapter 5, the formwork base-filling process will lead to formwork wall pressures which will exceed the hydrostatic pressure. This is due to the occurring viscous pressure losses, which add up to the hydrostatic pressure component. In order to sustain these high wall pressures during base-filling, the formwork walls and interconnections need to be sufficiently strong and stiff. Unfortunately, the currently available formwork design codes are not suited when the formwork base-filling method with SCC is applied, as will be explained in section 3.3 and section 3.4.
- These additional viscous pressure losses during base-pumping are strongly related with the rheology of the SCC. Therefore it is important to check, prior to the pumping, if the rheology of the delivered SCC is conforming with the specified formwork filling design requirements.
- As SCC is much more fluid than CVC and the formwork wall pressures are higher with base-filling compared to top-filling, the formwork design needs to be completely tight, in order to avoid “SEC” (*Self-Escaping Concrete*) [3.6]. This requirement is somewhat less stringent for CVC.

- Due to the use of SP's and VMA's in SCC, more attention needs to be given regarding the choice of the demoulding oil because of possible unwanted chemical interactions or surface imperfections, like staining or retention of air bubbles [3.10, 3.11].
- As already mentioned in section 3.2.1, when SCC is pumped from the base of the formwork, a shut-off valve is needed which must seal off tightly the inlet of the formwork when uncoupling the concrete supply duct. In order to avoid some concrete protruding at the inlet and thus to obtain a nice surface finish when the formwork walls are removed after concrete hardening, some companies have developed a special shut-off valve where the protruding concrete is pushed flush with the inner surface of the formwork via a special spindle, as shown in Fig. 3-9 [3.10]. Also at the MLCR and the Laboratory for Hydraulics (LfH) of UGent, a special shut-off valve with a spring controlled automatic closing system has been designed and tested during our formwork base-filling experiments.

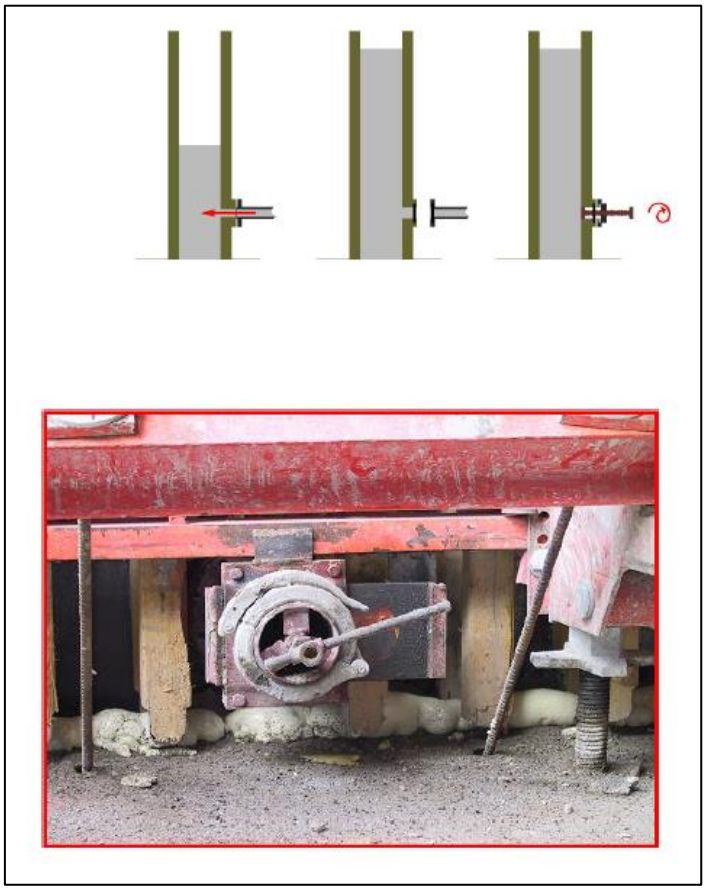

Fig. 3-9: Special design of the shut-off valve when pumping SCC from the base [3.10].

- The number of inlets and their positioning need to be carefully determined in order to avoid air pockets being formed during the base-filling process. The rebar configuration and the flow capacity of the selected SCC are therefore to be taken into account.
- As for the previous point, the pumping speed must also be selected in relation to the rebar density, the fluidity of the SCC and to the potential for entrapment of air. As will be shown in chapter 5, much higher casting speeds can be achieved than with top-filling.

3.2.4 Comments and what next in this study

Quite many researchers have already studied the top-filling process with SCC and the evolution of the formwork wall pressure during this filling process, as it is still today the most used filling technique, even with SCC. Very little research has been conducted regarding the base-filling process with SCC so far.

The objective of the following part of the present study is to determine the relevant casting parameters influencing the evolution of the formwork wall pressure during the base-filling process with fresh SCC and to develop mathematical models which will enable us to quantify the formwork wall pressures when taking into account these casting parameters.

3.3 Available formwork design codes

3.3.1 Introduction

Concrete in its fresh state has no shape. In order to give a structural element in concrete its required shape, a formwork is always required. This formwork is in most cases a temporary construction, which has to fulfil the following objectives:

- To give the concrete element its expected shape and geometrical accuracy;
- To provide the concrete element its required surface structure;
- To support the concrete during the initial setting and the hardening process.

A formwork, being a temporary construction, is quite expensive because the build-up is very labour intensive and it requires a lot of building materials for the containing walls. Nowadays, quite often formworks are made out of reusable system panels. The formwork costs can be as high as 40 to 60 % of the total concrete building costs.

For many construction jobs such as casting walls and columns up to heights of 3.3 m nothing changes, because the mainstream formwork systems (like for example Doka Framax Xlife) can safely handle fresh concrete pressures up to 80 kN/m². Once the formwork height exceeds the 3.3 m, together with high casting speeds, the fresh concrete pressures will be much higher, leading to unacceptable deformations, damage and the failure of the formwork structure. During casting, the formworks have to be able to bear the following loads:

- The deadweight of the fresh concrete, the weight of the steel rebars and the weight of the formwork construction itself;
- The variable loads inherent of the concrete filling procedure being used;
- The occasional loads, like for example wind loads.

Whereas it is quite easy to determine the vertical loads which are acting on the horizontal parts of a formwork, it is much less obvious to assess the horizontal loads acting on the vertical formwork walls. As mentioned by Taerwe and De Schutter [3.12] and Omran et al. [3.13], the magnitude of the horizontal load, induced by the fresh concrete on the formwork walls during casting, is depending on many factors, which are summarized in Table 3-1.

Observing the large quantity of these influencing factors, it is clear that it is certainly not straightforward to accurately determine these horizontal wall pressures for each particular formwork filling process. Since 1920 up to now, many researchers from different institutes have derived formulas and tabulated data based on filling experiments performed in laboratories and construction sites. This quite extensive knowledge has been translated into several formwork design codes.

However, practically all the available codes and standards on the design of formwork constructions are only valid for formwork filling processes with CVC being poured from the top, as will be explained next.

Table 3-1: Parameters affecting the formwork pressures [3.12, 3.13].

Material property	Placement conditions	Formwork characteristics
• Cement type and content • Use of supplementary cementitious materials and fillers • Size, type and content of coarse aggregates • Water content • Chemical admixtures • Density of the SCC • Concrete consistency • Thixotropy • Setting time	• Filling rate • Placement method (casting from the top versus bottom pumping) • Casting height • Consolidation method • Vibration magnitude and duration • Effect during placement • Ambient and concrete temperatures	• Dimensions of the cast • Steel reinforcement • Demoulding oil characteristics • Surface material and roughness of the formwork walls • Formwork permeability and drainage

3.3.2 ACI 347-04 - 2004: Guide to Formwork for Concrete

Before the formation of ACI Committee 347 in 1955, there had been an increase in the application of reinforced concrete for longer span structures and multi-storeyed structures with increased story heights. The necessity of a formwork design standard together with a more thorough knowledge concerning the behaviour of formworks was evident from the rising number of failures, sometimes resulting in the loss of life. The first report by the committee, based on a survey of current practices in the United States and Canada was published in 1957.

The second report was published in 1958 and comprised an in-depth review of test reports and design formulas for determining lateral pressures on vertical formworks. Throughout many revisions, this second report has evolved since then into the current guide around formwork design, published in 2004.

The current revision of this guide covers the following aspects [3.14]:

- A listing of essential information to be included in the contract documents;
- Design criteria regarding horizontal and vertical forces on formworks;
- Design considerations, including the required safety factors, to be used when determining the capacities of formwork accessories;
- Preparation of adequate formwork drawings;
- Construction and use of formworks, including safety considerations during the erection;
- Materials suitable for formworks;
- Formworks for special structures;
- Formworks for special methods of construction;
- And last but not least, the required qualification of personnel for inspection and testing.

In the remainder of the current section we will only focus on the design criteria regarding the horizontal and vertical loads acting on the formwork walls. This will also be the case for the other described formwork design codes in the next sections.

3.3.2.1 Vertical loads

The vertical loads consist of dead and live loads. The sum of the weight of the formwork, of the steel rebars and of the freshly poured concrete represents the dead load or deadweight. The live load comprises the weight of the workers, the equipment, the material storage, the runways and eventual impact loads. The vertical loads should include all loads transmitted from the floors above, in accordance to the proposed construction schedule.

According to this ACI guide, the formworks must be designed for a live load which should not be less than 2.4 kPa. When motorized carts are used during the erection process, the live load should not be less than 3.6 kPa. The design load for combined dead and live loads may not be less than 4.8 kPa, or 6.0 kPa if motorized carts are used.

3.3.2.2 Horizontal or lateral loads

For fresh concrete having a slump value of 175 mm or less, and placed with normal internal vibration to a depth of 1.2 m or less, the formwork for columns must be designed for a lateral pressure according to Eq. (3.29), with a minimum of $30.C_w$ kPa but in no case greater than $\rho.g.h$:

$$p_{\max} = C_w C_c \left(7.2 + \frac{785.R}{T + 17.8} \right) \tag{3.29}$$

where p_{max} is the maximum lateral pressure (kPa), R is the placement rate or casting speed (m/h), T is the temperature of the fresh concrete (°C), C_w is the unit weight coefficient (-) (see Table 3-2), C_c is the chemistry coefficient (-) (see Table 3-3), ρ is the density of the concrete (kg/m³), g is the gravitational constant (= 9.81 m/s²) and h is the depth of the fluid or plastic concrete from the top of the placement to the point of consideration in the formwork (m).

Table 3-2: Unit weight coefficient C_w [3.14].

Density of concrete	C_w
Less than 2240 kg/m³	$C_w = 0.5.[1 + (\rho/2320)]$ but no less than 0.80
2240 kg/m³ to 2400 kg/m³	1.0
More than 2400 kg/m³	$C_w = \rho/2320$

Table 3-3: Chemistry coefficient C_c [3.14].

Cement type or blend	C_c
Types I, II and III without retarders *	1.0
Types I, II and III with a retarder *	1.2
Other types or blends containing less than 70 % of slag or 40 % of fly ash without retarders *	1.2
Other types or blends containing less than 70 % of slag or 40 % of fly ash with a retarder *	1.4
Blends containing more than 70 % of slag or 40 % of fly ash	1.4

(* Retarders include any admixture, such as a retarder, retarding water reducer, retarding midrange water-reducing admixture, or high-range water-reducing admixture (super-plasticizer), that delays the setting of the fresh concrete.)

For walls, with a rate of placement of less than 2.1 m/h and a formwork height not exceeding 4.2 m, the maximum lateral pressure can be also calculated using Eq. (3.29), with a minimum of $30.C_w$ kPa but in no case greater than $\rho.g.h$.

For walls, with a placement rate less than 2.1 m/h where the formwork height exceeds 4.2 m, and for all walls with a casting speed between 2.1 m/h and 4.5 m/h, the maximum lateral pressure can be determined using Eq. (3.30), with a minimum of $30.C_w$ kPa but in no case greater than $\rho.g.h$:

$$p_{\max} = C_w C_c \left(7.2 + \frac{1156}{T + 17.8} + \frac{244.R}{T + 17.8} \right) \tag{3.30}$$

For the purpose of applying the pressure formulas, columns are defined as vertical elements with no plan dimension exceeding 2 m, whereas walls are defined as vertical elements with at least one plan dimension being greater than 2 m.

Unless the conditions mentioned above are met, formworks should be designed for the lateral pressure given by Eq. (3.31):

$$p = \rho.g.h \tag{3.31}$$

For columns or other forms that can be filled rapidly before stiffening of the concrete takes place, *h* should be taken as the full height of the formwork or the distance between horizontal construction joints when more than one placement of concrete is to be made. When working with SCC, Eq. (3.31) should be used, until the effect on formwork pressure is understood by measurement.

3.3.3 CIRIA report 108 - 1985: Concrete Pressure on Formwork

The CIRIA report 108 originated from the CERA report 1, dating from 1965 [3.15]. This original report was based on experimental research performed on more than 200 construction sites in the UK. According to Taerwe and De Schutter [3.12], the CERA report 1 presented a new theory based on pore water pressure. This theory was based on the assumption that the vertical load induced by the fresh concrete was bared by two essential components within the concrete mixture, the pore water and the solid skeleton. The pore water would totally convert these vertical loads to horizontal loads on the surrounding formwork walls, whereas the solid skeleton would only partly convert them to lateral wall pressures.

The method presented in the CERA report 1 for calculating concrete pressures on formworks had served the construction industry well since 1965.
However, the included design charts were limited to plain ordinary Portland cement (OPC) concretes, and more recent trends towards a wider use of admixtures or blended cements were not taken into account. Also, the commercial need for faster construction had resulted in a general increase in lift heights and casting speeds.

CIRIA instigated a new research programme of site formwork pressure measurements and the compilation of a comprehensive data file to contain both the new site measurements and previously obtained data. This file about formwork pressures contained over 350 sets of measurement data. Using this data in conjunction with recent advances in the understanding of the occurring mechanisms, a more improved method of estimating the concrete pressure on formwork was formulated, and published in the CIRIA report 108, in 1985 [3.16].

The CIRIA report 108 about formwork pressure covers the following topics:

- The (renewed) design method;
- Several notes for guidance;
- And finally, some illustrative examples.

Although, as stated in Table 3-1 of the introduction, many factors affect the resulting concrete pressure on formworks, the CIRIA report 108 only focusses on the influence of the vertical form height, the rate of placement or the casting speed, the concrete temperature during casting and the use of admixtures and fillers on the maximum formwork wall pressure being exerted by the fresh concrete.

These influences are implemented in Eq. (3.32):

$$p_{\max} = D.\left(C_1\sqrt{R} + C_2 K \sqrt{H - C_1\sqrt{R}} \right) \text{ or D.h, whichever is the smaller} \quad (3.32)$$

where p_{max} is the maximum formwork wall pressure (kN/m²), D (= $\rho.g$) is the weight density of the concrete (kN/m³), H is the vertical formwork height (m), h is the vertical pour height (m), K (= [36/(T + 16)]²) is the temperature coefficient (-), T is the temperature of the fresh concrete (°C), R is the rate at which the concrete rises vertically up to the formwork top (m/h).

C_1 is a coefficient dependent on the size and shape of the formwork (C_1 = 1.0 for walls; C_1 = 1.5 for columns) ((m.h)$^{1/2}$) and C_2 is the coefficient dependent on the constituent materials of the concrete (see Table 3-4) ((m)$^{1/2}$).

Table 3-4: Values of the coefficient C_2 [3.16].

Concrete type	C_2
OPC, RHPC or SRPC without admixtures *	0.3
OPC, RHPC or SRPC with any admixtures, except a retarder *	0.3
OPC, RHPC or SRPC with a retarder *	0.45
LHPBFC, PBFC, PPFAC or blends containing less than 70 % of GGBFS or 40 % of PFA without admixtures *	0.45
LHPBFC, PBFC, PPFAC or blends containing less than 70 % of GGBFS or 40 % of PFA with any admixture, except a retarder *	0.45
LHPBFC, PBFC, PPFAC or blends containing less than 70 % of GGBFS or 40 % of PFA with a retarder *	0.6
Blends containing more than 70 % of GGBFS or 40 % of PFA *	0.6

(* See the list of symbols and abbreviations in the beginning of this thesis.)

The design pressure envelope, already proposed in the original CERA report 1, is shown in Fig. 3-10.

Much like in the ACI 347-04 Formwork Guide, this design pressure envelope and the stated equations of the CIRIA report 108 also limits the maximum formwork pressure for very fluid concrete like SCC to the hydrostatic pressure component.

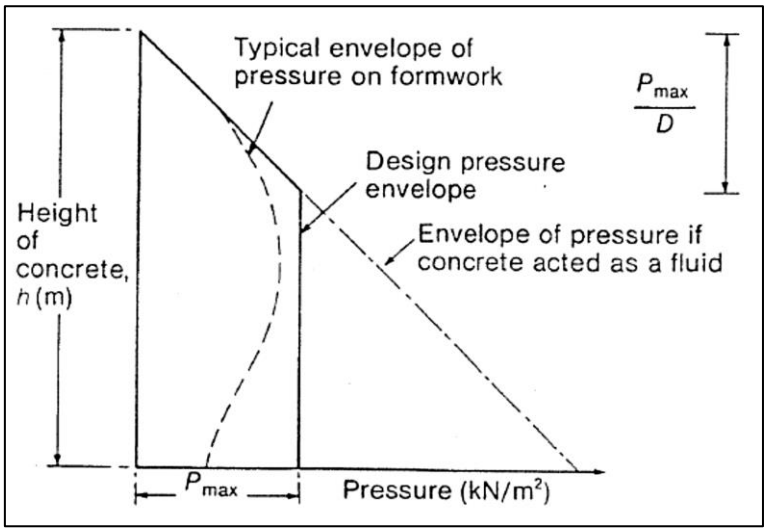

Fig. 3-10: Design pressure envelope according to the CIRIA report 108 [3.16].

3.3.4 DIN 18218 - 2010-01: Frischbetondruck auf lotrechte Schalungen

Compared to the original version of this standard published in 1980, the 2010 version also covers easy compacting concrete (ECC), with fluid and very fluid consistency (F5- and F6-grade concrete), and SCC. The loads are calculated in accordance with the partial safety concept familiar from the design standards in common use, like the series of Eurocode Standards. The influence of the fresh concrete temperature and the concrete compaction (vibration) is taken into account. Finally, test methods to determine the end of setting of concrete have also been specified.

This new version of the DIN 18218 standard may be applied for casting with CVC, complying to DIN EN 206-1 or DIN 1045-2, or to SCC, complying to the DafStb Guideline (German SCC Code of practice) entitled “Selbst-verdichtender Beton”. The maximum size of the aggregates in the fresh concrete mixture must however be limited to 63 mm.

This standard proposes a two-phase pressure build-up of the fresh concrete on the formwork walls after filling [3.17], very similar to the design pressure envelope of the CIRIA report shown in Fig. 3-10:

- An initial hydrostatic pressure build-up, which scales linearly with the casting height;
- Followed by a constant wall pressure.

This formwork wall pressure evolution is illustrated in Fig. 3-11 [3.17].

The design of a formwork, including its anchoring, shall be based on the design value of the fresh concrete pressure $\sigma_{hd} = \gamma_F.\sigma_{hk}$, with σ_{hk} being the characteristic value. The partial safety factor γ_F can be selected from DIN EN 12812. For the analyses at the ultimate limit state, the factor is $\gamma_F = 1.5$ for unfavourable actions. A partial safety factor of $\gamma_F = 1{,}0$ shall be used in cases where the fresh concrete pressure is assumed to act favourably. The characteristic value of the maximum possible fresh concrete pressure $\sigma_{hk,max}$ for various placing rates and consistency classes can be calculated using the equations given in Table 3-5 and Table 3-6, which are based on the following conditions:

- The fresh concrete density ρ is 25 kN/m^3. Where it has a different value, the calculated value of $\sigma_{hk,max}$ using the equations presented in Table 3-5 and Table 3-6 need to be multiplied by the factor $K_2 = \rho/25$ (ρ in kN/m³);
- The actual end of setting of the fresh concrete placed into the formwork does not exceed the end of setting time, t_E (t_E in h);
- The fresh concrete with a consistency class F1, F2, F3, F4, F5 or F6 is compacted using internal vibrators;
- The formwork need to be watertight (e.g. large-area formwork made of veneer plywood);
- The mean casting speed R (or v) of concrete of consistency class F1, F2, F3 or F4 does not exceed 7,0 m/h at any point;
- The concrete is poured in the opposite direction to the rise in level (i.e. it is placed from the top).

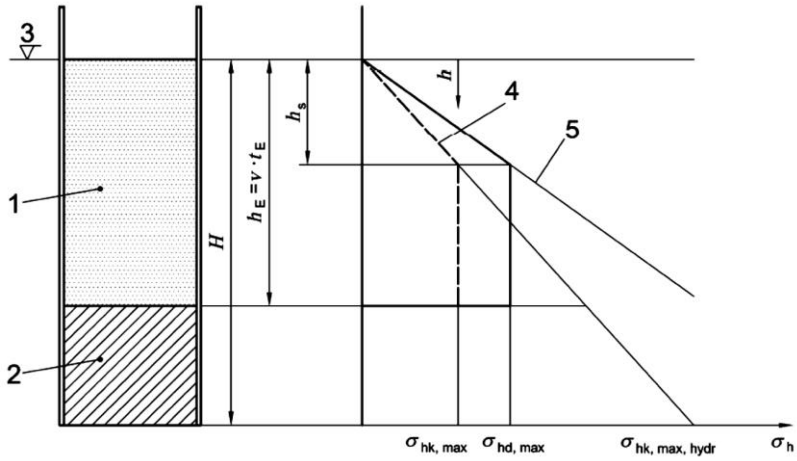

Key

1 fresh concrete
2 set (hardened) concrete
3 upper level of concrete
4 hydrostatic fresh concrete pressure
5 γ_F-times hydrostatic fresh concrete pressure

Fig. 3-11: Distribution of fresh concrete pressure over the height of the formwork [3.17].

According to the standard, if the concrete is pumped in the formwork from the bottom up to the top (such as when pumps are used for placing SCC), $\sigma_{hk,max}$ shall be assumed to be at least the hydrostatic fresh concrete pressure at the inlet location.

The maximum difference in height between the feed location and the upper level of the concrete should at no time be more than 3,5 m.

The end of setting of the fresh concrete is determined on the basis of its composition (*W/C* value, the cement type, additives, admixtures) and the temperature conditions (fresh concrete and ambient temperature combined with the type of formwork) at the time of placing, and is to be calculated during the initial testing phase (see the Vicat penetration method which is specified in the DIN EN 480-2 standard, or the knead-bag test method described in the Annex A of DIN 18218 - 2010-01).

Table 3-5: Characteristic values of max. lateral concrete pressure [3.17].

Consistency class	***Max. lateral fresh concrete pressure when placed in opposite direction to the rise in level (from above)*** $\sigma_{hk,max}$ (kN/m²)
F1	$(5.R + 21).K_1 \geq 25$
F2	$(10.R + 19).K_1 \geq 25$
F3	$(14.R + 18).K_1 \geq 25$
F4	$(17.R + 17).K_1 \geq 25$
F5	$25 + 30.R.K_1 \geq 30$
F6	$25 + 38.R.K_1 \geq 30$
SCC	$25 + 33.R.K_1 \geq 30$
Where: *R* (or *v* in the standard) is the placing rate (casting speed, poring rate) in m/h. K_1 is the factor taking into account the setting behaviour according to Table 7-6.	

Table 3-6: Factors K_1 for setting behaviour [3.17].

Consistency class	**Factors K_1**			
	End of setting t_E = 5 h	End of setting t_E = 10 h	End of setting t_E = 20 h	General [b]
F1 [a]	1.0	1.15	1.45	$1 + 0.03.(t_E - 5)$
F2 [a]	1.0	1.25	1.80	$1 + 0.053.(t_E - 5)$
F3 [a]	1.0	1.40	2.15	$1 + 0.077.(t_E - 5)$
F4 [a]	1.0	1.70	3.10	$1 + 0.14.(t_E - 5)$
F5, F6, SCC	1.0	2.00	4.00	$t_E / 5$
[a] Applies for concreting sections of a height *H* up to 10 m. [b] Applies for $5.h \leq t_E \leq 20.h$; t_E expressed in h.				

3.3.5 Summarizing remarks

In section 3.3, three of the most important standards regarding the concrete pressure on formworks walls during casting have been presented. They have been developed primarily for casting with CVC. Some modifications have been made in the newest editions of some of these standards regarding the use of SCC and regarding higher casting speeds, with a maximum of 7 m/h.

All of the presented standards are valid for casting from the top of a formwork, but only the DIN 18218 - 2010-01 standard includes some brief guidelines when the base-filling process is applied. The maximum formwork pressure in the presented standards is always limited to the hydrostatic pressure when very fluid concrete like SCC is used in conjunction with a high rate of placement.

A few researchers [3.18, 3.19] have published their mathematical models regarding formwork pressures during casting, but these models also focussed on top-filling processes with CVC. A very detailed overview of these models is given in the report presented by Khayat et al. [3.20]. Billberg [3.21], Ovarlez and Roussel [3.22] and Amziane et al. [3.23], they studied the top-filling process with SCC, specifically taking into account the wall pressure reducing effect of thixotropy and wall friction.

During our base-filling experiments with SCC, and at much higher placing rates than 7 m/h, we have experienced even higher wall pressures than the hydrostatic concrete pressure. The theoretical model explaining this observation will be presented in detail in section 3.4, and validated by the performed wall pressure measurements during our base-filling experiments, which will be presented in chapter 5.

This leads to the conclusion that at present none of the currently available formwork design standards are suitable for high speed base-pumping casting processes.

3.4 Formwork wall pressure during base-filling with SCC

3.4.1 Introduction

In section 3.2 we discussed two formwork filling processes with SCC: the top-filling process, where the fresh SCC is poured into the formwork from the top, and the base-filling process, where the fresh SCC is pumped into the formwork from the base. As mentioned in previous sections of chapter 3, the top-filling technique has already been studied quite intensively, whereas only very little research has been performed regarding the base-filling method.

In the remainder of this study, the focus is entirely dedicated towards the base-filling casting process and the related formwork pressures. In the current section, a mathematical model will be derived to predict analytically these wall pressures, whereas CFD models will be presented in chapter 6, which allow to determine numerically the formwork wall pressures during casting.

The analytical model will be built using the equations already derived in section 3.1 and a few additional concepts. The motivation for providing an analytical calculation method is to reduce the complexity of the formwork design calculations and to improve its practical use.

In section 3.4.3, a case example of a base-filling casting process will be used in order to compare the calculated formwork pressures using the analytical model and those obtained by applying the formulas mentioned in the formwork design standards which were presented in section 3.3. The calculated results using the analytical model will also be compared with the wall pressures measured during the base-filling experiment, in order to assess the validity of the presented analytical model and the available formwork design standards.

3.4.2 Analytical model

3.4.2.1 General considerations

In the base-filling configuration, the formwork is simply an extension of the supply duct, through which SCC is flowing. Therefore a large part of the SCC inside the formwork is constantly in motion, prohibiting the concrete to develop an internal structure able to bear its own weight without increasing the lateral pressure exerted on the formwork walls. Thus, with base-filling, almost no reduction of the formwork pressure due to thixotropy can be expected, certainly not when filling formworks at high casting rates. This will be further demonstrated in chapter 5.

3.4.2.2 Flow model derivation

As reported in the papers of the current author [3.8, 3.24], during the base-filling process, the formwork wall pressure will not only depend on the hydrostatic pressure, but also on the shear flow losses Δp_L. In turn, these shear flow losses depend on the filling velocity, the Herschel-Bulkley parameters (the yield stress, the consistency factor and the consistency index) (see section 3.1), the flow path length and also on the existence of local disturbances (for example, flow bifurcations due to bends, sudden expansions and/or contractions of the formwork cross-section, the presence of rebars).

To clarify this, consider a first point inside the column, just above the inlet column, where the SCC enters the formwork at the base, and a second point at the SCC-air interface. This configuration is shown in Fig. 3-12.

The Bernoulli equation, expressing the fluid flow physics between cross-section 1 and 2, (see section 3.1, Eq. (3.17)) then states that:

$$p_1 + \rho_{SCC}\frac{v_1^2}{2} + \rho_{SCC} g h_1 = p_2 + \rho_{SCC}\frac{v_2^2}{2} + \rho_{SCC} g h_2 + \Delta p_L \qquad (3.33)$$

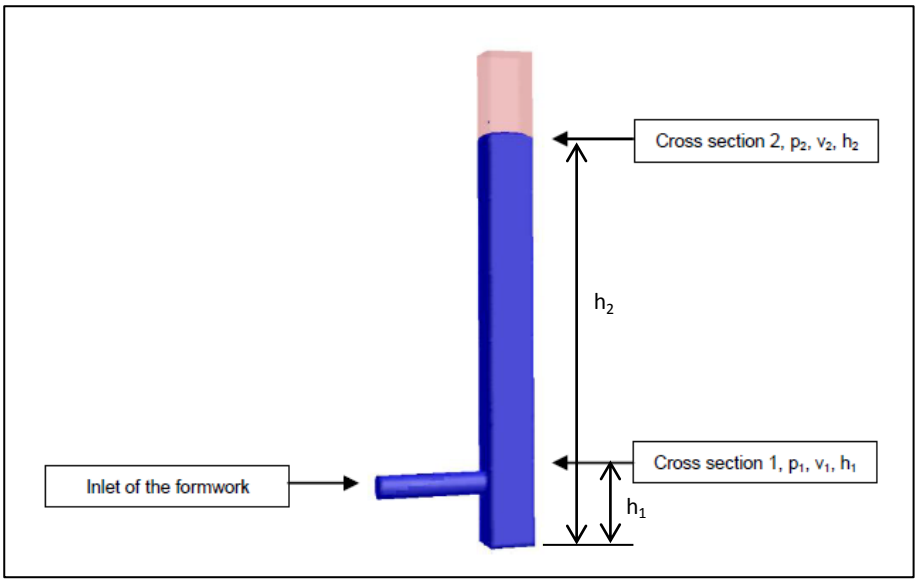

Fig. 3-12: Flow configuration inside a formwork - definition sketch.

As the cross-section of the column does not change over the entire height, so does the average filling velocity v also remain constant, and therefore v_1 equals v_2. The resulting pressure at the SCC-air interface is equal to the atmospheric pressure.

Referencing the static pressures p_1 and p_2 in Eq. (3.33) to the atmospheric pressure, and therefore only considering relative static pressures, p_2 equals zero. Eq. (3.33) then becomes:

$$p_{hor} = p_1 = \rho_{SCC} g (h_2 - h_1) + \Delta p_L \tag{3.34}$$

This clearly shows the additional contribution of the shear flow losses to the horizontal wall pressure p_{hor}, when the SCC is pumped in the formwork from the base. During the base-filling process, when the concrete surface inside the formwork has already passed the inlet and is moving towards the top, in the lower part of the formwork just under the inlet, the SCC is almost at rest.

Therefore, the maximum wall pressure at the base of the formwork $p_{max,base}$ can be estimated using Eq. (3.35).

$$p_{max,base} = p_1 + \rho_{SCC} g h_1 = \rho_{SCC} g (h_2 - h_1) + \Delta p_L + \rho_{SCC} g h_1 = \rho_{SCC} g h_2 + \Delta p_L \tag{3.35}$$

The validity of this equation will be proven by the results from the numerical simulations of the filling experiments being performed during this research, which are presented in chapter 6, as well as the performed wall pressure measurements. This will be discussed in the next section through a case example.

Knowing the pumping flow rate Q and the rheological characteristics of the selected SCC (τ_0, K and n), the shear flow losses Δp_L can be determined iteratively using Eq. (3.19), Eq. (3.25c), Eq. (3.25d) and Eq. (3.25e) from section 3.1.

Once these shear flow losses are calculated, they can be inserted in Eq. (3.35) in order to obtain the maximum occurring wall pressure at the base of the formwork during the base-filling casting process.

Carefully looking at the equations determining Δp_L, still one aspect remains to be clarified. The geometry of the cast element (formwork and rebar layout) is also influencing the shear flow losses, and as such the maximum wall pressure. This influence is clearly present throughout the geometrical parameters R (radius of the flow section) and L (length of the flow path).

For the cylindrical inlet duct it is rather obvious that R is the radius of the duct, but for the formwork of a column, beam or wall with rebars inside it is much less obvious how R should be interpreted.

From basic hydraulics theory we know that there is one parameter which describes the relative importance of the wall surface within a certain flow volume with respect to the shear flow losses, i.e. the hydraulic diameter D_h.

The hydraulic diameter is defined as:

$$D_H = \frac{4S}{P} \tag{3.36}$$

where S is the flow cross-section (m²) and P is the wetted perimeter (m).

Based on this hydraulic diameter we can define an equivalent radius R_{eq}, being equal to half the hydraulic diameter ($R_{eq} = D_H/2$), and use this equivalent radius inside Eq. (3.19), Eq. (3.25c), Eq. (3.25d) and Eq. (3.25e) in order to determine in the end the maximum occurring wall pressure.

This procedure will be applied in the case example presented next.

3.4.3 Comparison between available formwork design codes

3.4.3.1 Case example: base-filling process of a column formwork with rebars

In Fig. 3-13 the layout of a base-filling process with SCC of a column formwork with rebars is shown, which has been selected as a case example for comparing the available methods for predicting the maximum formwork wall pressures during base-filling casting.

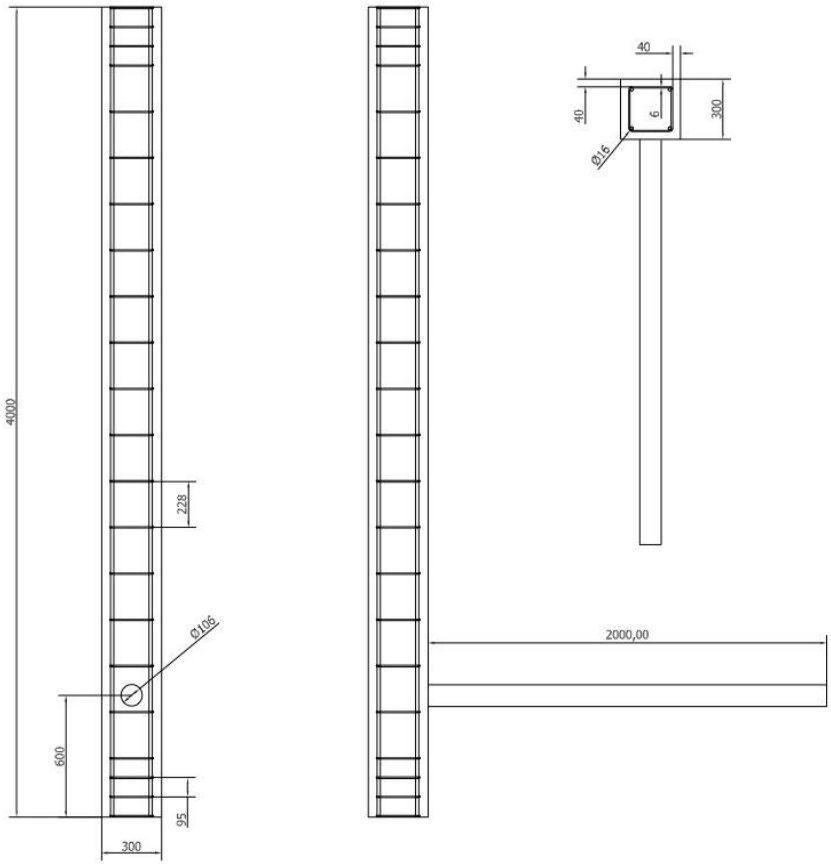

Fig. 3-13: Geometry and rebar configuration of the base-filling case example.

The reinforcement ratio is around 1 % and can therefore be categorized as being low, according to Eurocode 2: Design of concrete structures EN1992-1-1.

The selected SCC for this base-filling process has the following mixture composition for a reference volume of 1 m³:

- Sand 0/5: grain size between 0 mm and 5 mm - 895 kg/m³;
- Limestone aggregates 2/6.3: size between 2 mm and 6.3 mm - 725 kg/m³;
- Cement type III/A 42.5 LA: blast furnace cement, low alkaline - 300 kg/m³;
- Filler type: limestone filler - 300 kg/m³;
- Super-plasticiser type: polycarboxylether type super-plasticiser - 10.45 l/m³;
- Water: 160 l/m³;
- Water-to-cement ratio (W/C): 0.53;
- Water-to-powder ratio (W/P): 0.27.

The rheological characteristics, measured with a BML Contec-Viscometer 5, are represented by the following Herschel-Bulkley model parameters (see chapter 2):

- The yield stress τ_0: 207.7 Pa;
- The consistency factor K: 33.63 Pa.s^n;
- The consistency index n: 1.16.

The formwork with rebar, shown in Fig. 3-13, has been filled from the base with a pumping discharge Q of 2.56 l/s or 0.00256 m³/s. The measured density of the SCC in the fresh state is 2273 kg/m³.

The hydraulic diameter D_H is calculated using Eq. (3.36) with the following parameter values:

- The wetted flow cross-section (with the four vertical rebars Ø16 mm): $S = 0.3^2 - \pi \times 0.016^2 = 0.089\ m^2$;
- The wetted perimeter: $P = 4 \times 0.3 + 4 \times \pi \times 0.016 = 1.4\ m$;
- The hydraulic diameter: $D_H = \frac{4S}{P} = \frac{4 \times 0.089}{1.4} = 0.255\ m$.

The height of the column (h_2) is 4 m and the position of the inlet (h_1) is 0.6 m from the base, (see Fig. 3-13). The resulting flow path length L in the column is 4 m - 0.6 m = 3.4 m.

3.4.3.2 Case example: comparison of the formwork pressure calculation methods

In this section, the design code rules presented in section 3.3 as well as the new analytical model described in section 3.1 about predicting the occurring formwork pressures during casting will be applied on the base-filling process presented in the case example above.

These calculated formwork pressure results will be compared with the simulation results from a flow simulation based on a 3-D CFD model and with the measured formwork pressures during the corresponding filling experiment. The 3-D CFD model will be presented in detail in chapter 6.

3.4.3.2.1 ACI 347-04-2004 [3.14]

According to the ACI 347-04-2004 design code, for columns that are rapidly filled before the stiffening of the concrete takes place, Eq. (3.31) should be used to determine the maximum formwork wall pressure. This equation represents the occurring hydrostatic pressure. In this equation h should be taken as the full height of the formwork.

The horizontal formwork pressure according to Eq. (3.31) is:

$$p_{max} = \rho g h = 2273\ \frac{kg}{m^3} \times 9.81\ \frac{m}{s^2} \times 4\ m = 89192.52\ Pa = 0.89 \times 10^5 Pa$$

3.4.3.2.2 CIRIA report 108 - 1985 [3.16]

According to the CIRIA report 108 - 1985, for determining the maximum occurring formwork pressures during casting, Eq. (3.32) should be used.

The input parameters of Eq. (3.32) are:

- The weight density of the concrete: $D = \rho g = 2273 \times 9.81 = 22298.13\ \frac{kN}{m^3}$;
- The shape coefficient for columns: C_1 = 1.5;
- The placement rate or casting speed with an inlet duct Ø106 mm: R = 105 m/h;
- According to Table 3-4 for cement blends with a retarder: C_2 = 0.6;
- The temperature of the fresh concrete: T = 20 °C;
- The temperature coefficient: $K = \left(\frac{36}{T+16}\right)^2 = 1$;
- The vertical formwork height: H = 4 m.

The horizontal formwork pressure according to Eq. (3.32) is:

$$p_{max} = 22298.13 \left(1.5\sqrt{105} + 0.6 \times 1 \times \sqrt{4 - 1.5\sqrt{105}}\right)\ Pa$$

This equation is clearly not valid for the selected placement rate during our base-filling case experiment. The term under the second square root in the equation leads to a negative value for the mentioned input parameters.

The CIRIA report states that the formula $D.h = \rho.g.h$ should otherwise be used to determine the maximum occurring formwork pressure. In this case p_{max} also equals to 0.89 x 10^5 Pa.

3.4.3.2.3 DIN 18218 - 2010-01 [3.17]

Table 3-5 in section 3.3 summarizes the equations of the DIN 18218 - 2010-01 standard for calculating the maximum formwork wall pressure depending on the consistency class of the chosen concrete.

Unfortunately, these equations are only valid when cast from the top of the formwork.

The DIN standard states however that when fresh concrete is pumped from the bottom up to the top of the formwork, the maximum formwork wall pressure is assumed to be hydrostatic.

Therefore, also according to this standard, p_{max} should equate to 0.89 x 10^5 Pa.

3.4.3.2.4 Analytical model

The maximum formwork pressure at the bottom of the column can be determined by iteratively solving Eq. (3.25e) for the wall shear stress τ_w with the input parameters presented in section 3.4.3.1.

Having determined the wall shear stress, Eq. (3.19) and Eq. (3.35) must then be used to calculate the shear flow losses and the resulting maximum formwork wall pressure respectively.

The calculation results obtained with the analytical model are:

- The wall shear stress: τ_w = 315.8 Pa;
- The shear flow losses: Δp_L = 4.95 x 10^3 Pa/m;
- The maximum wall pressure at the bottom of the column: p_{max} = 1.06 x 10^5 Pa.

3.4.3.2.5 CFD model

The base-filling process of the case example has been modelled with a CFD model, of which the meshed geometry is shown in Fig. 3-14.

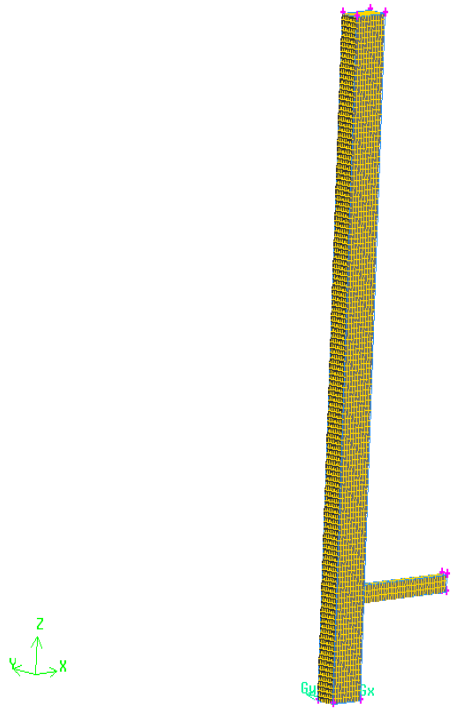

Fig. 3-14: Meshed geometry of column with rebars.

The Finite Volume Method (FVM), combined with the Volume of Fluid (VOF) method, has been used to numerically discretise and solve the flow equations for the field variables, being the pressure, the velocity components and the two phase volume fractions of SCC and air in each mesh cell of the flow domain. Further details of this CFD model will be given in chapter 4 and chapter 5.

3.4.3.2.6 Simulation results and measurements

Fig. 3-15 shows the experimentally measured formwork wall pressure at the base (and two other wall positions) of the column during the performed base-filling process selected for this case example. For comparison, the hydrostatic pressure evolution during the casting has also been included in the graph.

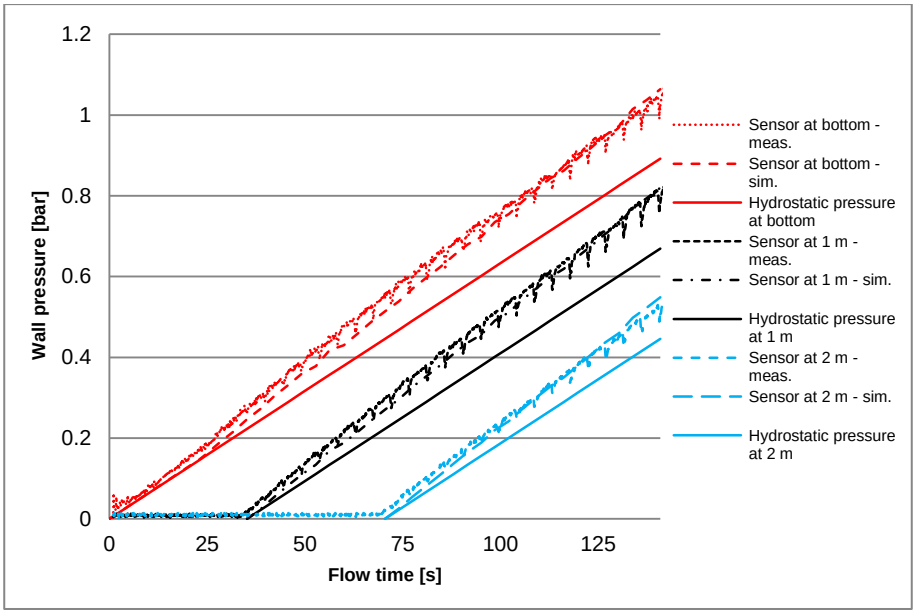

Fig. 3-15: Wall pressure measurements during the base-filling casting process.

The measurements shown in Fig. 3-15 reveal that the maximum formwork wall pressure p_{max} at the bottom of the column equals 1.064 x 10^5 Pa. The simulated maximum formwork wall pressure p_{max} at the bottom of the column reads 1.07 x 10^5 Pa.

3.4.4 Summarizing comments

For the case example presented in section 3.4.3.1, the measured and calculated maximum formwork wall pressure at the bottom of the column are summarized in the following table:

Table 3-7: Maximum formwork wall pressure p_{max} at the bottom of the column of the case example presented in Section 3.4.3.1.

Calculation method / measurement	Max. formwork wall pressure p_{max} (Pa)
ACI 347-04-2004	0.89×10^5
CIRIA report 108 - 1985	0.89×10^5
DIN 18218 - 2010	0.89×10^5
Analytical model (Section 3.1)	1.06×10^5
CFD model (Chapter 4 and 5)	1.07×10^5
Measurements	1.064×10^5
Hydrostatic pressure	0.89×10^5

Clearly none of the described formwork design standards are able to accurately predict the occurring maximum formwork wall pressure during the presented base-filling experiment with SCC. The calculated results differ with the measured results by 16 % ($= \frac{1.064-0.89}{1.064} \times 100\%$)!

Therefore the contribution of the shear flow losses to the maximum occurring wall pressure, and this in addition to the hydrostatic pressure component, is certainly not to be neglected during base-filling with SCC!

On the other hand, the analytical model and the numerical CFD model are apparently able to quite accurately determine the maximum formwork wall pressure during base-filling.

Additional validation of both formwork wall pressure calculation models will be presented in chapter 5.

3.5 References

[3.1] Hirsch Ch., "Numerical Computations of Internal and External Flows, Vol. 1 - Fundamentals of Numerical Discretization", John Wiley & Sons, New York (1989).

[3.2] Macosko C.W., "Rheology Principles, measurements and applications", Wiley-VCH, New-York (1994), 568 pages.

[3.3] Hagen G., "Ueber die Bewegung des Wassers in engen cylindrischen Rohren", Poggendorfs Ann. Phys. Chem. **46**, (1839), pp. 423-442.

[3.4] Poiseuille J.L.M., "Recherches expérimentales sur le mouvement des liquides dans les tubes de très-petits diameters", CR Acad. Sci. Paris. **11**, (1840),pp. 961-967 and 1041-1049.

[3.5] Poiseuille J.L.M., "Recherches expérimentales sur le mouvement des liquides dans les tubes de très-petits diameters", CR Acad. Sci. Paris. **12**, (1841), pp. 112-115.

[3.6] Feys D., "Interactions between Rheological Properties and Pumping of Self-Compacting Concrete", Ph-D dissertation, Ghent University, Ghent (2009).

[3.7] Potter D., Construction Photography, Asset Information : A052-02084.

[3.8] Tichko S., De Schutter G., Troch P., Vierendeels J., Verhoeven R., Lesage K., Cauberg N., "Influence of the viscosity of self-compacting concrete and the presence of rebars on the formwork pressure while filling bottom-up", Eng. Struct., vol. **101**, (2015), pp. 698-714.

[3.9] De Schutter G., Feys D., Verhoeven R., "Ecological profit for a concrete pipe factory due to self-compacting concrete technology", Proceedings of the 2nd International Conference on Sustainable Construction Materials and Technologies, Vol. 2, Eds. J. Zachar et al., Ancona, (2010), pp. 1281-1287.

[3.10] EFNARC, "European guidelines for self-compacting concrete", Joint Research Group, Brussels (2005), 68 pages.

[3.11] De Schutter G., Bartos P., Domone P., Gibbs J., "Self-Compacting Concrete", Whittles Publishing, Caithness (2008), 296 pages.

[3.12] Taerwe L., De Schutter G., "Betontechnologie", course notes (in Dutch) UGent, Ghent (2006), 250 pages.

[3.13] Omran A.F., Khayat K.H., Elaguab Y.M., "Effect of SCC Mixture Composition on Thixotropy and Formwork Pressure", J. Mater. Civ. Eng., ASCE (2012), pp. 876-888.

[3.14] ACI Committee 347-04, "Guide to Formwork for Concrete", ACI Standard, (2004).

[3.15] CERA, "CERA Research Report 1 - Pressure of concrete on formwork", (1965).

[3.16] CIRIA, "CIRIA Report 108 - Concrete pressure on formwork", Construction Industry Research and Information Association, London (1985).

[3.17] Deutsches Institut für Normung, "DIN 18218:2010-01 - Frischbetondruck auf lotrechte Schalungen", Beuth Verlag, Berlin, (2010).

[3.18] Adam M., Bennasr M., Santos Delgado H., "Poussée du béton frais sur les coffrages", Annales de l'ITBTP, (1965).

[3.19] Gardner N.J., "Formwork pressure and cement replacement by fly ash", American Concrete Institute, Farmington Hills, (1984).

[3.20] Khayat K.H., Bonen D., Shah S., Taylor P., "SCC Formwork Pressure - Task 1: Capturing existing knowledge on formwork pressure exerted by SCC", National Ready-Mix Concrete Research Foundation - American Concrete Institute, (2007).

[3.21] Billberg P., "Form pressure generated by SCC - Influence of Thixotropy and Structural Behaviour at Rest", Ph-D dissertation, Royal Institute of Technology, Stockholm, (2006).

[3.22] Ovarlez G., Roussel N., "A physical model for the prediction of lateral stress exerted by self-compacting concrete on formwork", Materials and Structures vol. 35, (2006), pp. 269-279.

[3.23] Amziane S., Perrot A., Ovarlez G., Roussel N., "SCC Formwork Pressure: Influence of Steel Rebars", 6th International RILEM Symposium on self-compacting, SCC 2010 Conference Proceedings vol. 2, Montreal, (2010), pp. 759-771.

[3.24] Tichko S., Van De Maele J., Vanmassenhove N., De Schutter G., Vierendeels J., Verhoeven R., Troch P., "Numerical simulation of formwork pressure while pumping self-compacting concrete bottom-up", Eng. Struct., vol. **70**, (2014), pp. 218-233.

Chapter 4: Numerical simulation techniques for concrete flow modelling

"In science there is only physics; all the rest is stamp collecting." - Lord Kelvin

4 Overview of this Chapter

In order to determine the most suitable modelling technique for simulating pressure driven SCC flows in supply ducts and formworks, a literature review of numerical techniques applied to fresh concrete flows has been performed, which is presented In section 4.1. For each of the investigated numerical methods, the advantages and disadvantages, as perceived by the author, have been evaluated and the finite volume method (FVM) combined with the volume of fluid (VOF) method has been selected. The motivation for this choice is reported in section 4.1.6.

The FVM-VOF combination is typically applied for simulating transient multiphase flows of two or more immiscible fluids, where the position of the interface between the fluids is of interest. For the case of formwork filling, two fluids or phases are considered: the air initially present in the empty formwork and the fresh concrete gradually replacing the air. Both methods are described in detail in section 4.2.

In section 4.3, the porous zone modelling technique is introduced, which allows to study the influence of the rebar configuration on the fresh concrete flow in a formwork without having to model the rebars explicitly and therefore reducing the pre-processing and the computational time significantly.

4.1 Literature review of numerical techniques for concrete flow modelling

4.1.1 The Discrete Element Method (DEM)

In this section, a numerical simulation method is introduced, which has the ability to model fresh concrete as a suspension of aggregates or solid particles in a fluid cement paste, including the interactions between the suspended particles and the suspending fluid. This modelling approach allows to study several phenomena like segregation, shear induced particle migration and blocking. Section 4.1.1 is divided into five main sub-sections. Section 4.1.1.1 describes the underlying principles and theory behind the Discrete Element Method (DEM). Section 4.1.1.2 focusses on the application of DEM to fresh concrete flow simulation. Section 4.1.1.3 highlights the very important aspect of model calibration and verification when using DEM to simulate fresh concrete flow. Section 4.1.1.4 shows some examples of application of DEM to fresh concrete testing and manufacturing processes. Finally, in section 4.1.1.5, an attempt has been made to summarize the benefits of applying DEM to fresh concrete flow modelling as well as some of the reported problems encountered so far during practical implementation.

4.1.1.1 Principles and theory behind DEM

4.1.1.1.1 Equations of motion

As mentioned by Mechtcherine et al. [4.1], DEM (as well as a derivative method called the Particle Method) provides a way to simulate and analyse the movement (translation and rotation) of distinct particles and their mutual interactions, including separation and automatic contact detection.

This method was originally developed as a numerical tool to perform research into the behaviour of granular materials.

A fundamental assumption of DEM, given by Cundall et al. [4.2], is that the material consists of separate discrete particles. The forces acting on each individual particle are computed according to the applicable laws of physics.

The particles are considered to be rigid and the contacts between neighbouring particles occur only at one point during a given time. The calculations make use of Newton's second law, describing the motion of particles, and the force-displacement law at the contacts.

Each individual particle moves according to Newton's second law and the kinematic equation for torque, presented in Eq. (4.1) and Eq. (4.2):

$$\vec{F}_i = m\left(\vec{\ddot{x}}_i - \vec{g}_i\right) \tag{4.1}$$

$$\vec{M}_i = I\vec{\dot{\omega}}_i \tag{4.2}$$

where $\vec{F}_i$ is the contact force acting on the particle (N), m is the mass of the particle (kg), $\vec{\ddot{x}}_i$ is the translational acceleration (m/s²), $\vec{g}_i$ is the gravitational acceleration constant (m/s²), $\vec{M}_i$ is the resultant moment acting on the particle (N.m), I is the mass moment of inertia (kg.m²) and $\vec{\dot{\omega}}_i$ is the angular acceleration of that particle (rad/s²).

The contact force vector $\vec{F}_i$ representing the action of particle A on particle B in a particle-to-particle contact is shown in Fig. 4-1. This contact force also represents the action of the wall on the particle for wall-to-particle contact.

This vector can be decomposed and resolved into its normal component and its tangential component with respect to the contact plane:

$$\vec{F}_i = \vec{F}_i^n + \vec{F}_i^t \tag{4.3}$$

where $\vec{F}_i^n$ is the normal contact force component and $\vec{F}_i^t$ represents the tangential contact force component. The force-displacement law relates these two force components to the corresponding components of the relative displacement (see section 4.1.1.2).

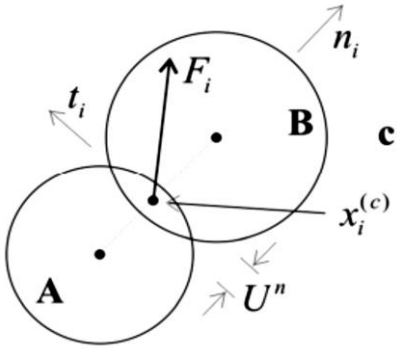

Fig. 4-1: Contact model of DEM [4.2, 4.7 and 4.8].

4.1.1.1.2 Numerical solution scheme

The presented dynamic behaviour is translated numerically using a time-stepping algorithm which assumes that the velocities and accelerations are constant within each time step. In DEM software codes, like ITASCA® PFC^{2D} and PFC^{3D}, EDEM®, LIGGHTS® and Ansys Fluent®, the equations of motion, represented by Eq. (4.1) and Eq. (4.2), are integrated using a central finite difference scheme [4.2].

The translational and angular velocities are calculated at $t \pm \Delta t/2$, Δt being the time step size. The translational displacements and rotational angles, the translational and angular accelerations, the forces and the moments are computed at $t \pm \Delta t$.

The accelerations are computed and updated after each time step according to the following finite difference scheme:

$$\vec{\ddot{x}}_i^{(t)} = \frac{1}{\Delta t}\left(\vec{\dot{x}}_i^{(t+\frac{\Delta t}{2})} - \vec{\dot{x}}_i^{(t-\frac{\Delta t}{2})}\right) \tag{4.4}$$

$$\vec{\dot{\omega}}_i^{(t)} = \frac{1}{\Delta t}\left(\vec{\omega}_i^{(t+\frac{\Delta t}{2})} - \vec{\omega}_i^{(t-\frac{\Delta t}{2})}\right) \tag{4.5}$$

Inserting these expressions in Eq. (4.1) and Eq. (4.2) we obtain:

$$\vec{\dot{x}}_i^{(t+\frac{\Delta t}{2})} = \vec{\dot{x}}_i^{(t-\frac{\Delta t}{2})} + \left(\frac{\vec{F}_i^{(t)}}{m} + \vec{g}_i\right)\Delta t \tag{4.6}$$

$$\vec{\omega}_i^{(t+\frac{\Delta t}{2})} = \vec{\omega}_i^{(t-\frac{\Delta t}{2})} + \frac{\vec{M}_i^{(t)}}{I}\Delta t \tag{4.7}$$

Finally, the positions are updated according to Eq. (4.8):

$$\vec{x}_i^{(t+\Delta t)} = \vec{x}_i^{(t)} + \vec{\dot{x}}_i^{(t+\frac{\Delta t}{2})}\Delta t \tag{4.8}$$

A similar discretization scheme is used for the rotations. The force-displacement law (see section 4.1.1.2) is then used to update the contact forces arising from the relative motion at each contact. This process is based on the relative motion between two entities in contact and the constitutive model used in the particular contact. Next, the law of motions are again applied to each particle to re-determine its velocities (translational and angular), the rotation and position. This is based on the resultant force and moment arising from the contact force and any other force acting on the particle, like gravity.

4.1.1.2 DEM in fresh concrete flow simulations

4.1.1.2.1 Fresh concrete modelling using DEM

Fresh concrete can be considered as a two-phase system: aggregates and cement paste or mortar. Mechtcherine et al. [4.1] have proposed to model these two phases using basic solid particles (discs (2-D) or spheres (3-D)), and the interactions between them are controlled by appropriate constitutive relations. This is illustrated in Fig. 4-2.

The use of simply shaped basic elements makes the contact detection quite easy and the calculation fast. If complex geometries are to be modelled like the confining formwork walls, the steel rebars, the fibre reinforcement inclusions or non-spherical aggregates, a number of these basic particles can be rigidly inter-connected to form the required shapes (see Fig. 4-2).

For each material in the DEM model, an appropriate density is assigned to the representative particles or particle groups.

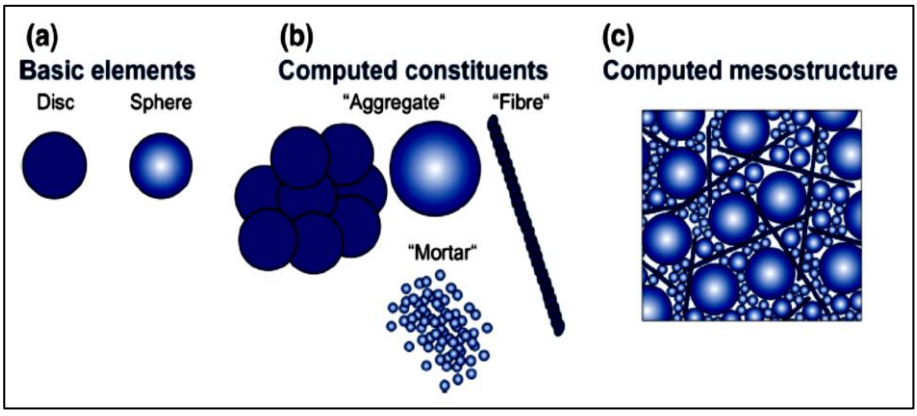

Fig. 4-2: DEM modelling of fresh concrete using poly-sized solid particles [4.1].

4.1.1.2.2 Constitutive relationships

Structural materials submitted to forces will deform. These deformations can be modelled by superimposing viscous, elastic and plastic effects. Basic rheological models describing these effects are therefore introduced, which enables the modelling of complex material behaviour. These basic models are 1-D models.

In DEM, the elastic deformations are modelled by a spring, whereas the plastic deformations are represented using a friction slider. Viscous interaction is simulated by a dashpot model, where the stress is proportional to the shear rate.

Fresh concrete, and SCC in particular, is a yield stress material, as described in chapter 2. It shows little or no deformation up to a certain stress level. Above the yield stress the material starts to flow. The corresponding rheological models for the normal and tangential direction, as proposed by Shyshko et al. [4.4], are shown in Fig. 4-3.

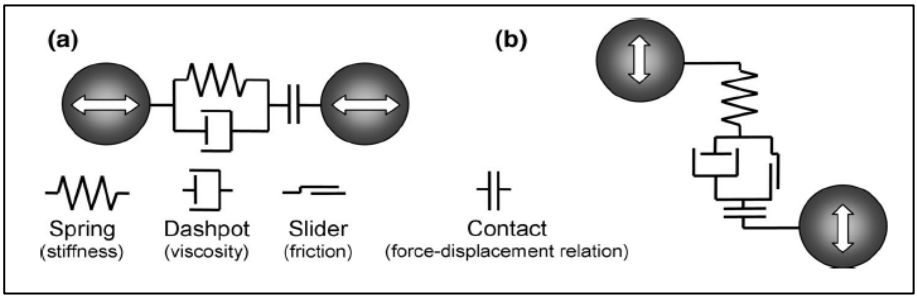

Fig. 4-3: Models for particle interaction: (a) normal direction, (b) tangential direction [4.4].

Besides the rheological elements spring, dashpot and slider, the two interaction models also include a contact element, which enables the definition of the strength of the contact, the loss of an old interaction by reaching a certain distance between two particles and the formation of a new interaction. The spring is very stiff and the threshold value of the slip function is at the level of the yield stress.

4.1.1.2.3 Parameter estimation

A major challenge of particle simulation is the estimation of the material models presented in the previous section. The behaviour of SCC in the fresh state can only be considered by an appropriate selection of these general model parameters describing the interactions between the individual particles. The calibration of these model parameters is usually performed using the results of the standard concrete tests, like slump or slump flow. The material parameters in the simulation of these reference tests need to be iteratively adjusted until the results of the real experiment are matching the results from the simulation.

As mentioned by Mechtcherine et al. [4.1] and by Shyshko [4.7], this calibration procedure is very difficult and time-consuming. Even more so, the evaluation of the obtained simulation results and the resulting parameter adjustments are not always straightforward and accurate. One method is to use a mathematical optimization tool for the parameter calibration. This reduces the work load and the empirical influence on the obtained results. Another approach is to estimate the simulation parameters based on measured material constants, describing its flow behaviour according to a particular rheological model like the Bingham model or the Herschel-Bulkley model presented in chapter 2.

However, a very important requirement for this approach is the reliable determination of the dependencies between the presented DEM constitutive parameters and the rheological parameters. At present, both methods are still in the development phase but some promising results have already been reported [4.3, 4.7].

4.1.1.2.4 Particle size effect

Applying DEM, it is possible to simulate the effect of the fresh concrete composition on its rheological behaviour by defining the components of the fresh concrete like the mortar, sand particles and the coarse aggregates using DEM particles of different sizes. However in [4.1, 4.5] a different approach was proposed. The fresh concrete behaviour was simulated using round particles of only one size. Such a single-size particles DEM model can be interpreted as a multitude of round or spherical aggregates of some average representative size, each being uniformly covered by a layer of cement paste. Such an approach revealed to have clear advantages with respect to the practical application of the presented DEM modelling method as the treatment of the collision between particles became relatively simple and the resulting computations quite fast.

Using small particles leads to long calculation times, due to the large number of particles in the computational domain. The maximum size of the particles is determined by the maximum aggregate size in the concrete mixture. A change in particle size evidently leads to an altered mechanical interaction between the particles, and as such to a modified rheology. Selecting larger particle sizes will lead to higher simulated values of the slump or slump flow diameter. This effect can be explained by the larger particles being heavier, with a higher gravitational force acting on them.

If the same flow behaviour is to be obtained, independent of the particle size, the maximum interaction forces between the particles should be proportional to their mass. Mechtcherine and Shyshko [4.4] proposed a corresponding correction coefficient *k*, defined in Eq. (4.9), to compensate for the particle size effect of the same density ρ.

$$k = \frac{m_i}{m_0} = \frac{\rho V_i}{\rho V_0} = \frac{\frac{3}{4}\pi R_i^3}{\frac{3}{4}\pi R_0^3} = \left(\frac{R_i}{R_0}\right)^3 \tag{4.9}$$

where m_i, V_i and R_i are the mass, the volume and the radius of the particles of different size, while m_0 and V_0 are representative for the reference particle size R_0.

4.1.1.3 Parameter calibration and validation

4.1.1.3.1 Parameter calibration based on slump or slump flow test results

In order to use DEM for modelling fresh concrete flows, it is necessary to determine the DEM constitutive parameters, shown in Fig. 4-3. As stated in section 4.1.1.2.1, they represent the interactions between the particles. Slump or slump flow measurements performed with fresh concrete batches are used to calibrate these parameters. The calibration ends when the final set of DEM parameters is able to accurately simulate the shape or spread at the end of the performed slump or slump flow reference tests. As already mentioned in section 4.1.1.2.3, this is not a simple job. More information about the DEM calibration procedure is presented in the technical article of Mechtcherine et al. [4.1] and in the Ph-D dissertation of Shyshko [4.7].

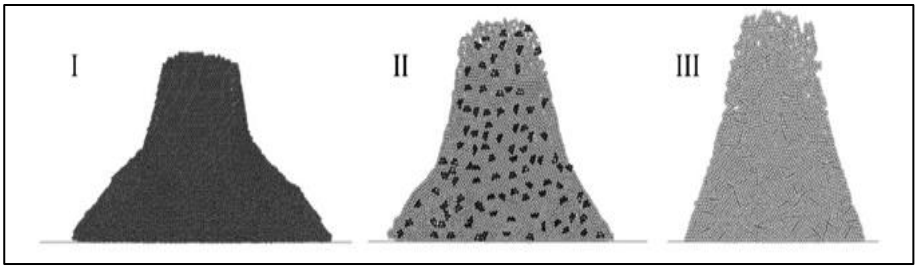

Fig. 4-4: Simulation of slump tests during parameter calibration [4.1].

Fig. 4-4 shows some examples of simulated slump tests during the calibration of the DEM constitutive parameters of traditional vibrated concrete, whereas Fig. 4-5 shows a simulated slump flow test with SCC.

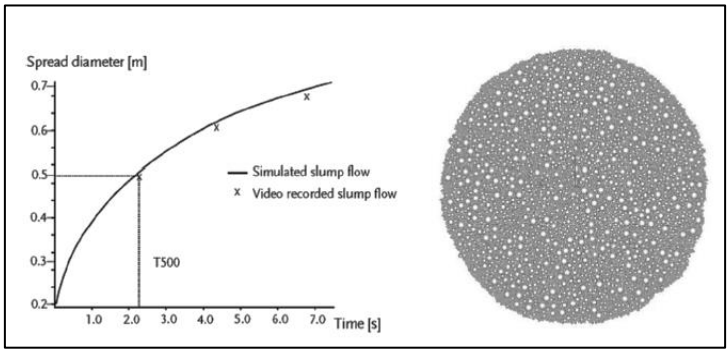

Fig. 4-5: Simulation of a slump flow test during parameter calibration [4.1].

The graph in Fig. 4-5 shows the resulting agreement between the simulated and measured concrete spread at the end of the slump flow test after proper calibration.

4.1.1.3.2 Model validation based on J-ring or L-box test results

As previously mentioned, the slump test or the slump flow test serves as the basis for model calibration. In order to be able to assess the predictive ability of the numerical simulation, other standard concrete test types are used as a reference to validate the model further while all the DEM parameters are held constant after the calibration phase. The L-box and J-ring test, which are common fresh SCC tests described in the work of De Schutter et al. [4.9], are usually used for this model validation step.

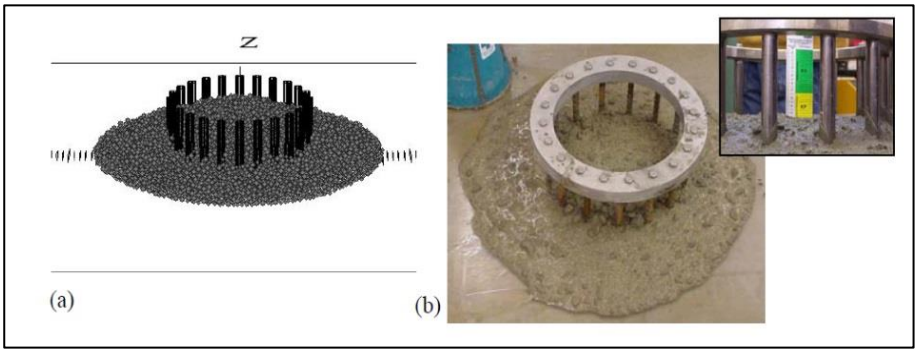

Fig. 4-6: Numerical (a) and experimental (b) results of a J-ring test with SCC [4.5].

Such a model validation, after parameter calibration using the experimental results of a J-ring test with SCC, is illustrated in Fig. 4-6. Another model validation is shown in Fig. 4-7, which is based on the experimental results of an L-box test with SCC at three different time steps.

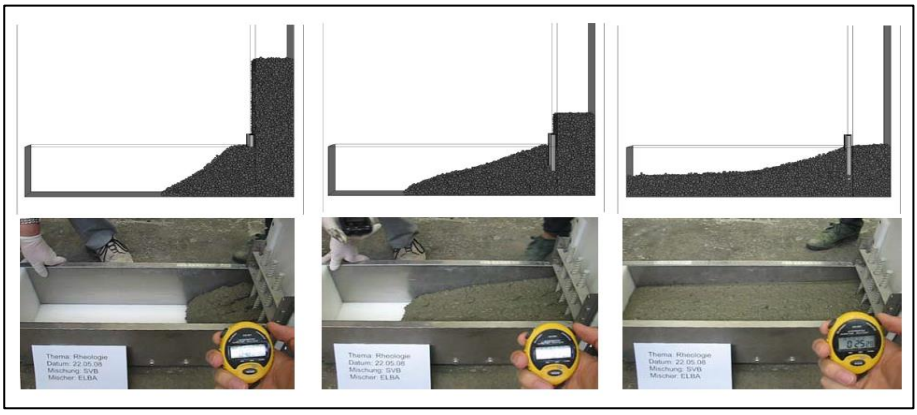

Fig. 4-7: Comparison between simulation (above) and experiment - L-box test [4.5].

4.1.1.4 A few practical applications of DEM

4.1.1.4.1 Mixing

In order to obtain a good quality cast it is absolutely necessary to produce a concrete mixture which is as homogeneous as possible. This is the task of the concrete mixer. DEM can be applied to optimize the concrete mixing process.

In this case, the purpose of a DEM simulation is to model the movement of the concrete mixture within the mixer and to analyse the quality of the blending of all the poured granular components. The mixing quality can be evaluated easily at any time without interrupting the virtual mixing process and the possible occurrence of dead zones can quickly be detected.

Fig. 4-8 illustrates the DEM simulation of a planetary mixer during different mixing stages. The picture on the left shows the start of the mixing process, where only one component is poured into the planetary mixer. The picture on the right shows the final stage, where the two components are mixed homogeneously.

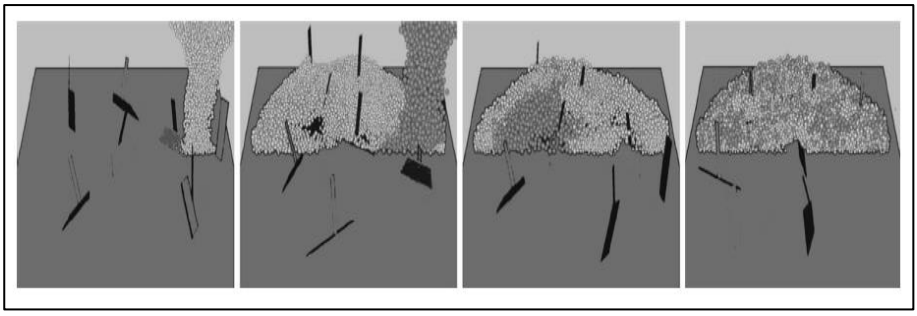

Fig. 4-8: DEM simulation of a planetary mixer [4.1]

4.1.1.4.2 Formwork filling processes

As for the mixing process, the aim of a good formwork filling process is to obtain a homogeneous and complete filling of the formwork volume with the fresh concrete.

DEM can equally be used to optimize a formwork filling process, although simulating the filling of large formworks is at present very difficult due to very long computation times.

Large simulation volumes require a large number of particles. Mechtcherine et al. [4.1] advise to zoom in on the critical sections of the formwork and only to use DEM for the analysis of these smaller fractions of the total volume.

Fig. 4-9 illustrates the filling process of a mould.

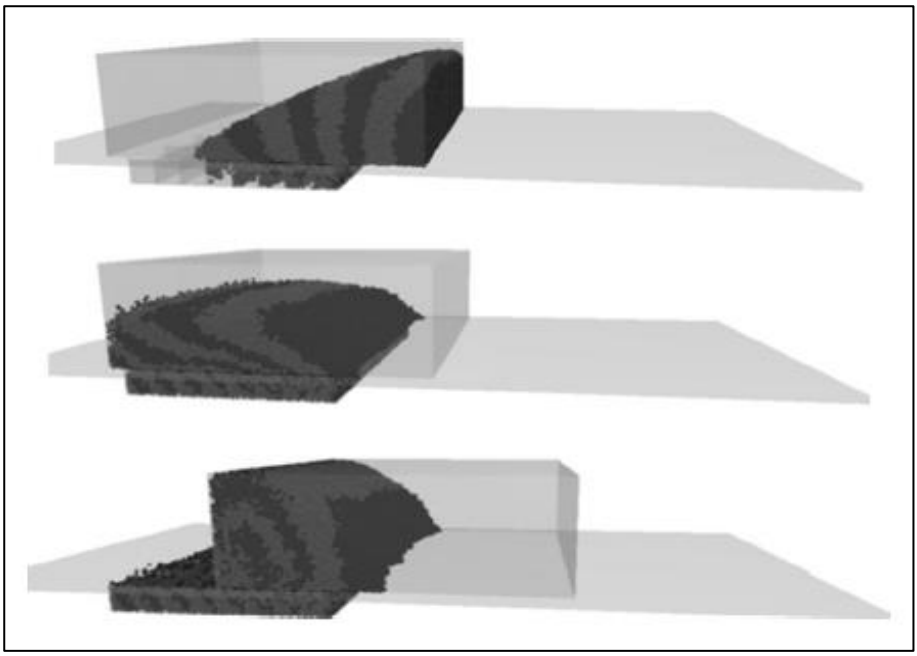

Fig. 4-9: DEM simulation of a mould process [4.10]

4.1.1.5 Advantages, disadvantages and future outcome of DEM

4.1.1.5.1 Advantages

As mentioned in the introduction of section 4.1.1, DEM has the ability to model fresh concrete as a suspension of aggregates or solid particles in a fluid cement paste, including the interactions between the suspended particles and the suspending fluid. This modelling approach enables the study of phenomena like segregation, shear induced particle migration and blocking.

These phenomena cannot be analysed with numerical simulation techniques like the Finite Difference Method (FDM), the Finite Element Method (FEM) or the Finite Volume Method (FVM). When using these simulation methods, the fluid is considered to be homogeneous and modelled as a continuum.

4.1.1.5.2 Disadvantages

As the calibration of the DEM constitutive parameters is at present still a significant problem regarding effort and accuracy, finding an improved and simplified way to adjust these simulation parameters is a major goal for future DEM developments. Also quite challenging is finding a mathematical relation between the rheological parameters of the fresh concrete and the DEM parameters describing the particle interactions, presented in section 4.1.1.2.2.

The presented DEM calibration and model validation requires the availability of experimental data of real fresh concrete mixtures. However, the primary goal of the numerical simulations is to design and optimize a formwork filling process in a purely virtual environment. The rheological parameters describing the rheology of the fresh concrete are actually one of the parameters of a filling process which need to be optimized through a series of optimization simulations. Due to the fact that at present no mathematical relations exist which relate the DEM constitutive parameters to these rheological parameters, using DEM to optimize the rheology of the fresh concrete is not very practical.

As reported in section 4.1.1.4.2, DEM can be used to optimize a casting process, although simulating the filling of large formworks is at present not economical due to very long computation times. The simulation of these large volumes requires a large number of particles.

4.1.1.5.3 Future perspectives

According to Mechtcherine et al. [4.1] and Shyshko et al. [4.3], DEM simulation models can help to analyse individual processes at different stages of the concrete life, including specific transitions from one state into another. The ultimate aim of such an approach is a kind of virtual concrete lab, which is demonstrated in Fig. 4-10.

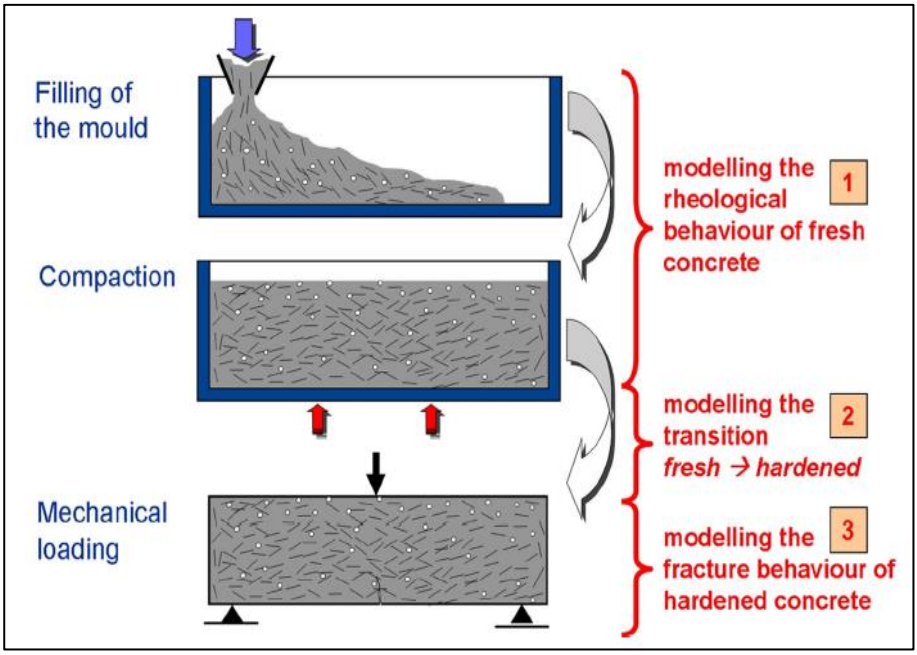

Fig. 4-10: Virtual concrete lab - overview of the different stages of concrete life [4.1].

4.1.2 Dissipative Particle Dynamics Method (DPD)

The Dissipative Particle Dynamics (DPD) method is introduced in the following sections,. This is a simulation technique which is closely related to DEM, presented in section 4.1.1, and the Lattice Boltzmann Method (LBM), which will be discussed in section 4.1.3.

There have been many theoretical advances made in understanding the rheological properties of simple suspensions like very dilute and semi-dilute suspensions, mostly composed of spherical particles. However, the understanding the of the flow of dense suspensions, like fresh concrete, with random particle shapes still remains a great challenge, as stated by Martys [4.11].

Two decades ago, Koelmann and Hoogerbrugge [4.12] introduced the DPD method with the aim to model a variety of complex fluid systems. One of the main advantages of this simulation method is that it can naturally accommodate many boundary conditions while not requiring meshing (or re-meshing) of the computational domain under study.

The DPD method could be considered as a molecular dynamics algorithm, where particles subjected to interatomic forces move according to Newton's laws. However, the particles in the DPD method are not atomistic but more like a mesoscopic representation of the modelled fluid.

Several philosophical views of the DPD method are existing in the scientific community:

- A first view is to consider the DPD method as a consequence of the systematic coarse graining of atomistic or microscopic domains. Although this view of the DPD method provides a general framework for understanding the structure of the DPD equations, which will be presented a little further, it is absolutely necessary to impose constitutive relations (stress - strain rate relations) to bridge the gap between the microscopic and the macroscopic domains.
- A second view is to interpret the DPD method as a class of Lagrangian formulations of the Navier-Stokes equations, presented in section 3.1.
- A third view, probably matching with the original intent, is that the DPD method can be regarded as a somewhat abstract cellular automata-based construct that, in certain flow regimes, recovers hydrodynamics consistent with the Navier-Stokes equations. This view is quite similar to the original idea behind LBM.

The challenge when applying the DPD method is therefore to carefully connect the solutions obtained with this method to the physical flow regimes of interest.

The three different approaches presented above are summarized and illustrated in Fig. 4-11 [4.13].

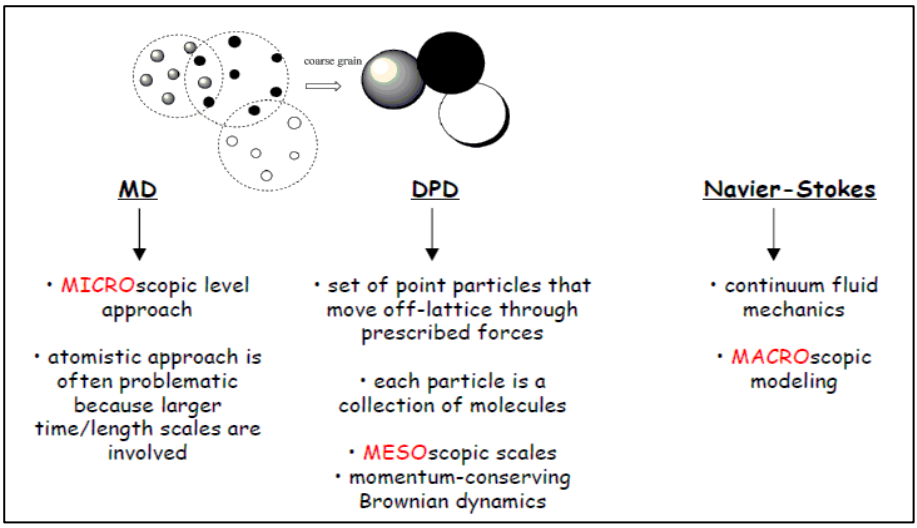

Fig. 4-11: The DPD method and other fluid modelling scales [4.13].

4.1.2.1 The DPD modelling scheme

4.1.2.1.1 Basic DPD equations

In the DPD method, as in molecular dynamics [4.14], the evolution of the position vector $\vec{r}_i$ and the momentum $\vec{p}_i = m_i\vec{v}_i$ of particle *i* with mass m_i and velocity $\vec{v}_i$ are described by the following equations:

$$\frac{\partial \vec{r}_i}{\partial t} = \vec{v}_i \tag{4.10}$$

$$\frac{\partial \vec{p}_i}{\partial t} = \sum_{j\neq i}^{N} \vec{F}_{ij} \tag{4.11}$$

where $\vec{F}_{ij}$ represents the force on particle *i* due to particle *j*.

These inter-particle forces are commonly composed of three components, the conservative part $\vec{F}_{ij}^{C}$, the dissipative part $\vec{F}_{ij}^{D}$ and the random component $\vec{F}_{ij}^{R}$ so that:

$$\vec{F}_{ij} = \vec{F}_{ij}^{C} + \vec{F}_{ij}^{D} + \vec{F}_{ij}^{R} \tag{4.12}$$

The conservative force component is simply a central repulsive force, derivable from some effective potential.

The dissipative force is proportional to the difference of the velocity of the particles, $\vec{v}_{ij} = \vec{v}_i - \vec{v}_j$, and acts as a force slowing down their relative motion through viscous effects.

The random force (usually based on a Gaussian random noise function) helps to maintain the temperature of the system and represents the thermal or vibrational energy, providing an additional viscous effect.

These contributions to the inter-particle forces are summarized in Fig. 4-13.

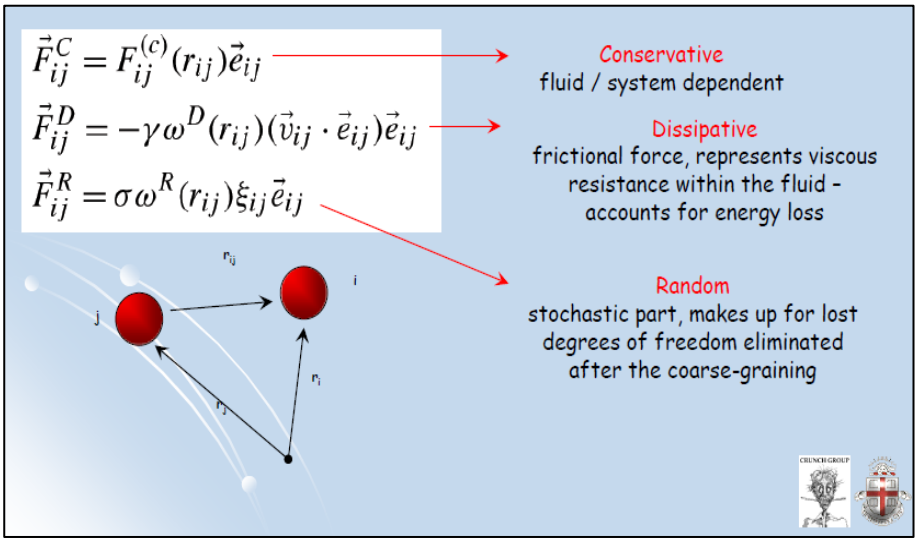

Fig. 4-12: DPD inter-particle forces [4.15].

The three forces components are represented by the following equations [4.11, 4.15 - 4.17]:

$$\vec{F}_{ij}^{C} = F_m\left(1 - r_{ij}\right)\vec{e}_{ij} \tag{4.13}$$

$$\vec{F}_{ij}^{D} = -\gamma w^{D}\left(r_{ij}\right)\left[\vec{e}_{ij}.\vec{v}_{ij}\right]\vec{e}_{ij} \tag{4.14}$$

$$\vec{F}_{ij}^{R} = \sigma w^{R}\left(r_{ij}\right)\xi_{ij}\vec{e}_{ij} \tag{4.15}$$

where the distance between the DPD particles *i* and *j* is represented by r_{ij}, $\vec{e}_{ij}$ is a unit vector pointing from particle *j* to particle *i*, w^D and w^R are weight functions and ξ_{ij} is a randomly fluctuating variable described by Gaussian statistics.

As stated by Karniadakis [4.18] and Español and Warren [4.19], in order to maintain a well-defined temperature in the system under study, the coefficients γ and σ, describing the strength of the dissipative and random forces respectively, must be coupled according to the fluctuation-dissipation theorem by the following equation:

$$k_b T = \frac{\sigma^2}{2\gamma} \tag{4.16}$$

where k_b is the Boltzmann constant (= 1.38 x 10^{23} J/K) and T is the temperature. According to Español and Warren [4.19], the following relation between $w^D(r_{ij})$ and $w^R(r_{ij})$ must fulfilled so that the DPD fluid system possesses a Gibbs-Boltzmann equilibrium state:

$$w^D(r_{ij}) = \left(w^R(r_{ij})\right)^2 \tag{4.17}$$

From the research performed by Groot and Warren [4.16] and Martys [4.11], the parameters and weight functions introduced in the previous equations are defined by the following relations:

For $r_{ij} < r_c$:

$$w^R(r_{ij}) = 1 - \frac{r_{ij}}{r_c} \tag{4.18}$$

For $r_{ij} > r_c$:

$$w^R(r_{ij}) = 0 \tag{4.19}$$

where r_c is the cut-off radius of the DPD particle. This is the distance beyond which a DPD particle cease to interact with other DPD particles. All lengths are typically defined in units of this cut-off radius of the DPD interaction.

The conservative parameter F_m in Eq. (4.13), determining the strength of the soft repulsion, is defined as:

$$F_m = \frac{75 k_b T}{\rho r_c^4} \tag{4.20}$$

where ρ is the global density of DPD particles.

4.1.2.1.2 Implementation of the DPD scheme

The original DPD algorithm of Koelman and Hoogerbrugge [4.12] used the Euler algorithm for the time integration. Groot and Warren [4.16] used a modified Verlet-algorithm in order to improve the numerical accuracy and to better characterize the thermal properties of the DPD simulation.

This modified Verlet time-stepping algorithm is presented through the following equations:

$$\vec{x}(\Delta t) = \vec{x}(0) + \vec{v}(0)\Delta t + \frac{(\Delta t)^2}{2}\vec{a}(0) \tag{4.21}$$

$$\vec{v}(\Delta t) = \vec{v}(0) + \frac{\Delta t}{2}[\vec{a}(0) + \vec{a}(\Delta t)] \tag{4.22}$$

where $\vec{a}(0) = \vec{F}\left(\vec{x}(0), \vec{\tilde{v}}(0)\right)/m$ is the acceleration term, which is depending on the position $\vec{x}(0)$ and an intermediate velocity $\vec{\tilde{v}}(0)$. The intermediate velocity in the acceleration term is calculated with the following equation:

$$\vec{\tilde{v}}(\Delta t) = \vec{v}(0) + \frac{\Delta t}{2}\vec{a}(0) \tag{4.23}$$

Rigid body motion is modelled by a subset of DPD particles, which are initially assigned to a location in space and as such approximates the shape of the solid object. This is quite similar to the DEM procedure presented in section 4.1.1.2.1.

The study performed by Groot and Warren [4.16] determined that choosing three particles per unit volume is the best practical choice for modelling a fluid phase. With this choice, the equilibrium properties of the considered fluid are reasonably well defined and choosing for higher particle densities quickly becomes very expensive computationally.

The resulting stress tensor has contributions arising from the propagation of momentum and inter-particle forces. The stress tensor is therefore defined by the following equation:

$$\sigma_{kl} = \frac{1}{Vm}\sum_i \vec{p}'_{ik}\,\vec{p}'_{il} + \frac{1}{2V}\sum_{ij}\vec{F}^k_{ij}\left(\vec{r}_i - \vec{r}_j\right)_l \tag{4.24}$$

where *i* and *j* refer to different particles, *k* and *l* refer to the Cartesian coordinate axes and $\vec{p}'_i$ represents the momentum of particle *i* relative to the macroscopic velocity field halfway its trajectory during a time step Δt.

According to the study of Martys [4.11], the DPD scheme presented above worked quite well for dilute and semi-dilute suspensions. However, for dense suspensions (volume fractions φ > 0.4), particle overlaps were observed during the performed simulations.

The DPD forces represented by the Eqs. (4.13 - 4.15) were in this case too weak to prevent the particles overlaps. In order to overcome this problem, Kim and Karrila [4.20] proposed to introduce additional lubrication forces. More detailed information regarding these lubrication forces is available in this reference study.

4.1.2.2 A few applications of the DPD method

A few successful applications of the DPD method are presented in the research article of Martys [4.11]. He managed to recover quite accurately the Einstein intrinsic viscosity for a dilute suspension of single-sized spheres in a fluid with known characteristics.

As mentioned by Feys [4.21] and by Martys [4.11], for very dilute to semi-dilute suspensions, the relative viscosity is described by the following equation:

$$\eta_r = \frac{\eta}{\eta_s} \approx 1 + \eta_0 \varphi + K_H \varphi^2 + \cdots \quad (4.25)$$

where η_r is the relative viscosity, η is the viscosity of the suspension, η_s is the viscosity of the suspending fluid, η_0 is the intrinsic viscosity, φ is the volume fraction of the suspended rigid bodies and K_H is the Huggins coefficient. For dilute suspensions composed of spheres the intrinsic viscosity equals to 2.5. The DPD simulations returned a value of 2.46 for a volume fraction equal to 0.0077, which is quite accurate.

Also for semi-dilute suspensions, the performed DPD simulations managed to effectively recover the longer range hydrodynamic interactions in the fluid, which are represented by the Huggins coefficient. Martys [4.11] performed a series of simulations with mono-sized spheres with varying volume fractions up to 0.2. The simulations returned a value of 6 for the Huggins coefficient, compared to the theoretical value of 5.

As already mentioned in the previous section, additional lubrication forces were introduced when simulating the flow of dense suspensions in order to prevent sphere overlaps. Applying the DPD method with these lubrication forces, Martys and Ferraris [4.22] presented some very promising simulation results of the flow of a dense suspension of spheres, like in fresh concrete, through rebars. This is illustrated in Fig. 4-13.

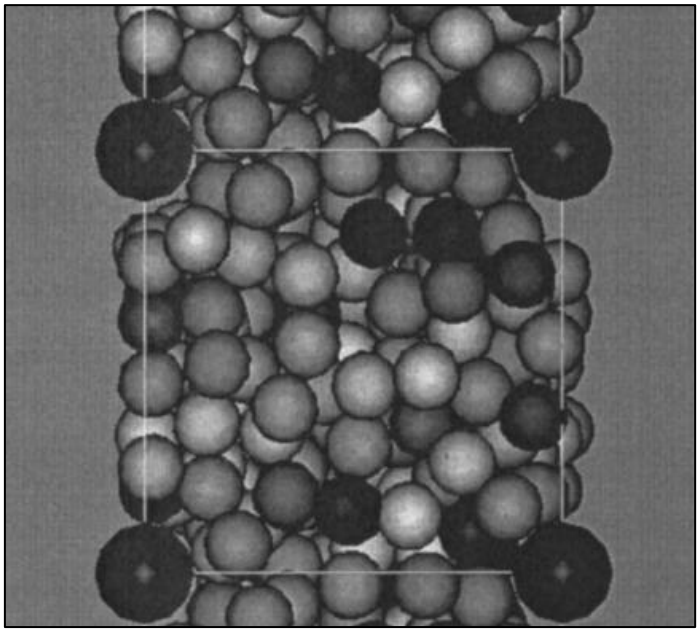

Fig. 4-13: Application of the DPD method to the flow of spheres through rebars (represented by the larger black spheres) [4.22].

The performed simulations revealed that jamming or blocking started to occur when the size of largest spheres became larger than one third of the gap spacing between the rebars. This limit has been extensively confirmed in practice.

4.1.2.3 Advantages and disadvantages of the DPD method

4.1.2.3.1 Advantages

One of the advantages of this simulation method, as reported by Martys [4.11], is that it can naturally accommodate many boundary conditions while not requiring the meshing (or re-meshing) of the computational domain under study.

As for DEM, the DPD method has the ability to study phenomena like segregation, shear induced particle migration and blocking during the placement of fresh concrete.

4.1.2.3.2 Disadvantages

As mentioned in the introduction of section 4.1.2, the big challenge when applying the DPD method is to carefully connect the solutions obtained with this method to the physical flow regimes of interest. Again as for DEM, it is certainly not obvious to relate the rheology of a fresh concrete to the many parameters of the inter-particle forces and the lubrication forces presented in section 4.1.2.1.

Although not specifically reported by Martys [4.11] and Martys and Ferraris [4.22], it can be assumed that the application of the DPD method in simulations involving quite large volumes, like for example formworks, will also lead to long computation times, for the same reasons which were mentioned when using DEM.

4.1.3 Lattice Boltzmann Method

In this section, the working principles and the related model equations of the Lattice Boltzmann Method (LBM) are presented.

In order to represent the non-Newtonian shear flow behaviour of fresh concrete, the Bingham model and the Herschel-Bulkley model are both implemented in the LBM framework. The observed limitations of these implementations are also discussed.

The modelling of boundary conditions in LBM, like a pressure condition (a Dirichlet condition), a velocity condition (Von Neumann condition), a no-slip - bounce-back condition at walls and a periodic boundary condition, is explained. A mass tracking algorithm representing the concrete - gas interface or free surface is discussed.

A few applications of LBM in fresh concrete flow modelling are briefly presented.

Finally, a number of reported advantages and disadvantages to the use of LBM are summarised.

4.1.3.1 Basic LBM framework and equations

4.1.3.1.1 LBM framework description

Fluid dynamics is traditionally described by the general conservation equations or the Navier-Stokes equations introduced in chapter 3. The numerical simulation methods introduced in the current chapter differentiate themselves by the way they solve the Navier-Stokes equations.

Numerical simulation techniques like the Finite Difference Method (FDM), the Finite Element Method (FEM) and the Finite Volume Method (FVM) formulate the problem by quantities such as the macroscopic velocity and the macroscopic pressure of the fluid continuum. The approach followed by the LBM is totally different, as is equally for the DEM and the DPD method.

The LBM originated towards the end of the 1980s, the beginning of the 1990s, when cellular automata began to be applied to the field of fluid dynamics. The LBM, contrary the formerly mentioned traditional simulation methods, is based on the Boltzmann equation applicable to ideal gasses. This method is not manipulating macroscopic quantities but it uses mesoscopic particle distribution functions instead.

In statistical mechanics, a gas system is treated as an ensemble of many similar molecules, particles (*N* in total), of which the distribution function $f(\vec{x},\vec{p},t)$ gives the probability of finding a particular molecule with a given position $\vec{x}$ and momentum $\vec{p}$. The positions and momenta of the remaining *N*-1 molecules remain unspecified, because no experiment can distinguish between them, and as such, the choice of the specific molecule does not matter.

The probable number of molecules with position coordinates between $\vec{x}-d\vec{x}$ and $\vec{x}+d\vec{x}$ and momentum values between $\vec{p}-d\vec{p}$ and $\vec{p}+d\vec{p}$ is given by $f(\vec{x},\vec{p},t)d\vec{x}d\vec{p}$. When the positions and the momenta of this set of molecules are known at a particular time *t* and there are no collisions between these molecules, incrementing the positions and momenta allows us to determine the distribution function *f* at a future time *t* + d*t*:

$$f(\vec{x}+d\vec{x},\vec{p}+d\vec{p},t+dt)d\vec{x}d\vec{p}=f(\vec{x},\vec{p},t)d\vec{x}d\vec{p} \tag{4.26}$$

This is called the streaming process. However; due to collisions, some molecules starting at $(\vec{x},\vec{p})$ will not arrive at $(\vec{x}+d\vec{x},\vec{p}+d\vec{p})$, whereas other molecules not starting at $(\vec{x},\vec{p})$ will arrive at $(\vec{x}+d\vec{x},\vec{p}+d\vec{p})$. Defining $\Gamma^{(-)}d\vec{x}d\vec{p}dt$ as the number of molecules that do not arrive in the expected portion of the phase space due to collisions during time d*t*, and $\Gamma^{(+)}d\vec{x}d\vec{p}dt$ as the number of molecules that start somewhere else than in $(\vec{x},\vec{p})$ and do arrive in the expected portion of the phase space due to collisions during the same time d*t*, Eq. (4.26) can be modified in order to account for the streaming and the collision process:

$$f(\vec{x}+d\vec{x},\vec{p}+d\vec{p},t+dt)d\vec{x}d\vec{p}=f(\vec{x},\vec{p},t)d\vec{x}d\vec{p}+\left[\Gamma^{(+)}-\Gamma^{(-)}\right]d\vec{x}d\vec{p}dt \tag{4.27}$$

Applying a Taylor series expansion of the LHS of Eq. (4.27) and keeping only the first order terms, leads to the well-known Boltzmann equation. More details of this derivation are to be found in the reference work of Sukop and Thorne [4.23] and Succi [4.24].

Boltzmann's original concept presented above is considerably simplified in Lattice Boltzmann models. The number of possible particle positions in the domain of interest and microscopic momenta is reduced to a limited set of possibilities. Also time is divided in a number of fixed time steps. Particle positions are confined to the nodes of the lattice.

Variations in momenta which are caused by the continuum velocities and varying particle masses are reduced in the LBM to 8 directions for a 2D model (D2Q9) and to 14 directions for a 3D model (D3Q15), 3 magnitudes and a single particle mass. In this nomenclature, proposed by Qian et al. [4.25], the letter D stands for the dimension of the model, and the letter Q represents the number of lattice velocities.

Because the particle mass is considered to be uniform (1 mass unit or *mu*), these particle velocities and momenta are always equivalent. The lattice unit *lu* represents the fundamental measure of length in the LMB models and the time steps *ts* (*Δt*) are the time unit.

Fig. 4-14 shows the Cartesian lattice and the discrete set of velocities $\vec{e}_a$ for the D2Q9 model, where a = 0, 1, …, 8 is a direction index and $\vec{e}_0 = 0$ is the velocity for the particles at rest.

The magnitude of the velocities $\vec{e}_1$ through $\vec{e}_4$ is 1 *lu*/*ts* and the velocity magnitude of $\vec{e}_5$ through $\vec{e}_8$ is $\sqrt{2}$ *lu*/*ts*. These lattice velocities are very convenient, as all of their *x*- and *y*-components are either 0 or ± 1.

Contrary to the original Boltzmann equation where the particle distribution functions *f* are continuous functions, in the LBM the single-particle distribution functions which appear in Eq. (4.27) are essentially discrete. The single-particle distribution functions can viewed as the direction-specific fluid densities.

As such, the macroscopic fluid density is defined as:

$$\rho = \sum_{a=0}^{8} f_a \tag{4.28}$$

Similarly, the macroscopic velocity $\vec{u}$ is an average of the lattice velocities, weighted by the directional frequencies f_a:

$$\vec{u} = \frac{1}{\rho}\sum_{a=0}^{8} f_a \vec{e}_a \tag{4.29}$$

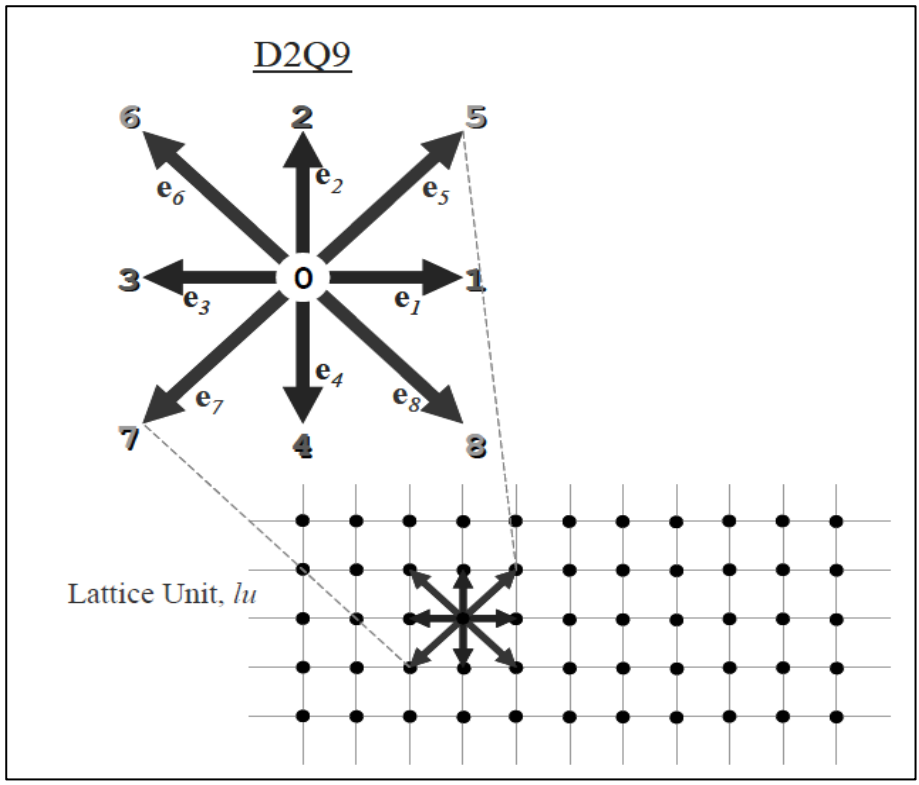

Fig. 4-14: D2Q9 lattice and related particle velocities [4.23].

The BGK (Bhatnagar- Gross - Krook) approximation is used in the simplest LBM scheme (see Succi [4.24]), where the streaming and collision process are modelled according to the following equation:

$$f_a(\vec{x} + \vec{e}_a \Delta t, t + \Delta t) = f_a(\vec{x}, t) - \frac{[f_a(\vec{x},t) - f_a^{eq}(\vec{x},t)]}{\tau} \tag{4.30}$$

where $f_a(\vec{x} + \vec{e}_a \Delta t, t + \Delta t) = f_a(\vec{x}, t)$ represents the part of the streaming process and $\frac{[f_a(\vec{x},t) - f_a^{eq}(\vec{x},t)]}{\tau}$ is the collision term.

The numerical treatment of Eq. (4.30) is a two-step procedure: the particle-particle collisions and the particle-wall collisions (bounce-back condition) are evaluated first, followed by the streaming step. The collision of the particles is considered as a relaxation towards a local equilibrium with a relaxation time τ.

For the D2Q9 lattice the equilibrium distribution function f_a^{eq} is defined as:

$$f_a^{eq}(\vec{x}, t) = w_a \rho(\vec{x}, t) \left[1 + 3\frac{\vec{e}_a \vec{u}}{c^2} + \frac{9}{2}\frac{(\vec{e}_a \vec{u})^2}{c^4} - \frac{3}{2}\frac{\vec{u}^2}{c^2}\right] \tag{4.31}$$

where the weights w_a are 4/9 for the particles at rest (a = 0), 1/9 for a = 1, 2, 3, 4 and 1/36 for a = 5, 6, 7, 8 and c is the basic speed on the lattice (c = 1 *lu*/*ts* in the simplest implementation of LBM).

For the D3Q15, the weights w_a are 2/9 for the particles at rest (a = 0, $\|\vec{e}_0\| = 0$), 1/9 for a = 1, …, 6 ($\|\vec{e}_a\| = 1$) and 1/72 for a = 7, …, 14 ($\|\vec{e}_a\| = \sqrt{3}$).

In the LBM, the kinematic viscosity ν of the fluid is related to the relaxation time τ, as shown in the following equation:

$$\nu = \frac{1}{3}\left(\tau - \frac{1}{2}\right) \tag{4.32}$$

According to this equation, the relaxation time τ must be larger than 0.5 in order to obtain a physically meaningful viscosity. According to Švec et al. [4.26], a value of 0.8 is required for Newtonian fluids. More considerations about the relaxation time are presented in the next section.

4.1.3.1.2 Implementation of the Bingham model and the Herschel-Bulkley model

In the case of a non-Newtonian fluid like CVC or SCC, the apparent viscosity of this fluid, ν_{app}, is a function of the shear rate tensor, $D_{ij}(\vec{x}, t)$ (see Eq. (3.3)), and the stress deviator tensor, $S_{ij}(\vec{x}, t)$. More information about the approximation equations for these tensors is provided in the work of Mei et al. [4.27]. By using Eq. (4.32), the apparent relaxation time, τ_{app}, can be determined from the apparent viscosity, however, as already mentioned in the previous section, the value of the relaxation time influences the behaviour of the LBM as well as its stability.

Unfortunately, due to the kinematic nature of the LBM and to the limited range of applicable relaxation times, the true behaviour of a Bingham material like CVC or a Herschel-Bulkley material like SCC cannot be modelled accurately. Švec et al. [4.26] implemented the Bingham model as a tri-viscosity fluid with an apparent viscosity defined as:

For $\tau_{app} \geq \tau_{max}$:

$$\nu_{app} = \frac{1}{3}\left(\tau_{max} - \frac{1}{2}\right) \tag{4.33}$$

For $\tau_{app} \leq \tau_{min}$:

$$\nu_{app} = \frac{1}{3}\left(\tau_{min} - \frac{1}{2}\right) \tag{4.34}$$

Otherwise:

$$\nu_{app} = \nu_{pl} + \frac{\tau_{0,B}}{\rho\dot{\gamma}} \tag{4.35}$$

where $\dot{\gamma}$ is the shear rate and related to second invariant of the shear rate tensor and $\tau_{0,B}$ and ν_{pl} are the yield stress and the plastic kinematic viscosity respectively of the Bingham material. Eq. (4.35) can be easily modified for a Herschel-Bulkley material as follows:

$$\nu_{app} = \frac{K\dot{\gamma}^{n-1}}{\rho} + \frac{\tau_{0,HB}}{\rho\dot{\gamma}} \tag{4.36}$$

where $\tau_{0,HB}$ is the yield stress of the Herschel-Bulkley material. Švec et al. [4.26] determined for their simulations with a Bingham material the following suitable limits for the relaxation times mentioned in Eq. (4.33) and Eq. (4.34): $\tau_{min} = 0.501$ and $\tau_{max} = 8$.

4.1.3.1.3 Types of boundary conditions

Boundary conditions are necessary before we can compute any meaningful results. In the current section details will be provided for periodic, bounce-back, constant pressure and constant velocity boundaries. More advanced information about the implementation of boundary conditions in LBM can be found in Sukop and Thorne [4.23] and Zhou et al. [4.27].

The most trivial boundary conditions are periodic. The system under study becomes closed at the limiting edges, which are treated as if they would be attached to the opposite edges. Fig. 4-15 shows the resulting topology of the computational domain, using these apparently connected edges.

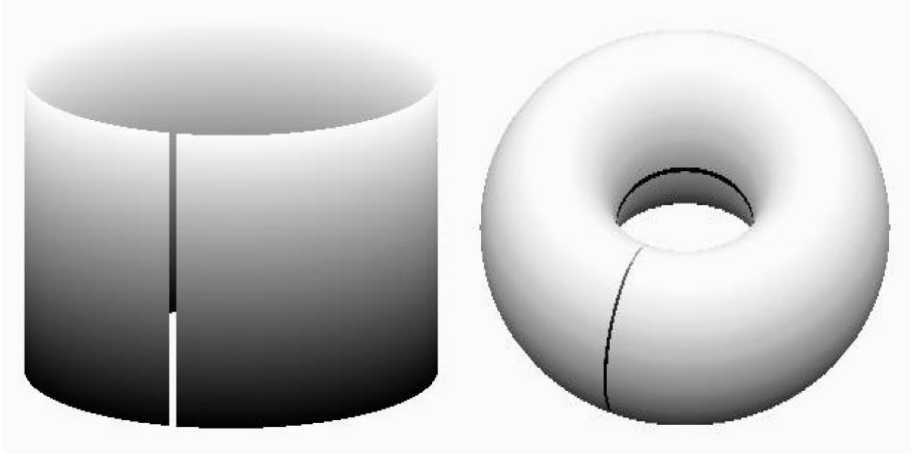

Fig. 4-15: Examples of a computational domain with periodic boundaries [4.23].

The next most important boundary condition is the no-slip condition at walls. In the LBM it is quite easy to implement this boundary condition using the simple "mid-plane" bounce-back scheme, in which the particle distribution functions f_a are temporarily stored inside the solids and re-emerge at the next time step.

This is illustrated in Fig. 4-16.

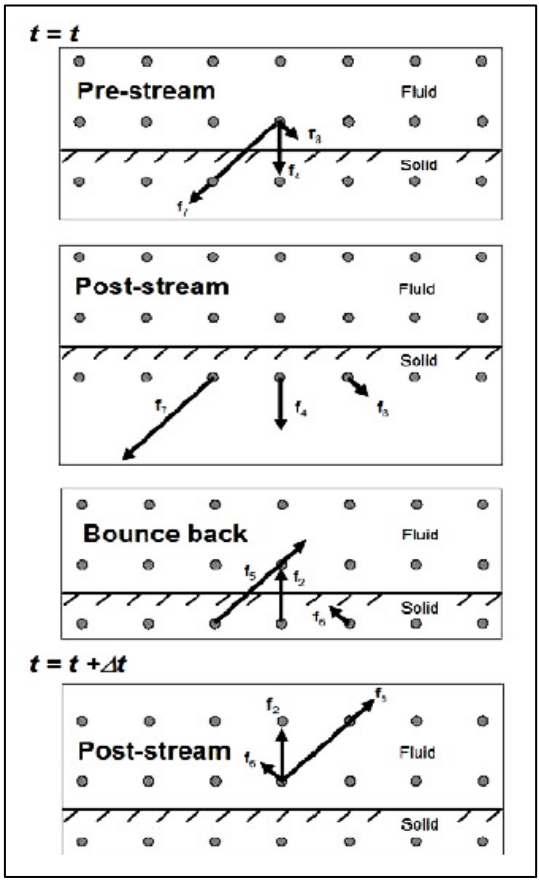

Fig. 4-16: Illustration of the mid-plane bounce-back scheme [4.23].

Von Neumann boundary conditions constrain the flux at the domain boundaries. A velocity vector consisting of *x*- and *y*-components $\vec{u}_0 = \begin{bmatrix} u_0 \\ v_0 \end{bmatrix}$ is specified from which the density or the pressure is computed based on the conditions inside the domain. Besides the macroscopic density or pressure, the unknown particle distribution functions also need to be computed. After the streaming process, three particle distribution functions are unknown at each lattice node point pointing from the boundary into the computational domain. These unknowns can be solved for in a way that maintains a specified velocity at their lattice nodes.

Dirichlet boundary conditions impose the pressure or the density at the boundaries of the computational domain. A density ρ_0 is specified, from which the velocity is computed. It is assumed that the velocity component tangent to the boundary is zero and that the normal component will be solved for. In addition to the unknown macroscopic velocity, after the streaming step, there are three unknown particle distribution functions at each lattice node pointing from the boundary into the domain. These unknowns can solved such as to maintain the specified pressure or density at their lattice nodes.

Further details about the implementation of the Dirichlet and the Von Neumann conditions can be found in the work of Sukop and Thorne [4.23].

4.1.3.1.4 Free surface modelling

Švec et al. [4.26] adopted a mass tracking algorithm that mimics the free surface between the fluid phase (for example the fresh concrete) and the gas phase (for example the air) by modifying the particle distribution functions. The lattice cells are differentiated into fluid, gas and interface cells, as shown in Fig. 4-17. The nodes with filled square marks belong to the fluid cells, whereas the grey cells represent the interface and the circle nodes belong to the gas cells. The dotted line is the actual free surface.

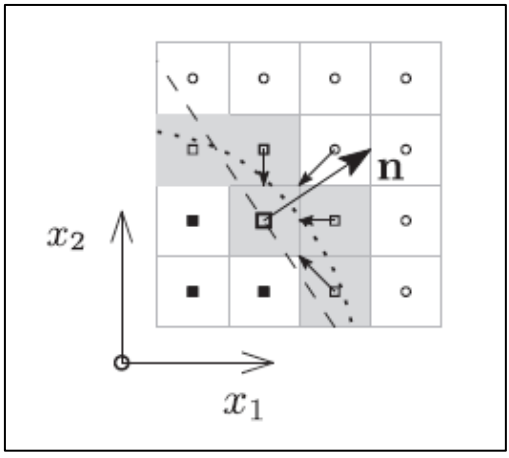

Fig. 4-17: Illustration of a mass tracking algorithm in LBM [4.26].

The LBM is not applied to the gas cells of the computational domain, no particle distribution functions are attributed to these cells. The fluid cells however are treated as ordinary LBM cells.

Interface cells form an intermediate boundary layer between the gas and fluid cells, and they are treated in the same way as the fluid cells, but with a local mass of the fluid of the cell, $m(\vec{x}, t)$, as an additional information.

When looking at an interface cell at position $\vec{x}$, during the streaming step of Eq. (4.30) an inflow of particle distributions coming the neighbouring cells and an outflow of the particle distributions leaving the concerned interface cell is occurring. The difference between the inflow and outflow of particle distributions causes a change of the mass of the interface cell. This is represented in the following equation:

$$m(\vec{x}, t + \Delta t) = m(\vec{x}, t) + \sum_a b_a \left[f_{\bar{a}}(\vec{x} + \vec{e}_a \Delta t, t) - f_a(\vec{x}, t) \right] \tag{4.37}$$

where $f_{\bar{a}}$ and f_a are particle distribution functions with opposite directions and:

$$b_a = \begin{cases} \frac{1}{2}[m(\vec{x}, t) + m(\vec{x} + \vec{e}_a \Delta t, t)] & if\ (\vec{x} + \vec{e}_a \Delta t, t)\ is\ an\ interface\ cell \\ 1 & if\ (\vec{x} + \vec{e}_a \Delta t, t)\ is\ a\ fluid\ cell \\ 0 & if\ (\vec{x} + \vec{e}_a \Delta t, t)\ is\ a\ gas\ cell \end{cases} \tag{4.38}$$

An interface cell changes into a fluid cell when the cell mass reaches the fluid density. On the other hand, when the mass of the interface cell drops down to zero, the cell has become a gas cell. When this happens, some of the surrounding cells are converted into interface cells in order to assure the consistency of the interface layer and to avoid direct contact between fluid cells and gas cells.

It has been reported by Švec et al. [4.26] that the proposed mass tracking algorithm however suffers from a few numerical artefacts like the occurrence of negative cell masses of some interface cells, or the occurrence of interface cells which are only surrounded by cells of one type (all fluid cells or all gas cells).

Both these artefacts lead to non-physical results. The authors of the proposed mass tracking algorithm have however found adequate solutions in order to overcome these numerical issues. More information is available in [4.26].

4.1.3.2 Application examples of LBM

A typical fresh concrete test that is very often used for validating a simulation model which is relying on a specific numerical modelling technique is the slump or slump flow test. Švec et al. [4.26] also used this test to assess the correctness and the accuracy of their free surface algorithm and its implementation in the LBM.

A free surface flow of a non-Newtonian fluid, characterised as a Bingham material, was studied by means of a slump test. The flow was driven by the gravitational force. Fig. 4-18 shows the shape of the free surface in the initial state, after 0.16 s and after 14.5 s.

The correct coupling of the free surface algorithm with the LBM and its ability to accurately simulate a Bingham behaviour is illustrated in Fig. 4-19, where the final shape of the slump flow cake is compared with an analytic solution obtained with the analytic model of Roussel and Coussot [4.28].

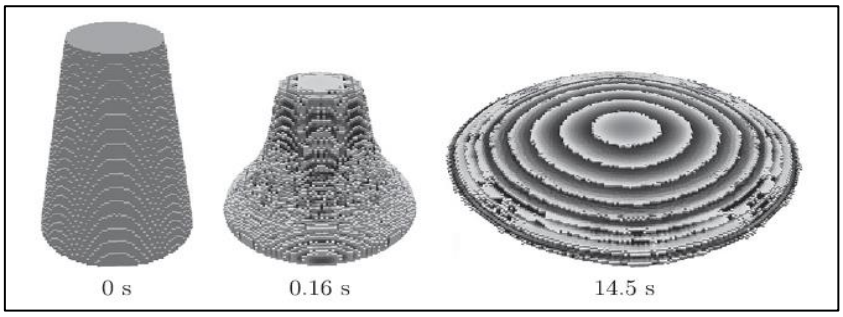

Fig. 4-18: LBM simulation of a slump test showing the free surface shape at three different time steps [4.26].

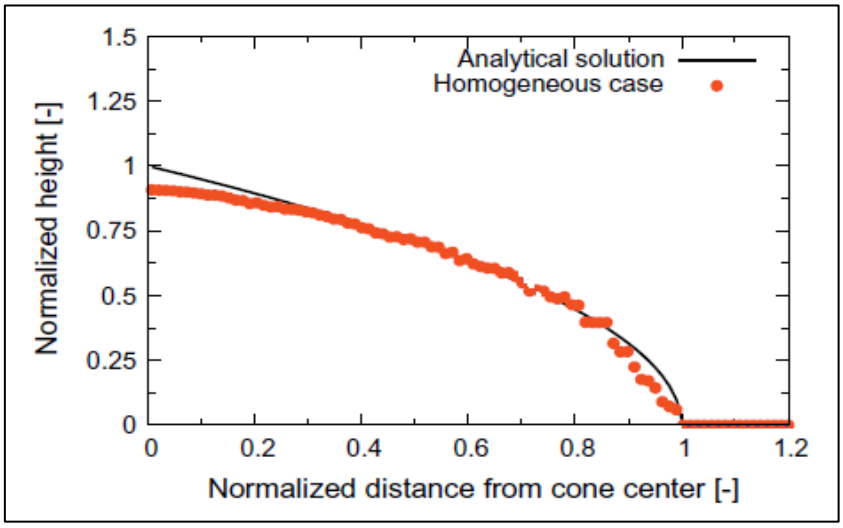

Fig. 4-19: Comparison of the final shape of the spread in a slump test [4.26].

4.1.3.3 Advantages and disadvantages of LBM

4.1.3.3.1 Advantages

The LBM is able to accurately simulate the flow of fresh concrete, as represented by a Bingham or by a Herschel-Bulkley model, although some limitations have been reported [4.26] (see section 4.1.3.1.2).

Benchmark tests that have been performed reveal that for transient incompressible laminar flow problems the LBM is generally faster than the traditional methods like FEM and FVM, which rely on the modelling of the macroscopic behaviour of fluids governed by the Navier-Stokes equations [4.29]. However, steady-state simulations with LBM are slower.

The alternative “bottom-up” approach helps to better understand the underlying physics of a given flow problem, especially the influence of microscopic properties on the macroscopic counterparts. The governing equations are very simple and straightforward to implement.

4.1.3.3.2 Disadvantages

As reported in section 4.1.3.1.2, due to the kinematic nature of the LBM and to the limited range of applicable relaxation times, the true behaviour of a Bingham material like CVC or a Herschel-Bulkley material like SCC cannot be modelled accurately.

Since the LBM is primarily based on the particle distributions, every macroscopic phenomenon must be converted to the microscopic level and vice versa, but often there is no unique way to make this transition. The accurate modelling in the LBM of external forces and boundary conditions are examples of this conversion challenge.

Each specific problem needs to be programmed separately using some programming language (C, Matlab or Python). Most of the currently available LBM software is open source, like OpenLB, Palabos, LB2D_Prime and LB3D_Prime, or is developed in-house.

4.1.4 Eulerian Multiphase Modelling

Eulerian multiphase modelling is quite complex, because this simulation technique solves a set of continuity and momentum equations for each phase being considered. The coupling between these phases is achieved through the pressure and through interphase exchange coefficients.

In multiphase modelling, a phase can be one of the physical phases of matter, like gas, liquid or solid, but it can also be defined as an identifiable class of material that has a particular inertial response to and interaction with the flow in which it is immersed.

In the case of fresh concrete, the cement paste or mortar can defined as the fluid phase, whereas the suspended aggregates can be treated as separate phases according to their nominal size.

Theoretically, any number of phases can be modelled, provided that sufficient memory is available. In practice though, the number of phases that can be handled is quite often limited by the convergence behaviour of the Eulerian model. This modelling technique is particularly suited for dispersed-phase volume fractions exceeding 10 %, so for high particle loading.

Using this modelling technique allows to study phenomena like segregation and blocking in fresh concrete during formwork filling. Some examples will be presented in section 4.1.4.2.

4.1.4.1 The Eulerian model

4.1.4.1.1 Conditions of use

When applying the Eulerian multiphase modelling technique, a solution is obtained based on the following considerations [4.8]:

- A single pressure is shared among all phases;
- The momentum and continuity equations are solved for each phase;
- For granular flows, the solid phase shear and bulk viscosities are determined by applying kinetic theory;
- As mentioned in the introduction, the coupling between these defined phases is achieved through the pressure and through interphase exchange coefficients;
- The numerical solution of the resulting model equations is obtained by applying the Finite Volume Method (FVM) (see section 4.1.5.1).

4.1.4.1.2 The volume fraction balance

The description of a multiphase flow is based on the concept of the phase volume fraction, denoted here by α_q. Volume fractions represent the space occupied by each phase, and as mentioned in the previous section, the laws of conservation of mass and momentum are satisfied by each phase individually. The derivation of these conservation equations can be done by ensemble averaging the local instantaneous balance for each of the phases [4.30].

The volume of phase *q* is defined by the following equation:

$$V_q = \int_V \alpha_q dV \tag{4.39}$$

As such, for *n* phases, the following equality holds:

$$\sum_{q=1}^{n} \alpha_q = 1 \tag{4.40}$$

4.1.4.1.3 The conservation of mass

When excluding mass transfer between phases as well as phase sources, the conservation of mass for phase *q* is:

$$\frac{\partial}{\partial t}\left(\alpha_q \rho_q\right) + \vec{\nabla}.\left(\alpha_q \rho_q \vec{v}_q\right) = 0 \tag{4.41}$$

where $\vec{v}_q$ is the velocity of phase *q*.

4.1.4.1.4 The conservation of momentum

The conservation of momentum for phase *q* is described with the following equation, in the absence of mass transfer between phases:

$$\frac{\partial}{\partial t}\left(\alpha_q \rho_q \vec{v}_q\right) + \vec{\nabla}.\left(\alpha_q \rho_q \vec{v}_q \vec{v}_q\right) = -\alpha_q \vec{\nabla} p + \vec{\nabla}.\bar{\bar{\tau}}_q + \alpha_q \rho_q \vec{g} + \sum_{p=1}^{n} \vec{R}_{pq} + \vec{F}_{lift,q} + \vec{F}_{vm,q} \quad (4.42)$$

where $\vec{F}_{vm,q}$ is a virtual mass force, $\vec{F}_{lift,q}$ is a lift force, $\vec{R}_{pq}$ is an interaction force between phases and $\bar{\bar{\tau}}_q$ is the stress tensor of phase *q*, defined by the following equation:

$$\bar{\bar{\tau}}_q = \alpha_q \mu_q \left(\vec{\nabla}\vec{v}_q + \vec{\nabla}\vec{v}_q^T\right) + \alpha_q \left(\lambda_q - \frac{2}{3}\mu_q\right)\vec{\nabla}.\vec{v}_q \quad (4.43)$$

In Eq. (4.43), μ_q and λ_q represent the shear and bulk viscosity of phase *q*. The interphase force $\vec{R}_{pq}$ depends on the friction, the pressure, the cohesion and other effects between the phases. In the Ansys Fluent® software for example, these interphase forces are modelled as follows [4.8]:

$$\sum_{p=1}^{n} \vec{R}_{pq} = \sum_{p=1}^{n} K_{pq}\left(\vec{v}_p - \vec{v}_q\right) \quad (4.44)$$

where K_{pq} is the interphase momentum exchange coefficient.

4.1.4.1.5 The lift force term

The lift forces act on a particle mainly due to velocity gradients in the primary-phase (the suspending fluid phase) flow field. The lift force will be more significant for larger particles.

Therefore, the lifting force acting on a secondary phase *q* in a primary phase p is computed using the following equation, presented by Drew et al. [4.31]:

$$\vec{F}_{lift,q} = -C_l \rho_q \alpha_p \left(\vec{v}_q - \vec{v}_p\right) \times \left(\vec{\nabla} \times \vec{v}_q\right) \quad (4.45)$$

where C_l is the lift coefficient, which typically is around 0.5 for inviscid fluid flows. However, it is to be noted that in most cases the lift force is small compared to the drag force.

4.1.4.1.6 The virtual mass force term

A virtual mass effect occurs when a secondary phase *p* accelerates relative to the primary phase *q*. The inertia of the primary-phase mass which is encountered by the accelerating particles exerts a virtual mass force on the particles, expressed by the following equation [4.31]:

$$\vec{F}_{vm,q} = \frac{1}{2}\rho_q \alpha_p \left[\left(\frac{\partial \vec{v}_q}{\partial t} - \frac{\partial \vec{v}_p}{\partial t}\right) + \left(\vec{v}_q.\vec{\nabla}\vec{v}_q - \vec{v}_p.\vec{\nabla}\vec{v}_p\right)\right] \quad (4.46)$$

The virtual mass effect is important when the secondary-phase density is much smaller than the primary-phase density.

4.1.4.2 *Application examples of Eulerian multiphase modelling*

The Eulerian multiphase modelling technique has been applied in this research to two fresh concrete flow cases. The first case is about the pumping tests with fresh SCC performed by Feys [4.21], which are described in more detail in section 6.1.

Fig. 4-20 shows the layout of the ducting circuit, which was used for these pumping tests, as well as the positions of the cross-sections from the multiphase computation that were further analysed.

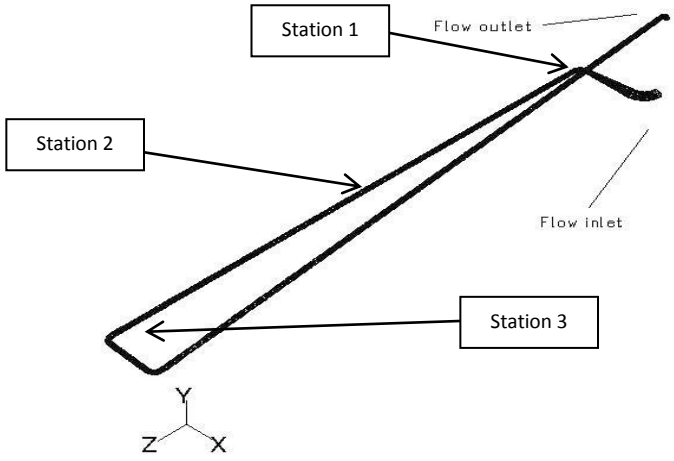

Fig. 4-20: Layout of the pumping circuit and indication of the analysed stations.

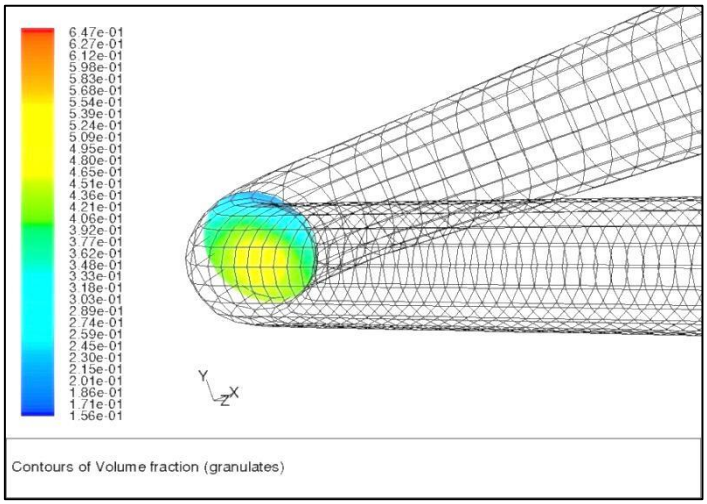

Fig. 4-21: Contour plot of the volume fraction of the aggregates at station 1.

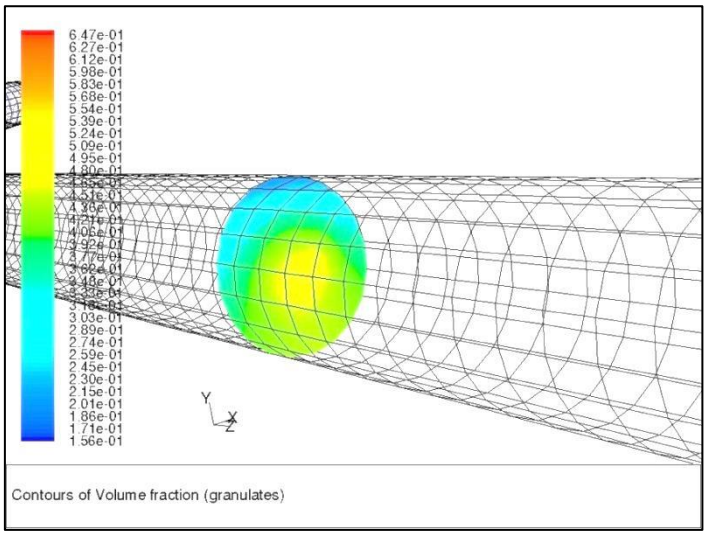

Fig. 4-22: Contour plot of the volume fraction of the aggregates at station 2.

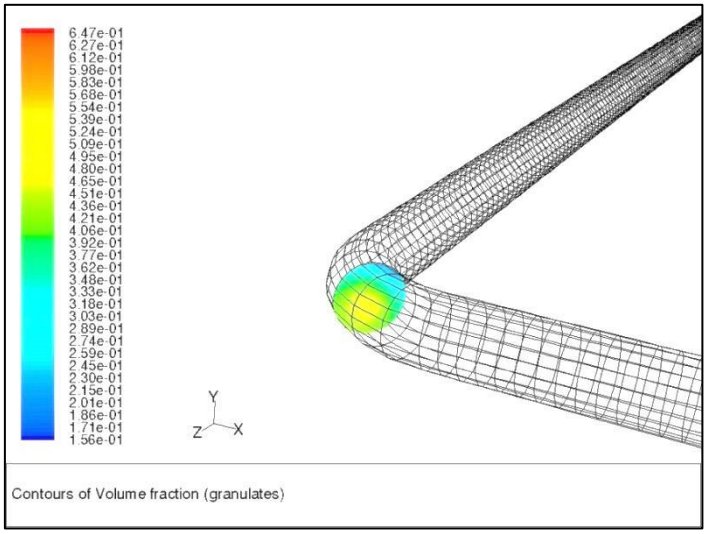

Fig. 4-23: Contour plot of the volume fraction of the aggregates at station 3.

From the analysed cross-sections, shown in Fig. 4-21 up to Fig. 4-23, several phenomena can be observed. Due to inertial and centrifugal effects the aggregates are somehow packed in the region of the larger radii in as seen in the duct bends (see Fig. 4-21 and Fig. 4-23). In Fig. 4-22, due to gravity the aggregates are more concentrated in the lower part of the duct. What is also to be noticed in all the presented cross-section plots, is that the highest volume fraction of aggregates is to be observed near the centre of the ducts, indicating shear driven particle migration.

The second case is about the base-filling tests with fresh SCC of the columns with rebars performed in the current research, which are described in more detail in section 5.2 and section 6.3. Fig. 4-24 shows the volume fraction contour plot of the aggregates at the lower part of the column. A minor segregation can be observed from this plot.

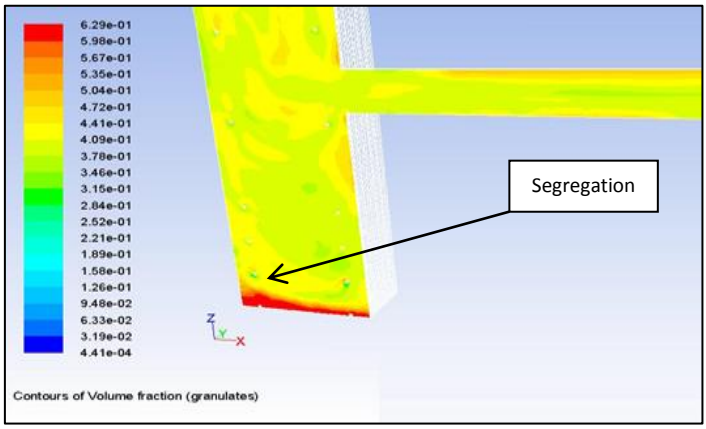

Fig. 4-24: Volume fraction contour plot of the aggregates at the lower part of the column.

4.1.4.3 Advantages and disadvantages of Eulerian multiphase modelling

4.1.4.3.1 Advantages

As mentioned in the introduction of section 4.1.4, the Eulerian multiphase modelling method has the ability to model concrete as a suspension of aggregates or solid particles in a fluid cement paste or mortar, including the interactions between the suspended particles and the suspending fluid. The fluid and the aggregates are defined as distinct phases. This modelling approach allows to study phenomena like inertial effects, segregation, shear induced particle migration and blocking, as shown in the previous section.

4.1.4.3.2 Disadvantages

Theoretically, any number of phases can be modelled, provided that sufficient memory is available. In practice though, the number of phases that can be handled is seriously limited by the convergence behaviour of the Eulerian model, as was observed in our research.

The Eulerian multiphase modelling method implemented in Ansys Fluent® proved to be quite fast for steady-state simulations, provided that the number of defined phases remained limited as mentioned above. However, for the transient simulations of our filling processes, this method revealed to have serious stability problems.

Although this modelling approach allows to study the phenomena mentioned in the previous section, it is a real challenge to determine the rheological properties of the phase which is defined as the suspending fluid phase and the interactions between this fluid phase and the defined classes of aggregates, because for each choice of these phases their properties will change. To our knowledge, it is currently not possible to measure the flow properties of these defined classes as well as their interactions, so it is very difficult to validate these models.

4.1.5 Finite Volume Method (FVM) - Volume of Fluid (VOF) Method

4.1.5.1 Basic concept of the FVM and the VOF method

In the Finite Volume Method (FVM), the integral formulation of the three conservation laws which were presented in chapter 3 is discretized directly in the physical space. It is the most widely applied method today in CFD, and this is likely to remain so in the foreseeable future. The reason behind the appeal to the FVM lies in its generality, its conceptual simplicity and its ease of implementation for arbitrary grids, structured as well as unstructured.

The FVM is based on cell-averaged values, which appear as a most fundamental quantity in CFD. This distinguishes the FVM from the finite difference (FDM) and the finite element method (FEM), where the main numerical quantities are the local function values at the mesh points.

Once a grid has been generated, in the FVM a local finite volume, also called control volume, is associated to each mesh point and the integral conservation laws are applied to this local volume.

This is a major distinction from the finite difference approach, where the discretized space is considered as a set of points, while in the FVM the discretized space is formed by a set of small cells, one cell being associated to one mesh point.

It is of extreme importance to maintain the global conservation of the basic flow quantities, mass, momentum and energy, at the discrete level and this puts conditions on the way the discretization process of the equations is performed. The FVM has the great advantage that the conservative discretization is automatically satisfied, through the direct discretization of the integral form of the conservation laws. This is a most fundamental property for numerical schemes [4.32, 4.33].

The FVM takes its full advantage on an arbitrary mesh, where a large number of options are open for the definition of the control volumes on which the conservation laws are expressed. Modifying the shape and location of the control volumes associated to a given mesh point, as well as varying the rules and accuracy for the evaluation of the fluxes through the control surfaces, gives a considerable flexibility to the FVM.

The VOF method, which has been developed by Hirt and Nichols [4.34], is a surface-tracking technique, applied to a fixed in space Eulerian mesh. It has been designed for two or more immiscible fluids where the position of the interface between the fluids is of interest. In the VOF method, a single set of momentum equations is shared by the defined fluids, and the volume fraction of each of the fluids in each computational cell is tracked throughout the domain.

The VOF formulation relies on the fact that two or more fluids (or phases) are not inter-penetrating. For each additional phase that you add to your model, a variable is introduced: the volume fraction of the fluid or phase in the computational cell. In each control volume, the volume fractions of all fluids or phases sum to unity.

The fields for all variables and properties are shared by the fluids and represent volume-averaged values, as long as the volume fraction of each of these fluids is known at each location. Thus the variables and properties in any given cell are either purely representative of one of the fluids, or representative of a mixture of the fluids, depending upon the volume fraction values.

In other words, if the q^{th} fluid's volume fraction in the cell is denoted as α_q, then the following three conditions are possible:

- $\alpha_q = 0$: The cell is empty (of the q^{th} fluid);
- $\alpha_q = 1$: The cell is full (of the q^{th} fluid);
- $0 < \alpha_q < 1$: The cell contains the interface between the q^{th} fluid and one or more of the other fluids.

Based on the local value of α_q , the appropriate properties and variables will be assigned to each control volume within the domain.

4.1.5.2 Mathematical description of the FVM-VOF scheme

The mathematical description of a flow is given by the Navier-Stokes equations, representing mass conservation, conservation of momentum and conservation of energy [4.32, 4.33].

The flow conditions observed during pumping and casting with SCC are laminar. Because the density and the viscosity of the fresh concrete are assumed to be independent of the typically very small temperature changes during a base-filling process, the conservation of energy is not considered. The remaining conservation equations, Eq. (3.1) and Eq. (3.2), were already introduced in section 3.1.2.

Eq. (3.1) and Eq. (3.2) are written in differential form. The most general description of these conservation laws is obtained when written in integral form. They describe the conservation of quantities, like specific mass and momentum, while being transported throughout the flow domain through convection and diffusion. These equations can be transformed into a generic form.

The generic form of a conservation of a transported quantity Ø (like the specific mass (Ø = 1) or momentum (Ø = $\vec{v}$)) is shown in Eq. (4.47):

$$\int_V \frac{\partial(\rho\emptyset)}{\partial t} dV + \oint_A \rho\emptyset\vec{v}.d\vec{A} = \oint_A \Gamma_\emptyset \vec{\nabla}\emptyset \,.\, d\vec{A} + \int_V S_\emptyset dV \qquad (4.47)$$

where ρ is the density or specific mass of the SCC (kg/m³), $\vec{v}$ is the velocity vector (m/s), $\vec{A}$ is the surface area vector (m²), $\Gamma_\emptyset$ is the diffusion coefficient for Ø (m²/s), $\vec{\nabla}\emptyset$ is the gradient of Ø and $S_\emptyset$ is the source of Ø per unit volume ([Ø]/m³).

Eq. (4.47) is applied to each control volume or cell of the grid in the computational domain. The 2-D triangular and the quadrilateral cell, shown in Fig. 4-25, are both examples of such a control volume. The integration of Eq. (4.47) on a cell of the mesh results in:

$$\frac{\partial(\rho\emptyset)}{\partial t} V + \sum_f^{N_{faces}} \rho_f \vec{v}_f \emptyset_f . \vec{A}_f = \sum_f^{N_{faces}} \Gamma_\emptyset \vec{\nabla}\emptyset_f . \vec{A}_f + S_\emptyset V \qquad (4.48)$$

where N_{faces} is the number of faces enclosing the cell, $\emptyset_f$ is the value of Ø convected through face *f*, $\rho_f \vec{v}_f \emptyset_f . \vec{A}_f$ is the mass flux through face *f*, $\vec{A}_f$ is the area vector of face *f*, $\vec{\nabla}\emptyset_f$ is the gradient of Ø at face *f* and *V* is the cell volume.

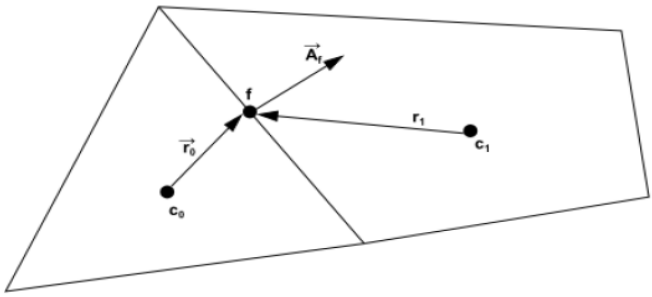

Fig. 4-25: Control volume - illustration of the integration of Eq. (4.47) [4.8, 4.35, 4.36].

The discretized transport equation, Eq. (4.48), contains the unknown variable Ø at the cell centre, as well as the unknown values in the surrounding neighbour cells. This equation will generally be non-linear with respect to these variables. Therefore Eq. (4.48) will be linearized in order to solve it.

The tracking of the interface(s) between the VOF phases is accomplished by the solution of a continuity equation for the volume fraction of one (or more) of the phases. For the q^{th} phase, this equation has the following generic form:

$$\frac{\partial}{\partial t}\left(\alpha_q \rho_q\right) + \vec{\nabla}.\left(\alpha_q \rho_q \vec{v}_q\right) = S_{\alpha_q} + \sum_{p=1}^{n}\left(\dot{m}_{pq} - \dot{m}_{qp}\right) \qquad (4.49)$$

where $\dot{m}_{qp}$ is the mass transfer from phase *q* to phase *p* and $\dot{m}_{pq}$ is the mass transfer from phase *p* to phase *q*. For the formwork filling processes two fluids or phases are considered: the air phase, initially filling the formwork, and the SCC phase, gradually replacing the air and filling the formwork. No mass transfer between these two phases are expected nor modelled. In our simulations, no source terms for the air and SCC phase (S_{α_q}) have been defined.

The volume fraction equation is not solved for the primary phase, which is in our case the air phase. The primary-phase volume fraction is computed based on the following constraint:

$$\sum_{q=1}^{n} \alpha_q = 1 \tag{4.50}$$

The volume fraction equation, Eq. (4.49), is solved implicitly or explicitly.

4.1.5.3 Application examples of the FVM and the VOF method

A first example of an application of the FVM combined with the VOF method is taken from the research work of Roussel [4.37]. This example presents the simulation of a multilayer casting process performed with SCC.

Contrary to the base-filling process, in this example a top-filling process has been modelled, where the rheological properties of the first layer were modified due to a thixotropic structural build-up. Fig. 4-26 clearly illustrates this multilayer cast, where the second layer is not mixing with the first layer due to the difference in rheology caused by thixotropy. The thixotropic model presented in section 2.2.2.4.2 was used for this simulation.

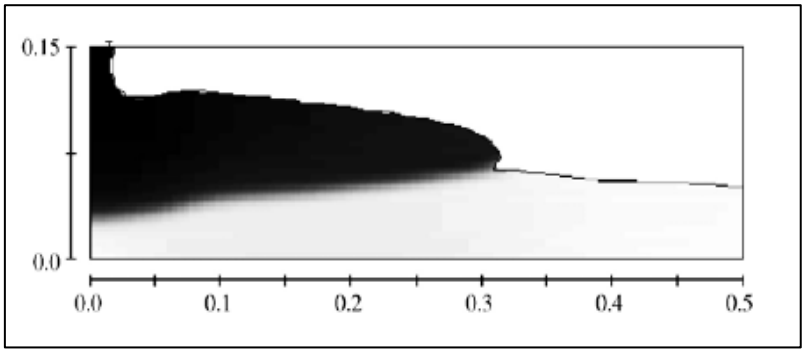

Fig. 4-26: Example of multilayer casting with SCC [4.37].

A second example of an application of the combined FVM-VOF scheme that is shown here, is taken from the general overview on computational modelling of fresh concrete flow presented by Roussel et al. [4.6].

In Fig. 4-27, the simulation of the casting process of a pre-cambered composite beam with very high strength concrete (100 MPa) is illustrated. The results of the simulations, carried out for various values of the rheological parameters (Bingham model), helped to determine the value of the minimum fluidity of the fresh concrete needed to cast the element.

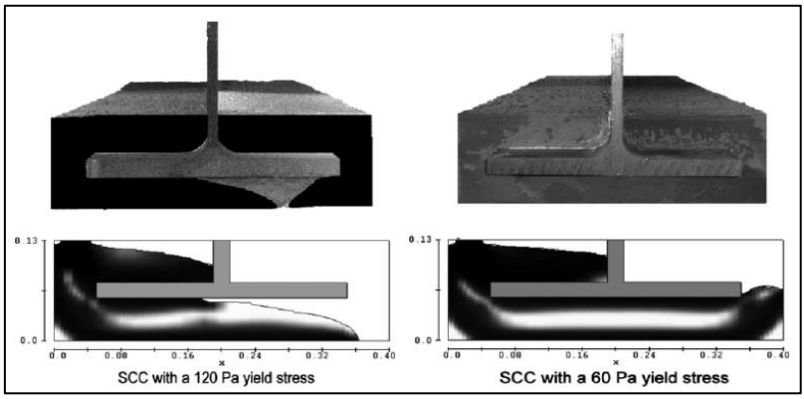

Fig. 4-27: Casting example of a concrete pre-cambered composite beam [4.6].

4.1.5.4 Advantages and disadvantages of the FVM and the VOF method

4.1.5.4.1 Advantages

The FVM and the VOF method is implemented in the multipurpose Ansys Fluent® software suite and is ready to be used throughout a user friendly graphical user interface (GUI). There is no need for separate programming using some specific programming language. This software can be used for any problem and is not dedicated to a particular flow problem.

The FVM has the big advantage that the conservative discretization is automatically satisfied, through the direct discretization of the integral form of the conservation laws. This is the most fundamental property for a numerical scheme.

The Bingham model and the Herschel-Bulkley model are both implemented in Ansys Fluent®, which is extremely useful, because the rheological parameters measured with the Tattersall Mk-II rheometer or the BML ConTec-Viscometer 5 rheometer, both used in our research, can be directly used as input in the software, or vice versa, the required rheology obtained from the simulations can be immediately interpreted in the concrete mixture design stage.

The occurring formwork wall pressures can be easily computed with the combined FVM-VOF scheme. The obtained wall pressures may then be applied in a mechanical analysis, performed within Ansys Mechanical®, in order to support the design process of the formwork layout.

4.1.5.4.2 Disadvantages

This combined method has not the ability to model concrete as a suspension of aggregates or solid particles in a fluid cement paste or mortar, including the interactions between the suspended particles and the suspending fluid. Therefore, phenomena like segregation, shear induced particle migration or blocking cannot be studied. The numerical simulation methods presented in the previous sections are more suited for this purpose.

Due to the considerable difference in rheology and density between the air and the concrete, this combined scheme can experience stability problems, which then will lead in some cases to small time steps and thus to rather long computation times.

4.1.6 Conclusions from the literature review on concrete flow modelling techniques

The main purpose of the current research is to quantify/predict the concrete pressure on the formwork walls during base-filling with fresh SCC through experiments and simulations.

In light of this goal and after analysing the advantages and disadvantages of each numerical simulation method presented in the previous sections, the combined FVM-VOF method was selected for the simulations performed in the current research, considering the important benefits which were mentioned in section 4.1.5.4.1.

The multipurpose Ansys Fluent® flow analysis software was selected for all the simulations performed in the current research.

4.2 Finite Volume Method (FVM) - Volume of Fluid (VOF) Method

4.2.1 Introduction

The definition of a CFD model involves several steps starting with the selection of a suitable mathematical model describing the physical problem and ending with solving the resulting numerical model. The following steps have to be defined during the process of setting up a numerical scheme [4.32]:

- Selection of a discretization method of the equations as well as the selection of the order of accuracy of the spatial (mesh) discretization and time discretization. In this study the FVM and the VOF method have been selected, as mentioned in section 4.1.6.
- Selection of a resolution method for the system of PDEs in time and for the iterative treatment of occurring non-linearities.
- Analysis of the selected numerical algorithm with respect to stability and convergence, as well as an investigation of the errors being generated.

These steps are presented schematically in Fig. 4-28.

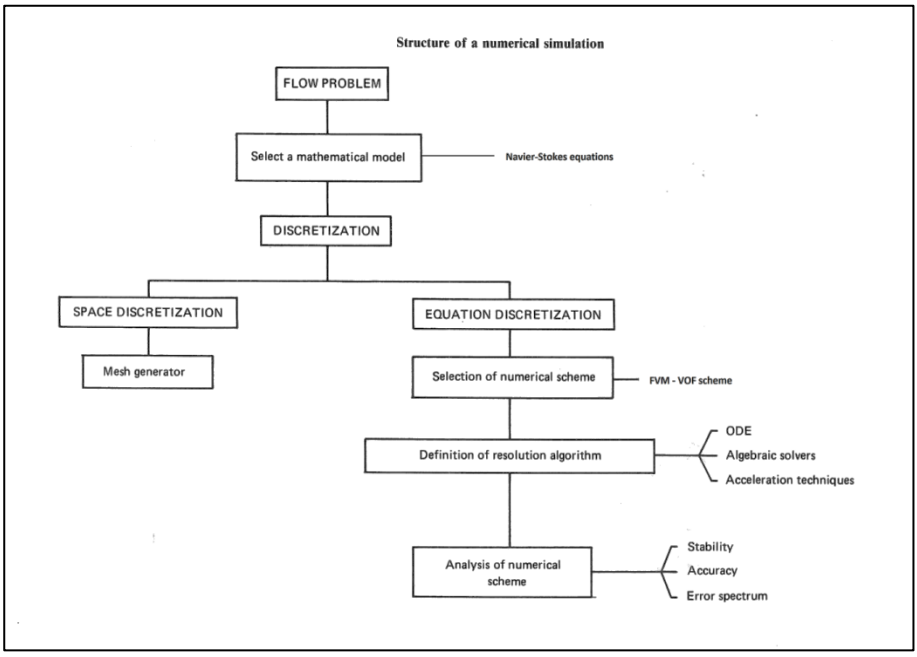

Fig. 4-28: General structure of the performed numerical simulations [4.32].

Depending on the physical problem to be solved, different mathematical descriptions exists, which will lead to different numerical schemes and solution techniques being selected. This is illustrated in Table 4-1.

Table 4-1: The structure of numerical schemes [4.32].

Physical problem	Mathematical model	Numerical scheme	Solution technique	Limitations
Time dependent	Time-dependent equations	Time and space discretization	ODE in time	Δt / Δx limitations
		Time accuracy required	Explicit	
			Implicit	Δt limited by accuracy
Time independent	*Steady-state equations*	Discretization of equations in space	Resolution of algebraic system of equations	Diagonal dominance criteria
	Linear		Direct method / Iterative method	Convergence rates Acceleration techniques
	Non-linear	Discretization of equations in space ⊕ Linearization procedure	⊕ Iterative solution of non-linearity	Acceleration of convergence rates
	Pseudo-unsteady formulation	Time integration towards steady state	ODE systems: Explicit	Δt limitations
	Time-dependent equations	Time accuracy not required	ODE systems: Implicit	Generally no Δt limitations for linear stability

This general overview helps to better understand why some of the available discretization methods and solution methods in Ansys Fluent® have been selected for our simulations. The selected discretization and solution methods will be further described in the next sections.

The Navier-Stokes equations, Eq. (3.1) and Eq. (3.2), have been introduced in section 3.1.2 and the discretized form of these equations, Eq. (4.48) and Eq. (4.49), relying on the FVM-VOF scheme, has been described in section 4.1.5.2. In the next section, additional details of the spatial and time discretization of Eq. (4.48) and Eq. (4.49) are presented.

4.2.2 Discretization

4.2.2.1 Spatial discretization

In Ansys Fluent® the discrete values of the transported quantity $\emptyset$ are stored by default at the cell centres (c_0 and c_1 in Fig. 4-25). However, face values $\emptyset_f$ are required for the convection term in Eq. (4.48) (second term on the left-hand side (lhs)) and must be interpolated from the cell centre values. This is accomplished using an upwind numerical scheme. Upwinding means that the face value $\emptyset_f$ is derived from quantities in the cell upstream, or "upwind", relative to the direction of the normal velocity.

In the simulations being performed during this research we have used first and second order upwind schemes: first-order upwind for the discretization of the Level-Set (LS) function in the VOF multiphase scheme (see section 4.2.3), and second-order upwind for the momentum discretization. The diffusion contribution in Eq. (4.48) (first term on the right-hand side (rhs)) is discretized using a central-differencing scheme and is therefore second-order accurate.

4.2.2.1.1 First order upwind scheme

When first-order accuracy is acceptable or desired, quantities at cell faces are determined by assuming that the cell-centre values of any field variable represent a cell-average value and is constant throughout the entire cell: the face quantities are identical to the cell quantities.

Thus when first-order upwinding is selected in a numerical scheme, the face value $\emptyset_f$ is set equal to the cell-centre value $\emptyset$ in the upstream cell.

4.2.2.1.2 Second order upwind scheme

When second-order accuracy is selected, the quantities at cell faces are computed using a multidimensional linear reconstruction approach [4.38], where the higher-order accuracy is achieved at cell faces through a Taylor series expansion of the cell-centered solution about the cell centroid.

Therefore, when second-order upwinding is chosen, the face value $\emptyset_f$ is computed using the following expression:

$$\emptyset_{f,SOU} = \emptyset + \vec{\nabla}\emptyset.\vec{r} \tag{4.51}$$

where $\emptyset$ and $\vec{\nabla}\emptyset$ are the cell-centered value and its gradient in the upstream cell and $\vec{r}$ is the displacement vector from the upstream cell centroid to the face centroid. This formulation requires the determination of the gradient $\vec{\nabla}\emptyset$ in each cell. The gradient $\vec{\nabla}\emptyset$ will be limited, so that no spurious maxima and minima are introduced. This will be further discussed in section 4.2.2.1.4.

4.2.2.1.3 Second order central-differencing scheme

As already mentioned in section 4.2.2.1, a second-order accurate central-differencing discretization scheme is applied to the diffusion contributing terms in Eq. (4.48). The central-differencing scheme calculates the face value for the transported quantity ($\emptyset_f$) according to Eq. (4.52):

$$\emptyset_{f,CD} = \frac{1}{2}(\emptyset_0 + \emptyset_1) + \frac{1}{2}\left(\vec{\nabla}\emptyset_0.\vec{r}_0 + \vec{\nabla}\emptyset_1.\vec{r}_1\right) \tag{4.52}$$

where the indices 0 and 1 refer to the cells that are sharing the face *f*, $\vec{\nabla}\emptyset_0$ and $\vec{\nabla}\emptyset_1$ are the reconstructed gradients at cells 0 and 1, respectively, and $\vec{r}$ is the vector directed from the cell centroid towards the face centroid (see Fig. 4-25).

It is known that central-differencing schemes [4.32, 4.33] can produce unbounded solutions and non-physical wiggles, which can lead to stability problems for the numerical procedure. These stability problems can often be avoided if a deferred correction is used for the central-differencing scheme. In this approach, the face value is calculated according to the following equation:

$$\emptyset_f = \emptyset_{f,UP} + \left(\emptyset_{f,CD} - \emptyset_{f,UP}\right) \tag{4.53}$$

where the indices *UP* stands for upwind. The upwind part (the first term on the rhs) is treated implicitly, while the difference between the central-difference and the upwind values is treated explicitly. Provided that the numerical solution converges, this approach leads to pure second-order differencing.

4.2.2.1.4 Evaluation of gradients

The gradient $\vec{\nabla}\emptyset$ of a transported quantity $\emptyset$ is used to discretize the convection and diffusion terms in the flow equations. These gradients are computed in Ansys Fluent® according to the following methods:

- Green-Gauss cell-based;
- Green-Gauss node-based;
- Least squares cell-based.

a) Green-Gauss theorem

When the Green-Gauss theorem is used to compute the gradient of the transported quantity $\emptyset$ at the cell centre c_0 (see Fig. 4-25 and Fig. 4-24), the following discrete form is written as:

$$\left(\vec{\nabla}\emptyset\right)_{c_0} = \frac{1}{V}\sum_f \vec{\emptyset}_f . \vec{A}_f \tag{4.54}$$

where $\emptyset_f$ is the value of $\emptyset$ at the cell face centroid, computed as explained in the following sections. The summation is over all the faces enclosing the cell.

b) Green-Gauss cell-based gradient evaluation

With the Green-Gauss cell based gradient evaluation method, the face value $\vec{\emptyset}_f$ in Eq. (4.54) is taken from the arithmetic average of the values at the neighbouring cell centres, that is:

$$\vec{\emptyset}_f = \frac{\emptyset_{c0}+\emptyset_{c_1}}{2} \tag{4.55}$$

c) Green-Gauss node-based gradient evaluation

When applying the Green-Gauss node-based gradient evaluation method, $\vec{\emptyset}_f$ is computed by taking the arithmetic average of the face nodal values:

$$\vec{\emptyset}_f = \frac{1}{N_f}\sum_n^{N_f} \vec{\emptyset}_n \tag{4.56}$$

where N_f is the number of nodes on face *f*. The nodal values $\vec{\emptyset}_n$ in Eq. (4.56) are computed from the weighted average of the cell values surrounding the nodes, following the approach proposed by Holmes and Connell [4.39] and Rauch et al. [4.40].

This scheme reconstructs the exact values of a linear function at a node from surrounding cell-centered values on arbitrary unstructured meshes by solving a constrained minimization problem, preserving a second-order spatial accuracy.

The node-based gradient is known to be more accurate than the cell-based gradient, especially on irregular (skewed and distorted) unstructured meshes. It is however relatively more expensive to compute than the cell-based gradient scheme.

d) Least squares cell-based

In this method the solution is assumed to vary linearly. In Fig. 4-29, the change in cell values between cell c_0 and c_i along the vector δr_i from the centroid of cell c_0 to cell c_i can be expressed as:

$$\left(\vec{\nabla}\emptyset\right)_{c_0} . \overrightarrow{\delta r_i} = \emptyset_{c_i} - \emptyset_{c_0} \tag{4.57}$$

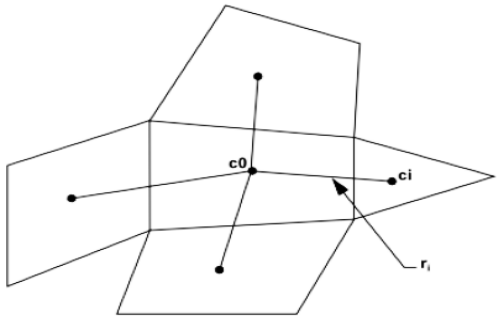

Fig. 4-29: Cell centroid evaluation [4.8, 4.35, 4.36].

If similar equations are written for each cell surrounding the cell c_0 we obtain the following system of equations written in compact form:

$$[J].\left(\vec{\nabla}\emptyset\right)_{c_0} = \Delta\emptyset \tag{4.58}$$

where *[J]* is the coefficient matrix which is purely a function of geometry. The cell gradient is determined by solving the minimization problem for the system of the non-square coefficient matrix in a least-squares sense.

The above linear system of equations is over-determined and can be solved by decomposing the coefficient matrix using the Gram-Schmidt process presented in [4.41], resulting in a matrix of weights for each cell. Thus for our cell-centered scheme this means that the three components of the weights (W^x_{i0}, W^y_{i0}, W^z_{i0}) are produced for each of the faces of cell c_0. Therefore, the gradient at the cell centre can then be computed by multiplying the weight factors by the difference term in Eq. (4.57):

$$\left(\frac{\partial\emptyset}{\partial x}\right)_{c_0} = \sum_{i=1}^{n} W_{i0}^{x}.\left(\emptyset_{c_i} - \emptyset_{c_0}\right) \tag{4.59}$$

$$\left(\frac{\partial\emptyset}{\partial y}\right)_{c_0} = \sum_{i=1}^{n} W_{i0}^{y}.\left(\emptyset_{c_i} - \emptyset_{c_0}\right) \tag{4.60}$$

$$\left(\frac{\partial\emptyset}{\partial z}\right)_{c_0} = \sum_{i=1}^{n} W_{i0}^{z}.\left(\emptyset_{c_i} - \emptyset_{c_0}\right) \tag{4.61}$$

On irregular (skewed and distorted) unstructured meshes, the accuracy of the least-squares gradient method is comparable to that of the node-based gradient (and both are much more superior compared to the cell-based gradient). However, it is less expensive to compute the least-squares gradient than the node-based gradient. Therefore, it has been selected as the default gradient method in Ansys Fluent®, and this method has also been selected for the numerical simulations performed during this research.

4.2.2.2 Time discretization

For transient simulations, the governing equations must be discretized in space and in time. The spatial discretization for the time-dependent equations is identical to the steady-state case presented in the previous section. Temporal discretization involves the integration of every term in the differential equations over a time step Δt. The integration of the transient term is straightforward, as shown below. A generic expression for the time evolution of some transported quantity $\emptyset$ is presented in Eq. (4.62):

$$\frac{\partial \emptyset}{\partial t} = F(\emptyset) \tag{4.62}$$

where the function $F(\emptyset)$ incorporates any spatial discretization. If the time derivative, $\frac{\partial \emptyset}{\partial t}$, is discretized using backward differences, then the first-order accurate temporal discretization is given by Eq. (4.63):

$$\frac{\emptyset^{n+1} - \emptyset^{n}}{\Delta t} = F(\emptyset) \tag{4.63}$$

and the second-order discretization is given by Eq. (4.64):

$$\frac{3\emptyset^{n+1} - 4\emptyset^{n} + \emptyset^{n-1}}{2\Delta t} = F(\emptyset) \tag{4.64}$$

where $\emptyset^{n+1}$ is the value at the next time level $t+\Delta t$, $\emptyset^{n}$ is the value at the current time level t and $\emptyset^{n-1}$ is the value at the previous time level $t-\Delta t$. Once the time derivative has been discretized, a choice remains for evaluating $F(\emptyset)$: in particular, which time level values of $\emptyset$ should be used when evaluating F. This choice will lead to an implicit or an explicit time integration scheme (see also Table 4-1).

In the simulations of the transient casting processes presented in chapter 6, an implicit time integration scheme has been selected. This is the default selection for the pressure-based solver implemented in Ansys Fluent®. More information about the pressure-based solver will be presented in the next section. When implicit time integration is selected when setting up the numerical model, the function $F(\emptyset)$ is evaluated at the future time level, that is:

$$\frac{\emptyset^{n+1} - \emptyset^{n}}{\Delta t} = F(\emptyset^{n+1}) \tag{4.65}$$

This process is referred to as implicit integration since $\emptyset^{n+1}$ in a given cell is related to $\emptyset^{n+1}$ in neighbouring cells through $F(\emptyset^{n+1})$:

$$\emptyset^{n+1} = \emptyset^{n} + \Delta t . F(\emptyset^{n+1}) \tag{4.66}$$

This implicit equation must be solved iteratively at each time level before moving to the next time step. The big advantage of the fully implicit scheme is that it is unconditionally stable with respect to the time step size.

However, the fully implicit scheme requires more computer memory for processing all the numerical data.

4.2.2.3 Solution

4.2.2.3.1 Overview of flow solvers

There are two major families of solvers, which are both implemented in Ansys Fluent®: a pressure-based solver and a density-based solver. Initially, the pressure-based solver was developed for low-speed incompressible flows, whereas the density-based solver was mainly used for high-speed compressible flows.

Now, both solver methods have been extended and reformulated to solve and operate for a wide range of flow conditions beyond their traditional or original intent.

In both methods the velocity field is obtained from the momentum equations. In the density-based approach, the continuity equation is used to obtain the density field while the pressure field is determined from the equation of state.

In the pressure-based approach, the pressure field is extracted by solving a pressure or pressure correction equation which is obtained by manipulating continuity and momentum equations.

For both methods, Ansys Fluent® will solve the governing integral equations for the conservation of mass and momentum, and (when appropriate) for energy and other transported quantities such as turbulence and chemical species.

In both cases, a control-volume-based simulation technique (see section 4.1.5 and section 4.2.2) is used that consists of:

- Division of the computational domain into discrete control volumes, resulting in a grid or mesh;
- Integration of the governing equations on the individual control volumes to construct the algebraic equations for the discrete dependent variables such as the velocities, pressure, temperature, and other conserved and/or transported quantities;
- Linearization of the discretized equations, and solution of the resultant linear equation system to yield updated values of the dependent variables.

Both solvers employ a similar discretization process (finite-volume-based), but the approach used to linearize and solve the discretized equations is different.

Because all the pumping processes and the formwork base-filling processes studied in this research are low speed and SCC is incompressible, a pressure-based solver has been chosen for simulating these processes.

4.2.2.3.2 Pressure-based solver

The pressure-based solver uses an algorithm which belongs to a general class of methods called the projection method [4.42]. In the projection method, the mass conservation (continuity) is achieved by solving a pressure (or pressure correction) equation. The pressure equation is derived from the continuity and the momentum equations in such a way that the velocity field, corrected by the pressure, satisfies the continuity.

Because the governing equations are non-linear and coupled to one another, the solution process is therefore iterative, i.e. the entire set of governing equations is solved repeatedly until the solution converges.

Two type of pressure-based solver algorithms are implemented in Ansys Fluent®: a segregated algorithm and a coupled algorithm.

a) The pressure-based segregated algorithm

The pressure-based solver uses a solution algorithm where the governing equations are solved sequentially (or segregated from one another). Because the governing equations are non-linear and coupled, the solution loop must be carried out iteratively in order to obtain a converged numerical solution.

In the segregated algorithm, the individual governing equations for the solution variables (the velocities, temperature, pressure and the turbulent properties) are solved one after another. The segregated algorithm is memory-efficient, since the discretized equations need only be stored in the memory one at a time. However, the solution convergence is relatively slow.

With the segregated algorithm, each iteration consists of the steps illustrated in Fig. 4-30 and outlined below:

1. Update fluid properties (for example, density, viscosity (including turbulent viscosity) and specific heat) based on the current solution;
2. Solve the momentum equations, one after another, using the recently updated values of pressure and face mass fluxes;
3. Solve the pressure correction equation using the recently obtained velocity field and the mass flux;
4. Correct face mass fluxes, pressure, and the velocity field using the pressure correction obtained from step 3;
5. Solve the equations for additional scalars, such as turbulent quantities, energy, species and radiation intensity using the current values of the solution variables;
6. Update the source terms arising from the interactions among the different phases being defined (for example, source term for the carrier phase due to discrete particles);
7. Finally, check for the convergence of the equations.

These steps are continued until the requested convergence criteria are met.

b) The pressure-based coupled algorithm

Unlike the segregated algorithm described above, the pressure-based coupled algorithm solves a coupled system of equations: the momentum equations and the pressure-based continuity equation. Thus, in the coupled algorithm, steps 2 and 3 in the segregated solution algorithm are replaced by a single step in which the coupled system of equations are solved. The remaining equations are solved in a decoupled fashion as in the segregated algorithm.

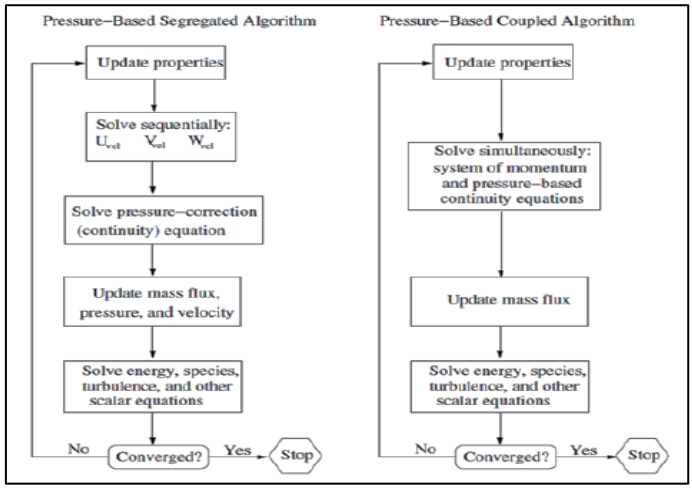

Fig. 4-30: Overview of the pressure-based solution methods [4.8].

Since the momentum and continuity equations are solved in a closely coupled manner, the rate of solution convergence is significantly improved when compared to the segregated algorithm. However, the resulting memory requirement increases by 1.5 to 2 times that of the segregated algorithm since the discrete system of all the momentum and the pressure-based continuity equations must be stored in memory when solving for the velocity and pressure fields (rather than just a single equation, as is the case with the segregated algorithm).

4.2.2.3.3 Pressure-velocity coupling

Pressure-velocity coupling is achieved by deriving an additional condition for pressure by manipulating the continuity equation (see Eq. (3.1)) [4.32, 4.33]. Ansys Fluent® provides five pressure-velocity coupling algorithms: SIMPLE, SIMPLEC, PISO, coupled and (for unsteady flows using the non-iterative time advancement scheme (NITA)) Fractional Step (FSM). All these schemes, except the coupled scheme, are based on the predictor-corrector approach. The SIMPLE, SIMPLEC, PISO and FSM pressure-velocity coupling algorithms are using the pressure-based segregated algorithm, while the coupled algorithm uses the pressure-based coupled solver. Further detailed information about the pressure-velocity coupling algorithms is presented in [4.8, 4.42-4.46].

4.2.3 Volume of Fluid (VOF) Method

4.2.3.1 Discretized volume fraction equation

As mentioned in section 4.1.5.2, this method which has been developed by Hirt and Nichols [4.34], is a surface-tracking technique, applied to a fixed in space Eulerian mesh.

It has been designed for two or more immiscible fluids where the position of the interface between the fluids is of interest. The basic concepts of this method have also been introduced in section 4.1.5.2.

For the base-filling simulation models presented in chapter 6, the volume fraction equation, Eq. (4.49) but without any mass source or mass transfer between the phases, will be solved explicitly for the two phases, air and SCC.

In Ansys Fluent®, the explicit approach uses a standard finite-difference interpolation scheme for the volume fraction values that were computed at the previous time step, as shown in Eq. (4.67):

$$\frac{\alpha_q^{n+1}\rho_q^{n+1}-\alpha_q^n\rho_q^n}{\Delta t}V+\sum_f\left(\rho_q^n U_f^n \alpha_{q,f}^n\right)=0 \qquad (4.67)$$

where $\alpha_{q,f}$ is the face value of the q^{th} volume fraction, V is de volume of the cell and U_f is the volume flux through face f, based on the normal velocity. This formulation does not require an iterative solution of the transport equation during each time step, as is needed for the implicit scheme.

4.2.3.2 Limitations of the VOF method implemented in Ansys Fluent®

The following restrictions apply to the VOF method implemented in Ansys Fluent®:

- The use of a pressure-based solver (see section 4.2.2.3.2) is required, which of course for modelling the performed formwork filling processes poses no problem;
- All control volumes within the computational domain must be filled with either a single fluid phase or a combination of phases. The VOF method does not allow for void regions where no fluid of any type is present;
- The VOF method requires a highly regular mesh (preferably full hexahedral) for obtaining an acceptable convergence rate. Also the variability of the mesh density influences the convergence rate considerably. This requirement has proven to be very challenging when modelling the performed base-filling experiments in this research;
- Only one of the phases can be defined as a compressible ideal gas;
- The second-order implicit time-stepping formulation cannot be used with the VOF explicit scheme. Only first-order implicit time-stepping is available (see also section 4.2.2.2).

4.2.3.3 Interpolation near the interface between phases

The control-volume formulation in Ansys Fluent® requires that the convection and the diffusion fluxes through the control volume faces be computed and balanced with source terms within the control volume itself.

In the geometric reconstruction (see next section) and the donor-acceptor schemes, Ansys Fluent® applies a special interpolation treatment to the cells that lie near and on the interface between two phases. Fig. 4-31 shows an actual interface shape, along with the interfaces assumed during computation applying these two methods. The explicit scheme treat these cells with the same interpolation method as the cells that are completely filled with one phase or the other (first-order upwind, see section 4.2.2.1.1).

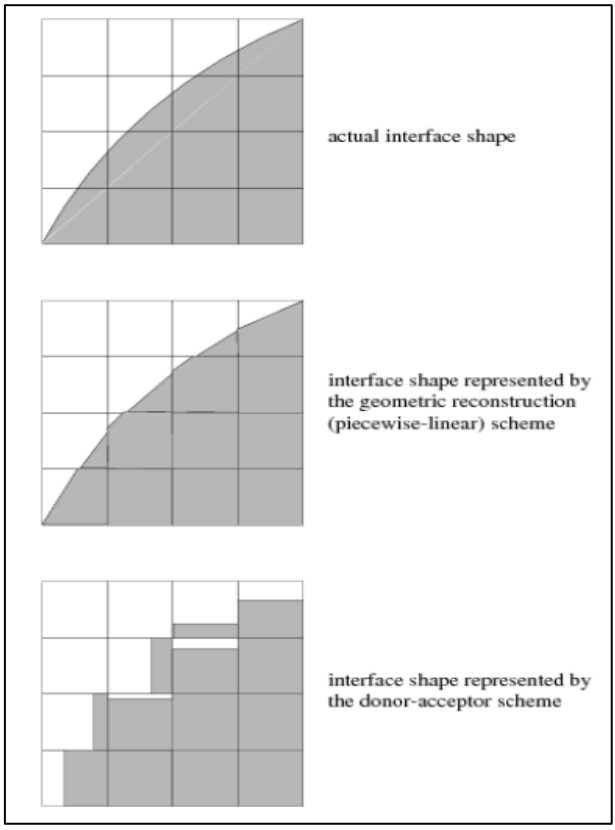

Fig. 4-31: Interface computations.

In the simulation models of the performed casting processes, which are presented in chapter 6, the geometric reconstruction scheme and the CICSAM scheme have been used to compute the moving SCC surface during the filling process. These two interface capturing schemes are explained further in the next sections.

4.2.3.3.1 The geometric reconstruction scheme

The geometric reconstruction scheme represents the interface between the fluids using a piecewise-linear approach. This scheme is the most accurate and it is applicable for general unstructured meshes based on the work of Youngs [4.47]. It assumes that the interface between two fluids has a linear slope within each cell, and it uses this linear shape for the calculation of the advection of fluid through the cell faces (see Fig. 4-31).

The geometric reconstruction scheme determines the interface between fluids as follows:

- The first step is calculating the position of the linear interface relative to the centre of each partially-filled cell, based on information about the volume fraction and its derivatives in the cell.
- The second step is calculating the advecting amount of fluid through each face using the computed linear interface representation and information about the normal and tangential velocity distribution on the face.
- The third step is calculating the volume fraction in each cell using the balance of fluxes calculated during the previous step.

4.2.3.3.2 The CICSAM scheme

The compressive interface capturing scheme for arbitrary meshes (CICSAM), based on the work of Ubbink [4.48], is a high resolution differencing scheme. This scheme is particularly suitable for flows with high ratios of viscosities between the phases.

CICSAM is implemented in Ansys Fluent® as an explicit scheme and it has the advantage of producing an interface that is almost as sharp as the geometric reconstruction scheme.

4.2.3.4 Interpolation of material properties

The properties appearing in the transport equations are determined by the presence of the component phases in each control volume of the mesh. In a two-phase system, if the phases are represented by the subscripts 1 and 2, and if the volume fraction of the second of these is being tracked, the density in each cell is computed according to Eq. (4.68).

$$\rho = \alpha_2 \rho_2 + (1 - \alpha_1)\rho_1 \tag{4.68}$$

In general, for an *n*-phase system, the volume-averaged density takes on the following form:

$$\rho = \sum_{q=1}^{n} \alpha_q \rho_q \tag{4.69}$$

All other properties, like the rheological parameters, are computed alike.

4.2.3.5 The momentum equation and the VOF method

A single momentum equation is solved throughout the domain, and the resulting velocity field is shared among the phases. The momentum equation (see Eq. (3.2)) is dependent on the volume fractions of all the phases through the material properties (the density ρ as well as the rheological (Herschel-Bulkley) material parameters (see chapter 2)).

A limitation of this shared-fields approximation is that in cases where quite large differences in velocity between the phases exist, the accuracy of the velocities computed near the interface can be adversely affected. Also, if the viscosity ratio between phases is higher than 10^3, this may lead to convergence difficulties. The CICSAM scheme is generally more suited for flows with high ratios of viscosities between the phases.

4.2.3.6 The coupled Level-Set (LS) and VOF method

Unlike in Fluent® v. 6.3 and Ansys Fluent® v. 12.0, in Ansys Fluent® v. 14.0 an additional interface-tracking method, called the Level-Set (LS) method, has been implemented which, combined with the VOF method, noticeably improves the calculation of the interface between phases during the transient flow.

The LS method is a popular interface-tracking method for computing two-phase flows with topologically complex interfaces. This is similar to the interface tracking method of the VOF model. According to Osher and Sethian [4.49], in the LS method the interface is captured and tracked by the LS function, defined as a signed distance from the interface.

Because the LS function is smooth and continuous, its spatial gradients can be accurately calculated. This in turn will produce accurate estimates of interface curvature and surface tension force caused by the curvature. However, the LS method is found to have a deficiency in preserving volume conservation, as stated by Olssen et al. [4.50].

On the other hand, the VOF method is naturally volume-conserved, as this method computes and tracks the volume fraction of a particular phase in each cell rather than the interface itself.

The weakness of the VOF method lies in the calculation of its spatial derivatives, since the VOF function (the volume fraction of a particular phase) is discontinuous across the interface.

To overcome the deficiencies of both methods, a coupled LS-VOF approach is provided in Ansys Fluent®. The coupled LS-VOF method is specifically designed for two-phase flows, where no mass transfer between the phases is occurring and it is applied to transient flow problems only.

The mesh should be restricted to quadrilateral, triangular or a combination of both for 2-D cases and restricted to hexahedral, tetrahedral or a combination of both for 3-D cases.

The LS function φ is defined as a signed distance to the interface. Accordingly, the interface is the zero level-set $\varphi(x,t)$ and can be expressed as $X = \{x \mid \varphi(x,t) = 0\}$ in a two-phase flow system:

$$\varphi(x,t) = \begin{cases} +|d| \; if \; x \; \in the \; primary \; phase \\ 0 \; if \; x \; \in X \\ -|d| \; if \; x \; \in the \; secondary \; phase \end{cases} \tag{4.70}$$

where d is the distance from the interface.

The normal and curvature of the interface, which is needed in the computation of the surface tension force, can then be estimated as:

$$\vec{n} = \frac{\vec{\nabla}\varphi}{|\vec{\nabla}\varphi|}\Big|_{\varphi=0} \tag{4.71}$$

$$\kappa = \vec{\nabla}.\frac{\vec{\nabla}\varphi}{|\vec{\nabla}\varphi|}\Big|_{\varphi=0} \tag{4.72}$$

The evolution of the LS function in time and space can be given in a similar fashion as for the VOF method:

$$\frac{\partial\varphi}{\partial t} + \vec{\nabla}.(\vec{u}\varphi) = 0 \tag{4.73}$$

where $\vec{u}$ is the underlying velocity field. The momentum equation is then written as:

$$\frac{\partial(\rho\vec{u})}{\partial t} + \vec{\nabla}.(\rho\vec{u}\vec{u}) = -\vec{\nabla}p + \vec{\nabla}.\bar{\bar{\tau}} - \sigma\kappa\delta(\varphi)\vec{\nabla}\varphi + \rho\vec{g} \tag{4.74}$$

where:

- ✓ $\delta(\varphi) = \frac{1+\cos\left(\frac{\pi\varphi}{a}\right)}{2a}$ if $|\varphi| < a$ and $a = 1.5h$ where h is the mesh grid spacing, otherwise;
- ✓ $\delta(\varphi) = 0$;
- ✓ σ is the surface tension coefficient.

Due to the nature of the transport equation of the LS function (see Eq. (4.73)), it is unlikely that the distance constraint of $|\vec{\nabla}\varphi| = 1$ is maintained after its solution. The reasons for this is due to the deformation of the interface, an uneven profile, and thickness across the interface. Those errors will accumulate during the iteration process and cause large errors in mass and momentum solutions.

A re-initialization process is therefore required for each time step. The geometrical interface-front construction method is used in this case. This geometrical method involves a simple concept and is reliable in producing accurate geometrical data for the interface front.

The values of the VOF and the LS function are both used to reconstruct the interface-front. Namely, the VOF method provides the size of the cut in the cell where the likely interface passes through, and the gradient of the level-set function determines the direction of the interface.

The concept of piecewise linear interface construction (PLIC) is also employed to construct the interface-front. The procedure for the interface-front reconstruction can be described as follows and as shown in Fig. 4-32:

1. Locate the interface front cells, where the sign(φ) is alternating or the value of the volume fraction is between 0 and 1, that is, a partially filled cell;
2. Calculate the normal of the interface segment in each front cell from the LS function gradients;
3. Position the cut-through, making sure at least one corner of the cell is occupied by the designated phase in relation to the neighbouring cells;
4. Find the intersection between the cell centreline normal to the interface and the interface so that the VOF is satisfied;
5. Find the intersection points between the interface line and the cell boundaries; these intersection points are designated as front points.

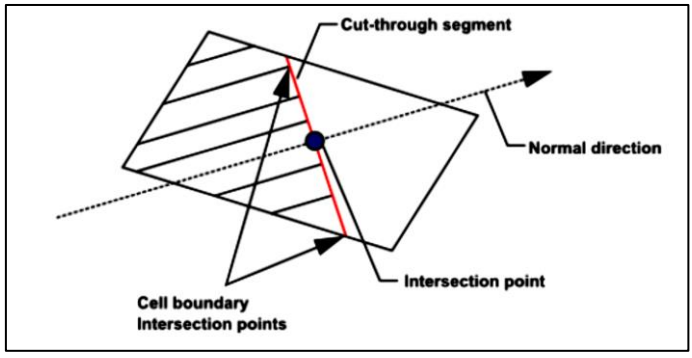

Fig. 4-32: Schematic view of the interface cut through the front cell.

Once the interface front is reconstructed, the procedure for the minimization of the distance from a given point to the surface is as follows:

1. Calculate the distance of the given point in the domain to each cut-segment of the front cell. The method for the distance calculation is:
    a. If the normal line starting from the given point to the interface intersects within the cut-segment, then the calculated distance will be taken as the distance to the interface;

b. If the intersection point is beyond the end points of the cut-segment, the shortest distance from the given point to the end points of the cut-segment will be taken as the distance to interface cut-segment, as shown in Fig. 4-33.

2. Minimize all possible distances from the given point to all front cut-segments, so as to represent the distance from the given point to the interface. Thus, the calculated values of these distances will be used to re-initialize the LS function.

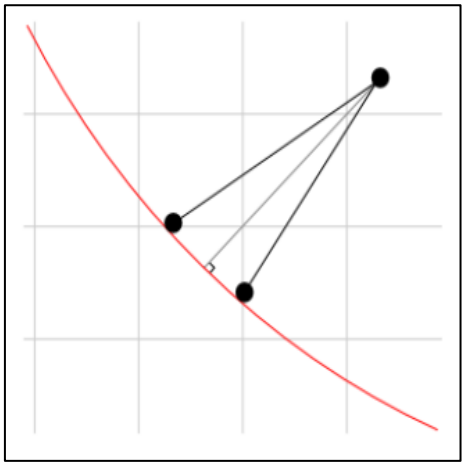

Fig. 4-33: Minimization procedure for the distance to the interface segment.

4.3 Finite Volume Method - Porous zone models

4.3.1 Introduction

In the previous chapter, the FVM and the VOF method were both introduced. By combining these methods, the time-dependent base-filling processes of formworks with SCC can be modelled by solving the conservation of mass and momentum in the whole computational domain and obtaining the pressure, the velocity components and the volume fractions of all the fluid phases involved at each mesh cell centre and for all time steps.

Applying these methods for simulating casting processes without rebars (see chapter 6) is straightforward. The pre-processing time as well as the computational time for solving the flow equations are acceptable for engineering purposes. However, the presence of rebars in concrete casts severely complicates matters when applying the FVM and the VOF method.

Modelling of each rebar significantly increases not only the computing time but also the pre-processing time, being the time to generate the geometry of the formwork and the rebar configuration and the computational mesh. This is shown in Fig.4-34.

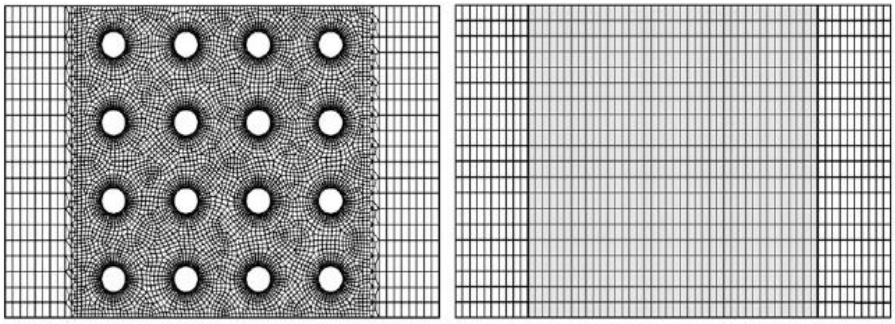

Fig. 4-34: Schematic representation of rebars (left) treated as a porous zone (right) [4.51].

In order to simplify pre-processing and to reduce the computational solving time, the idea of treating reinforcement as a porous medium was proposed by other researchers [4.51 - 4.54].

This technique is also applied in coastal engineering, where the porous skeleton is space-averaged by introducing a porosity and an expression for the losses, which can be treated as a source term.

4.3.2 Porous zone analogy

4.3.2.1 Fresh concrete considered as a fluid

As mentioned in chapter 2, a fundamental description of the concrete flow behaviour during casting is indispensable for special concrete types like SCC and HPC, or in the presence of heavily congested reinforcements.

This fundamental description involves a rheological approach of the fresh concrete workability/flowability.

For concrete in the fresh state the following different rheological approaches can be applied, depending on the scale of observation, as stated by Heirman [4.55] and Wallevik [4.56]:

- The suspension approach (local scale), or;
- The continuum approach (global scale).

4.3.2.1.1 Suspension approach

As shown in the right part of Fig. 4-35, fresh concrete can be considered as a suspension of solid particles (aggregates) with a broad range of size, shape and surface texture, dispersed in continuous liquid matrix (cement paste).

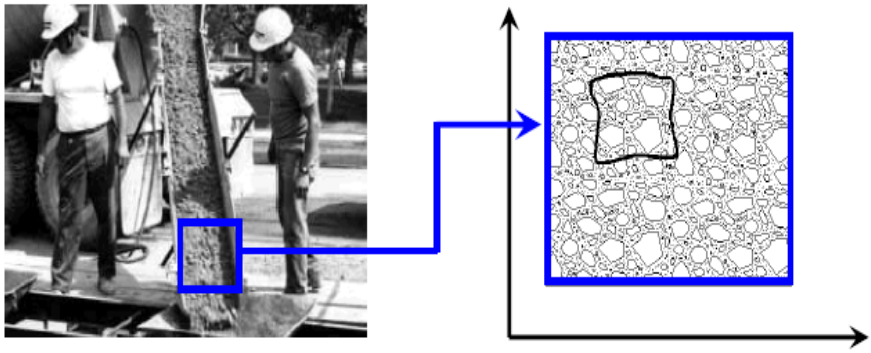

Fig. 4-35: Suspension approach for describing fresh concrete flowability [4.55, 4.56].

The suspension approach implies that various interactions interplay with the flow behaviour, according to Roussel et al. [4.57]:

- Surface forces (or colloidal interactions like van der Waals dispersion forces, electrostatic forces and steric hindrance). These forces are only important for the colloidal particles;
- Brownian (thermodynamic) forces, which are also only relevant for colloidal particles;
- Hydrodynamic forces (viscous drag, inertia);
- Various contact forces between particles (e.g. gravity).

Depending on the particle loading, the size and shape, the particle volume fraction and the external forces applied to the suspension, one or several of these interactions dominate the flow behaviour [4.58 - 4.60].

4.3.2.1.2 Continuum approach

In contrast to the suspension approach, the continuum approach consists of calculating only the motion of a large number of solid particles, without going into the detailed motion of every single one of them, only the so-called continuum particles (CP) are considered. A CP is defined as a material point, where its mass (density) is a smooth function of the volume.

In other words, the volume of the CP must be:

- Small compared to the whole volume occupied by the fluid;
- Large enough for its density to be independent of its volume [4.61].

This concept is illustrated in Fig. 4-36.

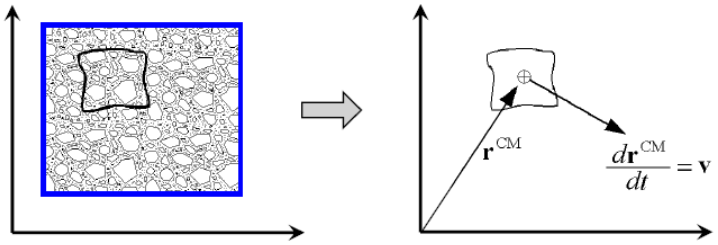

Fig. 4-36: Continuum approach for describing fresh concrete workability [4.55, 4.56].

In general, the continuum approach can only be used when the material can be considered as a homogeneous continuum, resulting in a global flow behaviour which can be described within the framework of continuum mechanics. In the present case, continuum/fluid rheology methods can be used to describe the material's flow.
In order to justify the continuum approach for the global flow behaviour of fresh concrete, Ferraris et al. [4.62] proposed that the following conditions should be fulfilled:

- Flowability: a certain degree of flow must be achieved (certainly fulfilled for SCC);
- Resistance to segregation: the concrete should retain a homogeneous composition while in its fresh state.

When comparing these conditions with the key properties of fresh SCC mixtures, it may be clear that the continuum approach is strongly applicable in order to describe the flow behaviour of fresh, well-designed (and so homogeneous) SCC mixtures.

Besides the homogeneity of the material, also the scale of observation is of great importance to choose whether or not the continuum approach is legitimate.

The flow of fresh SCC (size of coarsest particles ≈ 0.01 m) inside a typical formwork (smallest characteristic size ≈ 0.1 m) can be considered as the flow of a continuum (fluid) when the presence of the rebars can, as a first approximation, be neglected.

In some other cases however, the use of the suspension approach may be needed, as stated by Roussel et al. [4.6] (see also section 4.1.4):

- If the objective is to explain the correlation between the flow behaviour and the specific SCC mixture composition;
- If the objective is to take into account the presence of dense reinforcement, so that the scale of observation will be similar to the size of the coarsest particles;
- If the objective is to predict the passing ability (avoiding particle blocking through the formation of particle bridges between the reinforcement) or the resistance to dynamic segregation (avoiding segregation of the coarsest particles induced by the concrete flow.

In order to apply the porous zone concept, the previously stated conditions for a continuum need to be fulfilled.

4.3.2.2 The porous medium - additional source term in the momentum equation

To evaluate the influence of the porous zone on the flow, macroscopic averaging methods are used to modify the constitutive equation (see Eq. (2.5) or Eq. (2.6)), describing the flow behaviour of the fresh concrete, and the conservation of momentum equation (see Eq. (3.2)) in order to account for the presence of the porous matrix as a continuous medium [4.63].

According to Sorbie et al. [4.64], the porous zone is represented mathematically as an equivalent bundle of capillaries with an average hydraulic radius being defined in terms of the porous medium macroscopic parameters and/or properties such as the porosity and the permeability. This leads to the implementation of a modified version of Darcy's Law for non-Newtonian fluids in a porous zone.

From a computational point of view, the influence of the porous medium on the flow is modelled by the addition of a momentum sink or loss term to the conservation of momentum equation. The added momentum source term S_i in the direction i is:

$$S_i = -\frac{\mu_{app}}{k_i} v_i \tag{4.75}$$

where μ_{app} is the local apparent viscosity (Pa.s), k_i is the permeability coefficient in the direction i (m^2) and v_i is the Darcy's velocity in the direction i (m/s). In soil mechanics, v_i is called the filter "velocity" or the averaged velocity over the control volume.

For Newtonian materials, the apparent viscosity is the Newtonian viscosity of the material and it is independent of the local strain rate. However, for Bingham or Herschel-Bulkley materials, the apparent viscosity is dependent on the shear rate in the flowing material.

As the local shear rate within the porous zone is unknown and is a complex function of the geometry and the rebar configuration, it is necessary to define a so-called apparent shear rate $\dot{\gamma}_{\mathrm{app}}$ within the porous medium [4.65]:

$$\dot{\gamma}_{app} = \frac{\alpha . v_i}{\sqrt{k_i . \varphi}} \tag{4.76}$$

where φ is the porous medium porosity (-) and the coefficient α is the shift factor (-) (also called shape factor).

The value of the coefficient α is either measured through experiments [4.65] or computed using pore-scale modelling approaches [4.66].

Pearson and Tardy [4.63] reviewed the different mathematical approaches used to describe non-Newtonian flow in porous media and they concluded that, although α is in most studies considered as constant, it is a weak function of both bulk rheology and pore structure and that there is currently no theory able to predict its value reliably. Vasilic et al. [4.51] have calibrated α for a large range of concrete materials and for a parallel cylinders configuration, representative of rebars in formworks.

By introducing the apparent shear rate into the constitutive equation (Eq. (2.5) or Eq. (2.6)), the local apparent viscosity in the porous zone can be formulated as:

$$\mu_{app}(\dot{\gamma}_{app}) = \frac{\tau_0}{\dot{\gamma}_{app}} + \mu_p = \frac{\tau_0\sqrt{k_i.\varphi}}{\alpha.v_i} + \mu_p \tag{4.77}$$

or:

$$\mu_{app}(\dot{\gamma}_{app}) = \frac{\tau_0}{\dot{\gamma}_{app}} + K.\dot{\gamma}_{app}^{n-1} = \frac{\tau_0\sqrt{k_i.\varphi}}{\alpha.v_i} + K\left(\frac{\alpha.v_i}{\sqrt{k_i.\varphi}}\right)^{n-1} \tag{4.78}$$

The source term in the momentum equation (Eq. 3.2) becomes:

$$S_i = -\frac{1}{k_i}\left(\frac{\tau_0\sqrt{k_i.\varphi}}{\alpha} + \mu_p.v_i\right) \tag{4.79}$$

or:

$$S_i = -\frac{1}{k_i}\left(\frac{\tau_0\sqrt{k_i.\varphi}}{\alpha} + K.v_i\left(\frac{\alpha.v_i}{\sqrt{k_i.\varphi}}\right)^{n-1}\right) \tag{4.80}$$

4.3.3 How to determine the porous zone parameters?

In order to model the reinforced zone within a formwork as a porous zone, the porous zone parameters need to be determined, being the porosity, the permeability and the shift factor. The porosity can be calculated in a straightforward way. Much more difficult is to determine the permeability and the shift factor. These are unknown, and they have to be computed a priori.

4.3.3.1.1 How to determine the permeability of a porous zone?

The intrinsic permeability of a porous zone depends on its geometry and topology. It can be computed numerically, or measured experimentally during a steady-state filling process with a Newtonian fluid flowing through a sample formwork with rebars in it which has the required geometrical configuration.

Using Darcy's Law, the permeability can be calculated as follows:

$$k_i = \frac{\Delta L}{\Delta p}.\eta.v_i \tag{4.81}$$

where η is the viscosity of the Newtonian fluid (Pa.s), v_i is the Darcy velocity in the direction i (m/s), ΔL is the length of the porous zone in the direction i (m) and Δp is the pressure drop (either numerically computed or measured experimentally) between the inlet and outlet of the porous medium (Pa). It is interesting to mention that the porous zone analogy is perfectly applicable for flows with Newtonian fluids, regardless of the geometry (formwork and rebars), the Newtonian viscosity or the inlet velocity, as long as the flow stays laminar. In that case the pressure drop is linearly related to the flow rate. This confirms that the rebars can be treated as a porous medium.

Fig. 4-37 shows the computed permeability for the flow of a Newtonian fluid through an array of cylindrical bars with varying diameters (d) and with varying distances (M) between the bars [4.51], as illustrated in Fig. 4-38.

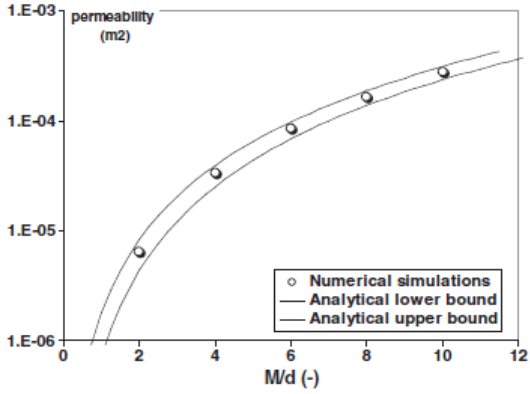

Fig. 4-37: Computed permeability of the flow configuration shown in Fig. 4-38 [4.51].

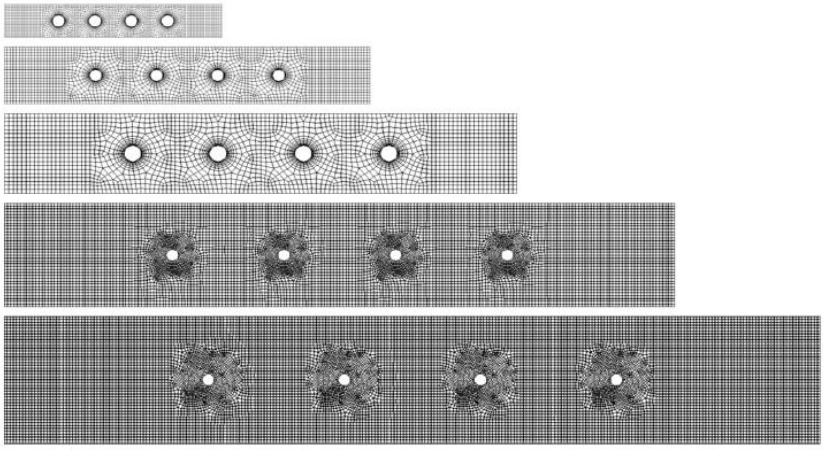

Fig. 4-38: Mesh used for the permeability computation with a Newtonian fluid [4.51].

The simulation results clearly show the large influence of the flow geometry on the resulting permeability of the equivalent porous zone, which is a serious disadvantage for the application of the porous zone analogy as it requires to build complex CFD models for each casting configuration prior to being able to use the porous zone concept for the optimization of other similar filling processes.

4.3.3.1.2 How to determine the shift factor of a porous zone?

As explained in section 4.3.2.2, the local apparent shear rate within a non-Newtonian fluid flowing through a porous medium can be computed from the value of the macroscopic Darcy velocity of the fluid v_i, the porosity φ, the permeability k_i and the shift factor α.

In order to determine the value of α and its dependency on the rheology of the chosen fluid, Vasilic et al. [4.51] have performed several simulations with different sets of rheological parameters. The selected fluids were all characterised as Bingham materials, and each of them were identified by their dimensionless Bingham number value, which expresses the relative contribution of the yield stress and the plastic viscosity, as presented in Eq. (4.82):

$$B_n = \frac{\tau_0}{\mu_p \cdot \dot{\gamma}_{app}} \tag{4.82}$$

Fig. 4-39 shows the dependency of the shift factor on the Bingham number (or the rheology of the material).

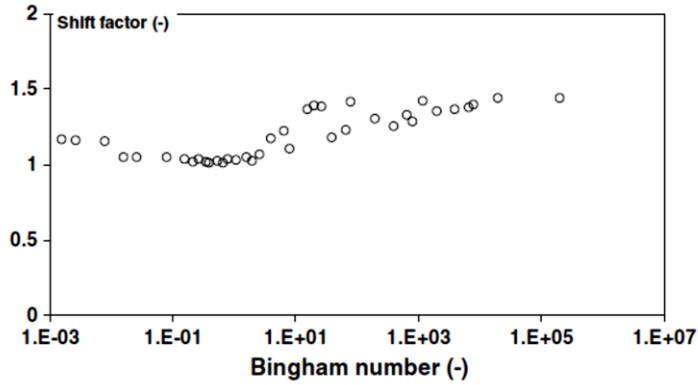

Fig. 4-39: Shift factor α as a function of the Bingham number B_n [4.51].

Fig. 4-39 reveals that on the studied range, the shift factor only weakly depends on the rheology and varies between 1 and 1.5. For most industrial casting processes, a value of 1.5 for the shift factor α seems to be adequate [4.51]. This value allows to accurately predict the filling ability of the chosen fluid for a given formwork and rebar configuration.

4.3.4 Promising results

Vasilic et al. reported some very promising results with applying the porous zone concept in numerical simulation models of non-Newtonian flows in computational domains including a network of rebars [4.51, 4.54].

In Fig. 4-40, the geometrical set-up of a casting experiment with a non-Newtonian carbopol suspension in a model formwork with different rebar configurations is presented.

Fig. 4-41 illustrates the shape of the simulated free surface at the end of the cast. The rebars have been modelled explicitly in this numerical model.

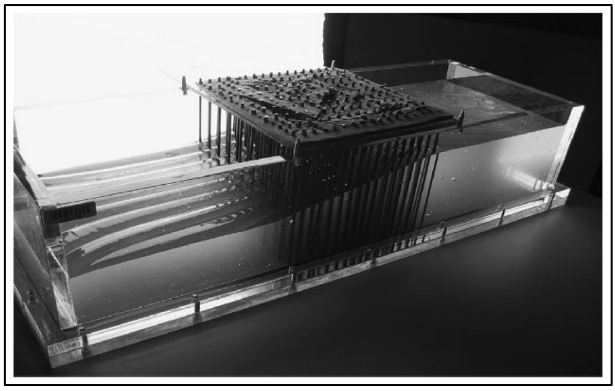

Fig. 4-40: Experimental set-up of the casting process [4.51].

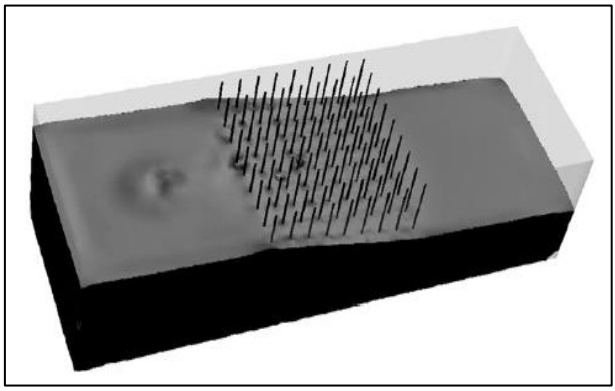

Fig. 4-41: Final shape of the cast with the rebars modelled explicitly [4.51].

In the following figure, the same experiment is simulated, but in this case the rebars have been modelled using the porous zone analogy.

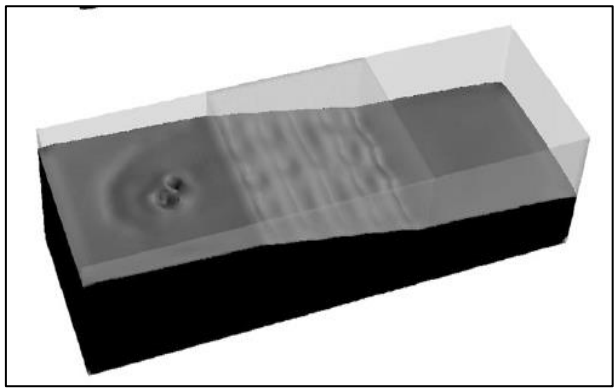

Fig. 4-42: Final shape of the cast with the rebars modelled as a porous zone [4.51].

For both simulations, the Ansys Fluent® software suite was used. Finally, Fig. 4-43 shows the very good agreement between the measured and simulated free surface along a section at the end of the casting process.

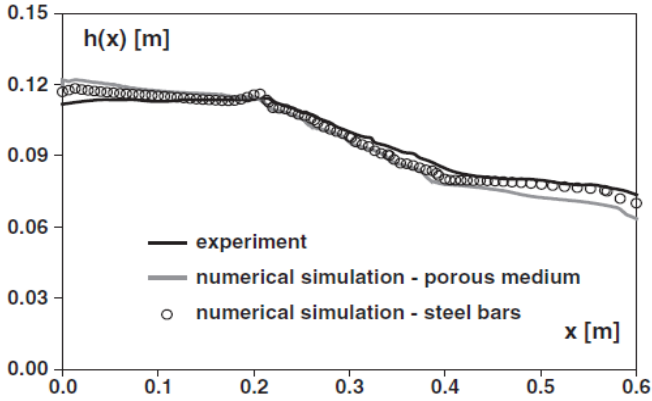

Fig. 4-43: Comparison between measurements and simulations [4.51].

The researchers who have performed this casting experiment [4.51] reported the following pre-processing and computation times for the two simulation models:

- Model with the rebars modelled explicitly: 170000 mesh cells, 2 hours for pre-processing and 10 hours for computation;
- Model with the rebars modelled as a porous zone: 60000 mesh cells, 20 min for pre-processing and 3.5 hours for computation.

According to these figures, a reduction of the total simulation time of 70 % was achieved. However, regarding the porous zone model, the time needed to determine the permeability for this specific casting configuration is not mentioned, nor included!

As already mentioned in section 4.3.3.2.1, before one can apply the porous zone concept, the permeability of the flow domain needs to be determined a priori, using a computational model where the rebars need to be modelled explicitly. The pre-processing and computation time needed for the pre-calibration of the porous medium is not to be neglected, certainly not for complex geometries with dense rebar configurations. Of course, once the porous zone parameters have been determined properly, applying the porous zone analogy will drastically speed up any additional simulations leading to the optimization of the casting process.

4.3.5 The pros and cons of the porous zone analogy

Although the results of the application of the porous zone concept, presented in the previous section, reveal that the use of this concept can drastically speed up the pre-processing and computation time, with very good resulting accuracy, the difficulty still remains to determine the porous zone parameters for all possible formwork and rebar configurations. Especially the determination of the permeability is still time consuming, as it requires to build the CFD model with all the rebars modelled explicitly anyway.

Therefore, this method could only be interesting for performing optimizations for standard formwork and rebar configurations, for which a set of porous zone parameters have been determined a priori and made available in a database. Hopefully these parameters will remain more or less constant or universal for each class of casting configuration.

4.4 References

[4.1] Mechtcherine V., Gram A., Krenzer K., Schwabe J.-H., Shyshko S., Roussel N., "Simulation of fresh concrete flow using Discrete Element Method (DEM): theory and application", Mat. And Struct **47** (2014), pp. 615-630.

[4.2] Cundall P.A., Konietzky H., Potyondy D.O., "PFC - Ein Neues Werkzeug für Numerische Modellierungen", Bautechnik **73** (1996), pp. 492-498.

[4.3] Mechtcherine V., Shyshko S., "Virtual concrete laboratory - Continuous numerical modelling of concrete from fresh to the hardened state", Springer-Verlag, Berlin-Heidelberg (2007), pp. 479-488.

[4.4] Shyshko S., Mechtcherine V., "Simulating the workability of fresh concrete", Proceedings of the International RILEM Symposium of Concrete Modelling - CONMOD '08 - Schlangen E. and De Schutter G. (eds), Delft (2008), pp. 173-181.

[4.5] Mechtcherine V., Shyshko S., "Self-Compacting Concrete Simulation using Distinct Element Method", Proceedings pro068 RILEM Publications - Wallevik O.H. and Kubens S. and Oesterheld S. (eds), (2009), pp. 171-179.

[4.6] Roussel N., Geiker M.R., Dufour F., Thrane L.N., Szabo P., "Computational modelling of concrete flow: General overview", Cem. And Conc. Res. **37** (2007), pp. 1298-1307.

[4.7] Shyshko S., "Numerical simulation of the rheological behaviour of fresh concrete", Ph-D dissertation Technischen Universität Dresden, (2013), 211 pages.

[4.8] Ansys Fluent v.14.0 Theory Guide, Fluent Inc. (2011), 826 pages.

[4.9] De Schutter G., Bartos P., Domone P., Gibbs J., "Self-Compacting Concrete", Whittles Publishing, Caithness (2008), 296 pages.

[4.10] Kuch H, Palzer S, Schwabe J-H, "Anwendung der Simulation bei der Verarbeitung von Gemengen", F.A. Finger-Institut für Baustoffkunde - Tagungsbericht der 16. Internationalen Baustofftagung - Bauhaus Universität - vol. 1, Weimar, (2006), pp 1321-1327.

[4.11] Martys N.S., "Study of a disspative particle dynamics based approach for modelling suspensions", ", J. Rheol. **49** (2005), pp. 401-424.

[4.12] Koelman J.M.V.A., Hoogerbrugge P.J., "Dynamic simulation of hard sphere suspensions under steady shear", Europhys. Lett. **21** (1993), pp. 363-368.

[4.13] Karniadakis G.E., "Dissipative Particle Dynamics: Foundation, Evolution and Applications - Lecture 1 - Overview", Brown University - MIT - CM4 - The CRUNCH group, (2010).

[4.14] Allen M.P., "Introduction to Molecular Dynamics Simulation", Centre for Scientific Computing and Department of Physics - University of Warwick - Coventry - UK, 27 pages.

[4.15] Karniadakis G.E., "Dissipative Particle Dynamics (DPD): An Overview", Division of Applied Mathematics at Brown University - Department of Mechanical Engineering at MIT - The CRUNCH group, (2010).

[4.16] Groot R.D., Warren P.B., "Dissipative particle dynamics: Bridging the gap between atomistic and mesoscopic simulation", J. Chem. Phys. **107** (1997), pp. 4423-4435.

[4.17] Moeendarbary E., NG T.Y., Zangeneh M., "Dissipative particle dynamics: Introduction, methodology and complex fluid applications - A review", Int. J. Applied Mechanics. **1** (2009), pp. 737-763.

[4.18] Karniadakis G.E., "Dissipative Particle Dynamics: Foundation, Evolution and Applications - Lecture 2 - Theoretical foundation and parametrization", Brown University - MIT - CM4 - The CRUNCH group, (2010).

[4.19] Español P., Warren P.B., "Statistical mechanics of dissipative particle dynamics", Europhys. Lett. **30** (1995), pp. 191-196.

[4.20] Kim S., Karrila S.J., "Microhydrodynamics: Principles and Selected Applications", Butterworth - Heinemann, Stoneham, MA (1991), 544 pages.

[4.21] Feys D., "Interactions between Rheological Properties and Pumping of Self-Compacting Concrete", Ph-D dissertation, Ghent University, Ghent (2009).

[4.22] Martys N., Ferraris C.F., "Simulations of SCC flow", from the Proceedings of the First North American Conference on the Design and Use of SCC, Chicago, IL (2003), pp. 27-30.

[4.23] Sukop M.C., Thorne D.T., "Lattice Boltzmann Modelling - An Introduction for Geoscientists and Engineers", Springer-Verlag, Berlin Heidelberg (2007), 172 pages.

[4.24] Succi S., “The Lattice Boltzmann Equation for Fluid Dynamics and Beyond”, Oxford Science Publications, Clarendon Press Oxford (2001), 300 pages.
[4.25] Qian Y.H., d’Humieres D., Lallemand P., “Lattice BGK models for Navier-Stokes equation”, Europhys. Lett. **17** (1992), pp. 479-484.
[4.26] Švec O., Skoček J., Stang H., Geiker M.R., Roussel N., “Free surface flow of a suspension of rigid particles in a non-Newtonian fluid: A Lattice Boltzmann approach”, J. Non-Newt. Fluid Mech. **179-180** (2012), pp. 32-42.
[4.27] Zhou Y., Zhang R., Staroselky I., Chen H., “Numerical simulation of laminar and turbulent buoyancy-driven flows using a Lattice Boltzmann based algorithm”, Int. J. Heat & Mass Transfer **47** (2004), pp. 4869-4879.
[4.28] Roussel N., Coussot P., ““Fifty-cent rheometer” for yield stress measurements: From slump to spreading flow”, J. Rheol. **49**, (2005), pp. 705-718.
[4.29] Geller S., Krafzcyk M., Tölke J., Turek S., Hron J., “Benchmark computations based on Lattice Boltzmann, Finite Element and Finite Volume Methods for laminar flows”, Computers & Fluids **35** (2006), pp.888-897.
[4.30] Anderson T.B., Jackson R., *“*A Fluid Mechanical Description of Fluidized Beds*”*, I & EC Fundam **6** (1967), pp. 527-534.
[4.31] Drew D.A., Lahey R.T., “In Particulate Two-Phase Flow”, Butterworth-Heinemann, Boston 1993), pp. 509-566.
[4.32] Hirsch Ch., “Numerical Computations of Internal and External Flows, Volume 1 - Fundamentals of Numerical Discretization”*,* John Wiley & Sons, New York (1989).
[4.33] Wendt J.F., Anderson J.D., Grundmann R., Degrez G., Dick E., Vierendeels J., “Computational Fluid Dynamics - An Introduction”, Springer-Verlag, Berlin Heidelberg (2009), 332 pages.
[4.34] Hirt C.W., Nichols B.D., “Volume of Fluid Method for the Dynamics of Free Boundaries”*,* J. Comput. Phys. **39**, (1981), pp. 201-225.
[4.35] Fluent v.6.3 User’s Guide, Fluent Inc. (2006), 2501 pages.
[4.36] Ansys Fluent v.12.0 Theory Guide, Fluent Inc. (2009), 816 pages.
[4.37] Roussel N., “A thixotropy model for fresh fluid concretes: Theory, validation and applications”, Cem. Conc. Res. **36** (2006), pp. 1797-1806.
[4.38] Barth T.J., Jesperson D., “The design and application of upwind schemes on unstructured meshes”, Technical report AIAA-89-0366 - AIAA 27th Aerospace Sciences Meeting, Reno - Nevada (USA) (1989), 13 pages.
[4.39] Holmes D.G., Connell S.D., “Solution of the 2D Navier-Stokes Equations on Unstructured Adaptive Grids”, AIAA 9th Computational Fluid Dynamics Conference, Buffalo (USA) (1989), 8 pages.
[4.40] Rauch R.D., Batira J.T., Yang N.T.Y., “Spatial Adaption Procedures on Unstructured Meshes for Accurate Unsteady Aerodynamic Flow Computations”, Technical report AIAA-91-1106, AIAA (1991), 18 pages.
[4.41] Anderson W.K., Bonhus D.L., “An Implicit Upwind Algorithm for Computing Turbulent Flows on Unstructured Grids”, Computers Fluids **23** (1994), pp. 1-26.
[4.42] Chorin A.J., “Numerical solution of Navier-Stokes equations”, Mathematics of Computation **22** (1968), pp. 745-762.
[4.43] Patankar S.V., “Numerical heat transfer and fluid flow”, Hemisphere Series, Washington DC (1980), 205 pages.
[4.44] Vandoormaal J.P., Raithby G.D., “Enhancements of the SIMPLE method for predicting incompressible fluid flows”, Num. Heat Transfer **7**, (1984), pp. 147-163.
[4.45] Issa R.I., “Solution of the implicitly discretized fluid flow equations by operator-splitting”, J. Comput. Phys. **62**, (1986), pp. 40-65.
[4.46] Versteeg H.K., Malalasekera W., “An Introduction to Computational Fluid Dynamics - The Finite Volume Method - First Edition”, Longman Scientific & Technical, (1995), 267 pages.
[4.47] Youngs D.L., “Time-Dependent Multi-Material Flow with Large Fluid Distortion”, Numerical Methods for Fluid Dynamics edited by K.W. Morton and M.J. Baines, Academic Press (1982), pp. 273-285.
[4.48] Ubbink O., “Numerical Prediction of Two Fluid Systems with Sharp Interfaces”, Ph-D thesis, Imperial College of Science, Technology and Medicine, London, England, (1997), 69 pages.
[4.49] Osher S., Sethian J.A., “Fonts Propagating with Curvature-dependent Speed: Algorithms based on Hamilton-Jacobi Formulations”, J. Comput. Phys. **79**, (1988), pp. 12-49.

[4.50] Olsson E., Kreiss G., Zahedi S., “A Conservative Level Set Method for Two Phase Flow II”, J. Comput. Phys. **225**, (2007), pp. 785-807.
[4.51] Vasilic K., Meng B., Kühne H.C., Roussel N., “Flow of fresh concrete through steel bars: A porous medium analogy”, Cem. Conc. Res. **41**, (2011), pp. 496-503.
[4.52] Nguyen T.I.H., “Outils pour la modélisation de la mise en œuvre des bétons”, Ph-D dissertation (in French), Laboratoire Central des Ponts et Chaussées (LCPC), Paris (2007), 122 pages.
[4.53] Roussel N., “Ecoulement et mise en œuvre des bétons”, OA59 - ISSN 161-028X (in French), Paris (2008), 109 pages.
[4.54] Vasilic K., Meng B., Kühne H.C., Roussel N., “Computational modelling of SCC flow: reinforcement network modelled as porous medium”, The RILEM International Symposium on Rheology of Cement Suspensions, Reykjavik (2009), pp. 148-154.
[4.55] Heirman G., “Modelling and quantification of the effect of mineral additions on the rheology of fresh powder type self-compacting concrete”, Ph-D dissertation, Catholic University of Leuven, Leuven (2011).
[4.56] Wallevik J.E., “Rheology of Particle Suspensions - Fresh Concrete, Mortar and Cement Paste with Various Types of Lignosulfonates”, Ph-D dissertation, NTNU, Trondheim (2003).
[4.57] Roussel N., Lemaître A., Flatt R.J., Coussot P., “Steady state flow of cement suspensions: a micro-mechanical state-of-the-art”, Cem. Conc. Res. **40**, (2010), pp. 77-84.
[4.58] Ancey C., “Plasticity and geophysical flows: a review”, J. non-Newt. Fluid Mech. **142** (2007), pp. 4-35.
[4.59] Coussot P., “Rheometry of Pastes, Suspensions and Granular Materials: Applications in Industry and Environment”, Phys. Rev. E **59** (1999), pp. 4445-4457.
[4.60] Feys D., Verhoeven R., De Schutter G., “Evaluation of time independent rheological models applicable to fresh self-compacting conrete”, Appl. Rheol. **17** (2007), pp. 56244.1-56244.10.
[4.61] Spurk J.H., Aksel N., “Fluid Mechanics”, Springer-Verlag, Berlin-Heidelberg (2008), 534 pages.
[4.62] Ferraris C.F., de Larrard F., Martis N.S., “Fresh concrete rheology: Recent developments”, Materials Science of Concrete VI John Wiley & Sons, New Jersey (2001), 28 pages.
[4.63] Pearson J.R.A., Tardy P.M.J., “Models for flow of non-Newtonian and complex fluids through porous media”, J. non-Newt. Fluid Mech. **102** (2002), pp. 447-473.
[4.64] Sorbie K.S., Clifford P.J., Jones E.R.W., “The rheology of pseudoplastic fluids in porous media using network modelling”, J. of Colloid and Interface Science **130**, (1989), pp. 508-534.
[4.65] Perrin C.I., Tardy P.M.J., Sorbie K.S., Crawshaw J.P., “Experimental and modelling study of Newtonian and non-Newtonian fluid flow in pore network micromodels”, J. of Colloid and Interface Science **295**, (2006), pp. 542-550.
[4.66] Canella W.J., Huh C., Seright R.S., “Prediction of Xanthan Rheology in Porous Media”, Proceedings of SPE - 63rd Ann. Tech. Conf. and Exhibition of SPE, Houston Texas (1988), 16 pages.
[4.67] Lopez X., Valvatne P.H., Blunt M., “Predictive network modelling of single-phase non-Newtonian flow in porous media”, J. non-Newt. Fluid Mech. **264** (2003), pp. 256-265.

Chapter 5: Full-scale casting tests with fresh SCC

"It is the weight, not numbers of experiments that is to be regarded." - Isaac Newton

5 Overview of this Chapter

During the present research, two series of formwork base-filling tests with SCC have been performed at the MLCR of Ghent University. In total, one large I-beam, ten columns and two walls have been cast. The influence on the formwork pressure of the viscosity of the SCC, the casting speed and the presence of rebars has been studied. This chapter is therefore divided in two main sections: section 5.1, where we describe the casting tests with SCC where no rebars were present inside the formworks and section 5.2, where the casting tests with rebars are discussed.

5.1 Formwork base-filling tests without rebars

5.1.1 Introduction

In this section we describe the two series of formwork base-filling tests with SCC without rebars. During the first series of filling tests, two walls and two columns were cast bottom-up with a low viscosity SCC at a constant filling rate. During the second series of casting tests, four column formworks were filled with two types of SCC mixtures, a low viscosity type and a high viscosity type, and at two casting speeds. These formwork filling tests were performed in order to determine experimentally the location and the magnitude of the maximum occurring formwork wall pressure during base-casting. The wall pressure measurements were finally compared with the computed wall pressures from the numerical flow simulations of these filling tests, which will be presented in detail in chapter 6.

5.1.2 First series of base-filling tests

5.1.2.1 General layout

This section describes the configuration of the four full-scale formwork base-filling tests [5.1]. During these base-filling tests, two columns and two walls without steel reinforcements were cast. The layout of the formworks is shown in Fig. 5-1, with centrally the two walls and at the right side the two columns.

The dimensions of the two columns are identical. The columns have a height of 2 m, a depth of 21 cm and a width of 17.4 cm. The SCC is pumped from the base of the formwork. The two walls have also identical dimensions (a height of 2 m, a length of 4 m and a thickness of 21 cm) but the position of the SCC inlet is different for the two walls. A Schwing concrete piston pump of type P 2023 is used for pumping the SCC inside the formworks.

Fig. 5-1: Layout of the four formwork base-filling tests.

In order to seal off the formworks when uncoupling the concrete supply ducts, a mechanical shut-off valve has been designed at the LfH and the MLCR of Ghent University. The three individual formwork configurations are shown schematically in Fig. 5-3. Due to handling requirements (connection and disconnection of the inlet duct, closing of the shut-off valve), the inlet of these formworks needed to be positioned at a certain limited height above the base. The position of the inlet above floor level (centre position) was 0.27 m for column type A, 0.285 m for column type B, 0.275 m for wall type A and 0.175 m for wall type B.

5.1.2.2 Measurements set-up

While the formworks were filled, the SCC discharge rate was measured at the concrete pump. The column formworks were filled at a rate of 5 l/s (casting rate = 490 m/h), while the formworks of the walls were filled at a rate of 6 l/s (casting rate = 25 m/h). The time of each filling process was recorded and the progression was monitored with several cameras.

The formwork pressure was also measured at several positions at the base of the formwork, where the maximum pressure on the formwork walls was expected.

Two types of pressure measurement devices were selected: manometers and electronic pressure transducers. The manometers were fixed on an intermediate water chamber, sealed with a rubber membrane, and flush mounted on the formwork.

The electronic pressure transducers were flush mounted on the formworks, without the intermediate water chamber configuration.

Fig. 5-2 shows the simple design of the pressure measurement system with the intermediate water chamber, as well as the hydraulic testing equipment, which was used for the calibration of these pressure measurement units.

The locations of the pressure measurements (red cross hared squares) for the walls and for the columns are shown on Fig. 5-3. The heights above the base of the formwork at which these measurements were mounted on the walls are summarized in Table 5-1.

The choice for these particular measurement positions was made due to practical implementation and accessibility requirements.

Fig. 5-2: Pressure measurement system.

Table 5-1: Positioning of the pressure measurement systems.

Formwork	Type	Location	Height [m]
Column A	Manometer + water chamber	Above the inlet	0.385
Column B	Manometer + water chamber	Above the inlet	0.385
Wall A	Electronic pressure sensor	Above the inlet (position 1)	0.4
	Manometer + water chamber	Position 2	0.41
	Manometer + water chamber	Position 3	0.41
	Electronic pressure sensor	Position 4	0.08
Wall B	Manometer + water chamber	Above the inlet (position 1)	0.35
	Manometer + water chamber	Position 2	0.12
	Manometer + water chamber	Position 3	0.08

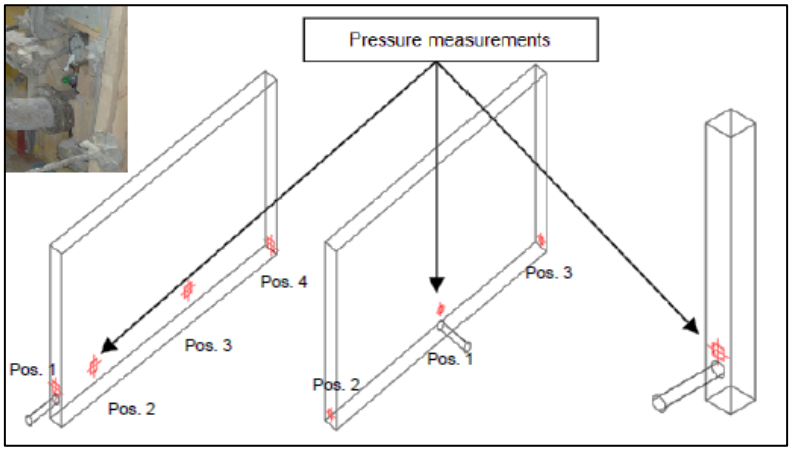

Fig. 5-3: Connections of the SCC inlet for the walls and for the columns.

At three different moments during the filling processes, a sample of concrete has been taken in order to investigate the fresh properties, by means of a Tattersall Mk-II rheometer and standard tests on SCC like slump flow, V-funnel, L-box, sieve stability and air content.

Detailed information about the configuration of the Tattersall Mk-II rheometer and its use has been presented in chapter 3, whereas a very complete description of the standard tests on SCC and their interpretation is given in [5.2-5.4].

A ready-mix company supplied the SCC mixture which was used in the filling processes. Table 5-2 lists the type and amount of ingredients that were used in the concrete mix:

Table 5-2: SCC mixture design per m³.

Ingredient	Comments	Quantity	Units
Sand 0/4	Grain size between 0 mm and 4 mm	805	kg/m³
Limestone aggregates 2/7	Aggregate size between 2 mm and 7 mm	450	kg/m³
Limestone aggregates 7/14	Aggregate size between 7 mm and 14 mm	265	kg/m³
Cement type C I 52.5 N	Portland cement	100	kg/m³
Cement type C III/A 42.5 LA	Blast furnace cement - Low Alkaline	265	kg/m³
Calcitec	Limestone filler	235	kg/m³
Rheomatrix	Viscosity modifying Agent (VMA)	0.5	kg/m³
Glenium 27	Polycarboxylether (PCE) type superplasticiser	7.2	l/m³
Water	-	193	l/m³

Although the SCC mixture design required a grading curve with a maximum aggregate size of 14 mm, it is still possible to have some aggregates with a larger size in the delivered SCC. Indeed after inspection, a limited number of aggregates with a maximum size of 20 mm have been observed (see also section 5.1.5.1). The water-to-cement ratio, *W*/*C*, is 0.53 and the water-to-powder ratio, *W*/*P*, is 0.32. The standard concrete tests and the rheometer measurements were performed on the chosen SCC mixture at three different moments during the filling tests:

- When the concrete mixing truck arrived at the MLCR, before the start of the first filling test - at time t = 0 min - SCC sample n° 1;
- After filling the first wall formwork (wall type A) - at time t = 16 min - SCC sample n° 2;
- After filling the last column formwork (column type B) - at time t = 47 min - SCC sample n° 3.

The results from the standard concrete tests, which are reported in appendix B, indicate that the delivered SCC mixture was very fluid. The performed rheological measurements also confirmed this observation. The SCC from sample n° 2 was taken from the top of wall type A. This second sample consisted mainly of cement paste with a small amount of aggregates, indicating the occurrence of segregation during the filling process.

The measurement results of the first and the last sample revealed that the rheology of the delivered SCC remained rather constant during the whole casting period. The Herschel-Bulkley model parameters, derived from the measurements performed with the Tattersall Mk-II rheometer, are also summarized in appendix B.

5.1.3 Second series of base-filling tests

5.1.3.1 Motivation

In order to further expand our knowledge and experience on the base-filling process with SCC, a second series of base-filling tests were performed.

The global objectives for these new formwork filling tests were:

- To test other pressure measurement devices;
- To study the influence of the rheology and more especially the apparent viscosity of the SCC on the formwork pressures;
- To study the influence of the casting rate on the formwork pressures;
- To study the influence of the presence of steel rebars on the formwork pressures
- To study segregation of the SCC while pumping bottom-up;
- To consolidate the theory on formwork pressure development presented in chapter 3 and reported in [5.5, 5.6];
- To fine tune the numerical models for these formwork filling processes (see chapter 6).

5.1.3.2 General layout

This section describes the configuration of five full-scale formwork base-filling tests without rebars. During these tests, four columns and one large I-beam were cast.

The layout of the formwork filling tests is shown in Fig. 5-4.

The filling tests were performed for practical reasons on two separate days, with an interval of one week between them.

Fig. 5-4: Layout of the base-filling tests of the columns and the I-beam.

Table 5-3 shows the casting conditions for these filling tests without rebars.

As already mentioned in the motivation, the influence of several casting parameters on the base filling process with SCC were studied.

Two powder type SCC mixtures were specifically designed for these filling tests with quite different rheological properties. The details of the two mixtures are presented a little further in this section, whereas the rheological properties of these SCC mixtures are summarized in appendix B.

During the second series of base-filling tests, also four column formworks with rebars were cast. This resulted in a total of eight cast columns, which were numbered sequentially for identification purposes. The odd numbers were given to the columns without rebars, while the even numbers were attributed to the columns with rebars.

The base-filling tests of the four columns with rebars are presented in section 5.2.

Table 5-3: Casting conditions for the formwork filling tests.

Day one	**Low viscosity SCC**	
Element	**Discharge rate [l/s]**	**Casting speed [m/h]**
I-beam	0.437 0.283 0.230 0.108	Four casting speeds (see Fig. 16-7)
Column 1	1.435	57 (low)
Column 3	2.794	110 (high)
Day two	**High viscosity SCC**	
Element	**Discharge rate [l/s]**	**Casting speed [m/h]**
Column 5	1.402	55 (low)
Column 7	2.614	103 (high)

The dimensions of the four columns are identical. The columns were 4 m high, with a depth and a width of 0.3 m. The inlet of the columns were positioned at 0.6 m above the ground. This inlet position was selected in order to easily mount the pressure measurement devices located at the base of the columns, and also to be able to put a basket underneath the inlet to collect the SCC when disconnecting the supply duct.

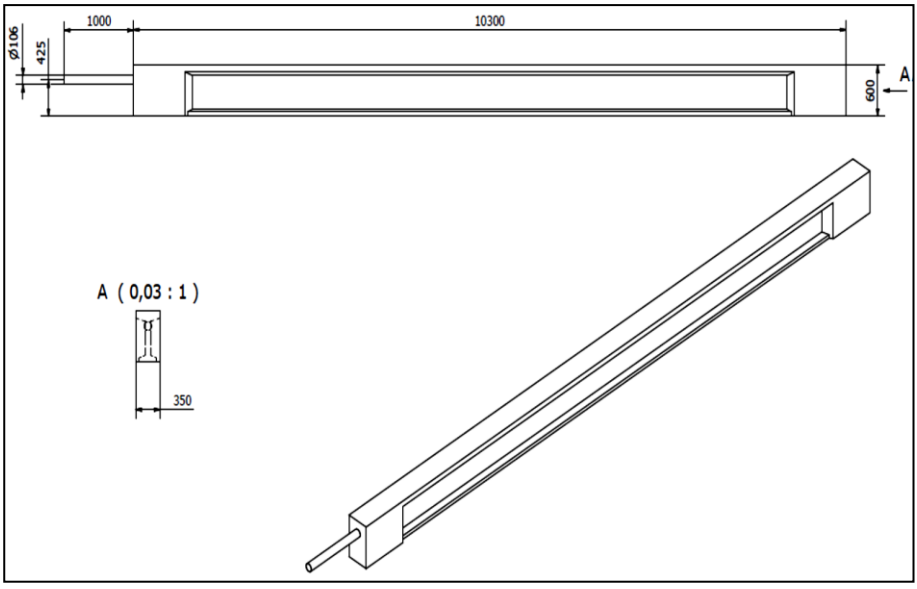

Fig. 5-5: Geometry of the I-beam.

The formwork of the I-beam was 10.3 m long, with a height of 0.6 m and a width of 0.35 m. The I-beam was cast without steel rebars or pre-stressing tendons. The inlet was positioned at 0.425 m above the floor of the formwork for the same practical reasons. Fig. 5-5 shows the geometry of the I-beam.

A Putzmeister concrete piston pump of type P 715 TD was used during the second series of base-filling tests for pumping the SCC inside the nine formworks. For the second series of filling tests, a mechanical shut-off valve was designed at the MLCR, as shown in Fig. 5-6, with the specific design requirements of being compact and easy to manipulate.

Fig. 5-6: Geometry of the shut-off valve and connection of the supply duct.

5.1.3.3 Measurements set-up

While the formworks were filled, the SCC discharge rate was measured at the concrete pump. The measured discharge rate was also cross-checked by dividing the total volume of the formwork by the time needed to fill the cast.

Table 5-3 summarizes the discharge rates as well as the resulting casting rates for the columns without rebars and the I-beam.

For the filling of the I-beam, the discharge rate was lowered four times during the filling process (see Fig. 5-7). This was done in order to avoid the concrete from flowing over the top edge of the first part of the formwork, immediately after the inlet (see also chapter 6). The casting process of the I-beam was monitored with several cameras.

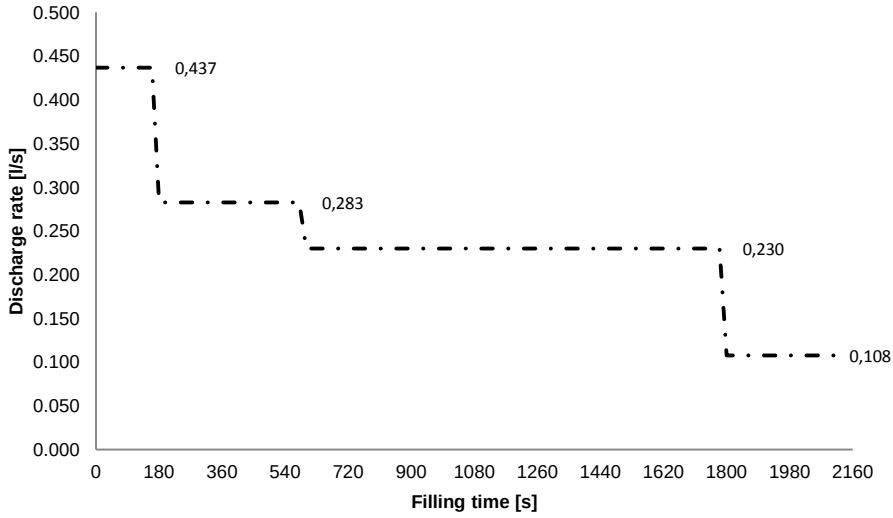

Fig. 5-7: Evolution of the discharge rate during the filling of the I-beam.

The evolution of the formwork pressure during the filling of the columns was also recorded at three different positions: at the base of the formwork, at 1 m from the base and at 2 m from the base. Fig. 5-8 shows the locations of the pressure measurements for the columns.

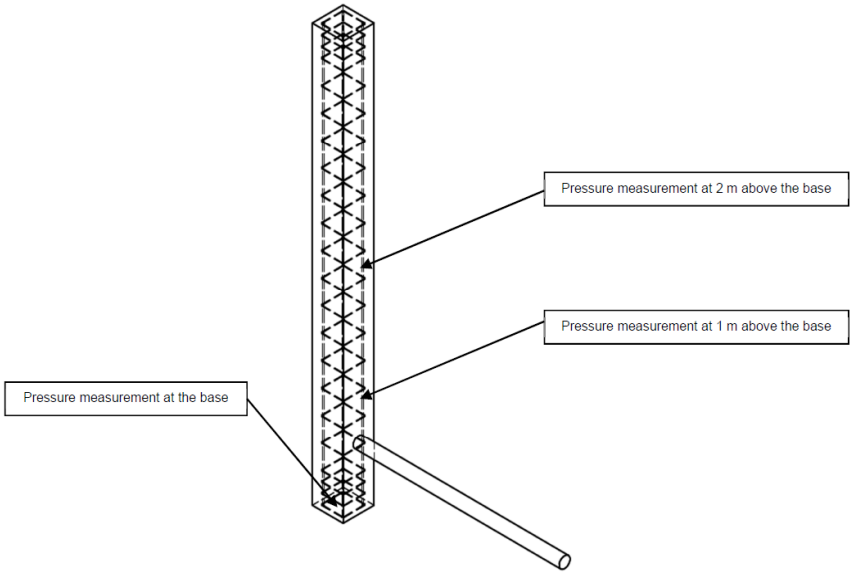

Fig. 5-8: Pressure measurement locations of the columns.

During the casting of the I-beam no formwork pressures were measured. Instead, the evolution of the concrete surface during the filling process was monitored at five different stations along the length of the I-beam, which is shown in Fig. 5-9.

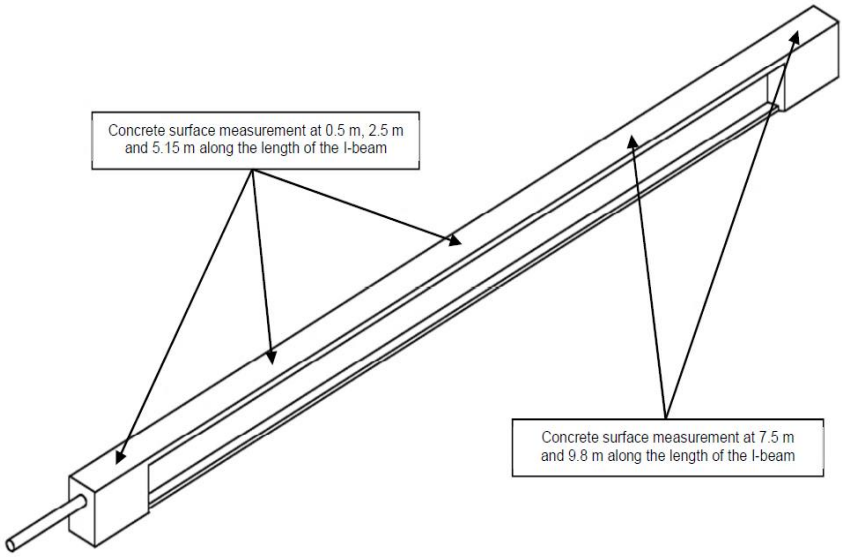

Fig. 5-9: Concrete surface monitoring stations along the I-beam.

Fig. 5-10 and Fig. 5-11 show the two types of electronic pressure sensors that were used for measuring and monitoring the formwork wall pressures during the column casting processes.

Fig. 5-10: Electronic pressure sensor type 1 [5.7].

Fig. 5-11: Electronic pressure sensor type 2 [5.7].

These pressure sensors were provided by the Belgian Building Research Institute (BBRI), which used them in their previous research program [5.7]. The pressure sensors were also calibrated with the hydraulic calibration unit, shown in Fig. 5-2. The pressure sensors of type 1 were mounted at the base of the columns, whereas the pressure sensors of type 2 were flush mounted on the walls of the formworks at 1 m and 2 m above the base (see Fig. 5-8).

As already mentioned, the formwork filling tests were performed with two SCC mixtures (see Table 5-3) on two separate days. A ready-mix company supplied both SCC mixtures. A low viscosity SCC was used for the filling tests on the first day, while a high viscosity SCC was used for the casting tests on the second day. Table 5-4 lists the selected types and the amounts of the ingredients of both SCC mixture designs.

Table 5-4: SCC mixture designs per m^3.

Low viscosity SCC mix			
Ingredient	**Comments**	**Quantity**	**Units**
Sand 0/5	Grain size between 0 mm and 5 mm	848	kg/m^3
Limestone aggregates 2/6.3	Aggregate size between 2 mm and 6.3 mm	695	kg/m^3
Cement type C III/A 42.5 LA	Blast furnace cement – Low Alkaline	360	kg/m^3
Calcitec	Limestone filler	240	kg/m^3
Glenium 27	Polycarboxylether (PCE) type super plasticiser	6.75	l/m^3
Water	-	190	l/m^3
W/C = 0.53 - W/P = 0.32			

High viscosity SCC mix			
Sand 0/5	Grain size between 0 mm and 5 mm	895	kg/m^3
Limestone aggregates 2/6.3	Aggregate size between 2 mm and 6.3 mm	725	kg/m^3
Cement type C III/A 42.5 LA	Blast furnace cement – Low Alkaline	300	kg/m^3
Calcitec	Limestone filler	300	kg/m^3
Glenium 27	Polycarboxylether (PCE) type super plasticiser	10.45	l/m^3
Water	-	160	l/m^3
W/C = 0.53 - W/P = 0.27			

The rheology of both SCC mixtures was measured with a BML Contec-Viscometer 5. The standard fresh SCC tests (slump flow, V-funnel, L-box, sieve stability, air content) and the rheometer measurements were performed with the low viscosity SCC mixture at three different moments during the filling tests of the first day:

- When the concrete mixing truck arrived at the MLCR, just before the filling of the I-beam - at time t = 0 min - SCC sample n° 1;
- Right after the filling of the I-beam and before the filling of the first column - at time t = 38 min - SCC sample n° 2;
- Immediately after the filling of the last column formwork - at time t = 82 min - SCC sample n° 3.

On the second testing day, the fresh concrete tests and rheometer measurements were performed with the high viscosity SCC mixture at the beginning (at time t = 0 min - SCC sample n° 4) and at the end (at time t = 35 min - SCC sample n° 5) of the filling tests.

The fresh SCC test results show that the selected SCC mixture designs are in accordance with the recommendations stated in [5.2], [5.3] and [5.8] for obtaining a good quality low and a high viscosity SCC. A visual inspection of the resulting homogeneity of the two SCC mixtures after the filling processes has been performed on a series of drilled samples of the cast columns. The visual inspection results also confirm the obtained high quality. The standard concrete test results, the rheometer measurements and the visual inspection results are reported in appendix B. The Herschel-Bulkley parameters were extracted from the rheometer measurements.

5.1.4 Measurement results

5.1.4.1 First series of base-filling tests

Because in our experiments the SCC was pumped from the base of the formworks up to the top, it was constantly in motion during the filling process. The time needed to fill each of the formworks was very short, around 16 s for both columns and around 280 s for both walls.

According to Roussel [5.9] and Billberg [5.10], the characteristic time to build up a thixotropic structure in most SCC mixes is about 280 s and higher. This motivates our belief that a possible reduction of the formwork wall pressure due to thixotropy (see also chapter 2) could be disregarded during the filling tests performed in this study.

Without the presence of a thixotropic structural build-up and the related wall pressure reduction, the formwork wall pressures are expected to be higher than hydrostatic due to the occurring viscous flow losses, according to the analytical model presented in chapter 3 (see Eq. (3.35)).

The wall pressure during the base-filling of the two walls has been measured at several positions close to the base of the formworks, as shown in Fig. 5-3.

The following graphs show the measured wall pressures at these locations.

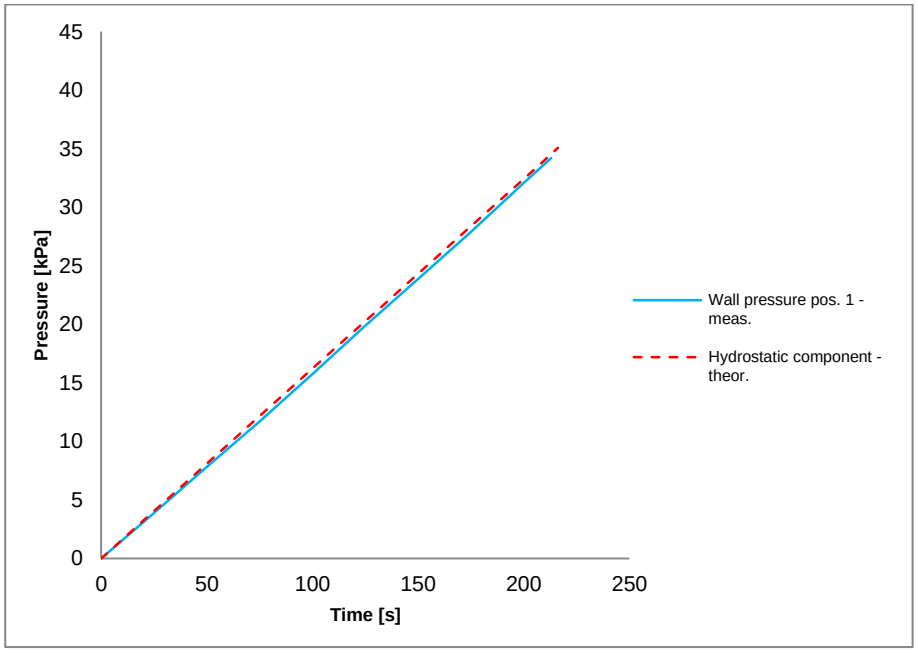

Fig. 5-12: Wall pressure at the electronic sensor above the inlet of wall type A - position 1.

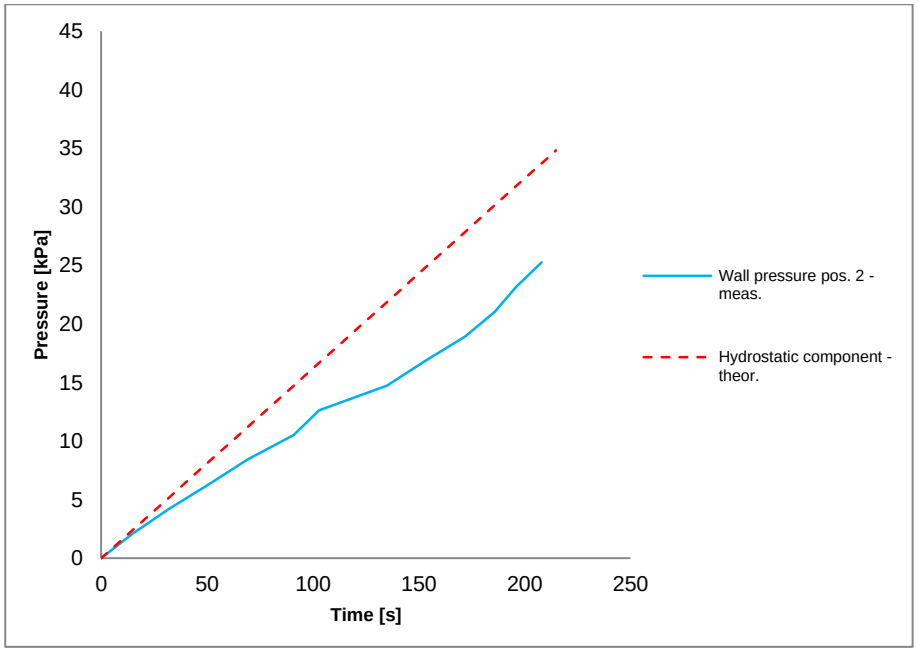

Fig. 5-13: Wall pressure at the manometer of wall type A - position 2.

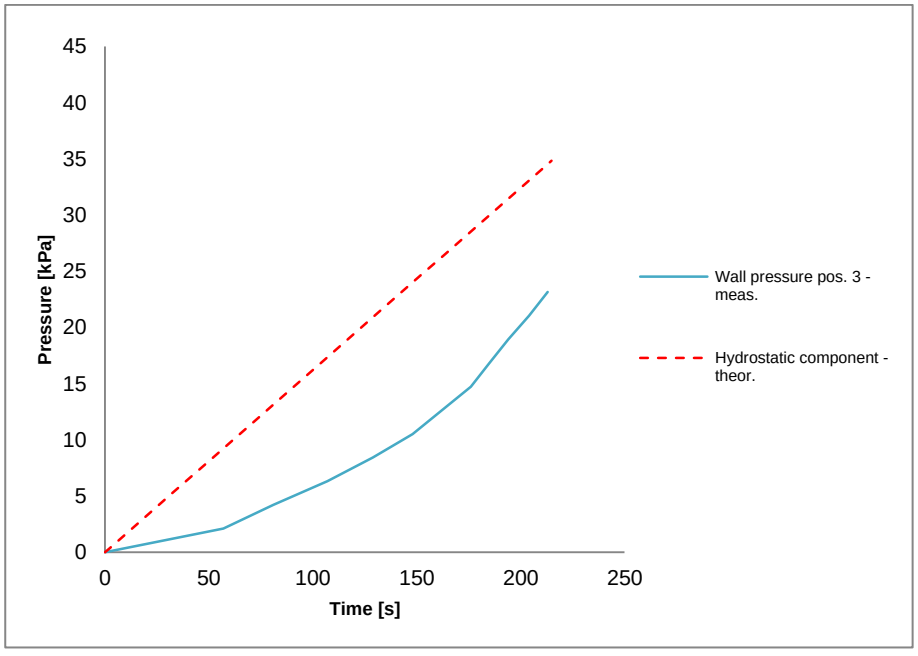

Fig. 5-14: Wall pressure at the manometer of wall type A - position 3.

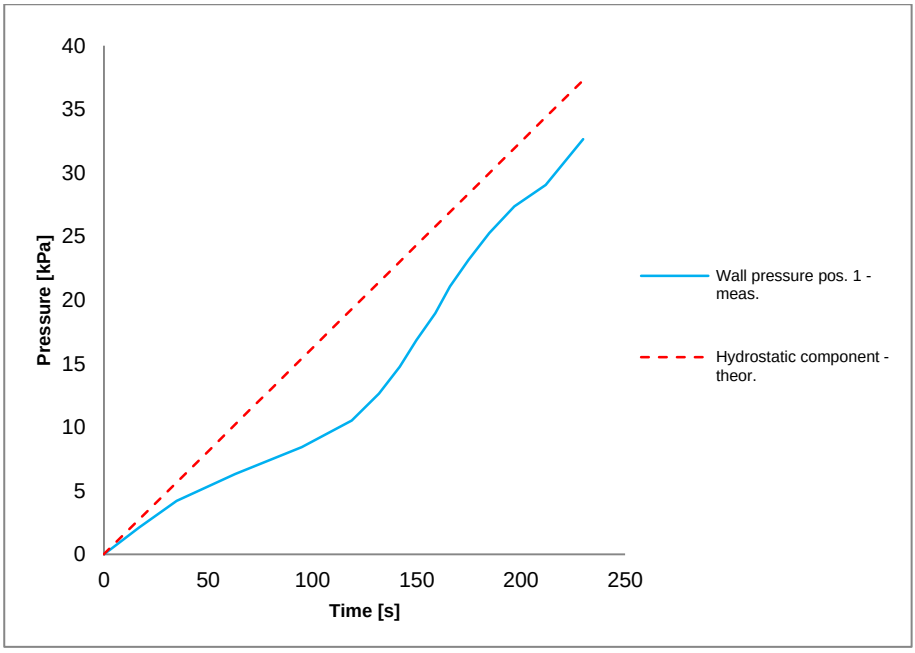

Fig. 5-15: Wall pressure at the manometer above the inlet of wall type B - position 1.

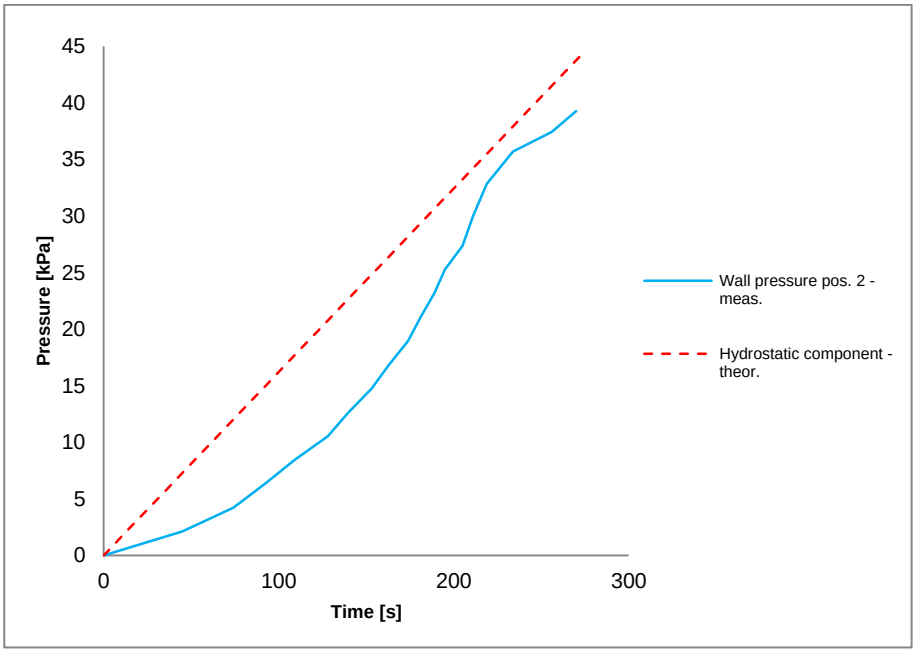

Fig. 5-16: Wall pressure at the manometer of wall type B - position 2.

The type of the pressure measurement devices used during the filling of two walls is listed in Table 5-1.

During the first series of formwork base-filling tests, some of the mounted pressure measurement devices were damaged by the coarse aggregates of the SCC right from the start of the experiment. This was the case for the electronic pressure sensor mounted at position 4 of wall type A, and the manometer with the intermediate water chamber mounted at position 3 of wall type B. For these two positions no wall pressures could be recorded.

Due to practical difficulties, it was not possible to stop the filling process of the two walls exactly at a height of 2 m. Therefore the resulting height was 1.955 m for wall type A and 2.061 m for wall type B.

As can be observed from Fig. 5-12, the wall pressure measured by the electronic pressure sensor at position 1 of wall type A is hydrostatic all the way during the filling process. The occurring viscous flow losses are very small due to the relatively low filling velocity (6 l/s or 0.006 m^3/s divided by 0.84 m^2 equals 0.00714 m/s).

According to Eq. (3.35), the wall pressure at position 1 is therefore hydrostatic. This is also confirmed by the simulations, as will be also shown in chapter 6. On the other hand, the wall pressures at the measurement positions 2 and 3 of wall type A are lower than the expected hydrostatic pressure level.

For wall type B, Fig. 5-15 and Fig. 5-16 also both reveal a wall pressure at the measurement positions which is lower than the hydrostatic pressure, although the difference between the expected hydrostatic wall pressure and the measured wall pressure is smaller than the wall pressure difference observed at position 2 and 3 of wall type A.

So the following question arises: in reality, are the occurring wall pressures at these locations really lower than the hydrostatic pressure or is this a measuring artefact? An answer to this question will be formulated in section 5.1.5.1.

Due to a much higher filling velocity (5 l/s or 0.005 m^3/s divided by 0.03654 m^2 equals 0.137 m/s) for the columns, the expected wall pressures should be higher than the hydrostatic pressure, because the hydraulic losses in these filling cases would be much higher than during the filling of the two walls.

Fig. 5-17 and Fig. 5-18 show the measured wall pressure evolution just above the inlet of the two columns. The wall pressures above the inlet were also measured with a manometer - intermediate water chamber device for both columns. As for the walls, it was also not possible to fill the two formworks of the columns exactly up to a height of 2 m. Therefore the resulting height was 2.012 m for column type A and 2.225 m for column type B.

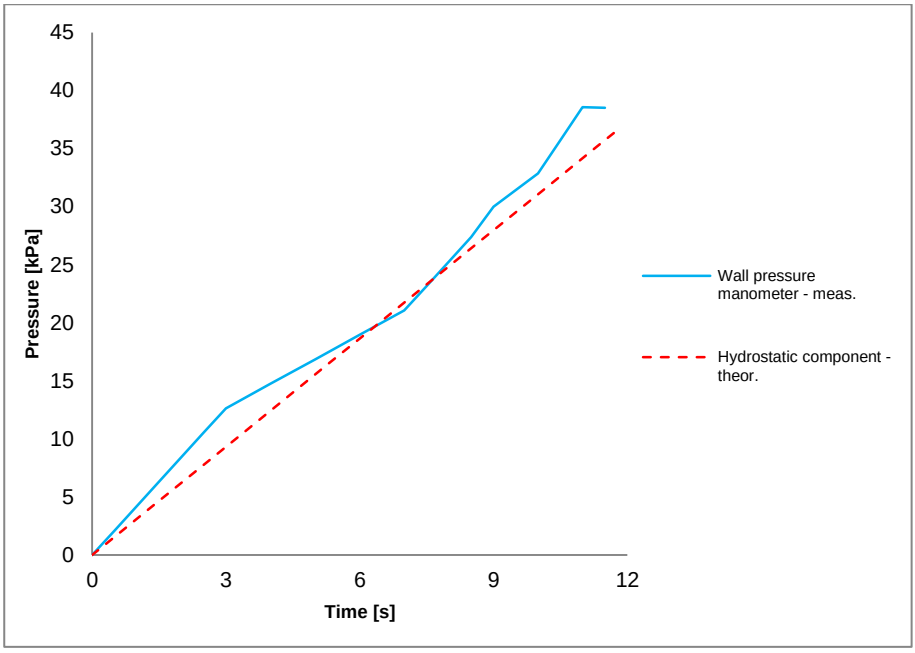

Fig. 5-17: Wall pressure above the inlet at the manometer of column type A.

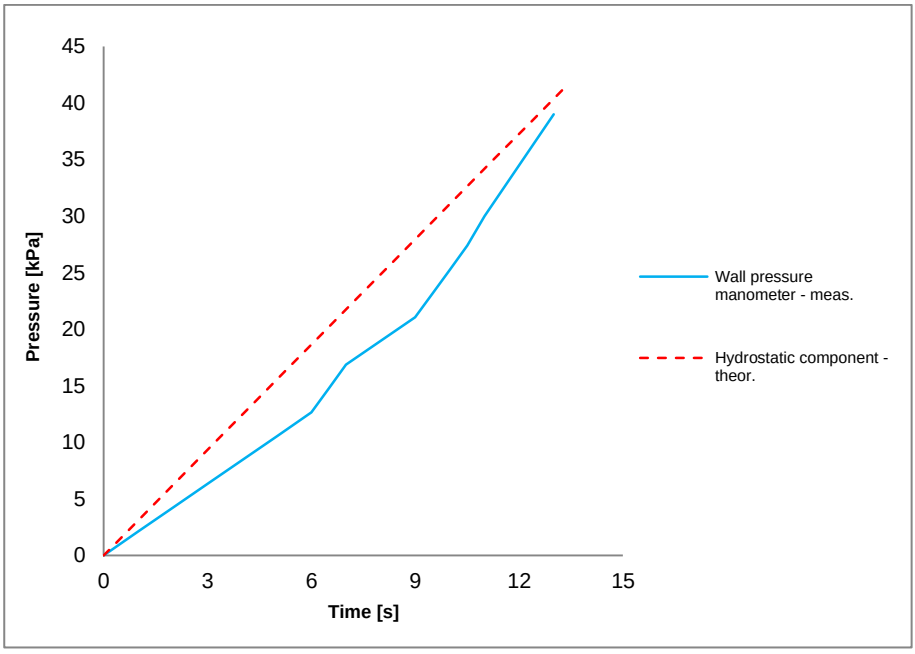

Fig. 5-18: Wall pressure above the inlet at the manometer of column type B.

When looking at the measured wall pressure evolution of column type A, we notice that the measured wall pressure above the inlet is indeed higher than the hydrostatic pressure. These measurements are consistent with the simulated wall pressures at the same measuring location, as will be shown in chapter 6.

On the other hand, the wall pressure recorded just above the inlet of column type B is lower than the hydrostatic pressure at the same location. So which measurement is telling us the real truth? More reflections about these observations in section 5.1.5.1.

5.1.4.2 Second series of base-filling tests

5.1.4.2.1 Wall pressure measurements

During these base-filling tests the wall pressure of the columns were measured at three positions along the height, as shown in Fig. 5-8.

The following graphs present the measured wall pressures and the related hydrostatic pressure at these locations.

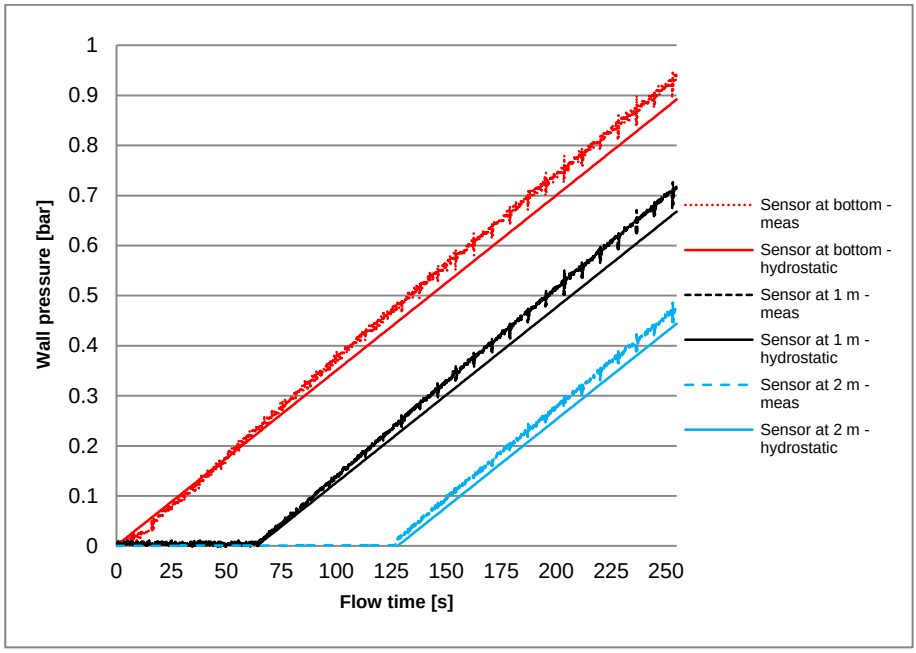

Fig. 5-19: Wall pressure of column 1 - no rebars - low viscosity SCC - low casting speed.

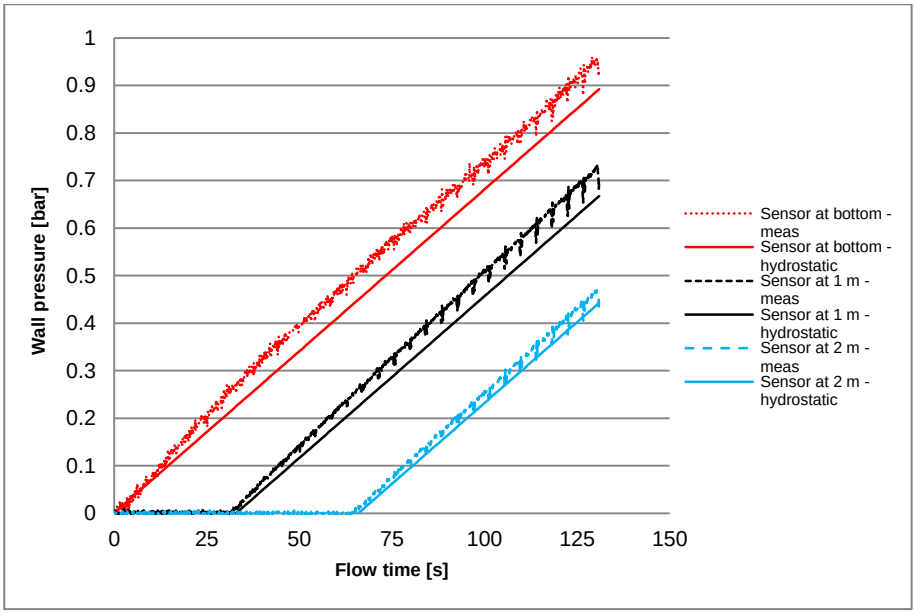

Fig. 5-20: Wall pressure of column 3 - no rebars - low viscosity SCC - high casting speed.

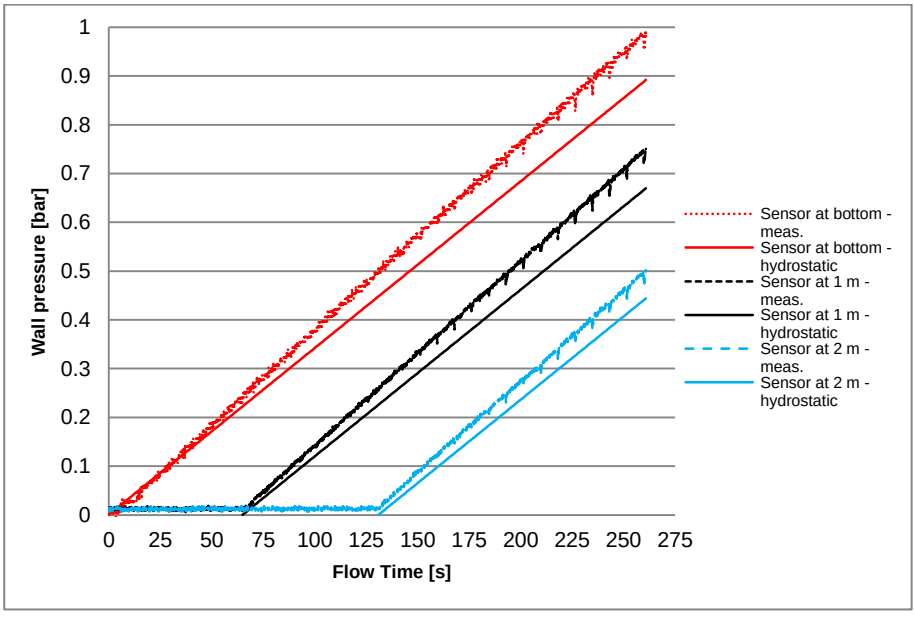

Fig. 5-21: Wall pressure of column 5 - no rebars - high viscosity SCC - low casting speed.

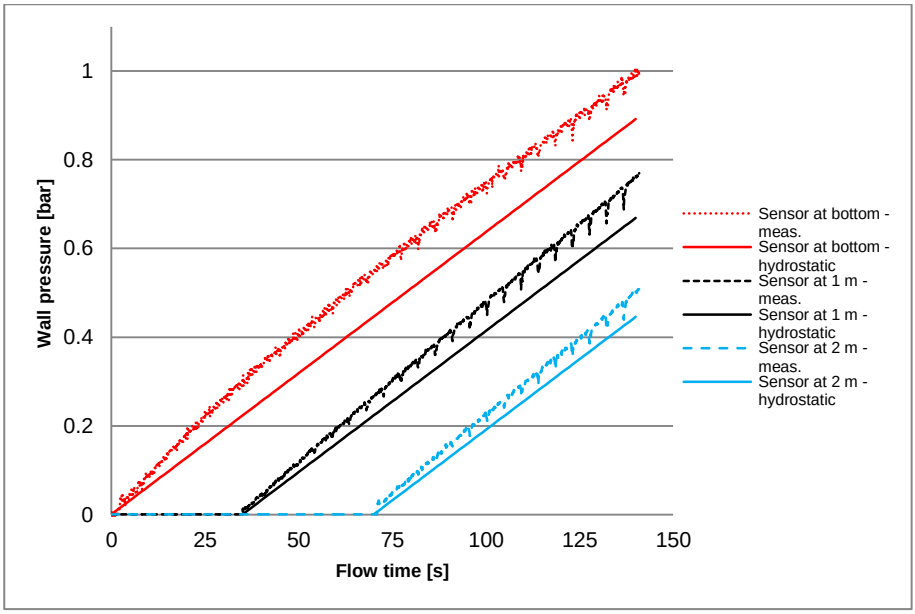

Fig. 5-22: Wall pressure of column 7 - no rebars - high viscosity SCC - high casting speed.

The pressure sensors mounted at the bottom of some of the columns show a slightly less linear curve than the other pressure sensors mounted at the walls of the columns. As mentioned in the research study of Cauberg et al. [5.7], these type of pressure sensors did not always measure correctly. Unfortunately, these were the only pressure sensors of the available set which could be mounted at the base of the columns. The other types could only be flush mounted at walls.

The presented graphs clearly show the impact of the shear flow losses on the resulting formwork wall pressures. The shear flow losses may certainly not be neglected regarding the maximum formwork wall pressures when the base-filling technique is used for casting.

5.1.4.2.2 Concrete surface measurements during the casting of the I-beam

As mentioned in section 5.1.3.3, the evolution of the concrete surface during the filling of the I-beam was measured at five different positions along the length of the I-beam, which are shown in Fig. 5-9. These free surface measurement results will be presented in chapter 6 and compared with the simulated concrete surface evolution.

5.1.4.2.3 Cast quality

As equally mentioned in section 5.1.3.3, a visual inspection has been performed on drilled samples taken at five equidistant locations along the height of the cast columns. The results from the visual inspection will be presented in section 5.2.3.2.

5.1.5 Discussion about the measured wall pressures

5.1.5.1 First series of base-filling tests

When analysing the measurements performed with the electronic pressure sensors and the manometer - intermediate water chamber units carefully, we can summarize the following observations:

- The electronic pressure sensor presents a linearly varying wall pressure with time, whereas the measurements done with the manometer - intermediate water chamber units lead to a non-linear evolution of the wall pressure.
- The wall pressure measured by the electronic pressure sensor above the inlet of wall type A and the manometer - intermediate water chamber unit above the inlet of column type A is in agreement with the theory derived in chapter 3.
- The other wall pressure measurements, also performed with the manometer - intermediate water chamber units, are lower than the hydrostatic pressure which is related to concrete height being cast in the formwork. These measurements are not in agreement with the theory derived in chapter 3.
- The measured wall pressure of the columns are higher than the measured wall pressure of the walls, although the hydrostatic pressure is the same for all casts.

Although the thixotropic parameters of Eq. (2.21) and Eq. (2.22) have not been determined through separate rheometer tests, as proposed by Roussel [5.9], we believe that, motivated by the statements made earlier in chapter 3 and section 5.1.4.1, thixotropy cannot be important durent our base-filling tests, and therefore thixotropy is not an explanation for the discrepancy between theory/simulation (see also chapter 6) and some of the measured wall pressures. Thixotropy could not have influenced the formwork pressure, because of the relatively short filling times and the SCC being constantly sheared during the whole filling process (certainly for the two columns, maybe less pronounced for the two walls).

However, the non-linear evolution of the measured formwork pressures of the walls can be related to the experienced shortcomings of the manometer - intermediate water chamber units used in the filling tests. The calibration of these pressure measurement units turned out to be difficult, due to the non-linear deformation of the plastic membranes when submitted to the concrete pressure, the variable surface tension of the chosen rubber membranes and the unavoidable inclusion of air bubbles into the water chambers. After the SCC had hardened and the formwork walls were removed, we observed that the granulates of the SCC were completely blocking the rubber membrane of the pressure measurement units of the two walls. The diameter of the circular measuring surface with the rubber membrane was 20 mm. Although the nominal maximum size of the granulates was 14 mm, some of them did have a diameter of about the same size as the pressure measurement opening (see also section 5.1.2.2). This blocking would surely result into lower wall pressures being measured during the formwork filling tests. We therefore carefully attribute the mere existence of the observed discrepancy between theory/numerical simulations and some of the measured wall pressures to a measuring artefact.

Further optimization of the design of the manometer - intermediate water chamber units is necessary in order to avoid the previously mentioned shortcomings. Although the present design of the manometer - intermediate water chamber units was simple and the costs for manufacturing these units were very low compared to the price of the electronic pressure sensors, it turned out that measuring the wall pressure with an electronic sensor is more accurate and more practical. It is also much more convenient to capture the measurement data electronically, instead of having to use camera's and stop watches to monitor the evolution of the manometers. This explains our motivation for the use of electronic pressure sensors during the second series of formwork base-filling tests.

The theory derived in chapter 3 reveals that the viscous flow losses add up to the hydrostatic pressure, thus further increasing the formwork pressure. This has been confirmed through some of the pressure measurements. Although the hydrostatic pressure is the same for all the cast structural elements because of equal height, the formwork pressure at the base of the columns is higher than for the walls. This is because the cross-section of the walls is much larger than the cross-section of the columns, and therefore the filling velocity and the resulting hydraulic losses in the columns are much higher than the filling velocity and the related hydraulic losses in the walls.

On the other hand, Feys [5.2] and Le [5.11] have clearly demonstrated that when pumping SCC through ducts, the hydraulic losses can be much lower than expected, due to the presence of a thin cement paste layer near the walls with a much lower viscosity than the concrete bulk viscosity. The effect of the thin paste layer near walls on the occurring hydraulic losses can be expected to become more important when the sum of the confining surfaces (formwork and rebars) is high for a given formwork volume. Thus, for accurately determining the hydraulic losses in ducts while pumping SCC to the formworks [5.2], a correct implementation of the no-slip condition applied to the thin cement paste layer near the walls becomes essential. More about this matter is presented in chapter 6.

In these first series of filling tests, the influence of the thin paste layer near walls is much less pronounced because of the relatively large cross-sections (certainly for the walls) and of the absence of rebars. However, further research is certainly needed in order to determine when a correct numerical implementation of the interaction between the thin cement paste layer and the walls, but also the interaction between the cement paste layer and the remaining concrete, becomes necessary. An attempt has been made in the second series of base-filling tests to further quantify the effect of the cement paste layer on the resulting viscous flow losses by including steel rebars and using different SCC mixtures. More about this subject in section 5.2.

5.1.5.2 Second series of base-filling tests

The following observations can be listed when analysing the measurements results of the second series of base-filling tests:

- Almost all the electronic pressure sensors measure a linearly varying wall pressure with time.
- During the filling processes of the columns, no decay of wall pressure due to thixotropy was measured. This is also fully consistent with our observations during the first series of base-filling experiments. Due to the high casting speeds and therefore very short filling times, there is little or no thixotropic structural build-up, which would reduce the wall pressure during the filling process.
- The measured wall pressures clearly reveal the impact of the viscous flow losses on the resulting formwork pressures during base-filling. These viscous flow losses truly add up to the hydrostatic pressure, as predicted by the analytical model presented in chapter 3.
- The higher the viscosity of the SCC, the higher the shear flow losses are for a specific casting speed.
- The higher the casting speed, the higher the shear flow losses are.

These observations are fully in line with the theory of basic hydraulics.

5.2 Formwork base-filling tests with rebars

5.2.1 Introduction

In the present chapter the influence of the presence of rebars on the formwork pressures during base-filling is evaluated. For this purpose we will focus on the columns with rebars which were cast during the second series of base-filling tests [5.6], already introduced in section 5.1.3.

During these base-filling tests, eight columns in total were cast, with two different types of SCC and at two different casting speeds, but only four of them were cast with steel rebars.

5.2.2 General layout and measuring set-up

The general layout of the base-filling tests of the columns with rebars is shown in Fig. 5-4. The dimensions (in mm) of the columns, as well as the layout of the rebar configuration, are shown in the following drawing.

As mentioned in section 5.1 and in the introduction, in total eight columns were cast during the second series of formwork filling tests. These casting tests were performed for practical reasons on two separate days, with an interval of one week between them. For identification purposes, they were sequentially numbered, and the even numbers were attributed to the four columns with rebars. Table 5-5 summarises the casting conditions for these columns.

For pumping the fresh SCC into the column formworks, a Putzmeister concrete piston pump of type P 715 TD was used and the discharge rates were measured at the concrete pump.

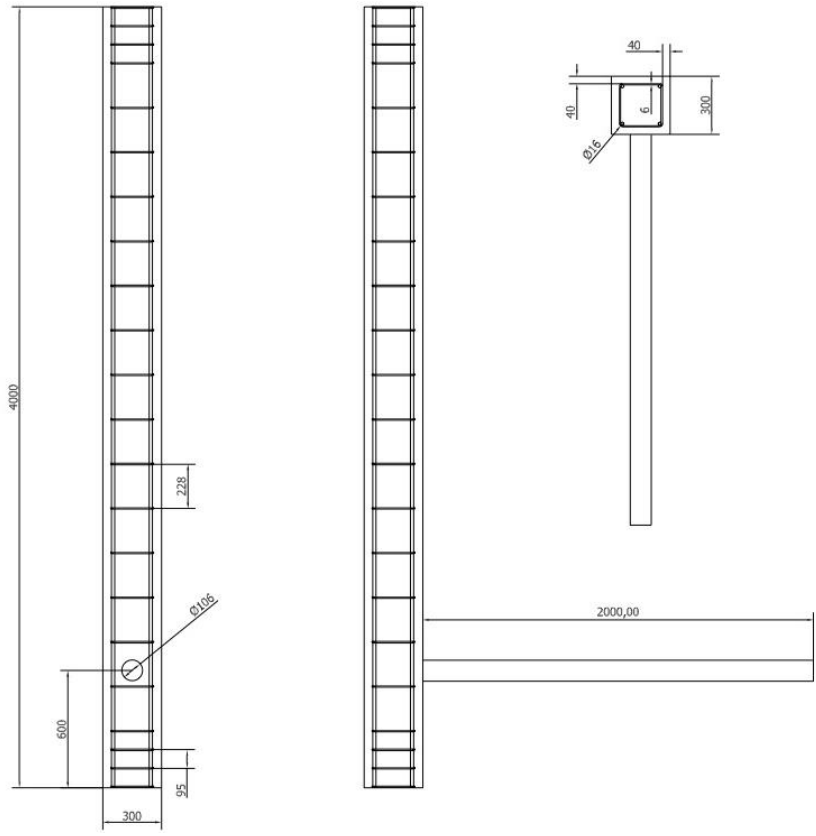

Fig. 5-23: Geometry and rebar configuration of the columns.

The details of the chosen SCC mixtures have already been presented in section 5.1 (see Table 5-4).

Table 5-5: Casting conditions for the formwork filling tests.

Day one	**Low viscosity SCC**	
Element	**Discharge rate [l/s]**	**Casting speed [m/h]**
Column 2	1.388	56 (low)
Column 4	2.632 (not completely filled)	108 (high) (not completely filled)
Day two	**High viscosity SCC**	
Element	**Discharge rate [l/s]**	**Casting speed [m/h]**
Column 6	1.313	54 (low)
Column 8	2.560	105 (high)

Standard concrete tests have been performed and the test results show that the selected SCC mixture designs are in accordance with the recommendations stated in [5.2, 5.3, 5.8] for obtaining a low and a high viscosity SCC of good quality. A visual inspection of the homogeneity of the two SCC mixtures in the hardened state has been performed on drilled samples of the cast columns. The results from this visual inspection are presented in the section 5.2.3.2, and they also confirm the obtained high quality.

The standard fresh concrete test results together with the rheometer measurements and the Herschel-Bulkley concrete model parameters are reported in appendix B.

The formwork pressures were measured at three different locations on the formwork during casting. The measuring layout is shown in Fig. 5-8. The two types of pressure sensors that were used are shown in Fig. 5-10 and Fig. 5-11 (type 1 at the bottom of the formwork and type 2 flush mounted at the front wall of formwork).

5.2.3 Measurement results

5.2.3.1 Pressure measurements

The following graphs show the measured wall pressure together with the related hydrostatic pressure at the bottom of the formwork, at 1 m from the base and at 2 m from the base.

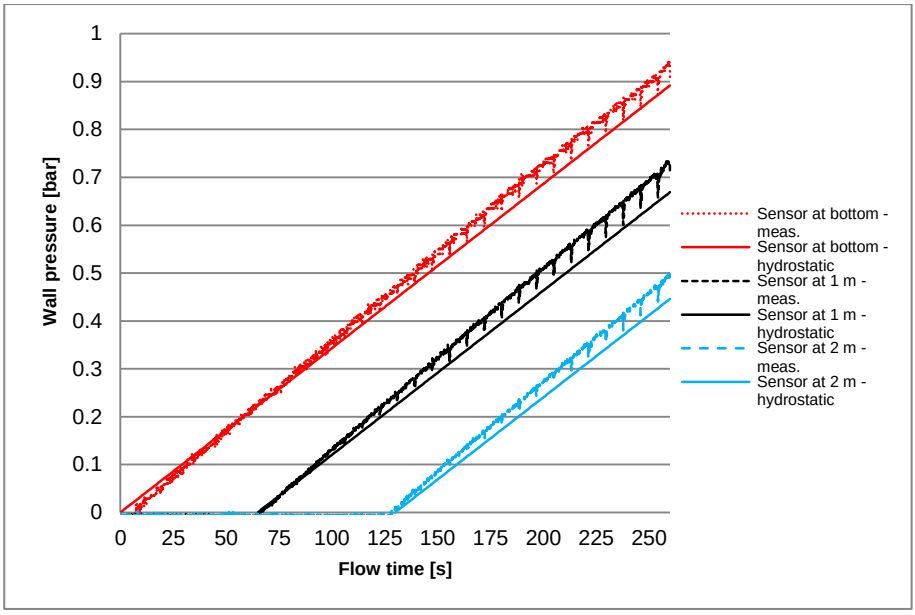

Fig. 5-24: Wall pressure of column 2 - with rebars - low viscosity SCC - low casting speed.

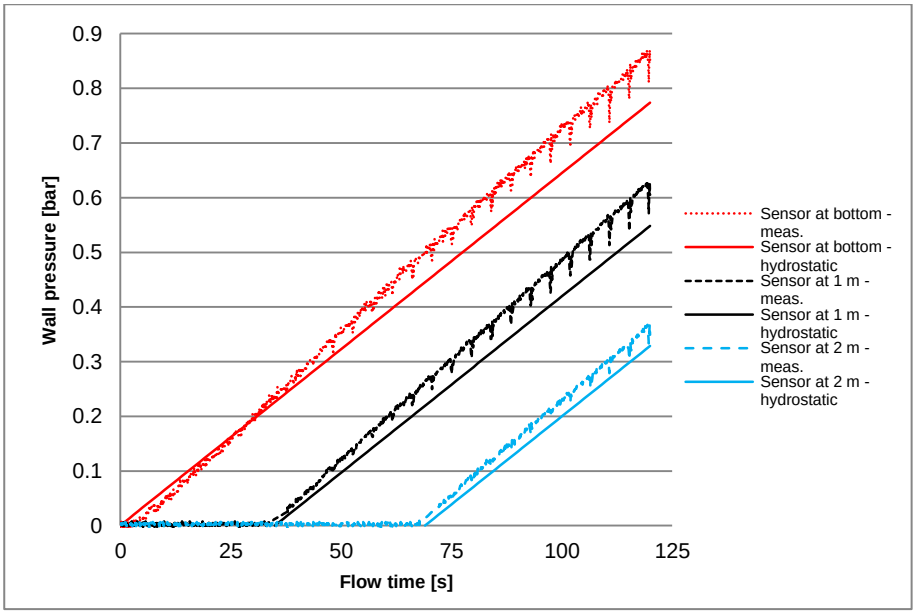

Fig. 5-25: Wall pressure of column 4 - with rebars - low viscosity SCC - high casting speed.

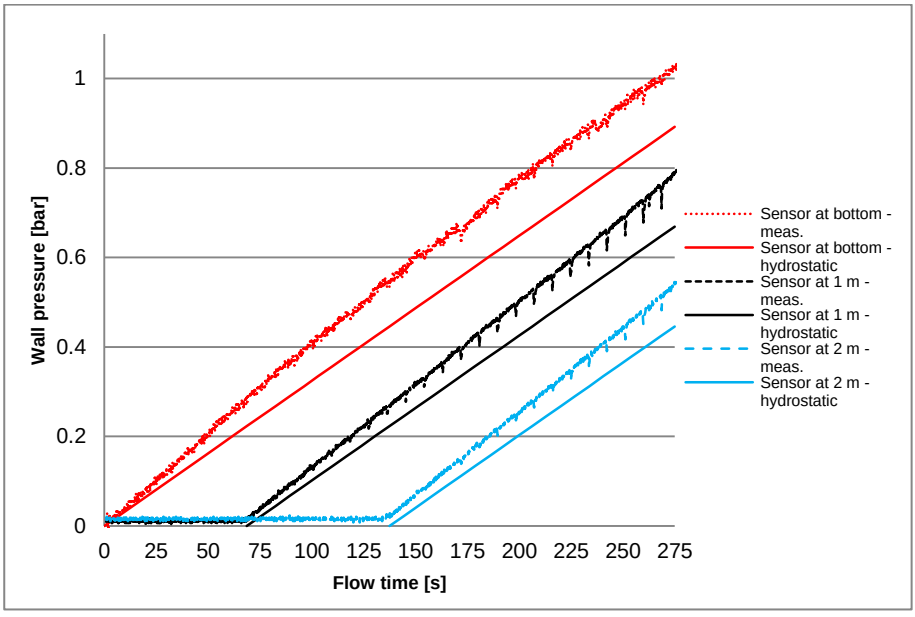

Fig. 5-26: Wall pressure of column 6 - with rebars - high viscosity SCC - low casting speed.

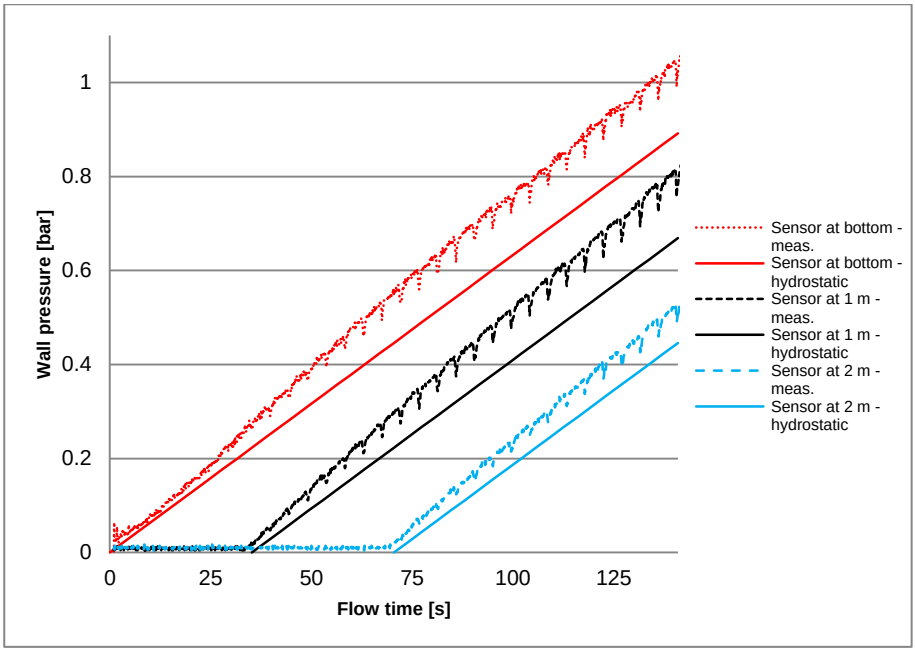

Fig. 5-27: Wall pressure of column 8 - with rebars - high viscosity SCC - high casting speed.

As already mentioned in section 5.1, the pressure sensors mounted at the bottom of some of the columns show a less linear curve than the other pressure sensors flush mounted at the walls of the columns. Cauberg et al. [5.7] mentioned in their research report that these type of pressure sensors did not always measure correctly.

Unfortunately, these were the only pressure sensors of the available set which could be mounted at the base of the columns, as the other sensor type could only be flush mounted at walls.

As for the base-filling experiments without rebars, which were presented in section 5.1, the presented graphs also clearly reveal the impact of the shear flow losses on the resulting formwork wall pressures. Besides the observations mentioned in section 5.1.5.2, it is clear that the presence of rebars reduces the flow cross-section, leading to higher flow losses as function of the casting speed.

Making a parallel with the work done by Amziane et al. [5.12], which highlights that when filling from the top, the rebars create new friction areas which reduce formwork pressure when the concrete is left at rest. In the present study, on the contrary, the rebars increase the pressure because the concrete is filled from the bottom and while flowing towards the top of the formwork the rebars create additional surfaces of viscous dissipation (or friction).

The shear flow losses represent 7 % (low viscosity SCC - low casting speed - without rebars) up to 16 % (high viscosity SCC - high casting speed - with rebars) of the total wall pressure for the performed filling tests with steel rebars. The shear flow losses may certainly not be neglected regarding the maximum formwork wall pressures when the base-filling technique is used for casting.

However, other researchers reported that the density of the fresh concrete increases during casting, because the air is pushed out due to the pumping pressure and the local pressure at flow bifurcations inside the formwork. This could lead to higher hydrostatic pressures than reported here, and as such to a lower contribution of the shear flow losses to the total wall pressure.

Unfortunately, the density of the fresh concrete already inside the formworks was not measured during our filling experiments.

5.2.3.2 Cast quality - visual inspection

As previously mentioned in section 5.1 and in section 5.2.2, a visual inspection has been performed on drilled samples taken at five equidistant locations along the height of the cast columns. Sample 1 is positioned near the bottom of each column, whereas sample 5 is positioned near the top of each column.

The visual inspection results on the polished surfaces of the drilled samples are summarized in Table 5-6 for casting with a low viscosity SCC at a high casting speed and with rebars in the column formwork. Column 4 was cast under these filling conditions (see also Table 5-5). The visual inspection results of the remaining drilled samples are presented in appendix B.

All the sample pictures shown in Table 5-6 reveal a very good resulting homogeneity after the performed filling process. No segregation can be observed. This is quite remarkable when taking into account the very high casting speeds used in the performed base-filling processes, compared to the casting speeds which are normally used for casting CVC or SCC when applying the top-filling procedure.

Table 5-6: Results of the visual inspection performed on drilled samples of column 4.

	Column 4 - low viscosity SCC - high casting speed - with rebars
Position 1	
Position 2	
Position 3	
Position 4	
Position 5	

5.3 References

[5.1] Van De Maele J., Vanmassenhove N., "Vullen van een bekisting met zelfverdichtend beton door het pompen van onderaan", Master thesis (in Dutch), Ghent University, Ghent (2010).

[5.2] Feys D., "Interactions between Rheological Properties and Pumping of Self-Compacting Concrete", Ph-D dissertation, Ghent University, Ghent (2009).

[5.3] De Schutter G., Bartos P., Domone P., Gibbs J., "Self-Compacting Concrete", Whittles Publishing, Caithness, (2008), 296 pages.

[5.4] EFNARC, "European guidelines for self-compacting concrete", Joint Research Group, Brussels (2005), 68 pages.

[5.5] Tichko S., Van De Maele J., Vanmassenhove N., De Schutter G., Vierendeels J., Verhoeven R., Troch P., "Numerical simulation of formwork pressure while pumping self-compacting concrete bottom-up", Eng. Struct., vol. **70**, (2014), pp. 218-233.

[5.6] Tichko S., De Schutter G., Troch P., Vierendeels J., Verhoeven R., Lesage K., Cauberg N., "Influence of the viscosity of self-compacting concrete and the presence of rebars on the formwork pressure while filling bottom-up", Eng. Struct., vol. **101**, (2015), pp. 698-714.

[5.7] Cauberg N., Desmyter J., Piérard J., Parmentier B., "Bekistingsdruk bij zelfverdichtend beton" - WTCB dossiers (in Dutch) - Katern 7, nr. 3, WTCB, Limeltte (2006).

[5.8] Desnerck P., "Compressive, bond and shear behaviour of powder-type self-compacting concrete", Ph-D dissertation, Ghent University, Ghent (2011).

[5.9] Roussel N., "A thixotropy model for fresh fluid concretes: Theory, validation and applications", Cem. Conc. Res. **36**, (2006), pp. 1797-1806.

[5.10] Billberg P., "Form pressure generated by SCC - Influence of Thixotropy and Structural Behaviour at Rest", Ph-D dissertation, Royal Institute of Technology, Stockholm (2006).

[5.11] Le H.D., De Schutter G., Kadri E.H., Aggoun S., Vierendeels J., Troch P., "Velocity profile of Self Compacting Concrete and Traditional Concrete flowing in a half open pipe", 3rd International conference on Concrete Repair, Rehabilitation and Retrofitting (ICCRRR -2012), CRC Press, pp.1382-1387.

[5.12] Amziane S., Perrot A., Ovarlez G., Roussel N., "SCC Formwork Pressure: Influence of Steel Rebars", 6th International RILEM Symposium on self-compacting, SCC 2010 Conference Proceedings vol. 2, Montreal (2010), pp. 759-771.

Chapter 6: Numerical simulation of the casting tests with fresh SCC

"There are thinks known and there are things unknown, and in between are the doors of perception." - Aldous Huxley

6 Overview of this Chapter

Chapter 6 is divided in three main sections. Section 6.1 presents the numerical model that has been built for the simulation of the pumping tests with different SCC mixtures which have been conducted by Feys [6.1]. The results of these simulations reveal that a quite complex boundary condition is needed at the walls in order to adequately predict to occurring shear flow losses and the resulting pressure on the duct walls. In section 6.2, the simulations of the base-filling tests without rebars, which were presented in section 5.1, are described in detail. The sensitivity analysis, performed on the Herschel-Bulkley parameters in relation with the simulated pressure losses, clearly prove the necessity for accurate determination of these rheological model parameters. Finally, in section 6.3, the simulations of the base-filling tests with the rebars, being described in section 5.2, are fully explained. Also the application and validation of the new analytical model derived in chapter 3, for predicting the pressure losses and the wall pressure during base-casting with SCC is presented.

6.1 Simulation of the pumping tests with SCC

In this section, the flow of fresh SCC in supply ducts is studied and the performed simulations are presented [6.1, 6.2]. The aim of these simulations is to accurately calculate the occurring pressure losses within the supply ducts when pumping SCC into the formwork, and as such to be able to determine the required pumping pressure of the concrete pump at a specific SCC delivery rate. In section 6.1.1, a concise overview of the currently available state-of-the-art analytical models predicting these pressure losses is given. In section 6.1.2, the general layout and the measurement set-up of the full scale pumping tests that have been performed at the MLCR of Ghent University are introduced. In section 6.1.3, the related CFD model together with the simulation results are described extensively. Finally in section 6.1.4, a comparison is made between the analytical results, the collected measurements of the full-scale tests and the CFD results.

6.1.1 Analytical flow models for fresh SCC

6.1.1.1 Rheological models for fresh SCC

As already mentioned in chapter 2, the behaviour of fresh concrete may be described using a yield stress model such as the Bingham model or the Herschel-Bulkley model as long as steady state flow is reached [6.3, 6.4]. Both models have been already introduced in chapter 2. They are represented by Eq. (2.5) and Eq. (2.6) respectively.

The flow of SCC in the conveying ducts during the performed pumping tests was steady for each flow rate considered. Therefore the use of these simple material models for describing the flow behaviour of the fresh SCC during the pumping tests is justified.

In his research work, Feys [6.1] has clearly shown that shear thickening is occurring during the flow of SCC in ducts. In order to capture the shear thickening behaviour, Yahia et al. [6.5] proposed the following modification to the Bingham material model:

$$\tau_{MB} = \tau_{0,MB} + \mu_{MB}\dot{\gamma} + c_{MB}\dot{\gamma}^2 \tag{6.1}$$

where the subscript *MB* stands for modified Bingham and c_{MB} is a second order parameter (Pa.s²).

6.1.1.2 Analytical flow models for fresh SCC

As already described in chapter 3, the laminar flow of Newtonian fluids in ducts is described analytically by the well-known Poiseuille formula (see also Eq. (3.28)), relating the flow rate Q_P with the total pressure loss Δp_{tot} over the length of the duct:

$$Q_P = \frac{\pi R^4 \Delta p_{tot}}{8\eta L} \tag{6.2}$$

where η is the dynamic viscosity of the Newtonian fluid (Pa.s), R is the radius of the duct (m) and L is the length of the duct (m).

Extending this formula for materials like fresh SCC, using the previously mentioned Bingham model leads to the Buckingham-Reiner equation (Eq. (6.3) and also Eq. (3.27)):

$$Q_B = \pi \frac{3R^4\Delta p_{tot}^4 + 16\tau_{0,B}^4 L^4 - 8\tau_{0,B} L R^3 \Delta p_{tot}^3}{24\Delta p_{tot}^3 L \mu_{p,B}} \tag{6.3}$$

For the modified Bingham material model, Calie [6.33] derived the following equation:

$$Q_{MB} = \frac{\pi R^3}{840 c_{MB}^4 \tau_w^3} \begin{bmatrix} -\mu_{MB}^7 + W\mu_{MB}^6 + 140\mu_{MB} c_{MB}^3 \left(\tau_{0,MB}^3 - \tau_w^3\right) \\ -2W\mu_{MB}^4 c_{MB}\left(\tau_w + 6\tau_{0,MB}\right) + 14\mu_{MB}^5 c_{MB}\tau_{0,MB} \\ -70\tau_{0,MB}^2 c_{MB}^2 \mu_{MB}^3 - 8Wc_{MB}^3 \tau_w \tau_{0,MB}\left(3\tau_w + 4\tau_{0,MB}\right) \\ +2W\mu_{MB}^2 c_{MB}^2 \left(3\tau_w^2 + 24\tau_{0,MB}^2 + 8\tau_w\tau_{0,MB}\right) \\ +120Wc_{MB}^3\tau_w^3 - 64Wc_{MB}^3\tau_{0,MB}^3 \end{bmatrix} \tag{6.4}$$

where τ_w represents the shear stress at the wall (= $\Delta p_{tot}.R/(2L)$) (Pa) and the parameter W equals $\sqrt{\mu_{MB}^2 + 4c_{MB}\tau_w - 4c_{MB}\tau_{0,MB}}$.

Unfortunately, due to the fact that the Herschel-Bulkley material parameters of the selected SCC mixture for the pumping tests (LM7 - see next section) were not measured by Feys, the new analytical model which has been derived in chapter 3 of the present research cannot be used for comparison between the other models and the performed pressure measurements. Therefore, only Eq. (6.2), Eq. (6.3) and Eq. (6.4) will be used in section 6.1.4 to evaluate the pressure losses of the flow of SCC in ducts analytically.

6.1.2 The pumping tests with SCC performed by Feys

In this section, the full-scale pumping tests that have been performed by Feys [19.1] at the MLCR of Ghent University in Belgium are described. For these tests, 18 SCC mixtures (coded as OBC1, LM1 – LM17) as well as one traditional concrete mixture (coded as TC1) were developed and pumped through piping circuits.

The objective for carrying out these tests was to investigate the impact of the rheology of the fresh SCC mixtures on the pressure losses, but also the influence of the pumping process on the rheology of these mixtures. As such, the rheological properties, the pressure losses and the discharges were measured during these pumping tests.

This knowledge is not only essential for pumping of fresh SCC through conveying ducts, but is equally important during base-casting. This clarifies the link between the research performed by Feys and the current research.

Three piping layouts were designed and built. Most of the pumping tests were performed using a short circuit as shown in Fig. 6-1 and Fig. 6-2.

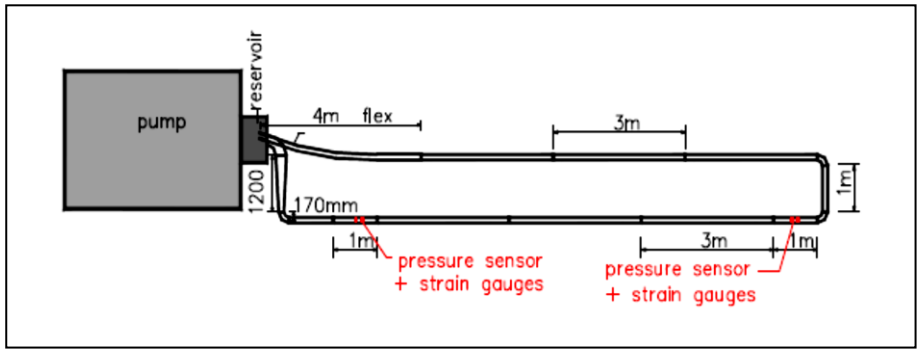

Fig. 6-1: Design of the short pumping circuit of 27 m.

Before each test, a sample of concrete was taken in order to investigate the fresh properties, by means of a Tattersall Mk-II rheometer and standard tests on SCC like slump flow, V-funnel, L-box, sieve stability and air content.

The pressure losses were measured in the straight horizontal part of the circuit with electronic pressure transducers as well as strain gauges.

The discharges were determined by filling a sampling reservoir and measuring the weight variation during a certain time span with a load cell. With known density, the volume variation with time could be calculated, and the discharge was consequently known.

For the simulations presented in section 6.1, two test cases have been selected from the complete set of the performed pumping tests, after careful elimination of the non-equilibrium pumping cycles, the segregating concretes and the doubtful rheometer results.

Table 6-1 summarizes the fresh concrete properties of the selected SCC mixture, LM7, together with the measured discharges and the pressure losses [6.1].

Fig.6-2: Actual layout of the short pumping circuit.

Table 6.-1: Measured fresh properties of LM7 and measured discharge and pressure losses per unit length.

Fresh properties	**Pumping cycle 3**	**Pumping cycle 4**
Slump flow (mm)	695	710
V-funnel (s)	3	3.5
L-box (-)	0.91	0.93
Density ρ (kg/m³)	2375	2375
Yield stress τ_0 (Pa)	31.2	29.4
Viscosity μ at 0/s (Pa s)	16.4	14.7
Viscosity μ at 5/s (Pa s)	20.1	17.8
Shear thickening (c/μ)	0.023	0.021
Flow parameters	**Discharge *Q* (l/s)**	**Pressure loss *Δp/L* (Pa/m)**
Pumping cycle 3	5.49	7.45
	7.99	11.66
	12.44	20.57
	16.88	30.49
	20.16	40.76
Pumping cycle 4	5.35	8.67
	8,52	13.79
	12.29	21.09
	15.79	29.66
	20.17	39.98

6.1.3 The CFD model of the pumping tests with SCC

6.1.3.1 Governing equations

According to the theory presented in chapter 3, the most general description of a fluid flow is obtained from the Navier-Stokes equations [5.6 - 5.8], which for steady, isothermal, laminar flows are represented by Eq. (3.1) and Eq. (3.2) without the time derivative.

The stress tensor $\bar{\bar{\tau}}$ is modelled using the Bingham material model (see Eq. (2.5)). These equations are solved for the pressures and the velocities over the entire computational domain with the aid of the Fluent® v.6.3 software code [6.9], in which the Bingham material model is implemented.

6.1.3.2 Computational domain

In order to perform the numerical simulation of the SCC flow through the short circuit as illustrated in Fig. 6-1, a 3-D geometry is constructed and meshed with the Fluent Gambit® v.2.3.16 pre-processor, using the Cooper meshing scheme [6.10]. Fig. 6-3 presents the resulting hexahedral mesh cells forming the computational domain.

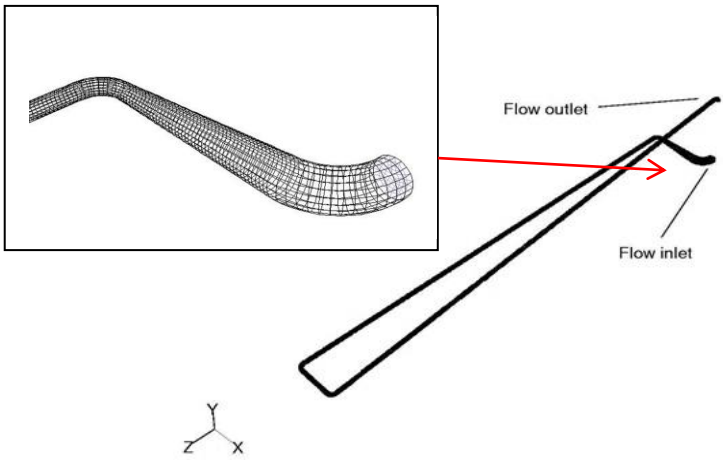

Fig. 6-3: Computational domain of the short pumping circuit.

The “EquiSize Skew” and the “EquiAngle Skew” mesh quality parameters, computed by the Fluent Gambit® software, have a maximum value of 0.4 and a mean value of 0.2, indicating a good quality of the constructed mesh [6.10].

6.1.3.3 Boundary conditions

In order to solve the stated Navier-Stokes equations, a set of boundary conditions need to be applied to the computational domain. At the flow inlet, a uniform velocity profile of the incoming SCC over the cross-section of the inlet pipe is imposed. This uniform velocity is computed from the measured volumetric flow rate during a pumping test and the inlet pipe diameter.

At the flow outlet, the pumped SCC falls into an open reservoir. Therefore a zero gauge pressure condition is applied at the outlet. At the pipe walls a no-slip condition is assumed.

6.1.3.4 Numerical discretization of the model equations and solver settings

The governing flow equations presented in chapter 3 are discretized using the FVM and they are solved with a 3-D, double precision, pressure-based solver (see chapter 4). Table 6-2 summarizes the solver settings of the numerical model.

Table 6-2: Solver controls.

Parameter/control	Value/setting
Velocity formulation	Absolute
Pressure-velocity coupling	SIMPLE
Pressure discretization	Standard
Momentum discretization	Second order upwind

6.1.4 Comparison of the simulations and the measurements

As mentioned in section 6.1.1.2, Eq. (6.2), Eq. (6.3) and Eq. (6.4) are used to calculate the pressure losses per unit length analytically. The results of these calculations, together with the simulation results from the CFD model, are presented in Table 6-3. The pressure losses from the CFD model were calculated as the pressure difference between two cross-sections in the horizontal part of the piping circuit where the pressure sensors were mounted (see Fig. 6-1).

The complete set of calculated data, presented in Table 6-3, as well as the measured pressure losses, summarized in Table 6-1, are combined in Fig. 6-4 and in Fig. 6-5 for pumping cycle 3 and pumping cycle 4 respectively.

Both Fig. 6-4 and Fig. 6-5 show a good agreement between the pressure losses obtained from the CFD simulations and the pressure losses per unit length when using the Poiseuille formula and the Buckingham-Reiner formula.

Table 6-3: Calculated pressure losses per unit length, $\Delta p/L$, for the pumping cycles 3 and 4 using the Poiseuille formula, the Buckingham-Reiner equation, the modified Bingham expression and the CFD model, indicated with indices P, B, MB and CFD respectively.

Pumping cycle 3				
Discharge Q (l/s)	**$(\Delta p/L)_P$**	**$(\Delta p/L)_B$**	**$(\Delta p/L)_{MB}$**	**$(\Delta p/L)_{CFD}$**
5.49	29.1	30.6	55.1	30.1
7.99	42.3	43.9	95.5	43.1
12.44	65.8	67.4	192.0	66.4
16.88	89.3	90.9	319.2	89.7
20.16	106.7	108.3	434.3	107.0
Pumping cycle 4				
Discharge Q (l/s)	**$(\Delta p/L)_P$**	**$(\Delta p/L)_B$**	**$(\Delta p/L)_{MB}$**	**$(\Delta p/L)_{CFD}$**
5.35	25.4	26.9	45.9	26.4
8.52	40.4	41.9	90.0	41.2
12.29	58.3	59.8	159.4	58.9
15.79	74.9	76.4	240.5	75.4
20.17	95.7	97.2	364.5	96.2

The good agreement between the Poiseuille formula for Newtonian fluids and the Buckingham-Reiner formula for Bingham materials is related to the fact that the influence of the yield stress on the resulting pressure losses is very small, as will be explained and illustrated in section 6.2.

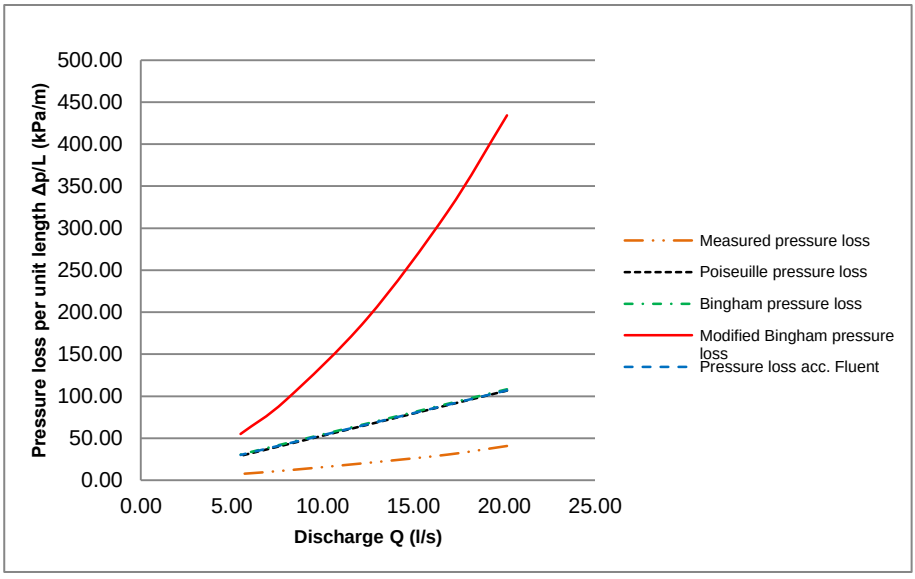

Fig. 6-4: Pressure loss vs. discharge for pumping cycle 3.

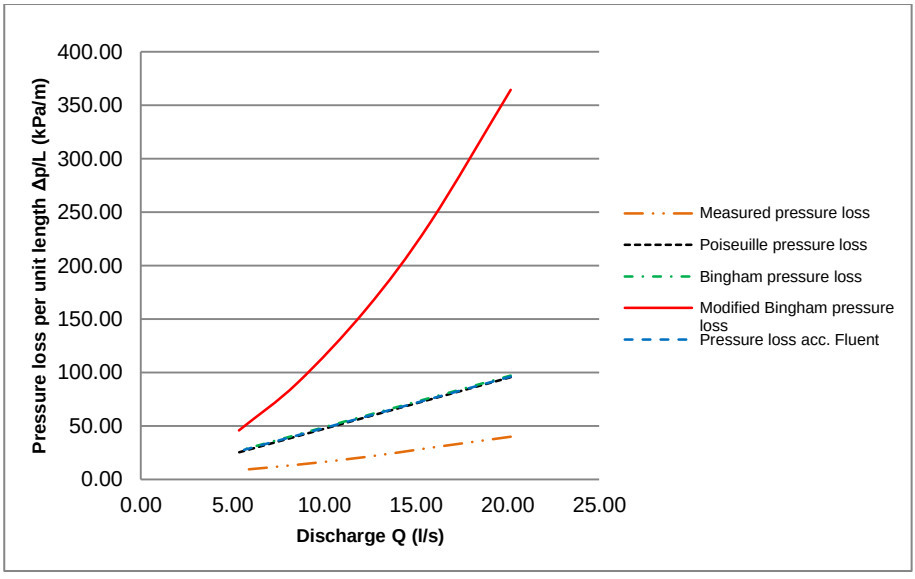

Fig. 6-5: Pressure loss vs. discharge for pumping cycle 4.

The overestimation of the occurring pressure losses when applying the analytical equations presented in section 6.1.1.2 has already been reported by Feys [6.1]. This is quite obviously also the case when using a CFD model based on a Bingham material description.

Unlike the effect of slippage at walls, which has been observed and reported by Kaplan [6.11], this overestimation of the pressure losses can be attributed to the combination of three different phenomena influencing the fresh SCC properties, as mentioned by Feys [6.1]:

- Geometrical wall effect
- Thixotropy (or structural breakdown)
- Dynamic segregation

The geometrical wall effect can be explained by the fact that the aggregates in the fresh concrete cannot penetrate into the rigid wall of the duct. As a result, the concentration of aggregates decreases when approaching the duct wall, creating a kind of lubrication layer, mainly formed by cement paste. This has also been observed and reported by Le et al. [6.12]. The viscosity of this lubrication layer is several times lower than the viscosity of the SCC mix.

Dynamic segregation [6.1, 6.11, 6.13] is defined as a migration of coarse aggregates into zones of smaller shear rates. The aggregates are believed to move to the centre of the pipe until nearly maximum packing density is achieved. This effect has to be added to the geometric wall effect, further stimulating the creation of this lubrication layer.

Thixotropy (or structural breakdown), which has been explained extensively in chapter 2, is characterized by a reversible build-up and breakdown of an internal structure, depending on the local value of the shear rate. Near the duct walls, the shear rate is very high, leading to the breakdown of the internal structure and thus a much lower viscosity.

The numerical simulations of pumping fresh concrete through conveying pipes deliver the same results as the available analytical solutions. On the other hand, the experimental results show lower pressure losses compared to the analytical solutions and the numerical results. Three effects, which reduce the viscosity of the SCC near the pipe walls, have been identified, but their quantification is still undefined.

Further research is needed to study these effects in detail, experimentally as well as numerically, which will hopefully lead to the development of new mathematical models quantifying these phenomena. These new mathematical models could then be implemented in numerical models through the use of user defined functions. This would certainly reduce the overestimation of the calculated pressure losses and bring the obtained simulation results closer to the measured ones. This important subject will be presented and discussed in more detail in the next section.

6.2 Simulation of the formwork base-filling tests without rebars

In the current section, the CFD models of the formwork base-filling tests without rebars and the simulation results will be explained in detail. This section is divided in two major parts describing the numerical models of the two series of casting tests performed at the MLCR of Ghent University.

When optimizing a formwork base-filling process, some design parameters can be modified and others are fixed and may not be altered. The following list summarizes the constraints and the different design parameters of a cast:

- The geometry of the cast: this parameter is defined in the architectural and the structural stability design stage and is as such a fixed constraint when designing a casting process;
- The rebar configuration: the layout of the steel reinforcement is also determined during the stability design phase, and is therefore a given constraint for the filling process. Both the geometry and the rebar configuration will determine the resulting computational domain for the numerical flow simulations;
- The number and the positions of the fresh concrete supply inlets in a formwork: these design parameters must be determined and also fine-tuned;
- The casting speed: varying this design parameter will influence the construction pace, the quality of the cast, and last but not least, the resulting formwork pressures and therefore the mechanical design of the formwork layout;
- The rheology of the fresh concrete: the rheological parameters as design parameters will have an impact on the hydraulic losses and the resulting formwork wall pressures, as well as on the final quality of the cast elements (segregation resistance, concrete strength and durability).

The influence of the casting speed on the formwork pressures will be discussed in section 6.2.2.

6.2.1 First series of base-filling tests

6.2.1.1 Influence of the rheological parameters on the formwork pressure

In order to quantify the influence of the rheology of the fresh SCC, represented by the Herschel-Bulkley parameters, on the viscous shear flow losses, a sensitivity analysis has been performed [6.15, 6.28]. The details of the related numerical models are explained in the following sections, but the results of this sensitivity analysis are already shown here, in order to clearly demonstrate the contribution of each rheological parameter to the hydraulic losses and therefore to the wall pressure.

The simulations of the sensitivity analysis and the base-filling tests have been performed with three different versions of the Ansys Fluent® software: v.6.3, v.12.1 and v.14.0. This was due to a consecutive upgrade of the software.

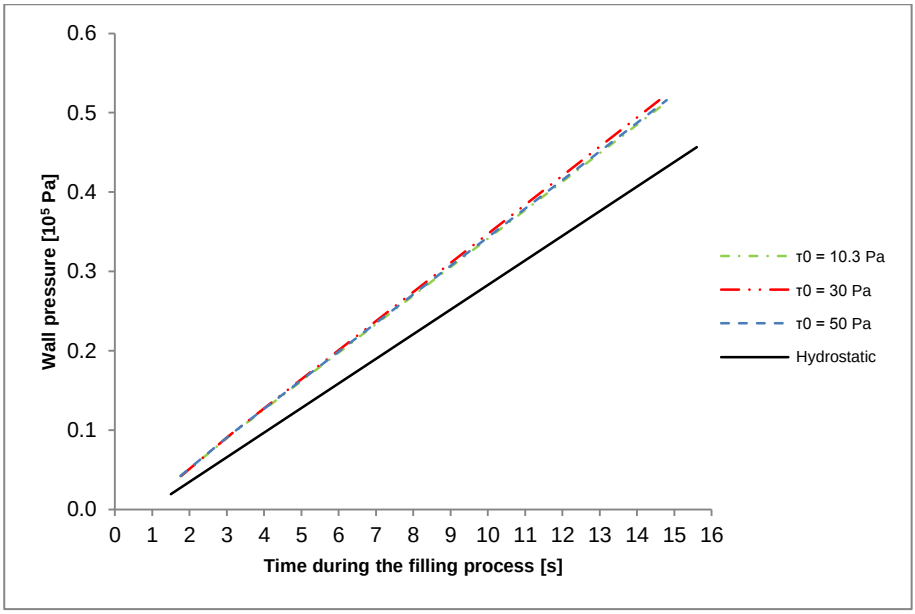

Fig. 6-6: Influence of the yield stress value on the maximum formwork pressure (ρ_{SCC} = 2314.4 kg/m³, K_{HB} = 10 Pa.s^n, n_{HB} = 1.35).

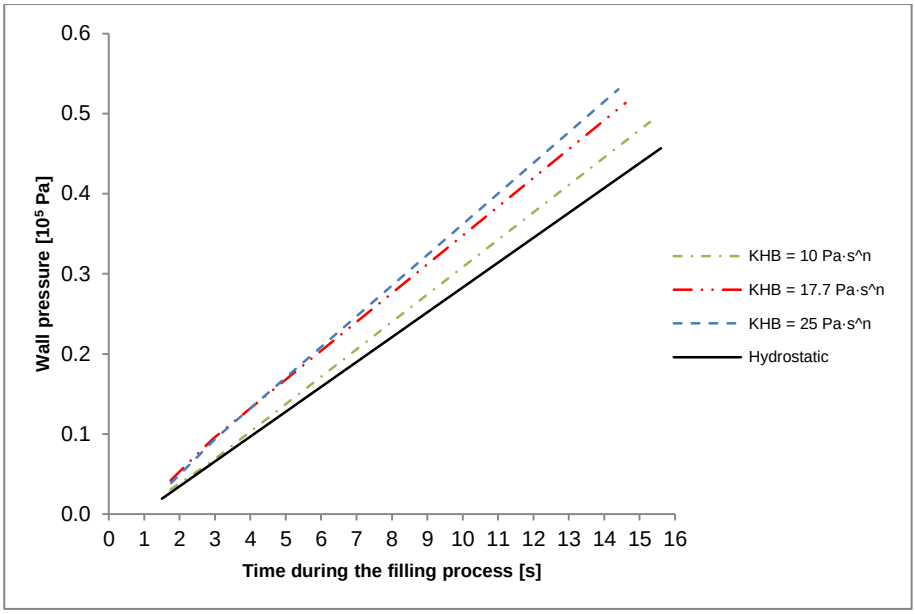

Fig. 6-7: Influence of the consistency factor on the maximum formwork pressure (ρ_{SCC} = 2314.4 kg/m³, τ_0 = 10.3 Pa, n_{HB} = 1.35).

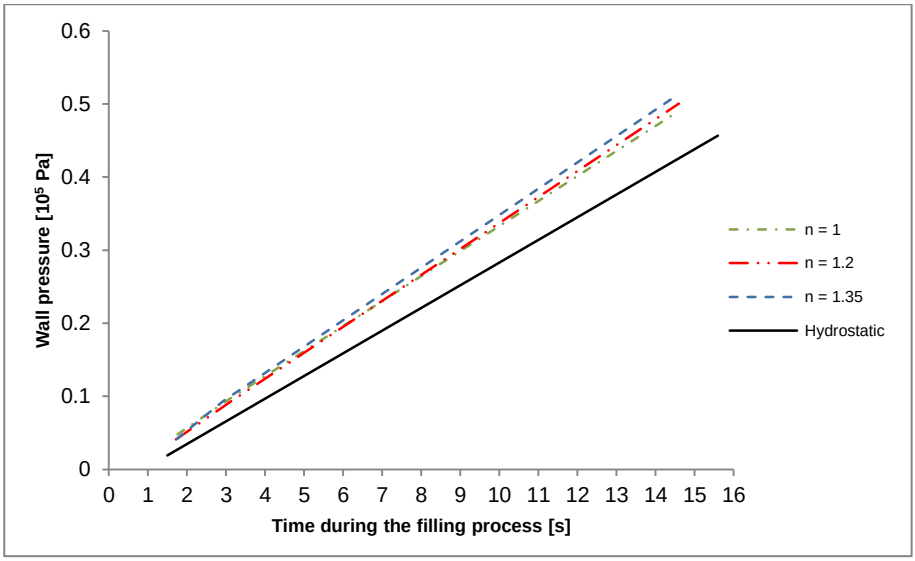

Fig. 6-8: Influence of the consistency index on the maximum formwork pressure (ρ_{SCC} = 2314.4 kg/m³, τ_0 = 10.3 Pa, K_{HB} = 10 Pa.s^n).

Fig. 6-6 shows the results of the simulations in terms of wall pressure performed with three different yield stress values, ranging from 10.3 Pa to 50 Pa. In Fig. 6-7, the results of the simulations performed with three different consistency factors, ranging from 10 Pa.s^n to 25 Pa.s^n, are presented while Fig. 6-8 shows the results of the simulations performed with four different consistency indices, ranging from 1 to 1.35.

For the value ranges of the Herschel-Bulkley parameters used in this sensitivity analysis, the influence of the yield stress value on the wall pressure is very limited, whereas the influence of the consistency factor and the consistency index is more pronounced. It is therefore important to accurately determine the rheology of the manufactured SCC through measurement [6.1, 6.16 - 6.20] prior to casting.

6.2.1.2 Model equations

The model equations for the simulation of the filling processes have been described in detail in chapter 3. Unlike for the simulation of the flow of SCC through ducts, being discussed in section 6.1, where the steady Navier-Stokes equations were solved, casting is a transient process and therefore the time dependent Navier-Stokes equations (Eq. (3.1) and Eq. (3.2)) need to be solved in time and in space.

The Volume of Fluid (VOF) method, being developed by Hirt and Nichols [6.24] and presented in chapter 4, is used to capture the evolution of the interface between the SCC and the air during the formwork filling process. The VOF method can model two or more immiscible fluids by solving a single set of momentum equations and tracking the volume fraction of each of the fluids throughout the domain.

Special attention is to be given towards the numerical treatment of the stress tensor $\bar{\bar{\tau}}$ in the momentum conservation equation, Eq. (3.2). The stress tensor $\bar{\bar{\tau}}$ for SCC is modelled using the Herschel-Bulkley material model (see chapter 2, Eq. (2.6)), which is discontinuous for shear rates close to zero. For zero shear rate, the apparent viscosity becomes infinite. This cannot be handled properly in a numerical code, and in order to avoid this mathematical singularity, in Ansys Fluent® v.6.3 as well as in Ansys Fluent® v.12.1 and v.14.0, a modified Herschel-Bulkley model has been implemented [6.9, 6.21, 6.22].

The Herschel-Bulkley model has been transformed into a two-zone model: a first zone for shear rates lower than a critical shear rate $\dot{\gamma}_c$ (= τ_0/μ_0) where the "rigid" material behaves like a viscous fluid with a very high viscosity μ_0, and a second zone for shear rates higher than the critical shear rate $\dot{\gamma}_c$ where the material follows the original Herschel-Bulkley model.

In Ansys Fluent® v.6.3, the equations for the two-zone Herschel-Bulkley model are:

For $\dot{\gamma} > \dot{\gamma}_c$:

$$\eta = \frac{\tau_{0,HB}}{\dot{\gamma}} + K_{HB}\left[\left(\dot{\gamma}\right)^{n_{HB}-1} - \left(\dot{\gamma}_c\right)^{n_{HB}-1}\right] \tag{6.5}$$

For $\dot{\gamma} \le \dot{\gamma}_c$:

$$\eta = \mu_0 \tag{6.6}$$

whereas in Ansys Fluent® v.12.1 and v.14.0, the two-zone Herschel-Bulkley model is represented by the following equations:

For $\dot{\gamma} > \dot{\gamma}_c$:

$$\eta = \frac{\tau_{0,HB}}{\dot{\gamma}} + k\left(\frac{\dot{\gamma}}{\dot{\gamma}_c}\right)^{n_{HB}-1} \tag{6.7}$$

For $\dot{\gamma} \le \dot{\gamma}_c$:

$$\eta = \tau_{0,HB}\frac{\left(2-\dot{\gamma}/\dot{\gamma}_c\right)}{\dot{\gamma}_c} + k\left[\left(2-n_{HB}\right) + \left(n_{HB}-1\right)\frac{\dot{\gamma}}{\dot{\gamma}_c}\right] \tag{6.8}$$

where η is the apparent viscosity of the material (Pa.s), $\dot{\gamma}_c$ is the critical shear rate in the material (1/s) and $k = K_{HB}(\dot{\gamma}_c)^{n_{HB}-1}$.

When applying Eq. (6.5) and Eq. (6.6), the transition between the two zones is less smooth than when using Eq. (6.7) and Eq. (6.8). Therefore, the two-zone Herschel-Bulkley equations implemented in Ansys Fluent® v.12.1 and v.14.0 improve the stability of the resulting numerical scheme.

The critical shear rate, as defined in Ansys Fluent® for this two-zone Herschel-Bulkley model, is not to be confused with the definition mentioned in other literature [6.1, 6.23]. When a critical shear rate is mentioned further in this work, we refer to the Ansys Fluent® definition stated above.

Determining the most appropriate value of the critical shear rate in the modified Herschel-Bulkley model is important. As mentioned in [6.9, 6.21, 6.22, 6.24], the VOF method tends to be less robust when the apparent viscosities of the fluids involved are largely differing from each other. The numerical stability as well as the accuracy of the obtained numerical results are impaired. Selecting a small value for the critical shear rate in the two-zone Herschel-Bulkley model above will result into a limited but very high apparent viscosity when the shear rate approaches zero. In order to assess the most adequate value for this critical shear rate parameter, a small 2-D VOF model has been created, which is shown in Fig. 6-9.

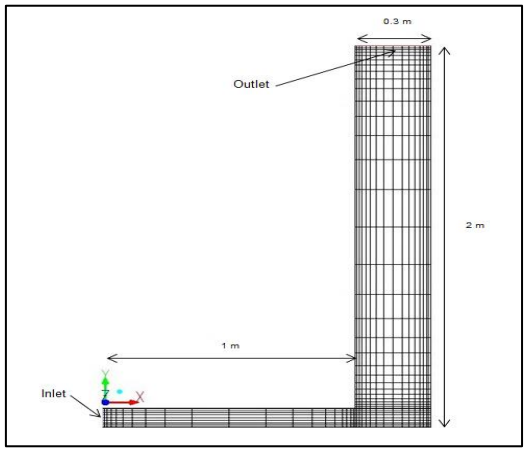

Fig. 6-9: 2D VOF model for the determination of the appropriate critical shear rate value.

This 2-D model is used to investigate the influence of this critical shear rate parameter on the numerical stability and the accuracy of the simulated results (velocities and wall pressures). The input properties for this simplified 2-D model are:

- The critical shear rate: 0.123 s^{-1} and 1 s^{-1}
- The Herschel-Bulkley yield stress: 76.73 Pa
- The Herschel-Bulkley consistency factor: 11.45 $Pa.s^{n}$
- The Herschel-Bulkley consistency index: 1.6
- The filling velocity at the inlet: 0.05 m/s
- The density of the concrete: 2273 kg/m^3

The shear stress and the apparent viscosity according to the Herschel-Bulkley two-zone model are plotted for the three critical shear rate values in Fig. 6-10 a-b. As expected, when choosing a larger critical shear rate value, the apparent viscosity for shear rates close to zero is considerably reduced. This improves the numerical stability of the VOF model, which allows larger time steps to be used and therefore a reduction of the total calculation time. For this experiment, the choice of the larger critical shear rate value leads to a reduction in calculation time of about 12 %.

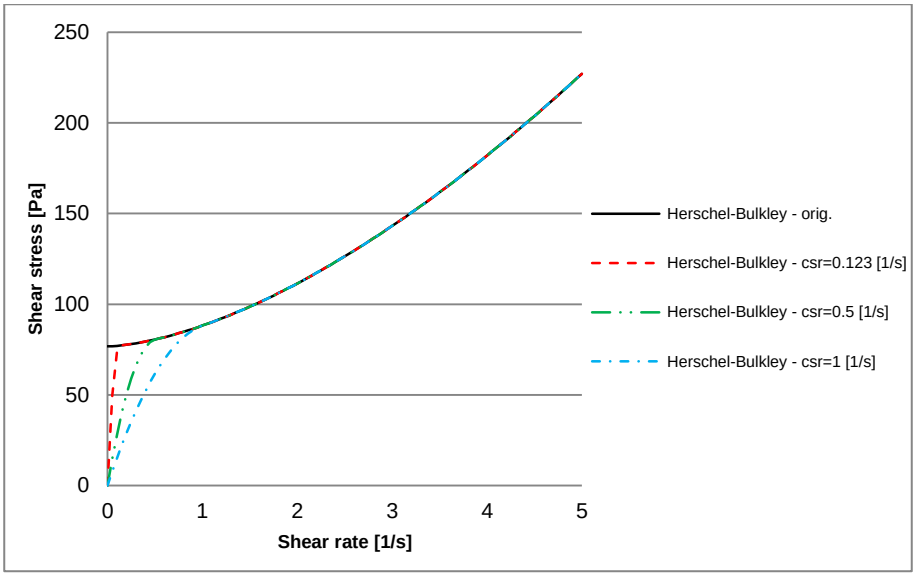

a) Ansys Fluent v. 12.1 and v. 14.0 two-zone Herschel-Bulkley model for three different critical share rate values $\dot{\gamma}$.

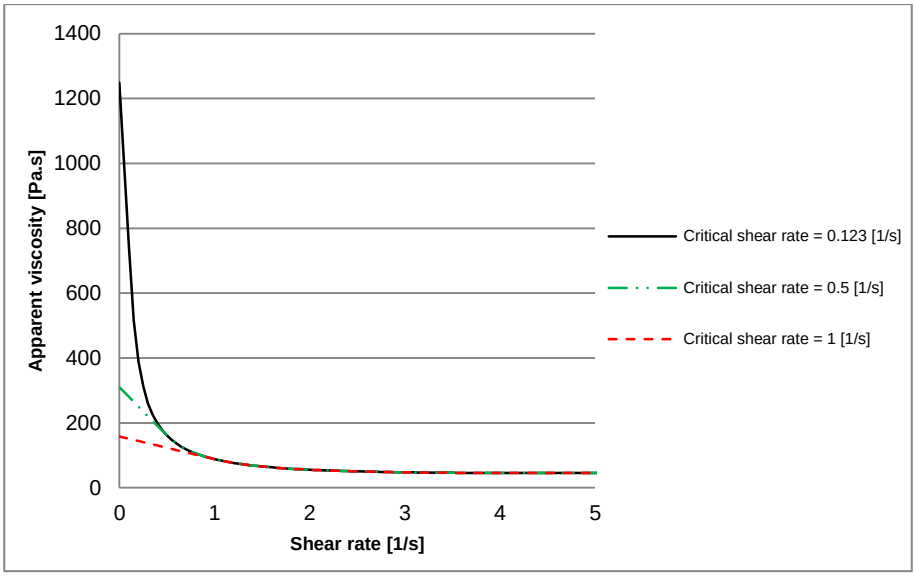

b) Apparent viscosity for three different critical shear rate values $\dot{\gamma}$.

Fig. 6-10: Two-zone Herschel-Bulkley model - influence of the critical shear rate parameter.

The computed velocity profile in a cross-section of the column at mid height is shown in Fig. 6-11 for the chosen critical shear rate values of 0.123 s^{-1} (left) and 1 s^{-1} (right).

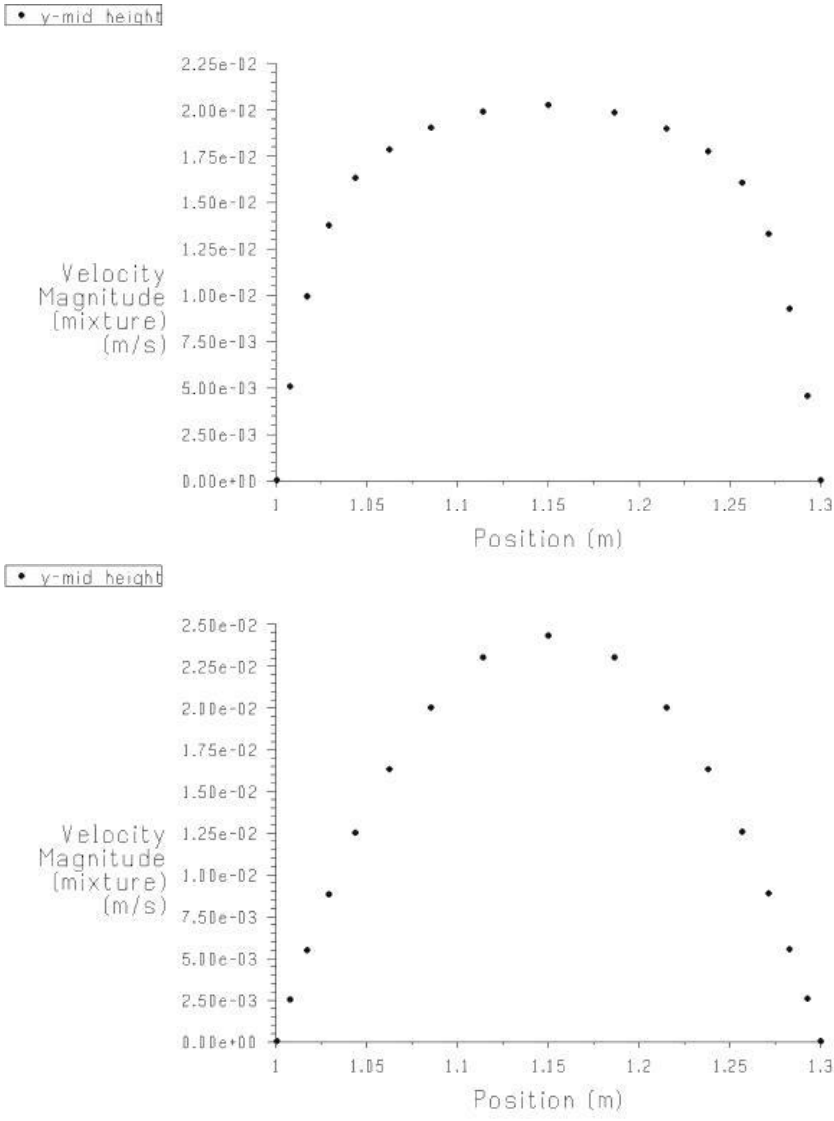

Fig. 6-11: Velocity profile of v_y at mid height for a critical shear rate $\dot{\gamma}_c$ = 0.123 s^{-1} (left) and for $\dot{\gamma}_c$ = 1 s^{-1} (right).

The simulated wall pressures at the bottom and at mid height of the column as a function of time are shown in Fig. 6-12.

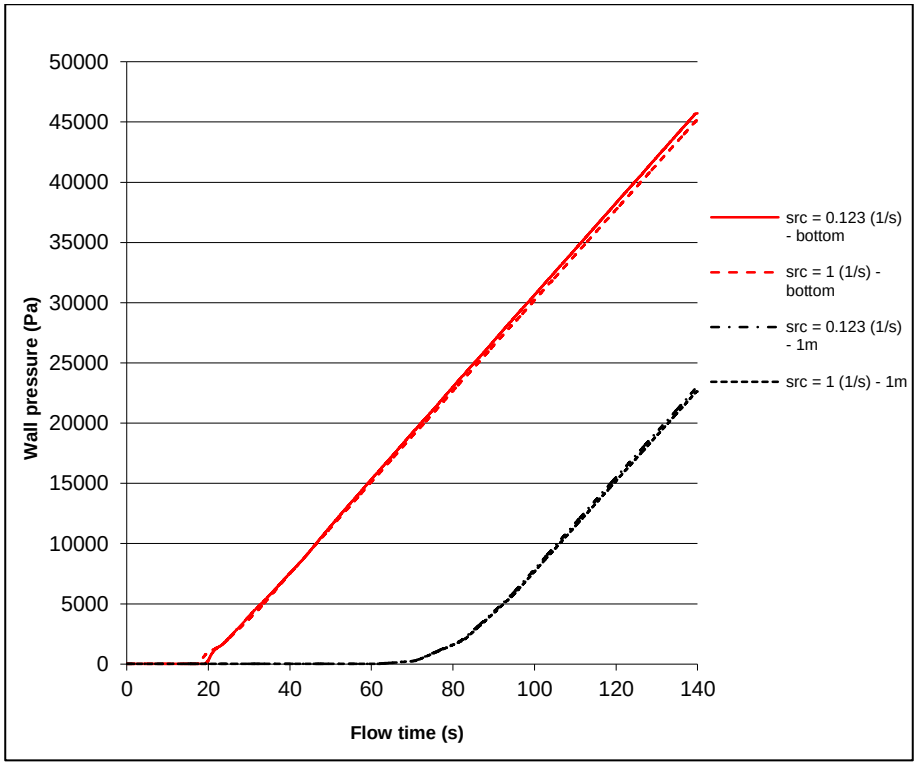

Fig. 6-12: Simulated wall pressures of the 2-D VOF test model.

The chosen critical shear rate value also very clearly influences the resulting velocity profile, but not the calculated wall pressures. The yield stress determines the zone of plug flow, as stated by Feys [6.1]. The plug zone is characterised by a (almost) uniform velocity of the material (solid body motion), leading to a flat velocity profile in the unsheared centre zone.

A small critical shear rate value will preserve the influence of the yield stress (see Fig. 6-10a), leading to the velocity profile illustrated in the left graph of Fig. 6-11. On the other hand, choosing a larger value for the critical shear rate will lead to an almost Newtonian fluid behaviour at low shear rates, with a typical parabolic velocity profile for laminar conditions, as can be seen in the right graph of Fig. 6-11.

The fact that the selected critical shear rate values have a very limited impact on the calculated wall pressures can be explained by the following argumentation. Fig. 6-10 shows that a small critical shear rate value preserves the influence of the yield stress and results in high apparent viscosities for low shear rates, while a larger critical shear rate value leads to opposite observations. In chapter 3, it was stated that for the formwork base-filling process with SCC, the formwork wall pressure did not only depend on the hydrostatic pressure, but also on the flow shear losses.

The hydrostatic pressure component is not depending on the yield stress or the apparent viscosity. So this pressure component is not influenced by the choice of the critical shear rate value. The influence of the critical shear rate on the flow shear losses remains to be assessed.

In the plug flow zone, related to the yield stress, the shear rates are very low and therefore the contribution to the flow shear losses is limited, while close to the wall, where the influence of the yield stress is to be neglected, the shear rates are much higher and thus leading to a bigger contribution. This small contribution of the yield stress to the wall pressures has also been mentioned in section 6.2.1.1 and in section 6.1 [6.14, 6.15 and 6.28].

Fig. 6-12 shows that a lower critical shear rate value results in slightly higher wall pressures. This can be explained by the higher velocity gradient (see Fig. 6-11 - left), and thus higher shear rate value, close to the wall, resulting in higher shear losses.

Also for the lower shear rates in the centre of the flow cross-section, the shear stresses will be underestimated when calculated according to the almost Newtonian curve in the first zone, compared to the original Herschel-Bulkley curve. Therefore the contribution of the low shear rates to the flow shear losses will be less.

The simulated shear rates in the 2-D VOF model range from 0 s^{-1} to 1 s^{-1} in the column and 0 s^{-1} to 10 s^{-1} in the inlet pipe, which is in accordance with shear rate ranges observed in real formwork filling processes, as stated by Roussel [6.25].

Because the shear rates in the simulation models of the presented filling tests vary between 0 s^{-1} (in the centre of the domain) and 1 s^{-1} (close to walls), a value of 0.5 s^{-1} has been chosen for the critical shear rate, as a compromise between keeping the influence of the yield stress on the SCC flow and promoting numerical stability.

6.2.1.3 Computational domain

The first step in a numerical simulation is the creation of the geometry of the computational domain, and while doing this, defining the boundaries of the system under study.

For the numerical simulation of the SCC flow through the formworks, shown in Fig. 5-1 of chapter 5, a 3-D geometry is constructed for each cast element and meshed with the Fluent Gambit® v.2.3 pre-processor [6.10].

Fig. 6-13, Fig. 6-14 and Fig. 6-15 show the resulting high quality hexahedral meshes for the columns and the walls.

After performing a grid convergence study, these highly regular meshes provided the most accurate simulation results at an acceptable computation time.

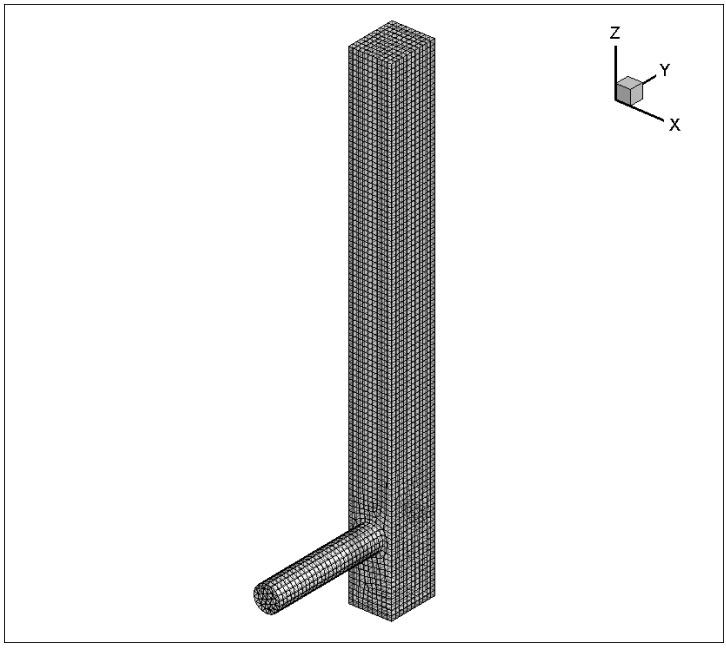

Fig. 6-13: Computational domain for the column filling process.

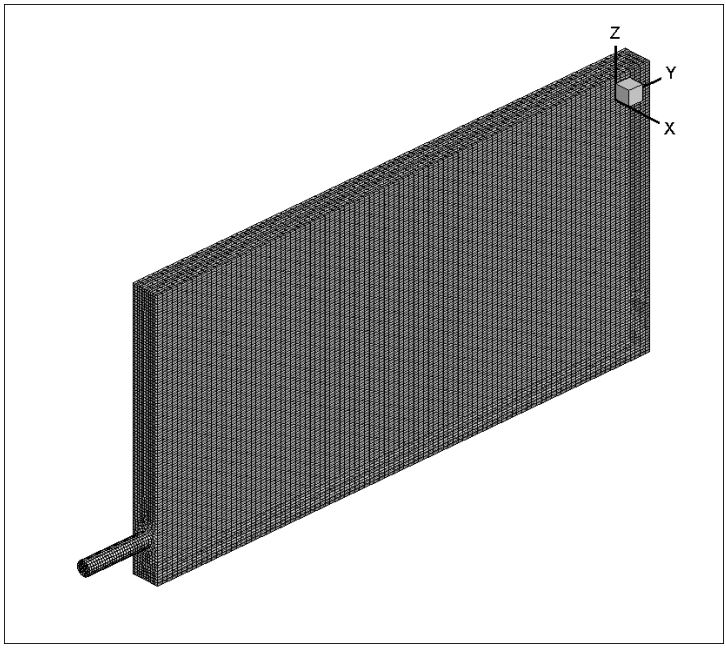

Fig. 6-14: Computational domain for the wall type A filling process.

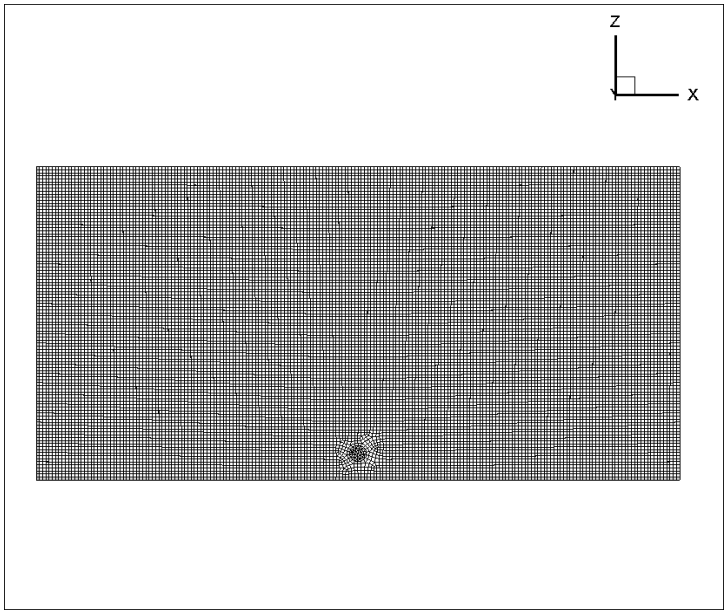

Fig. 6-15: Computational domain for the wall type B filling process.

6.2.1.4 Boundary conditions

Boundary conditions need to be applied to the computational domain, in order to obtain solutions for the model equations presented in chapter 4.

At the flow inlet, a uniform velocity profile of the incoming SCC and the volume fraction of the SCC phase are imposed, while at the top of the formwork, the pressure is atmospheric, resulting in a zero gauge pressure condition at the outlet.

The inlet conditions, shown in Table 6-4, are derived from the flow measurements performed during the filling tests and the geometry of the inlet duct. The length of the inlet duct used in the present numerical models has been determined from small preliminary simulations, which aimed at obtaining laminar flow conditions with a fully developed parabolic velocity profile at the end of the inlet duct.

Table 6-4: Inlet conditions.

Structural element	**Flow rate [l/s]**	**Inlet pipe diameter [mm]**	**Uniform inlet velocity [m/s]**	**Casting speed [m/h]**
Columns	5	106	0.57	490
Walls	6	106	0.68	25

At the duct and formwork walls, a no-slip condition is assumed. Feys [6.1] and Le et al. [6.12] have observed the presence of a very fine lubrication layer of cement paste close to solid walls, in which large velocity gradients are present and for which the validity of this no-slip condition has been confirmed.

Further comments regarding the applied wall boundary condition and the lubrication layer are made in section 6.2.1.7.2 and in section 6.3.

6.2.1.5 Solution of the model equations

As already mentioned in section 6.2.1.2, the Navier-Stokes equations are discretized combining the FVM and the VOF method and they are solved with a 3-D, double precision, implicit pressure-based solver.

The solver settings of the numerical simulation models are summarized in Table 6-5 and they are explained in detail in chapter 4.

Table 6-5: Solver controls.

Controls	Columns	Wall type A and B
Multiphase VOF model/scheme	2 phases	2 phases
Flow regime	Laminar	Laminar
VOF scheme	Explicit	Explicit
Transient controls	NITA[a]	NITA[a]
Unsteady formulation	1st order implicit	1st order implicit
Body force formulation	Implicit body force	Implicit body force
Momentum discretization	2nd order upwind	2nd order upwind
Volume fraction discretization	Geo-reconstruct	CICSAM[b]
Pressure discretization	Body force weighted	Body force weighted
Pressure-velocity coupling	Fractional step method	Fractional step method

[a] Non-Iterative Time Advancement
[b] Compressive Interface Capturing Scheme for Arbitrary Meshes

6.2.1.6 Simulations of the filling tests

The material properties of the fresh SCC mixture are required in order to perform the numerical simulations of the base-filling tests.

The complete set of fresh concrete properties were obtained through measurement and are reported in appendix B. The density and the Herschel-Bulkley parameters for the simulations are presented in the following table.

Table 6-6: Fresh properties of the SCC used in the simulations.

Property	Value	Units
Density ρ_{SCC}	2314	[kg/m³]
Yield stress $\tau_{0,HB}$	10.3	[Pa]
Consistency index n_{HB}	1.35	[-]
Consistency factor K_{HB}	17.7	[Pa.s^n]
Critical shear rate $\dot{\gamma}_c$	0.36	[1/s]

The VOF method proves to be very reliable in accurately capturing the time evolution of the SCC-air interface during the formwork filling processes. Combining the FVM and the VOF method, it is possible through simulation to optimize the formwork filling process during the design phase, as was stated in the introduction of section 6.2.

The number of inlets and their positioning on the formwork can be determined in order to avoid the creation of unwanted air pockets during the casting process. The self-levelling property of the chosen SCC mix during the filling process can also be verified.

Fig. 6-16, Fig. 6-17 and Fig. 6-18 show the simulated formwork filling processes of the two columns and the two walls respectively.

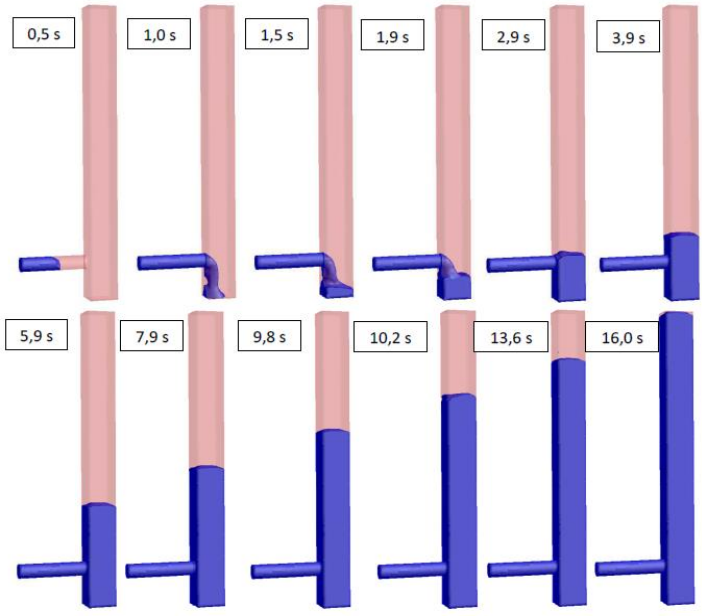

Fig. 6-16: Simulated filling process of the columns.

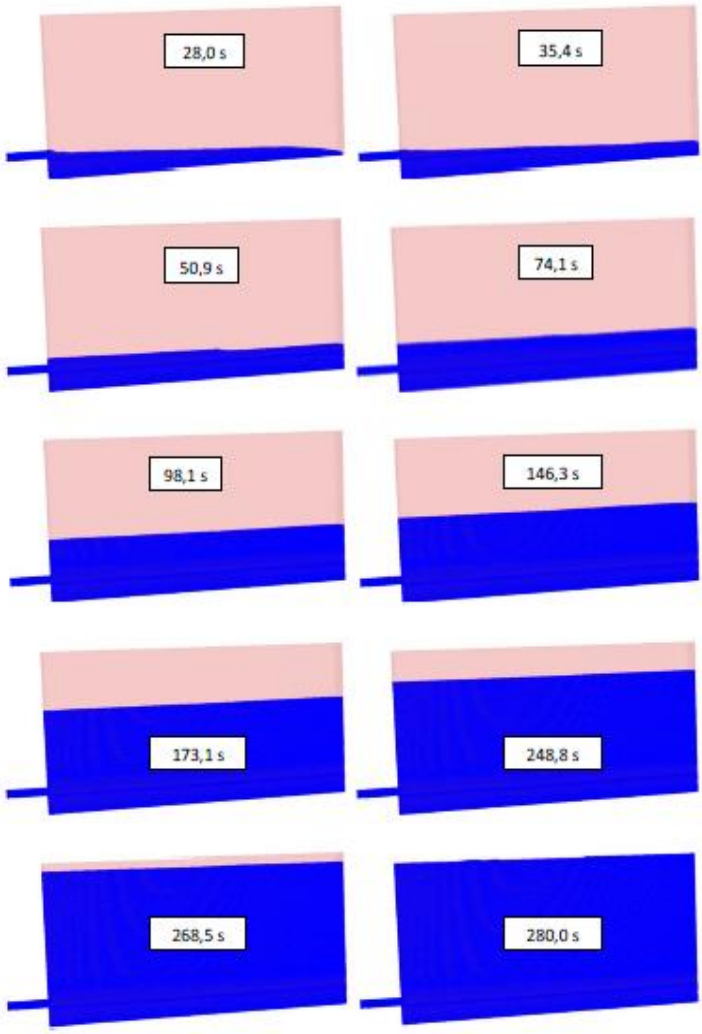

Fig. 6-17: Simulated filling process of wall type A.

Fig. 6-17 and Fig. 6-18 clearly show the evolution of the shape of the concrete surface during the base-filling processes. A small slope within the concrete surface can be observed during the initial stages of the wall casting processes. This slope gradually disappears towards the end of the filling processes due to the self-levelling properties of the SCC.

The simulated shape of the concrete surface was in good agreement with the observed shape during the formwork filling tests. This is qualitatively demonstrated in Fig. 6-19 for the columns and in Fig. 6-20 for the walls.

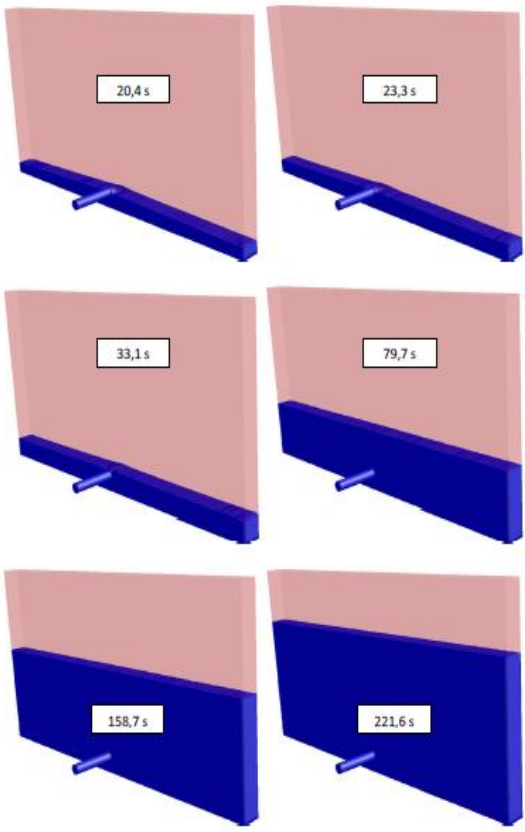

Fig. 6-18: Simulated filling process of wall type B.

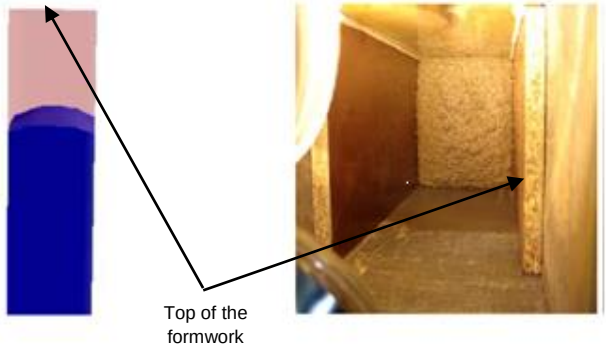

Fig. 6-19: Comparison of the simulated SCC-air interface with the on-site observation for column type A at t = 14 s.

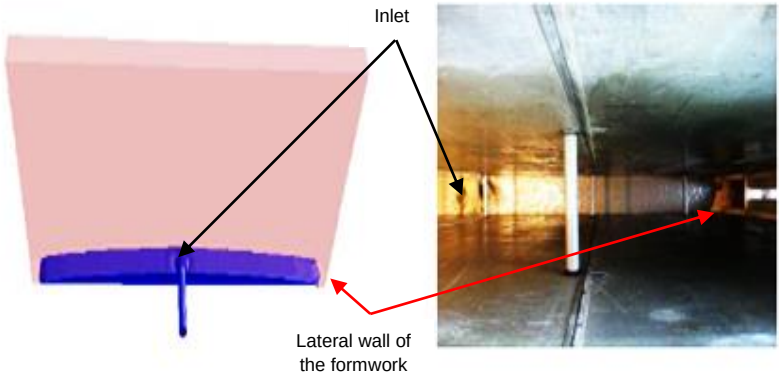

Fig. 6-20: Comparison of the simulated SCC-air interface with the on-site observation for wall type B at t = 18 s.

6.2.1.7 Comparison of the results and discussion

6.2.1.7.1 Comparison of the results

Because in our experiments the SCC was pumped from the base of the formworks up to the top, it was constantly in motion during the filling process. The time needed to fill each of the formworks was very short, around 16 s for both columns and around 280 s for both walls.

According to Billberg [6.16] and Roussel [6.25], the characteristic time to build up a thixotropic structure in most SCC mixtures is about 280 s and higher (see also chapter 3). This motivates our assumption that a possible reduction of the formwork wall pressure due to thixotropy can be disregarded during the first series of formwork filling tests.

Without a thixotropic structural build-up, the formwork pressures are expected to be slightly higher than hydrostatic for low filling velocities (see Eq. (3.35) in chapter 3), because at these low filling velocities the resulting hydraulic losses will be much smaller than the hydrostatic pressure component.

Therefore, in the first series of formwork filling experiments, formwork wall pressures that are slightly higher than hydrostatic can be expected during the filling of the two walls due to the relatively low casting speeds when compared to the column base-filling tests.

The wall pressure during the filling of the two walls has been measured at several positions close to the base of the formworks, as shown in Fig. 5-3 of chapter 5. The following graphs show the measured wall pressures and the simulated wall pressures at these locations.

The type of the pressure measurement devices used during the filling of two walls is listed in Table 5-1 of chapter 5.

During casting, some of the pressure measurement devices were damaged by the coarse aggregates of the SCC right from the start of the experiment. This was the case for the electronic pressure sensor mounted at position 4 of wall type A, and the manometer with the intermediate water chamber mounted at position 3 of wall type B. For these two positions no wall pressures could be recorded.

Due to practical difficulties, it was not possible to stop the filling process of the two walls exactly at a height of 2 m. Therefore the resulting height was 1.955 m for wall type A and 2.061 m for wall type B.

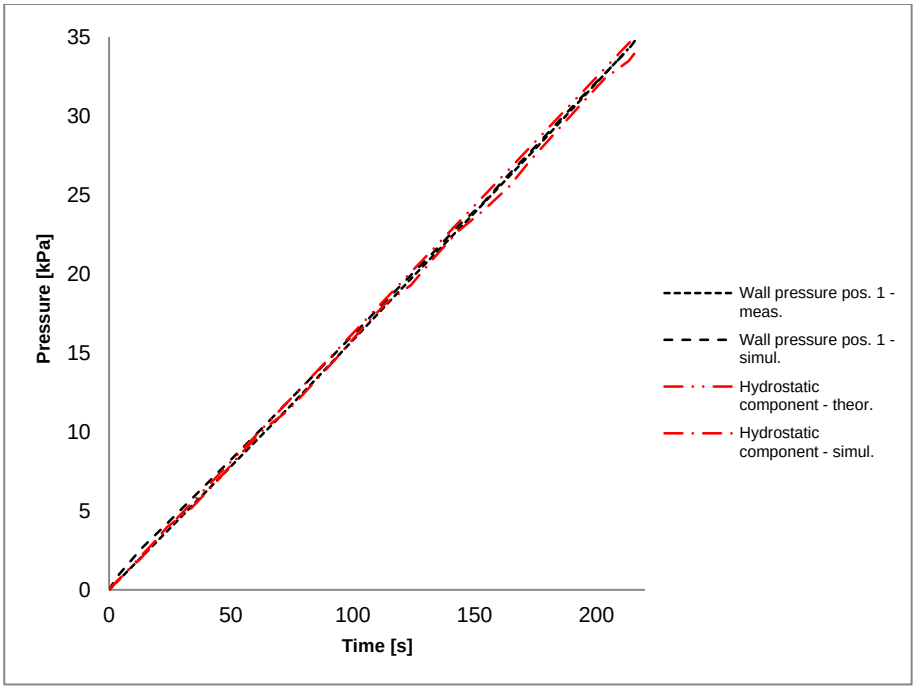

Fig. 6-21: Wall pressure at the electronic pressure transducer of wall type A - pos. 1.

As can be observed from Fig. 6-21, the wall pressure measured by the electronic pressure sensor at position 1 of wall type A remains slightly higher than hydrostatic all the way during the filling process, and is therefore in agreement with the expected wall pressure derived from Eq. (3.35) when the hydraulic losses are small due to the low filling velocity of 0.00714 m/s. The simulated wall pressure at the same location is also a little higher than hydrostatic.

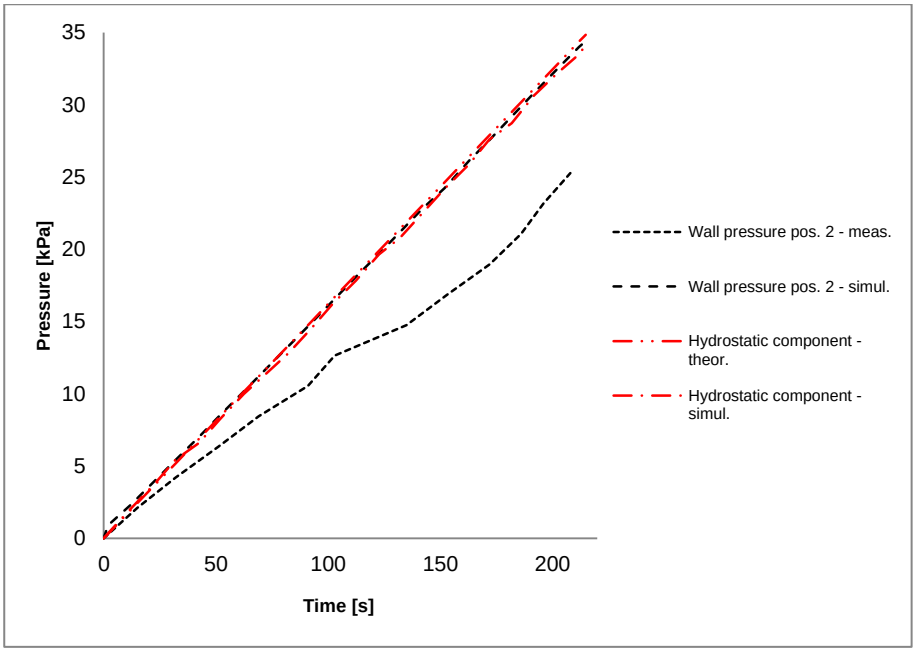

Fig. 6-22: Wall pressure at the manometer of wall type A - position 2.

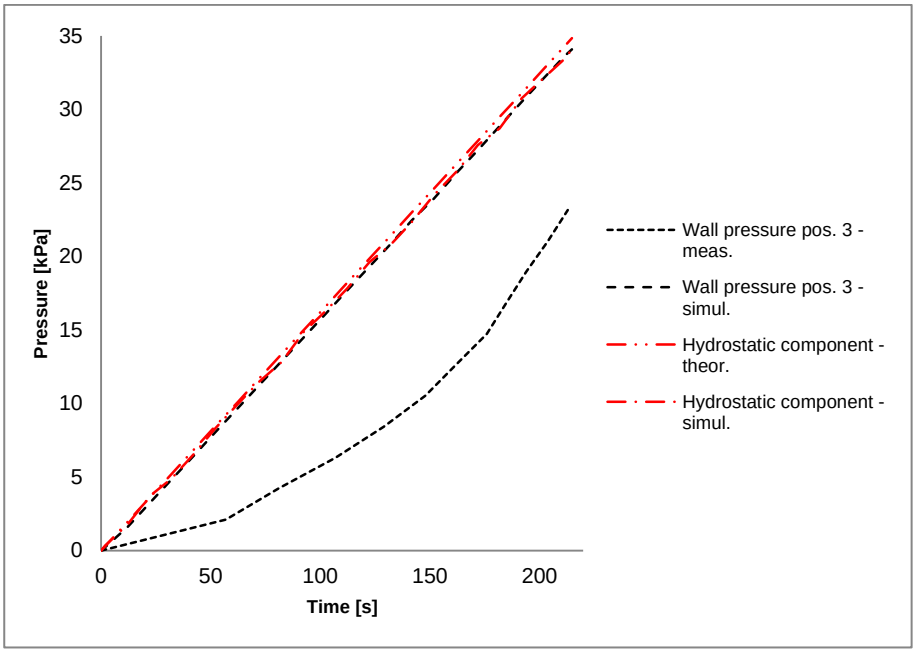

Fig. 6-23: Wall pressure at the manometer of wall type A - position 3.

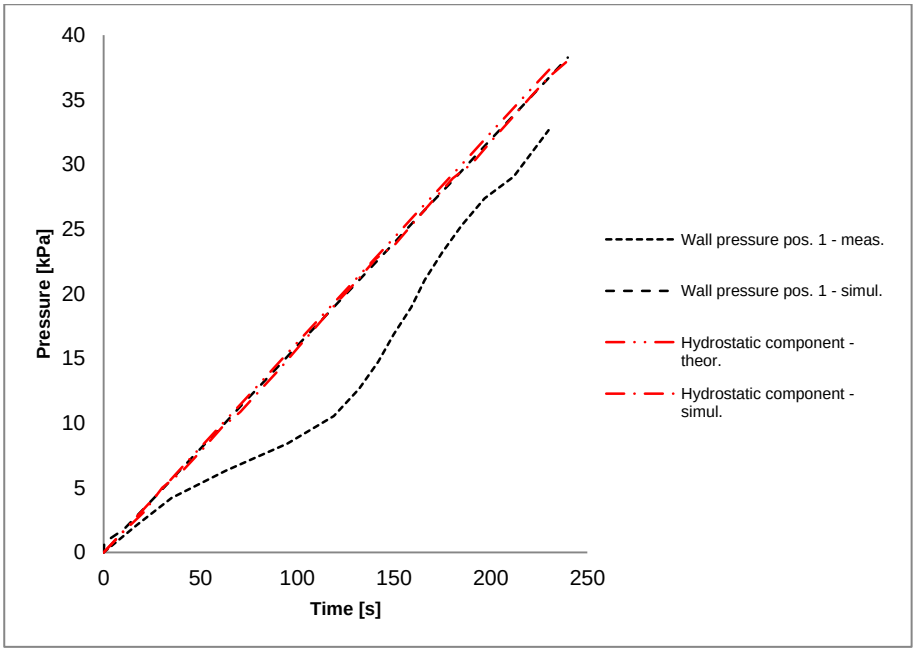

Fig. 6-24: Wall pressure at the manometer above the inlet of wall type B - position 1.

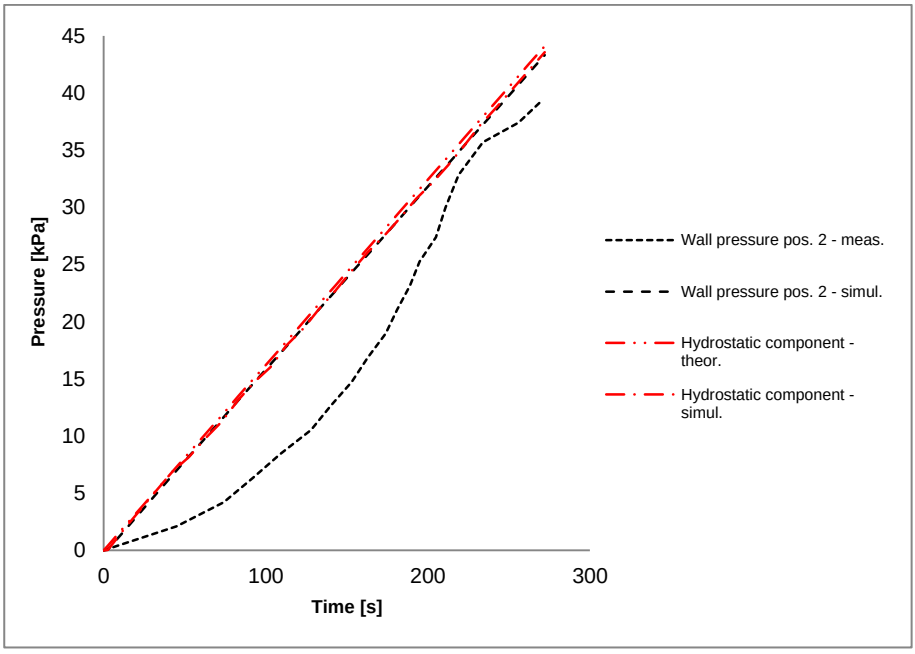

Fig. 6-25: Wall pressure at the manometer of wall type B - position 2.

On the other hand, the wall pressures at the measurement positions 2 and 3 of wall type A are lower than the expected and simulated wall pressure. For wall type B, Fig. 6-24 and Fig. 6-25 also show a wall pressure at the measurement positions which is lower than the hydrostatic pressure, although the difference between the expected hydrostatic wall pressure and the measured wall pressure is smaller than the wall pressure difference observed at position 2 and 3 of wall type A.

In reality, are the occurring wall pressures at these locations really lower than the hydrostatic pressure or is this a measuring artefact? An answer to this question will be formulated in the discussion in the next section.

Due to the higher filling velocity of 0.137 m/s for the columns, we expect the wall pressures to be higher than the hydrostatic pressure, because the hydraulic losses in these filling cases should be higher than during the filling of the two walls. Fig. 6-26 and Fig. 6-27 show the measured wall pressure evolution just above the inlet of the two columns. The wall pressures above the inlet were measured with a manometer - intermediate water chamber device.

As for the walls, it was also not possible to fill the two formworks of the columns exactly up to a height of 2 m. Therefore the resulting height was 2.012 m for column type A and 2.225 m for column type B.

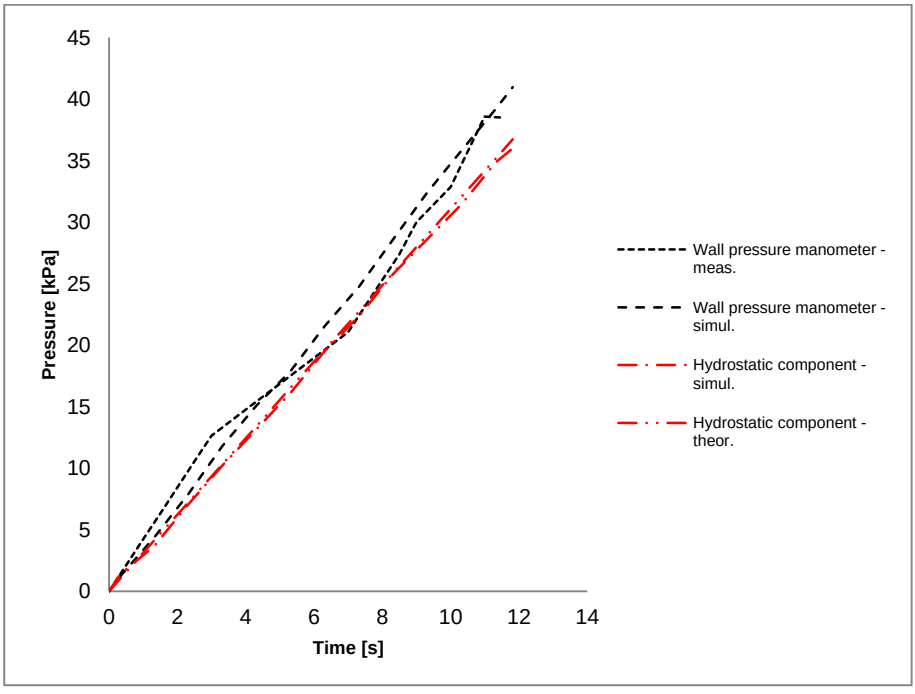

Fig. 6-26: Wall pressure above the inlet at the manometer of column type A.

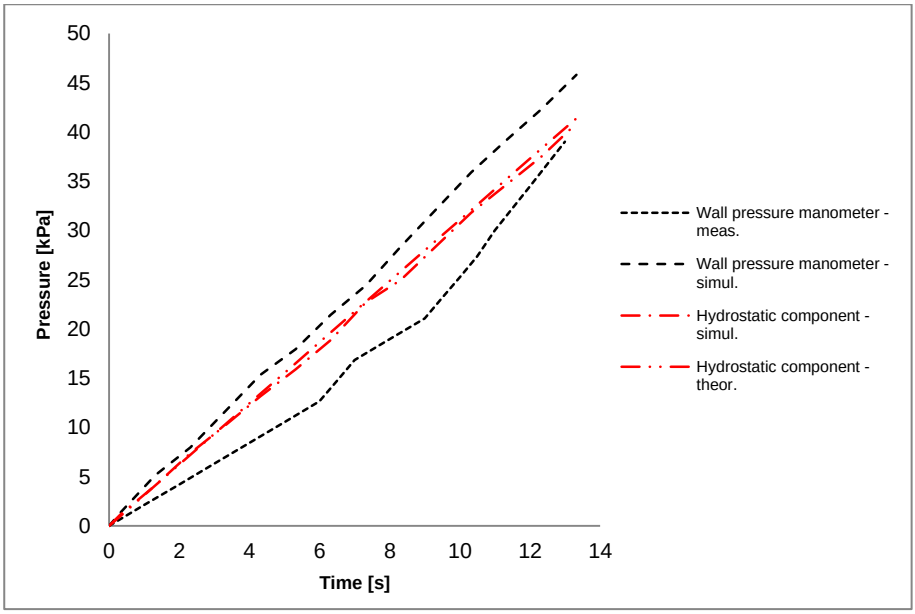

Fig. 6-27: Wall pressure above the inlet at the manometer of column type B.

When looking at the measured wall pressure evolution of column type A, we notice that the measured wall pressure above the inlet is indeed higher than the hydrostatic pressure: these measurements are consistent with the simulated wall pressures at the same measuring location. On the other hand, the wall pressure recorded just above the inlet of column type B is lower than the hydrostatic pressure at the same location. This observed discrepancy will also be discussed in the next section.

Finally, some additional reflections regarding the flow of SCC inside the formworks during the performed filling tests. Fig. 6-28 shows the simulated wall pressure just above the inlet of column type A. Due to the SCC flow pattern in the 90° bend at the inlet, there is a difference between the wall pressure at the front of the column and wall pressure at back of the column, where the entering SCC is hitting the wall. This wall pressure difference just above the inlet will be more pronounced at high filling velocities, and so, is only relevant in our column filling tests. The difference is about 130 Pa. Compared to the absolute value of the wall pressure above the inlet, this small pressure difference is rather insignificant. The concrete velocities in the formwork below the inlet are very small. This is illustrated in Fig. 6-29, where the velocity vector plot in the centre plane of column type A is shown. For the two walls the velocities in the lower zone are even much lower. The contribution of the hydraulic losses to the wall pressure in the region below the inlet will be very small, and we may conclude that the difference between the wall pressure at the bottom of the formwork and the wall pressure at the measurement location just above the inlet is the hydrostatic pressure due to the height of SCC below the manometer position. The simulation results shown in the following table prove the validity of Eq. (3.35).

Table 6-7: Comparison of the simulated wall pressures of column type A at two locations (simulation time t = 14.1 s).

Simulated wall pressure at the manometer location above the inlet (h = 0.385 m)	36287 Pa
Simulated wall pressure at the base of the column	44964 Pa
Difference between the simulated wall pressure of the two locations	8752 Pa
Hydrostatic pressure component of the SCC between the manometer and the base	9.81 m/s² x 2314.4 kg/m³ x 0.385 m = 8741 Pa

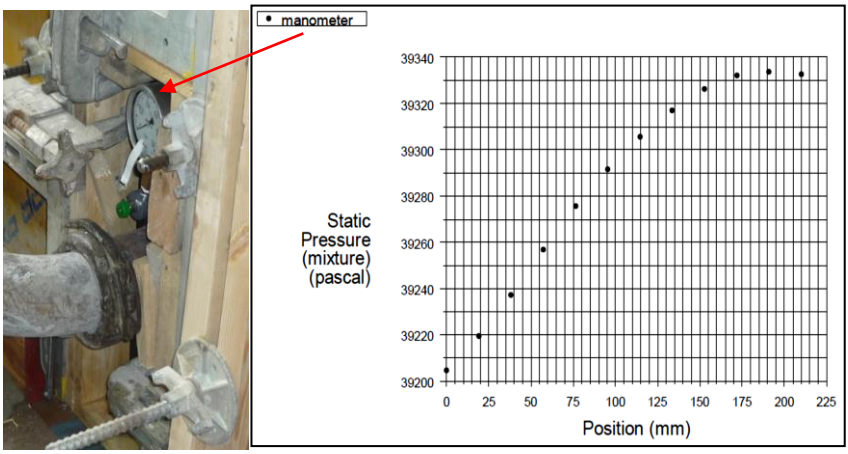

Fig. 6-28: Simulated wall pressure just above the inlet of the columns (at 0 mm = pressure measurement, at 210 mm = formwork wall facing the inlet).

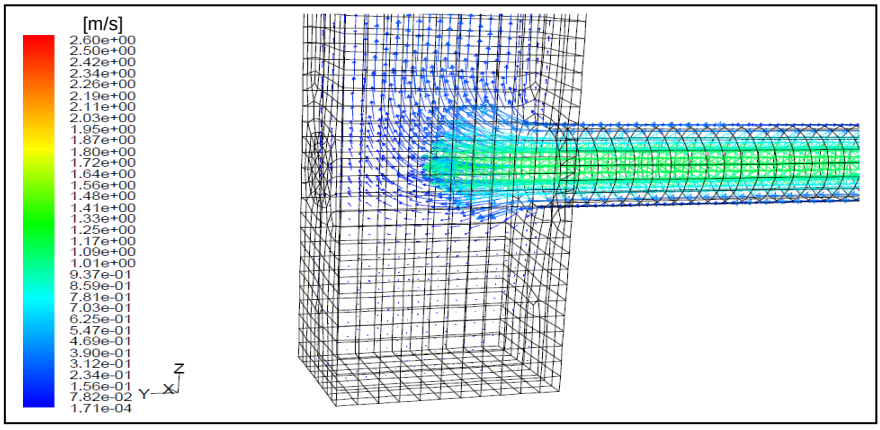

Fig. 6-29: Vector plot of the simulated velocities below the inlet of column type A at simulation time t = 14.1 s.

6.2.1.7.2 Discussion

When studying the measurements performed with the electronic pressure sensors and the manometer - intermediate water chamber units carefully, we can summarize the following observations:

- The electronic pressure sensor presents a linearly varying wall pressure with time, whereas the measurements done with the manometer - intermediate water chamber units lead to a non-linear evolution of the wall pressure.
- The wall pressure measured by the electronic pressure sensor above the inlet of wall type A and the manometer - intermediate water chamber unit above the inlet of column type A are both in agreement with the theory derived in chapter 3 and with the simulation results.
- The other wall pressure measurements, performed with manometer - intermediate water chamber units, are lower than the simulated wall pressures and even lower than the hydrostatic pressure which is related to concrete height being cast in the formwork. These measurements are not in agreement with the theory derived in chapter 3.
- The measured wall pressures of the columns are higher than the measured wall pressures of the walls, although the hydrostatic pressure component remains equal for all casts.

Although the thixotropic parameters of Eq. (2.21) and Eq. (2.22) have not been determined through a series of separate rheometer tests, as proposed by Roussel [6.25], we believe that, motivated by the statements made earlier in section 6.2.1.7.1, thixotropy cannot be important in our base-filling tests, and as such thixotropy is not an explanation for the observed discrepancy between theory/simulation and some of the measured wall pressures. Thixotropy could not have influenced the formwork wall pressure, because of the short filling times and the SCC being constantly sheared during the whole filling process (certainly for the columns, maybe less for the walls).

However, the non-linear evolution of the measured formwork pressures of the walls, shown in Fig. 6-21 up to Fig. 6-25, are related to the experienced shortcomings of the manometer - intermediate water chamber units used in the filling tests. The calibration of these pressure measurement units turned out to be very difficult, due to the non-linear deformation of the plastic membranes submitted to the concrete pressure, the variable surface tension of the used membranes and the unavoidable inclusion of air bubbles into the water chambers. After the SCC had hardened and the formwork walls were removed, we observed that the aggregates of the SCC were completely blocking the rubber membrane of the pressure measurement units of the two walls. The diameter of the circular measuring surface with the rubber membrane was 20 mm. Although the nominal maximum size of the coarse aggregates was 14 mm (see chapter 5 and appendix B), some of them did have a diameter of about the same size as the pressure measurement opening. This blocking would surely result into lower wall pressures being measured during the formwork filling tests. We therefore attribute the mere existence of the discrepancy between theory/numerical simulations and some of the measured wall pressures to a measuring artefact.

Further optimization of the design of the manometer - intermediate water chamber units is necessary in order to avoid the previously mentioned shortcomings. Although the present design of the manometer - intermediate water chamber units was simple and the costs for manufacturing these units were very low compared to the price of the electronic pressure sensors, it turned out that measuring the wall pressure with an electronic sensor is more accurate and more practical. It is also much more convenient to capture the measurement data electronically, instead of having to use camera's and stop watches to monitor the evolution of the manometers.

The simulation results and the pressure measurements clearly show the contribution of the hydraulic losses to the formwork wall pressures. For formworks being filled from the base at a high casting rate, the hydraulic losses become important, certainly for highly viscous SCC. The theory derived in chapter 3 as well as the simulations reveal that the hydraulic losses add up to the hydrostatic pressure, thus increasing the formwork pressure even more. This is clearly seen in all the simulation results and in some of the pressure measurements. Although the hydrostatic pressure is the same for all cast structural elements because of equal height, the formwork pressure at the base of the columns is higher than for the walls. This is because the cross-section of the walls is much larger than the cross-section of the columns, and therefore the filling velocity and the resulting flow losses in the columns are much higher than the filling velocity and the related hydraulic losses in the walls.

The hydraulic losses, when pumping SCC from the base of the formworks up to the top, will even increase more if the flow cross-section of the formwork is reduced due to the presence of steel reinforcements or if the viscosity of the chosen SCC is higher, as will be shown in section 6.2.2 and in section 6.3. On the other hand, Feys [6.1] and Le et al. [6.12] have clearly demonstrated that when pumping SCC through ducts, the hydraulic losses are much lower than expected, due to the presence of a thin cement paste layer near the walls with a much lower viscosity than the concrete bulk viscosity (see also section 6.1). The effect of the thin paste layer near walls on the occurring hydraulic losses can be expected to be much more important when the ratio between the sum of the wall surfaces (formwork and rebars) and the total formwork volume reaches a certain (yet undetermined) value.

So for accurately determining the hydraulic losses in ducts while pumping SCC to the formworks [6.1], the correct implementation of the no-slip condition applied to the thin cement paste layer near the walls becomes essential. In the first series of base-filling tests, this influence is much less pronounced because of the relatively large cross-sections (certainly for the walls) and of the absence of rebars.

Further research is necessary in order to determine the threshold value of this previously mentioned ratio of wall surface to formwork volume, for which a correct numerical implementation of the interaction between the thin cement paste layer and the walls, but also the interaction of the cement paste layer and the remaining concrete becomes necessary.

These effects will be further analysed and quantified in section 6.3, when presenting the simulation results of the full-scale formwork base-filling tests with different SCC mixtures, different casting speeds and with steel rebars being present. For these casting tests, electronic pressure sensors have been used in order to measure the occurring formwork wall pressures more accurately and to rule out any measuring artefacts.

When more details on the formwork base-filling process are required and accurate measurements cannot be implemented or are very difficult to perform, numerical simulations can be carried out using the implemented Herschel-Bulkley material model, describing the relation between the applied shear rate and the resulting shear stress inside the fresh SCC, in combination with the VOF method. These CFD simulations can predict the formwork pressures, the flow and time evolution of the casting process accurately, provided the correct input data is supplied.

6.2.2 Second series of base-filling tests

6.2.2.1 Overview of the numerical models

As mentioned in chapter 5, during the second series of formwork filling tests eight columns and one large I-beam have been cast with two different SCC mixtures and at two casting speeds. Four columns without rebars and four columns with rebars were cast. The large I-beam was cast without rebars or pre-stressing tendons. These nine formwork base-filling processes have been modelled using Ansys Fluent® v.12.1 and v.14.0 and the simulations were also performed using the FVM and the VOF method. An additional interface tracking method, the Level Set (LS) method, has been implemented in Ansys Fluent v.14.0 [6.22, 6.26 and 6.27] which, when used in combination with the VOF method, highly improved the simulation of the moving free concrete surface during the filling process. The following sections describe in detail the numerical models, which have been used for simulating the casting experiments without rebars of the second series of base-filling tests.

6.2.2.2 Model equations

The same equations as formulated in section 6.2.1.2 were solved in the numerical models of the second series of casting tests.

6.2.2.3 Computational domain

For the numerical simulation of the SCC flow through the formworks, illustrated in Fig. 5-4 and Fig. 5-5, a 3-D geometry is constructed for each cast element and meshed with the Fluent Gambit® v.2.3 pre-processor. Due to symmetry, only half of each geometry is modelled.

Fig. 6-30 and Fig. 6-31 show the resulting high quality mesh for the columns and for the large I-beam.

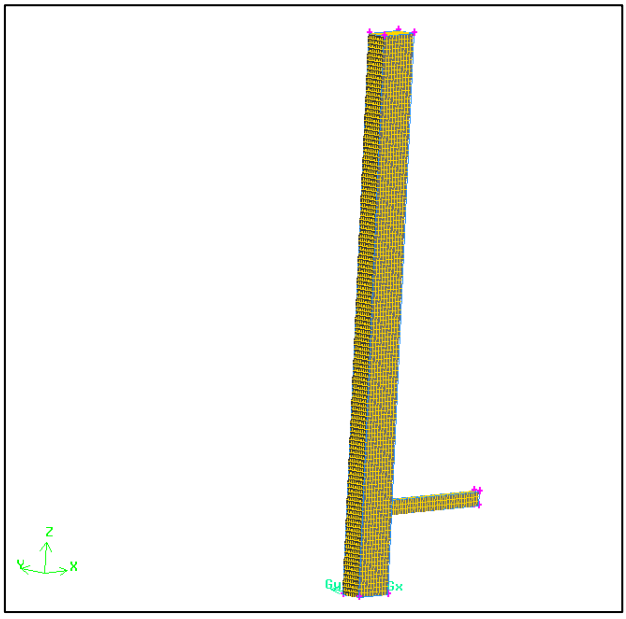

Fig. 6-30: Computational domain for the column filling process.

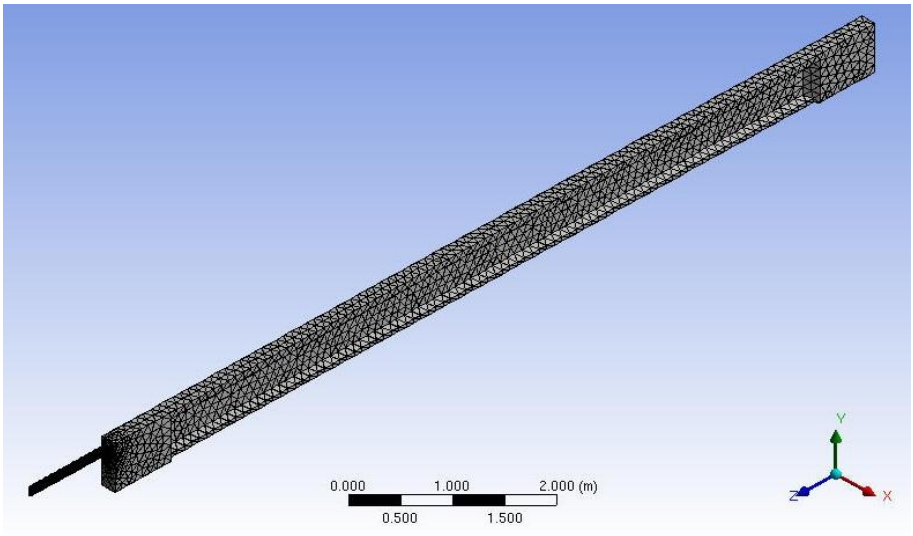

Fig. 6-31: Computational domain for the I-beam filling process.

The implemented VOF(-LS) discretization scheme proved to be much more stable when using a full hexahedral mesh instead of a tetrahedral mesh. Unfortunately, formworks with more complex shapes and/or more complex rebar configurations will not be easily meshed with hexahedral elements.

6.2.2.4 Boundary conditions

Boundary conditions need to be applied to the computational domain, in order to obtain solutions for the model equations mentioned in section 6.2.1.2. At the flow inlet, a uniform velocity profile of the incoming SCC and the volume fraction of the SCC phase is imposed, while at the top of the formwork, the pressure is atmospheric, resulting in a zero gauge pressure condition at the outlet. At the walls, a no-slip condition is assumed. The imposed inlet conditions are derived from the flow measurements performed during the filling tests (see Table 5-3 and Fig. 5-7) and the geometry of the inlet duct. The length of the inlet duct used in the present numerical models has been determined from small preliminary simulations, which aimed at obtaining for laminar flow conditions a fully developed velocity profile at the end of the duct, when the SCC is entering the formwork.

6.2.2.5 Solution of the model equations

The flow equations are discretized applying the FVM-VOF-LS scheme and they are solved with a 3-D, double precision, implicit pressure-based solver.

Table 6-8: Solver controls.

Controls	Ansys Fluent v.12.1	Ansys Fluent v.14.0
Multiphase model/scheme	2 phases VOF	2 phases VOF-LS
Flow regime	Laminar	Laminar
VOF scheme	Explicit	Explicit
Transient controls	NITA[a]	-
Unsteady formulation	1st order implicit	1st order implicit
Body force formulation	Implicit body force	Implicit body force
Momentum discretization	2nd order upwind	2nd order upwind
Volume fraction discretization	Geo-reconstruct	Geo-reconstruct
Level-set function discretization	-	1st order upwind
Gradient discretization	Least squares cell based	Least squares cell based
Pressure discretization	Body force weighted	PRESTO![b]
Pressure-velocity coupling	Fractional step method	SIMPLE[c]

[a] Non-Iterative Time Advancement

[b] Pressure Staggering Option

[c] Semi-Implicit Method for Pressure-Linked Equations

The solver settings used in the performed numerical simulations of the formwork filling tests are listed in Table 6-8.

6.2.2.6 Formwork filling simulations

The density and the Herschel-Bulkley parameters of the fresh SCC need to be known in order to perform the numerical simulations of the filling processes. The measured densities and the rheological properties are summarized in Table B-6 and Table B-7 of appendix B.

The numerical models with the previously mentioned solver settings were able to accurately simulate the transient base-filling processes of the columns but not of the large I-beam.

The SCC height was recorded at five different positions along the I-beam, as indicated in Fig. 5-9. The measurement results and the related simulation results at these five stations are summarized in Fig. 6-34. Fig. 6-32 shows the simulated SCC free surface at the end of the filling process.

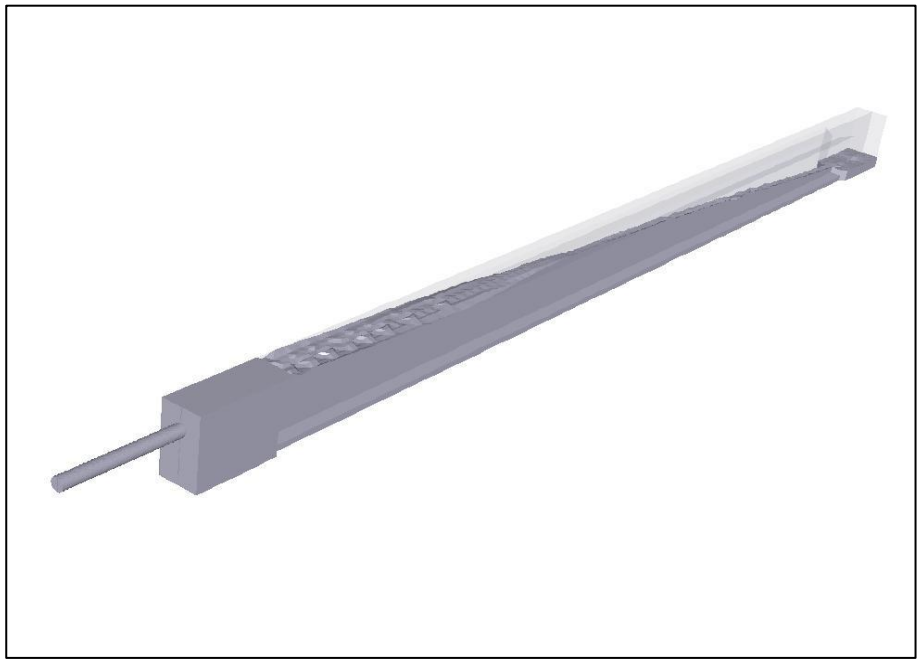

Fig. 6-32: Simulated filling process of the I-beam.

While there was no SCC overflow during the actual I-beam filling process (see Fig. 6-33), the simulation results did predict an overfilling at the first measuring station (50 cm), right after the inlet. Fig. 6-34 reveals that the SCC experiences more flow resistance during the simulation than during the real filling process, leading to an over-filling in the first stations and an under-filling in the last stations of the I-beam. This could be attributed to the wall effect mentioned in section 6.2.1.7.2. More reflections about this matter in section 6.3.

Fig. 6-33: SCC surface just after the inlet at the end of the I-beam filling process.

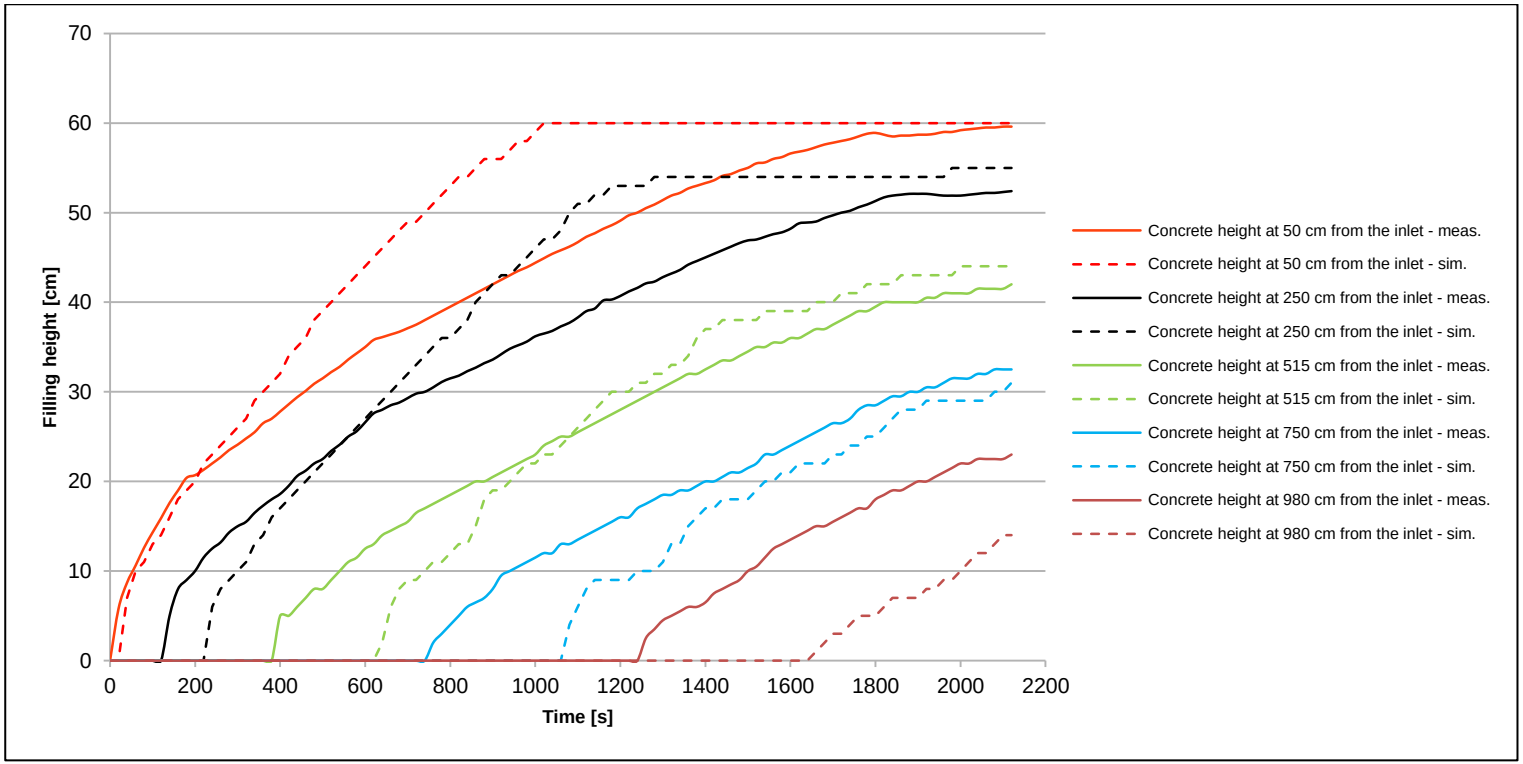

Fig. 6-34: Measured (--) and simulated (- -) SCC filling heights at five stations during the filling process of the I-beam.

6.2.2.7 *Analysis of the results*

In chapter 3 we stated that for the base filling process, according to the Bernoulli equation (see Eq. (3.33)), the formwork wall pressure is the sum of the hydrostatic pressure and the shear flow losses.

The wall pressure during the filling of the columns has been measured at several positions, as shown in Fig. 5-8 of chapter 5.

The following graphs show the measured formwork wall pressures, the simulated wall pressures and the hydrostatic pressure at these locations.

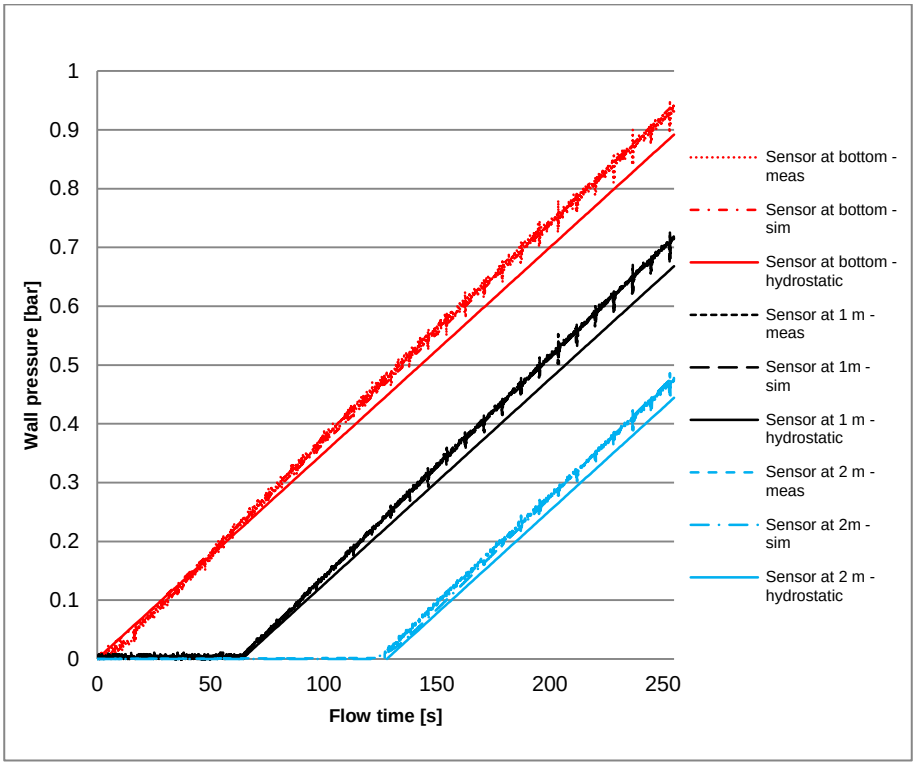

Fig. 6-35: Wall pressure p_{wall} at manometer positions of column 1 - no rebars - low viscosity SCC - low casting speed.

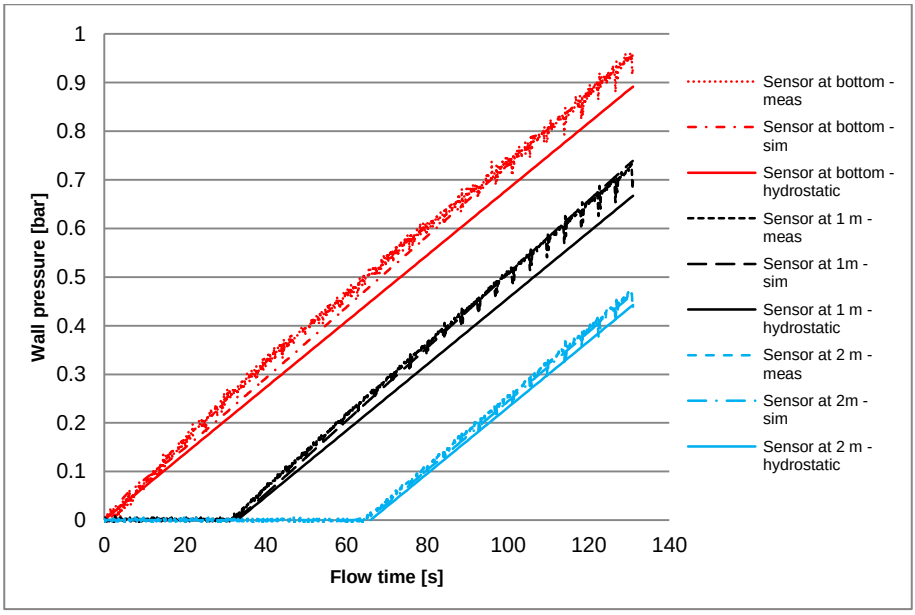

Fig. 6-36: Wall pressure p_{wall} at manometer positions of column 3 - no rebars - low viscosity SCC - high casting speed.

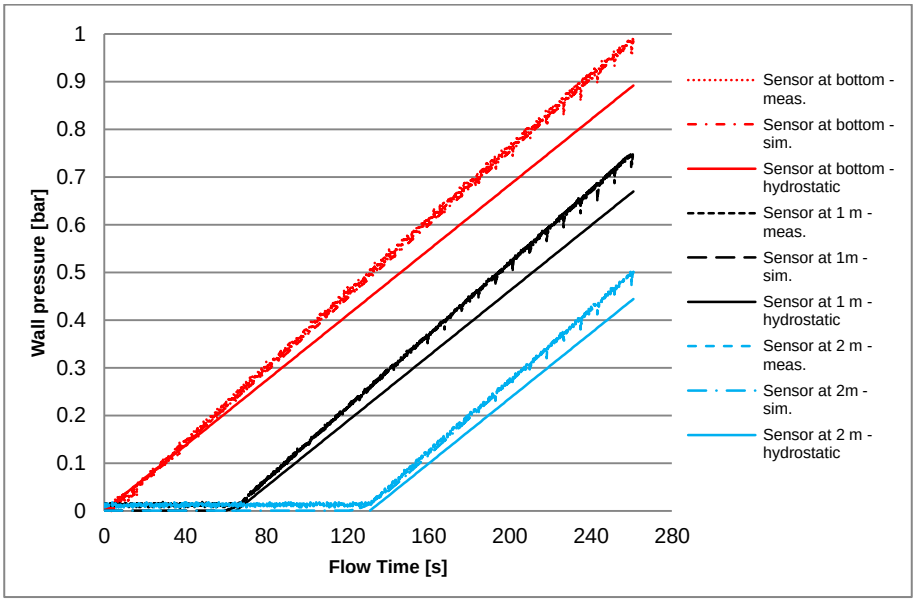

Fig. 6-37: Wall pressure p_{wall} at manometer positions of column 5 - no rebars - high viscosity SCC - low casting speed.

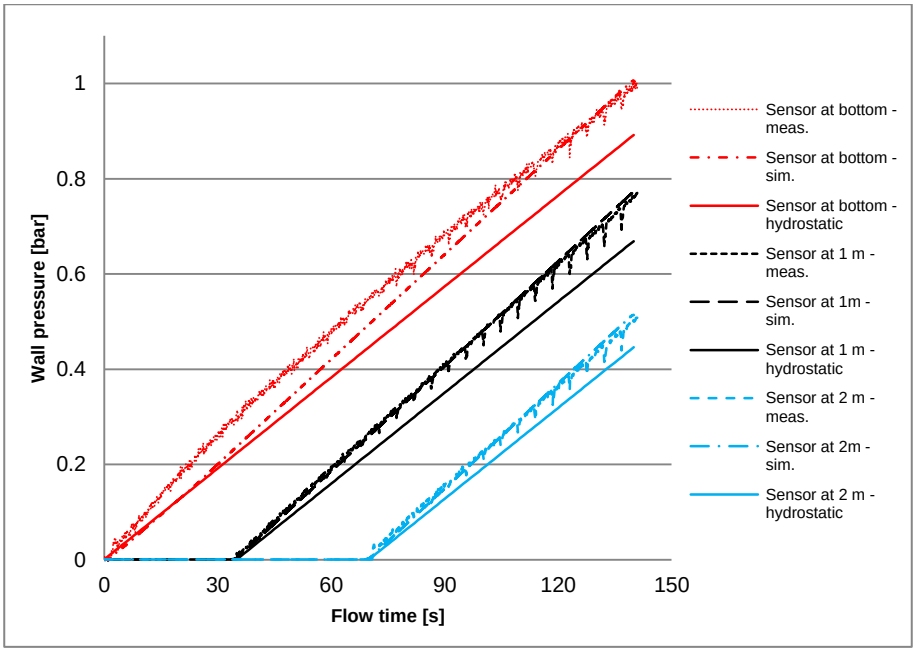

Fig. 6-38: Wall pressure p_{wall} at manometer positions of column 7 - no rebars - high viscosity SCC - high casting speed.

When analysing the presented graphs, we observe a very good agreement between the measurements and the simulation results. As also mentioned in chapter 5, the pressure sensors mounted at the bottom of some of the columns reveal a less linear curve than the other two pressure sensors mounted at the walls of the columns. Cauberg et al. [6.29] mentioned in their research study that these type of pressure sensors did not always measure correctly. They could not determine the cause of the faulty operation. The presented graphs also clearly show the impact of the shear flow losses on the resulting formwork wall pressures. The shear flow losses may certainly not be neglected regarding the maximum formwork wall pressures when the base-filling technique is used for casting.

6.2.3 Conclusions

Two series of large-scale formwork filling tests by pumping self-compacting concrete (SCC) bottom-up have been performed and simulated using computational fluid dynamics (CFD) modelling techniques. The following conclusions are formulated:

- When pumping SCC from the bottom, in principle hydrostatic pressures can be expected increased with the hydraulic pressure losses. The hydraulic losses become more important for high casting rates, small formwork cross-sections (e.g. columns) or when using an SCC with a high viscosity.

- When pumping SCC from the bottom it is possible to noticeably reduce the casting times by applying high casting rates. However, stronger and stiffer formwork wall systems will be required to sustain the higher wall pressures.
- The use of a manometer, mounted on an intermediate water chamber and sealed with a rubber membrane, to measure the wall pressures in a formwork during casting leads to inaccurate measurements. The use of electronic pressure sensors to measure formwork wall pressures is therefore to be preferred. It is much more convenient to directly capture the wall pressure data in a digital format for further analysis.
- In case of a high casting rate, the effect of thixotropy on the formwork pressure can be disregarded. The second series of base-filling tests confirm this statement, as no decay of the measured wall pressures was observed during casting.
- The correct determination of the rheological material parameters of the SCC mix used in the filling process is important, as these parameters have an influence on the resulting formwork wall pressures, especially the consistency factor and the consistency index.

The formwork filling process and the related formwork pressures can be accurately simulated by means of the FVM-VOF-LS modelling technique. These kind of CFD simulations allow to optimize the formwork filling process during the design phase.

6.3 Simulation of the formwork base-filling tests with rebars

In the current chapter, the CFD models, the CFD simulations and the new analytical model of the formwork base-filling tests with rebars, that have also been performed at the MLCR of Ghent University, are presented. This section is divided in four parts:

- In a first part, the numerical model based on the combined FVM-VOF-LS scheme is described;
- In a second part, the numerical model based on a combination of the FVM-VOF-LS method and porous zone modelling is described;
- In a third part, the influence of the thin cement paste layer near walls on the resulting shear flow losses, which has already been introduced in section 6.1 and section 6.2, is further discussed;
- In a last part, the application to the performed pumping and base-filling experiments of the extended Poiseuille flow model for calculating the maximum wall pressure, derived in chapter 3, is presented.

6.3.1 CFD model based on the FVM-VOF-LS scheme

6.3.1.1 Numerical model configuration

The model equations for describing the base-filling experiments with rebars are again the well-known Navier Stokes conservation equations, presented in chapter 3.

The resulting model equations are solved in time and space for the static pressure, the three velocity components and the volume fractions of the two fluids being present during the base-filling process, SCC and air. The selected numerical scheme is based on the combined FVM-VOF-LS method, also presented in chapter 4. The discretized model equations of the filling tests with rebars are solved with Ansys Fluent® v.14.0, with the same solver settings as listed in Table 6-8. The technical details of the selected settings are explained in chapter 4 as well.

The material properties of the selected SCC mixture are summarized in Table B-6 and Table B-7 of appendix B. At the flow inlet, a uniform velocity profile of the incoming SCC and the volume fraction of the SCC phase is imposed, while at the top of the formwork, the pressure is atmospheric, resulting in a zero gauge pressure condition at the outlet. At the walls, a no-slip condition is assumed. The imposed inlet conditions are derived from flow measurements performed during the filling tests (see Table 5-5 of chapter 5) and the geometry of the inlet duct. The length of the inlet duct used in the present numerical models has been determined from small preliminary simulations, which aimed at obtaining for laminar flow conditions a fully developed velocity profile at the end of the duct, when the SCC is entering the formwork.

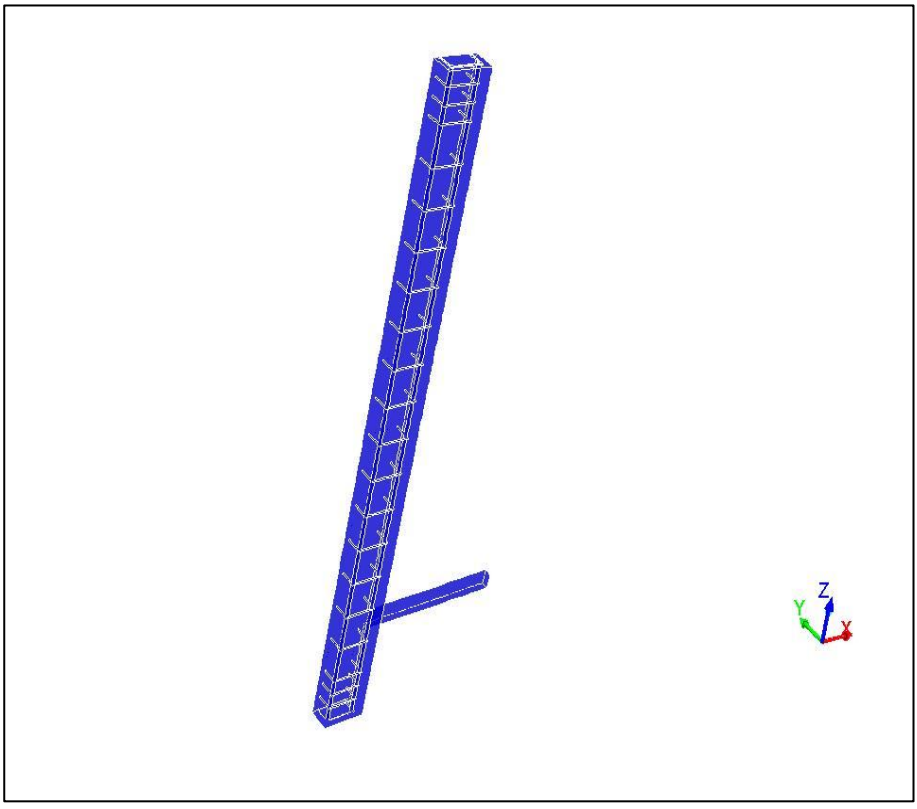

Fig. 6-39: 3-D geometry used for the base-filling process with rebars.

A 3-D geometry is constructed for the numerical simulations of the base-filling processes with rebars and meshed with the Fluent Gambit v.2.3 pre-processor. Due to symmetry, only half of the formwork geometry is modelled. Fig. 6-39 shows the resulting geometry.

In order to avoid point contacts between the longitudinal rebars and the crossing transverse reinforcement bars, all the rebars have been modelled as prismatic bars instead of cylindrical ones.

By doing this, the contacts between the rebars become small flat surfaces instead of points, which drastically improves the mesh generation process.

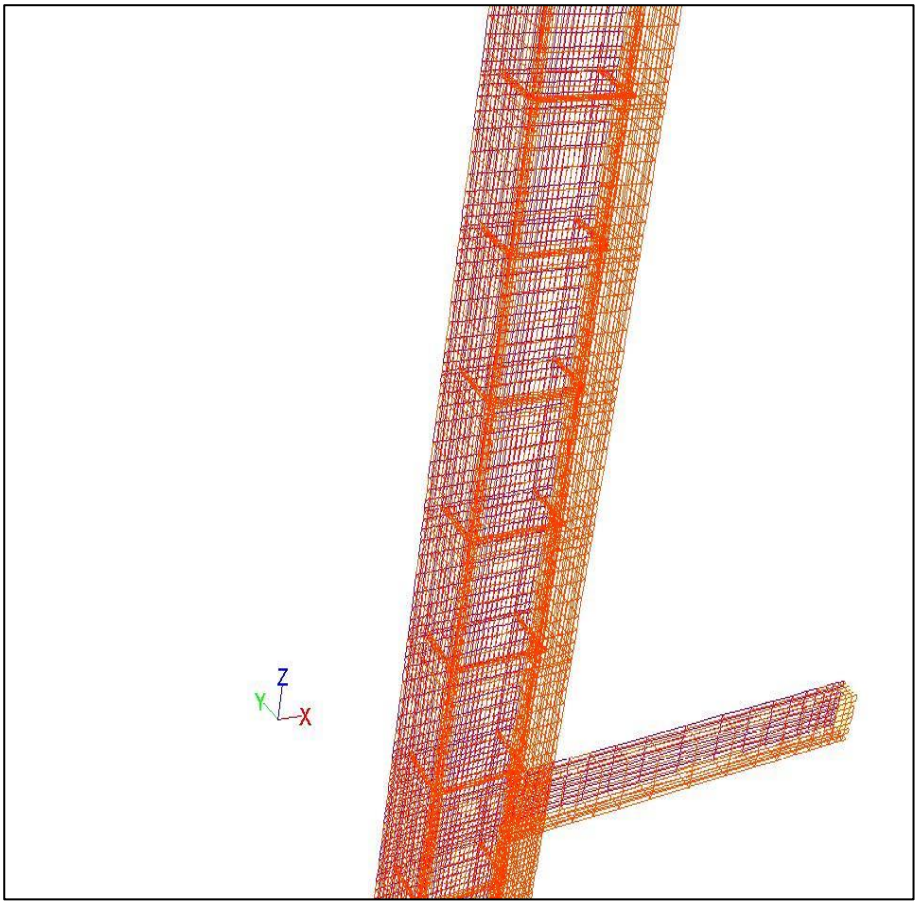

Fig. 6-40: Hexahedral mesh used for the base-filling process with rebars.

This small modification of the geometry made it possible to generate a full hexahedral mesh, shown in Fig. 6-40, leading to a higher numerical stability of the resulting numerical scheme and a faster computation.

6.3.1.2 *Analysis of the results*

In chapter 3 we stated that for the base-filling process, according to the Bernoulli equation (see Eq. (3.33)), the formwork wall pressure is the sum of the hydrostatic pressure and the shear flow losses. This has already been confirmed in chapter 5 and in section 6.2, when discussing the base-filling processes without rebars and the related numerical simulations.

In order to also validate this statement when SCC is pumped from the base into the columns with rebars, the wall pressure has been measured at several positions, as illustrated in Fig. 5-8 of chapter 5.

The following graphs present the measured wall pressures, the simulated wall pressures and the hydrostatic pressure at these locations.

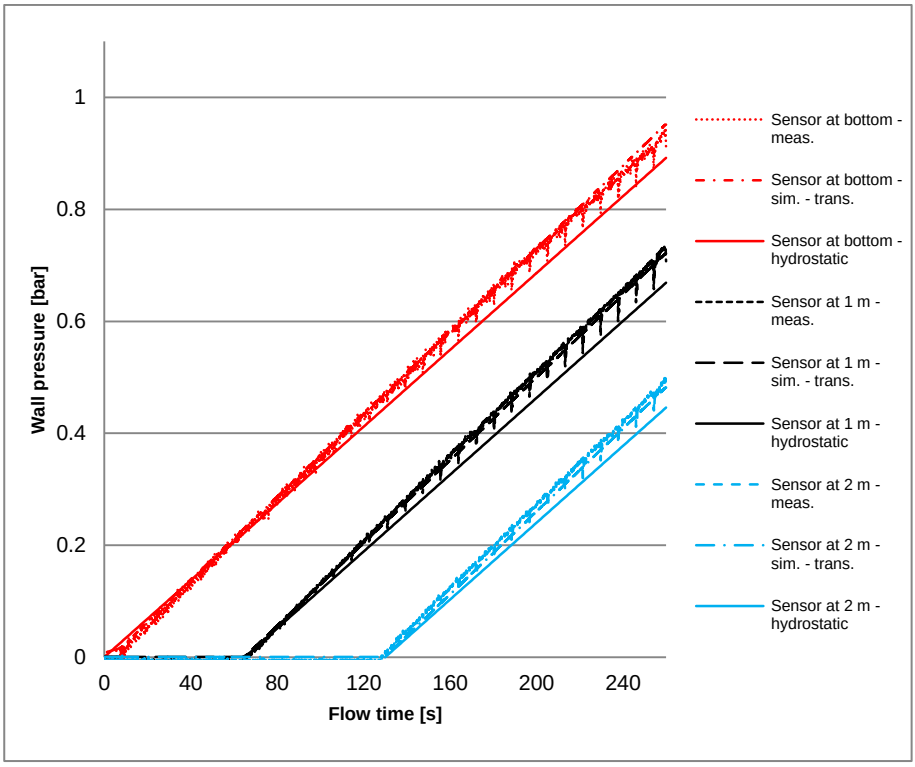

Fig. 6-41: Wall pressure p_{wall} at manometer positions of column 2 - with rebars - low viscosity SCC - low casting speed.

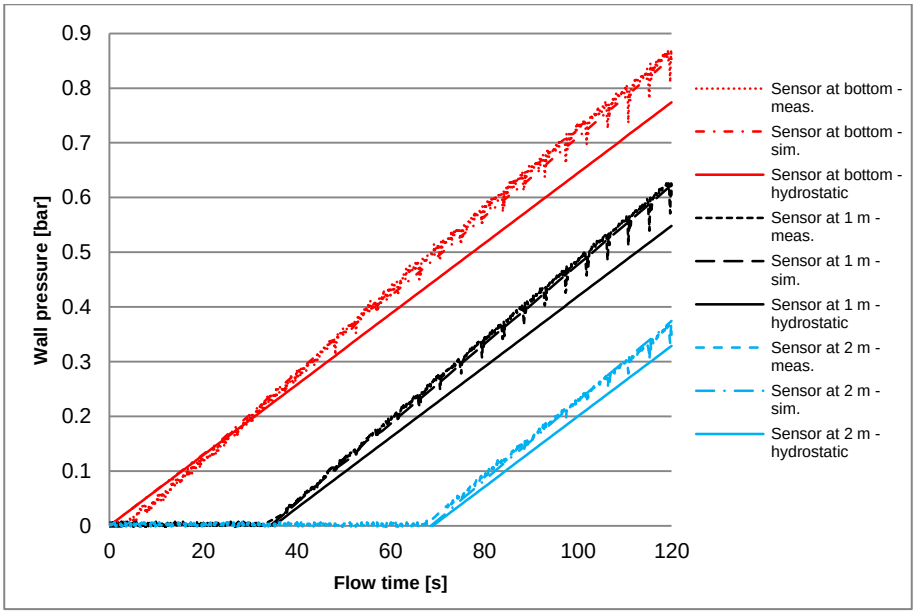

Fig. 6-42: Wall pressure p_{wall} at manometer positions of column 4 - with rebars - low viscosity SCC - high casting speed.

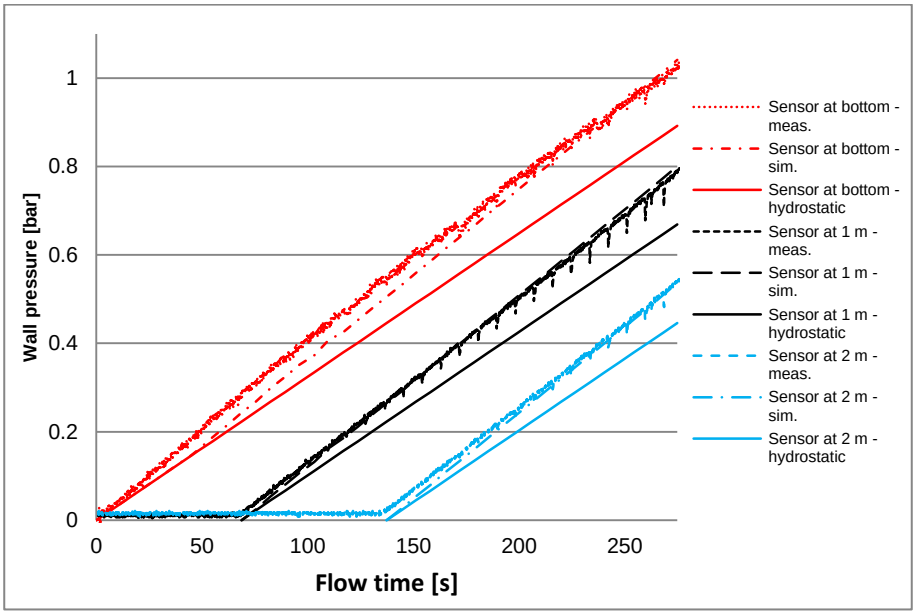

Fig. 6-43: Wall pressure p_{wall} at manometer positions of column 6 - with rebars - high viscosity SCC - low casting speed.

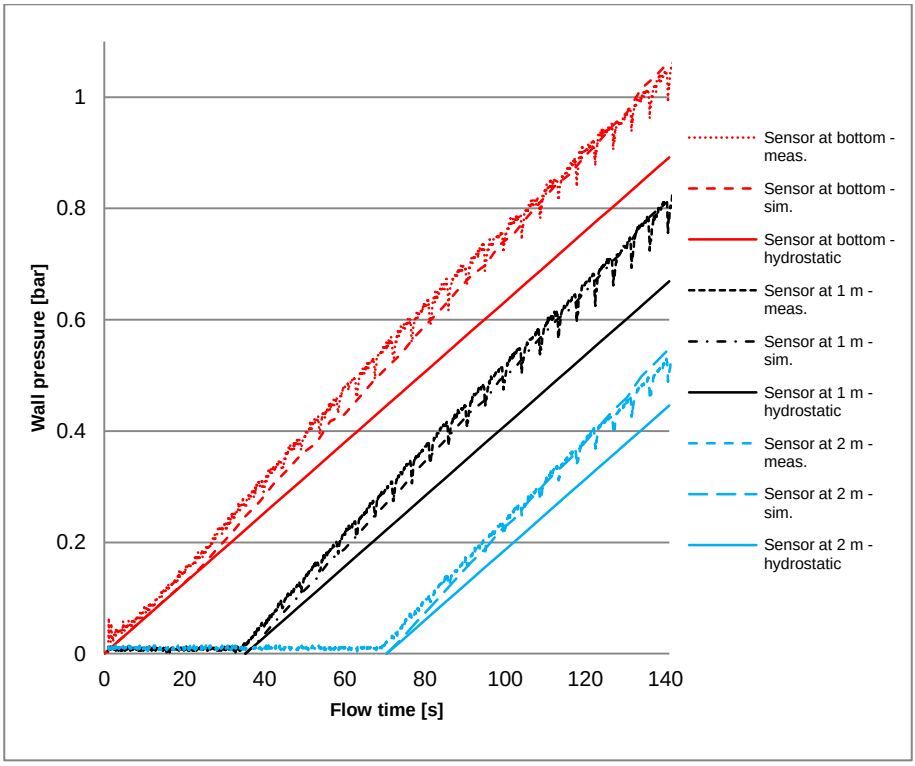

Fig. 6-44: Wall pressure p_{wall} at manometer positions of column 8 - with rebars - high viscosity SCC - high casting speed.

As for the base-filling processes without rebars, we observe a very good agreement between the measurements and the simulation results.

The presented graphs also clearly show the impact of the shear flow losses on the resulting formwork wall pressures. The shear flow losses represent from 7 % (low viscosity SCC - low casting speed) up to 16 % (high viscosity SCC - high casting speed) of the total wall pressure for the performed filling tests with steel rebars. With base-filling, the shear flow losses may certainly not be neglected regarding the maximum formwork wall pressures.

As already mentioned in section 5.2.3.1, other researchers reported that the density of the fresh concrete increases during casting, because the air is pushed out due to the pumping pressure and the local pressure at flow bifurcations inside the formwork.

This may lead to higher hydrostatic pressures than reported here, and as such to a lower contribution of the shear flow losses to the total wall pressure. Unfortunately, the density of the fresh concrete already inside the formworks was not measured during our filling experiments.

6.3.1.3 General observations

The following observations can be noted when analysing the previous graphs:

- When pumping SCC from the bottom, the resulting formwork wall pressure is the sum of the hydrostatic pressure component and the hydraulic pressure losses. These hydraulic losses become more important for high casting rates, small formwork cross-sections (columns) or when using an SCC with a high viscosity.
- The presence of rebars reduces the flow cross-section, leading to higher flow losses as function of the casting speed.
- When pumping SCC from the bottom it is possible to noticeably reduce the casting times by applying high casting rates. However, much stronger and stiffer formwork wall systems will be required to sustain the higher wall pressures.
- The pressure sensors mounted at the bottom of some of the columns show a less linear curve than the other two pressure sensors mounted at the walls of the columns. This observed non-linearity is more pronounced during filling with high viscosity SCC. As already mentioned in chapter 5 and in section 6.2, Cauberg et al. [6.29] also noticed during their measurements that these type of pressure sensors did not always measure correctly.
- In case of a high casting rate, the effect of thixotropy on the formwork pressure can be disregarded. The base-filling tests with rebars also confirm this, no decay of the measured wall pressures was observed during casting.

As for base-filling processes without rebars discussed in chapter 5 and in section 6.2, these observations are again fully in line with the theory of basic hydraulics. As such, it would be very practical if the flow pressures of the base filling process could be calculated by hand, using analytical formulas derived in a similar way as for piping circuits with Newtonian fluids. More about this in section 6.3.4.

6.3.2 CFD model based on the FVM-VOF-LS scheme and porous zone (PZ) modelling

6.3.2.1 Numerical model configuration

In chapter 4 we discussed the implementation of a porous zone concept in the numerical models of casting processes. Instead of modelling the rebars in a formwork explicitly, as described in section 6.3.1.1, these rebars are introduced implicitly in the numerical model of a filling process using a porous zone analogy.

The challenge here is to determine the intrinsic permeability of the porous zone representing the influence of the rebars on the occurring shear flow losses and, as such, on the resulting formwork wall pressure.

In [6.30 - 6.32], analytical expressions for the permeability of a porous media with cylindrical intrusions (rebars) have been proposed. Two flow patterns inside the porous zone have been studied: a flow perpendicular to the cylinder axis and a flow parallel to the cylinder axes.

In Fig. 6-45, the flow domain around the cylindrical intrusions is illustrated, where R_i is the radius of the cylindrical intrusion (m) and R is the radius of the surrounding fluid shell (m).

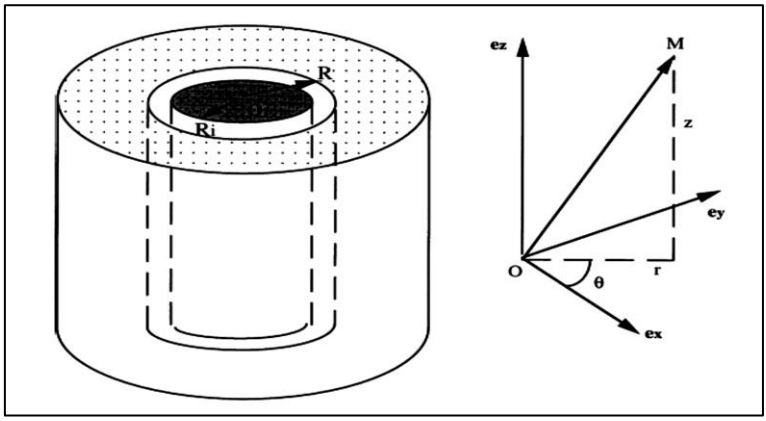

Fig. 6-45: Generic fluid-solid cylindrical inclusion [6.31].

For the transverse flow:

✓ Lower limit of the permeability, K_{Tl} (m²):

$$\frac{K_{Tl}}{R^2} = -\frac{\ln\rho + \frac{(1-\rho^2)}{(1+\rho^2)}}{4} \tag{6.9}$$

✓ Upper limit of the permeability, K_{Tu} (m²):

$$\frac{K_{Tu}}{R^2} = -\frac{\ln\rho + \frac{(1-\rho^4)}{2(1+\rho^4)}}{4} \tag{6.10}$$

For the longitudinal flow:

✓ Lower limit of the permeability, K_{Ll} (m²):

$$\frac{K_{Ll}}{R^2} = -\frac{\ln\rho + \frac{(1-\rho^2)}{(1+\rho^2)}}{2} \tag{6.11}$$

✓ Upper limit of the permeability, K_{Lu} (m²):

$$\frac{K_{Lu}}{R^2} = -\frac{\ln\rho + \frac{(1-\rho^2)(3-\rho^2)}{4}}{2} \tag{6.12}$$

where ρ is the ratio between R_i and R.

However, when looking at the actual rebar configuration shown in Fig. 6-39 (and Fig. 5-23), none of these formulas is able to solely determine the resulting permeability in the three main Cartesian flow directions inside the formwork. In each main flow direction, both a transverse and a longitudinal flow around the rebars is occurring simultaneously. It is clear that Eq. (6.9) up to Eq. (6.12) must be combined in order to determine the resulting permeability in one of the three Cartesian flow directions.

In order to simplify the permeability calculations in the main flow direction, one may only take into consideration the four longitudinal rebars of diameter 16 mm, and as such, neglect the transverse rebars of diameter 6 mm. The upper limit of the permeability in the three main flow directions (X- and Y-direction in the cross-section of the column, Z-direction in the height of the column) is then calculated using Eq. (6.10) and Eq. (6.12):

a) X- and Y-direction (see Fig. 5-23 - Eq. (6.10)):

- ✓ R_i = 8 mm = 0.008 m
- ✓ R = (300 mm - 2 x 48 mm)/2 = 102 mm = 0.102 m
- ρ = 8/102 = 0.0784
- ✓ $K_{Tp} = -\frac{0.102^2}{4}\left[ln(0.0784) + \frac{1-0.0784^4}{2(1+0.0784^4)}\right] = 0.0053\ m^2$

b) Z-direction (see Fig. 5-23 - Eq. (6.12)):

- ✓ R_i = 8 mm = 0.008 m
- ✓ R = (300 mm - 2 x 48 mm)/2 = 102 mm = 0.102 m
- ρ = 8/102 = 0.0784
- ✓ $K_{Lp} = -\frac{0.102^2}{2}\left[ln(0.0784) + \frac{(1-0.0784^2)(3-0.0784^2)}{4}\right] = 0.0094\ m^2$

Another method to determine the permeabilities has been presented in section 4.3.3.1.1 of chapter 4. Using Eq. (4.81), the permeabilities in the three flow directions can be calculated when knowing the pressure drop over a certain flow path length inside the porous zone. This pressure drop can be measured during a real filling process or computed numerically using a CFD model with the rebars modelled explicitly. The latter method is however less interesting from a design point of view, as it requires a full-scale filling process to be performed or a complex CFD model to be built prior to start designing a similar filling process using a porous model analogy, which does not make much sense. As such, the former method using a mathematical model predicting the permeabilities is to be preferred.

Fig. 6-46 shows the very good agreement between the formwork wall pressures at three sensor positions of the base-filling process of column 8 (high viscosity SCC, high casting speed, with rebars) simulated with a FVM-VOF-LS model and the rebars modelled explicitly, and the wall pressures simulated with a FVM-VOF-LS model but with the rebars modelled implicitly using a porous zone analogy with calculated permeabilities based on the analytical expressions of Boutin [6.31].

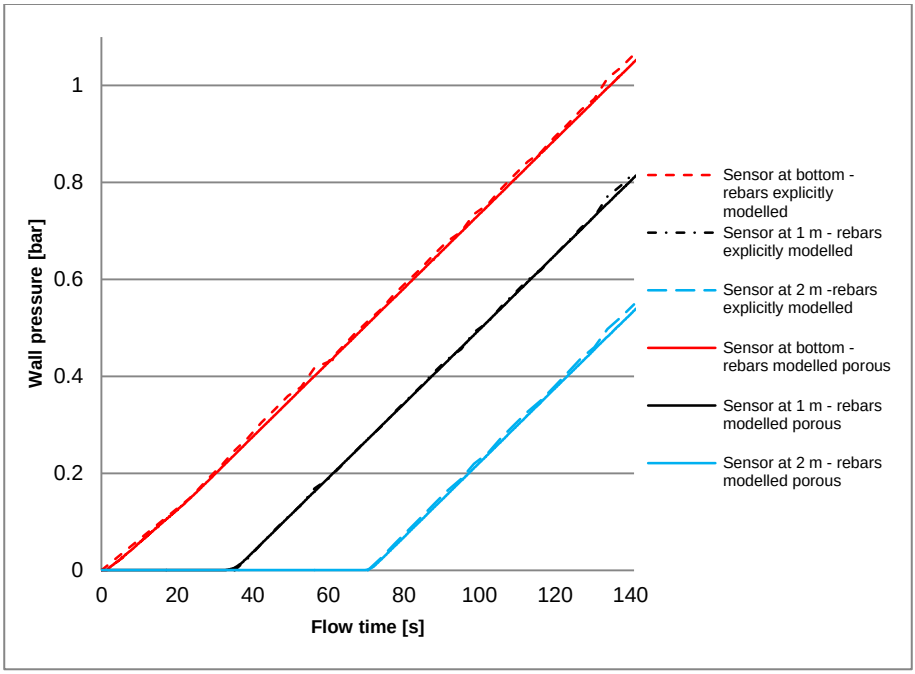

Fig. 6-46: Comparison of the simulated wall pressures of column 8 using a CFD model with the rebars modelled explicitly and modelled implicitly (porous zone analogy).

The very small difference which can be observed, is probably due to the fact that the transverse reinforcement bars have been neglected in the permeability calculations. So for the rebar configuration shown in Fig. 6-39, the influence of the transverse reinforcement bars on the resulting permeability seems to be very small.

As such, the simplification introduced in the former permeability calculations seem to be quite adequate for this case. Although the pre-processing and computation time were drastically reduced (1 day compared to 5 days on the same calculation server), as reported in [6.32] and in chapter 4, the question still remains whether these kind of simplifications or assumptions will always be straightforward for all possible rebar configurations.

6.3.3 Influence of the thin cement paste layer on the hydraulic losses

The numerical models with the previously mentioned solver settings are able to accurately simulate the transient filling process of the columns, however, some attention should be paid to the definition of the wall boundary condition in the numerical models. In all the simulations presented so far, a no-slip condition has been assumed at the solid boundaries.

When pumping SCC through narrow confinements like supply ducts, or in formworks with small cross-sections like for example the large I-beam filling process presented in section 6.2, the resistance to flow is much lower than expected, due to the presence of a thin cement paste layer near the walls with a much lower viscosity than the concrete bulk viscosity. As stated in section 6.1.4,.this can be attributed to the wall effect, mentioned by Feys [6.1] and Tichko et al. [6.2, 6.28] and demonstrated by Le et al. [6.12].

In order to incorporate this wall effect in numerical models, at least two methods may be implemented. One method is to model a thin layer, immediately next to all the flow confining walls, where the properties of the cement paste layer should be attributed, while in the remaining flow domain the bulk properties of the SCC are to be used [6.12]. Another method is to consider a certain slip between the walls and the flowing SCC, which can be implemented in Ansys Fluent® by defining a specified wall shear stress.

Unfortunately, both wall models are not easy to implement in practice: the first method requires the knowledge of the rheological properties of the cement paste for a certain SCC mixture, which is extremely difficult to extract from this concrete mix [6.12], and the second method requires the shear stress to be known in this slip layer.

It should of course be possible to fit empirically the required model parameters for these wall models based on experimental data, but it is doubtful that these fits would be universally valid. Nevertheless, Le [6.12] provided some formula to estimate the rheological properties of the slip layer when the rheological properties of the concrete are known. Of course, the general validity of his formula is still to be checked, but it could give a way out.

Therefore it would be very interesting to determine, prior to modelling, if this wall effect is going to have a serious impact on the calculation of the flow shear losses or not. From basic hydraulics theory we know that there is one parameter which describes the relative importance of the wall surface within a certain flow volume with regard to flow losses, i.e. the hydraulic diameter D_h.

The hydraulic diameter is defined by the following equation:

$$D_h = \frac{4S}{P} \tag{6.13}$$

where S is the wetted flow cross-section (m²), P is the wetted perimeter (m).

For the following performed pumping/filling experiments, this hydraulic diameter D_h has been calculated according to Eq. (6.13). The presence of rebars in the flow cross-section have been taken into account when determining the resulting cross-section S and the resulting perimeter P:

- Pumping tests performed in 2009 by Feys [6.2] and simulated by Tichko [6.2] in 2010 (see Fig. 6-2):

  ✓ For these pumping tests, steel ducts were used with an internal diameter of 106 mm. The cross-section of these ducts was entirely filled with SCC and therefore the hydraulic diameter D_h according to Eq. (21.5) is also 106 mm or 0.106 m.

- Formwork filling tests performed by Tichko et al. in 2010 [6.15] (see Fig. 5-1):

  ✓ During these filling tests, two walls and two columns without steel rebars were cast. The cross-section of the two columns was 0.174 m by 0.21 m, the resulting hydraulic diameter D_h being 0.19 m. The cross-section of the two walls was 4 m by 0.21 m, leading to a hydraulic diameter D_h of 0.399 m.

- Formwork filling tests performed by Tichko et al. in 2012 [6.28] (see Fig. 5-4):

  ✓ The cross-section of the columns without rebars was 0.3 m by 0.3 m, as mentioned in chapter 5, resulting in a hydraulic diameter D_h which is equal to 0.3 m. The cross-section of the columns with rebars was also 0.3 m by 0.3 m, but reduced by the cross-section of the four longitudinal rebars at some stations along the height, each with a diameter of 16 mm (see Fig. 5-23), resulting in a hydraulic diameter D_h of 0.255 m, or even additionally reduced by the transverse reinforcement bars leading to a hydraulic diameter D_h of 0.189 m. The average hydraulic diameter $D_{h,avg}$ is 0.222 m. The I-beam cross-sectional dimensions are shown in Fig. 6-47:

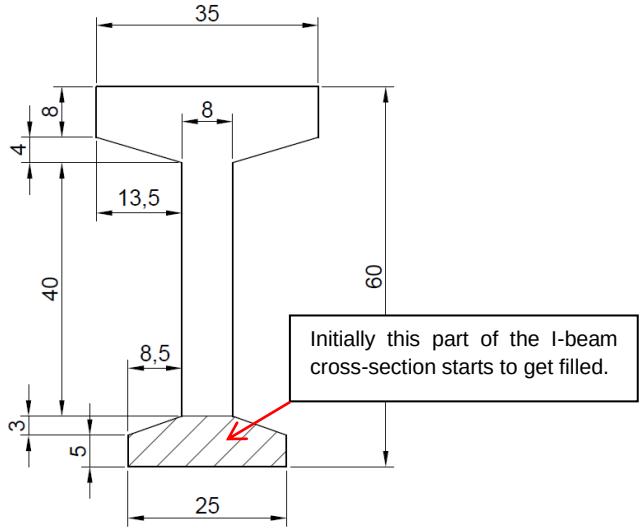

Fig. 6-47: Cross-section of the I-beam for the hydraulic diameter calculation.

- ✓ Initially, only the bottom part of the I-beam starts to get filled. For this lower wetted part of the total cross-section, the hydraulic diameter D_h is 0.132 m. For a totally filled cross-section of the I-beam, the hydraulic diameter D_h is equal to 0.194 m.

Table 6-9 summarizes the calculated hydraulic diameters for all the performed pumping/filling experiments with SCC, as well as the observations made regarding the measured and simulated hydraulic losses/wall pressures:

Table 6-9: Summary of the calculated hydraulic diameters.

Experiment	Hydraulic diameter D_h [mm]	Observations
Pumping tests - Feys (2009) [6.1]:		
• Steel ducts - D_i = 0.106 m	106	Serious overestimation of the shear flow losses.
Filling tests - Tichko (2010) [6.15]:		No overestimation of the shear flow losses. The simulated filling processes matched the real filling processes regarding the shear flow losses.
• Column - 0.174 m by 0.21 m	190	
• Wall - 4 m by 0.21 m	399	
Filling tests - Tichko (2012) [6.28]:		
• Column without rebars - 0.3 m by 0.3 m	300	No overestimation of the shear flow losses.
• Column with Ø6-Ø16 mm rebars - 0.3 m by 0.3 m	222	No overestimation of the shear flow losses.
• I-beam - lower part of the cross-section	132	Overestimation of the shear flow losses.
• I-beam - total cross-section	194	This situation did not occur.

From the observations summarized in Table 6-9, the critical hydraulic diameter $D_{h,crit}$ value seems to be between 106 mm and 190 mm. More experiments will need to be performed in order to more accurately determine this critical hydraulic diameter value.

Most probably, the relation with other model parameters like the viscosity of the selected SCC will determine the importance of the wall shear layer effect on the resulting flow losses as well. Possibly a “critical” Reynolds number value, taking into account the hydraulic diameter D_h, the apparent viscosity η of the SCC and the filling velocity could be an alternative for determining whether the wall shear layer effect should be taken into account in the numerical model or not. Then the problem will be to select an appropriate apparent viscosity value for this critical Reynold number calculation, because the apparent viscosity is continuously changing for each shear rate value within the flow domain (see also Fig. 6-10).

However, Kaplan [6.11] and Le [6.12] demonstrated that a certain flow path length is needed to in order to develop the lubrication layer. Regarding the filling of the I-beam, the walls have not been pre-wetted. As such, it is questionable whether this lubrication layer could have developed or not. Further research is needed.

In this case, the higher resistance to flow observed in the simulations could be attributed to a modified rheology of the SCC during the pumping process, which has not been taken into account in the numerical simulations.

As will be explained in the next section, the hydraulic diameter D_h value of all the formwork configurations presented in Table 6-9 will allow us to analytically determine the maximum formwork pressure occurring during casting, avoiding the need to build complex CFD models.

6.3.4 Application of the extended Poiseuille flow model

The observations already formulated in section 6.3.1.3, regarding the occurring shear flow losses and the related formwork wall pressures during base-filling, are fully in line with the theory of basic hydraulics.

As such, it would be very practical if the flow pressures of the base filling process could be calculated by hand, using analytical formulas derived in a similar way as for piping circuits with Newtonian fluids.

In the previous section, we mentioned the interesting application of the definition of the hydraulic diameter D_h, expressing the relative importance of wall shear for a certain flow volume. This definition allows us to define the base filling process as a pipe flow process with a pipe diameter equal to the hydraulic diameter D_h.

For Newtonian fluids, the shear flow losses are calculated using the well-known Poiseuille equation. Feys [6.1] re-derived the Poiseuille equation and applied the same philosophy for obtaining an analytical equation for the shear flow losses, when a yield stress material law following the Bingham or modified Bingham relation was used for characterising the flow behaviour of fresh concrete. For the Bingham model, this derivation procedure leads to the well-known Buckingham-Reiner equation.

In chapter 3, a new analytical model was derived for determining the shear flow losses when the Herschel-Bulkley model is used for representing the flow behaviour of SCC in the fresh state. This analytical model will allow us to easily calculate the flow losses and therefore also the wall pressure according to the model also presented in chapter 3, and this without the need of a complex CFD model.

In order to assess the validity of the newly derived analytical model, the maximum formwork wall pressures (at the bottom of the formwork) of all the performed base-filling experiments [6.15, 6.28] and presented in this research work have been recalculated and compared with the wall pressures obtained from detailed CFD simulations.

The results from the analytical model as well as the CFD results are summarized in the following table.

Table 6-10.a: Comparison of the wall pressures from the analytical model and the CFD simulations.

Formwork base-filling tests - 2010 [6.15]											
Cast	ρ_{SCC} **(kg/m³)**	$\tau_{0,HB}$ **(Pa)**	K_{HB} **(Pa.s^n)**	n_{HB} **(-)**	Q_{HB} **(m³/s)**	D_H **(Table 21-1) (m)**	h_{cast} **(m)**	h_{inlet} **(m)**	$L=h_{cast}-h_{inlet}$ **(m)**	p_{max} **- analyt. (Pa)**	p_{max} **- CFD (Pa)**
Column type A	2314	10.3	17.7	1.35	0.005	0.190	2	0.27	1.63	5.466×10^4	5.358×10^4
Wall type A	2314	10.3	17.7	1.35	0.006	0.399	1.955	0.275	1.68	4.487×10^4	4.571×10^4

Table 6-10.b: Comparison of the wall pressures from the analytical model and the CFD simulations.

Formwork base-filling tests - 2012 [6.28]											
Cast	ρ_{SCC} (kg/m³)	$\tau_{0,HB}$ (Pa)	K_{HB} (Pa.s^n)	n_{HB} (-)	Q_{HB} (m³/s)	D_H (Table 21-1) (m)	h_{cast} (m)	h_{inlet} (m)	$L=h_{cast}-h_{inlet}$ (m)	p_{max} - analyt. (Pa)	p_{max} - CFD (Pa)
Column 1	2273	76.73	11.45	1.6	0.00144	0.3	4	0.6	3.4	$9.349x10^4$	$9.425x10^4$
Column 2	2273	76.73	11.45	1.6	0.00139	0.222	4	0.6	3.4	$9.615x10^4$	$9.579x10^4$
Column 3	2273	123.75	6.29	1.8	0.00279	0.3	4	0.6	3.4	$9.620x10^4$	$9.564x10^4$
Column 4	2273	123.75	6.29	1.8	0.00263	0.222	3.5	0.6	2.9	$8.789x10^4$	$8.557x10^4$
Column 5	2273	111.93	22.81	1.48	0.00140	0.3	4	0.6	3.4	$9.600x10^4$	$9.845x10^4$
Column 6	2273	111.93	22.81	1.48	0.00131	0.222	4	0.6	3.4	$9.974x10^4$	$1.041x10^5$
Column 7	2273	207.7	33.63	1.16	0.00261	0.3	4	0.6	3.4	$1.021x10^5$	$1.059x10^5$
Column 8	2273	207.7	33.63	1.16	0.00256	0.222	4	0.6	3.4	$1.136x10^5$	$1.064x10^5$

The agreement between the analytical results and the CFD results is excellent considering the important reduction of the complexity of the 3-D flow inside the formwork to a 1-D equivalent flow through the introduction of the hydraulic diameter concept.

6.3.5 Conclusions

Large scale formwork base-filling tests with rebars have been performed and combined with computational fluid dynamics (CFD) techniques as well as with analytical modelling. The following conclusions are summarized:

- When pumping SCC from the bottom, in principle hydrostatic formwork pressures can be expected, increased with the hydraulic pressure losses. The hydraulic losses become more important in case of a higher filling velocity, a smaller cross-section of the formwork (e.g. columns, formworks with a dense rebar configuration) or a higher apparent viscosity of the SCC.
- Electronic pressure sensors are able to measure the formwork wall pressures accurately and in a straightforward way. The wall pressure data is recorded digitally, which allows further detailed analysis of the measured wall pressures.
- The measured wall pressures clearly show no decay during the base- filling processes performed in the this study. As also mentioned in section 6.3.1.3, the effect of thixotropy on the formwork pressure for this type of very fast casts can be disregarded.
- The correct determination of the rheological material parameters of the SCC used in the filling process is essential, as these parameters have an important influence on the resulting formwork wall pressures, especially the consistency factor and the consistency index. The filling tests performed in this study reveal that the yield stress seems to have a very limited influence on the resulting formwork wall pressure, due to implementation in Ansys Fluent® of the two-zone Herschel-Bulkley model presented in section 6.2.1.2.
- The time dependent formwork filling process and the resulting formwork pressure evolution can be accurately simulated by means of CFD techniques in combination with a Volume of Fluid (VOF) approach for the simulation of the free concrete surface.
- The use of a porous zone analogy when modelling rebars seems to be very promising. Although the pre-processing and computation time can be firmly reduced, the correct determination in a design stage of the permeabilities remains a challenging task.
- When only the maximum formwork wall pressure needs to be evaluated, two calculation ways can be chosen: performing a steady state analysis (only looking at the end of the filling process, when the formwork is completely filled) using a highly detailed CFD model, or, using the new analytical model derived in the present study which allows to quickly and accurately determine the formwork pressure without the need of a complex CFD model.

6.4 References

[6.1] Feys D., "Interactions between Rheological Properties and Pumping of Self-Compacting Concrete", Ph-D dissertation, Ghent University, Ghent (2009).

[6.2] Tichko S., Feys D., De Schutter G., Vierendeels J., Verhoeven R., Troch P., "Numerical Modelling of the Flow of Self-Compacting Concrete in Conveying Pipes", 6th International RILEM Symposium on self-compacting concrete, SCC 2010 Conference Proceedings vol. **2**, Montreal (2010), pp. 719-728.

[6.3] Tattersall G.H., Banfill P.F.G., "The Rheology of Fresh Concrete", Pitman Books Ltd., London (1983).

[6.4] Roussel N., Lemaître A., "Steady state flow of cement suspensions: A micromechanical state of the art", Cem. Conc. Res. **40**, (2010), pp. 77-84.

[6.5] Yahia A., Khayat K.H., "Analytical Models for Estimating the Yield Stress of High-Performance Pseudo-Plastic Grout", Cem. Conc. Res. **31**, (2001), pp. 731-738.

[6.6] Hirsch Ch., "Numerical Computations of Internal and External Flows, Volume 1 - Fundamentals of Numerical Discretization", John Wiley & Sons, New York (1989).

[6.7] Wendt J.F., Anderson J.D., Grundmann R., Degrez G., Dick E., Vierendeels J., "Computational Fluid Dynamics - An Introduction", Springer-Verlag, Berlin Heidelberg (2009), 332 pages.

[6.8] Versteeg H.K., Malalasekera W., "An Introduction to Computational Fluid Dynamics - The Finite Volume Method - First Edition", Longman Scientific & Technical, (1995), 267 pages.

[6.9] Fluent v.6.3 User's Guide, Fluent Inc. (2006), 2501 pages.

[6.10] Gambit v.2.3 Modelling Guide, Fluent Inc. (2006), pages.

[6.11] Kaplan D., "Pumping of concretes", Ph-D dissertation (in French), Laboratoire Central des Ponts et Chaussées (LCPC), Paris (2001).

[6.12] Le H.D., De Schutter G., Kadri E.H., Aggoun S., Vierendeels J., Troch P., "Velocity profile of Self Compacting Concrete and Traditional Concrete flowing in a half open pipe", 3rd International conference on Concrete Repair, Rehabilitation and Retrofitting (ICCRRR -2012), CRC Press, pp.1382-1387.

[6.13] Ovarlez G., Bertrand F., Rodts S., "Local determination of the constitutive law of a dense suspension of non-colloidal particles through magnetic resonance imaging", J. Rheol. **50**, (2006), pp. 259-292.

[6.14] Van De Maele J., Vanmassenhove N., "Vullen van een bekisting met zelfverdichtend beton door het pompen van onderaan", Master thesis (in Dutch), Ghent University, Ghent (2010).

[6.15] Tichko S., Van De Maele J., Vanmassenhove N., De Schutter G., Vierendeels J., Verhoeven R., Troch P., "Numerical simulation of formwork pressure while pumping self-compacting concrete bottom-up", Eng. Struct., vol. **70**, (2014), pp. 218-233.

[6.16] Billberg P., "Form pressure generated by SCC - Influence of Thixotropy and Structural Behaviour at Rest", Ph-D dissertation, Royal Institute of Technology, Stockholm, (2006).

[6.17] Wallevik J.E., "Rheology of Particle Suspensions - Fresh Concrete, Mortar and Cement Paste with Various Types of Lignosulfonates", Ph-D dissertation, NTNU, Trondheim (2003).

[6.18] Hu C., de Larrard F., Sedran F., Boulay C., Bosc F., Deflorenne F., "Validation of the BTRHEOM, the new rheometer for soft-to-fluid concrete", Materials and Structures **29**, (1996), pp. 620-631.

[6.19] Le H.D., Vierendeels J., Tichko S., Troch P., Kadri E.H., Aggoun S., De Schutter G., "Computational fluid dynamics calibration of Tattersall MK-II type rheometer for concrete", Applied Rheology **23**, (2013), 12 pages.

[6.20] Mechtcherine V., Nerella V.N., Kasten K., "Testing pumpability of concrete using Sliding Pipe Rheometer", Construction and Building Materials **53**, (2014), pp. 312-323.

[6.21] Ansys Fluent v.12.0 Theory Guide, Fluent Inc. (2009), 816 pages.

[6.22] Ansys Fluent v.14.0 Theory Guide, Fluent Inc. (2011), 826 pages.

[6.23] Roussel N., "Steady state flow of cement suspensions: A micromechanical state of the art", Cem. Conc. Res. **40**, (2010), pp. 77-84.

[6.24] Hirt C.W., Nichols B.D., "Volume of Fluid Method for the Dynamics of Free Boundaries", J. Comput. Phys. **39**, (1981), pp. 201-225.

[6.25] Roussel N., “A thixotropy model for fresh fluid concretes: Theory, validation and applications”, Cem. Conc. Res. **36**, (2006), pp. 1797-1806.
[6.26] Osher S., Sethian J.A., “Fonts Propagating with Curvature-dependent Speed: Algorithms based on Hamilton-Jacobi Formulations”, J. Comput. Phys. **79**, (1988), pp. 12-49.
[6.27] Olsson E., Kreiss G., Zahedi S., “A Conservative Level Set Method for Two Phase Flow II”, J. Comput. Phys. **225**, (2007), pp. 785-807.
[6.28] Tichko S., De Schutter G., Troch P., Vierendeels J., Verhoeven R., Lesage K., Cauberg N., “Influence of the viscosity of self-compacting concrete and the presence of rebars on the formwork pressure while filling bottom-up”, Eng. Struct., vol. **101**, (2015), pp. 698-714.
[6.29] Cauberg N., Desmyter J., Piérard J., Parmentier B., “Bekistingsdruk bij zelfverdichtend beton” - WTCB dossiers (in Dutch) - Katern 7, nr. 3, WTCB, Limeltte (2006).
[6.30] Sanchez-Palencia E., “Non-Homogeneous Media and Vibration Theory”, Springer-Verlag, Berlin-Heidelberg, (1980), 398 pages.
[6.31] Boutin C., “Study of permeability by periodic and self-consistent homogenisation”, European Journal of Mechanics **19**, Elsevier, (2000), pp. 603-632.
[6.32] Vasilic K., Meng B., Kühne H.C., Roussel N., “Flow of fresh concrete through steel bars: A porous medium analogy”, Cem. Conc. Res. **41**, (2011), pp. 496-503.
[6.33] Calie B., “Pumping of Self-Compacting Concrete under pressure,” Master thesis (in Dutch), Ghent University, Ghent (2007).

Chapter 7: Conclusions

"A fool thinks himself to be wise, but a wise man knows himself to be a fool." - William Shakespeare

7 Overview of this Chapter

In this chapter all the conclusions drawn from the performed research and reported in the individual chapters of this manuscript are summarized. A number of propositions for further research are also formulated.

7.1 General conclusions of this doctoral thesis

The general conclusions of the current doctoral research are:

- When pumping SCC from the bottom, in principle hydrostatic formwork pressures can be expected increased with the hydraulic pressure losses. The shear flow losses become more important for high casting rates, small formwork cross-sections (e.g. columns) or when using an SCC with a high viscosity. The presence of rebars further reduces the flow cross-section, leading to higher flow losses. These observations are fully in line with the theory of basic hydraulics. The shear flow losses measured during the performed base-filling tests ranged from 7 % up to 16 % of the total wall pressure. Therefore they may certainly not be neglected regarding the maximum formwork wall pressures when the base-filling technique is used for casting.
- When pumping SCC from the bottom it is possible to noticeably reduce the casting times by applying high casting rates. However, stronger and stiffer formwork wall systems will be required to sustain the higher wall pressures.
- In case of a high casting rate, the effect of thixotropy on the formwork pressure can surely be disregarded. The second series of base-filling tests confirm this statement, as no decay of the measured wall pressures was observed during casting.
- The correct determination of the rheological material parameters of the SCC mixture used in the formwork filling process is important, as these parameters have an influence on the resulting formwork wall pressures, especially the consistency factor and the consistency index of the Herschel-Bulkley model.
- The formwork filling process and the related formwork pressures can be accurately simulated by means of the FVM-VOF-LS modelling technique. These kind of CFD simulations allow to optimize the formwork filling process during the design phase. When only the maximum formwork pressures are of interest, then a simple and very quick steady state simulation is sufficient because the maximum wall pressures are occurring when the formwork is completely filled. On the other hand, when the possible occurrence of air voids due to non-adequate positioning of the supply inlets needs to be detected or the self-levelling properties of a selected SCC mixture needs to be assessed, then a transient simulation relying on the combined FVM-VOF-LS scheme has to be performed.

- The combination of the FVM-VOF-LS scheme and the porous zone analogy for rebars proves to be very promising as it drastically reduces the pre-processing time and the computation time. Although the determination of the porous zone parameters for complex rebar configurations remains a challenge, for the standard rebar layout used in our filling tests the simulation results obtained with the FVM-VOF-LS scheme and the rebars modelled as a porous zone were in very good agreement with simulations of the numerical models with rebars modelled explicitly.
- Last but certainly not least, the maximum formwork wall pressures calculated with the newly derived analytical model proved to be in very good agreement with the simulation results from the numerical models. When using the analytical model the calculation time is extremely small, but no detailed information about the local velocities in the flow domain is available. However, the pressure losses and the maximum wall pressure calculated with the analytical model allow to quickly determine the required capacity of the concrete supply and the necessary strength and stiffness of the formwork wall elements.

7.2 Propositions for further research

In the following list, some ideas and propositions for further research are presented:

- As mentioned in chapter 6, the use in the present research of the combined FVM-VOF-LS simulation technique required a highly regular mesh being preferably composed of hexahedral mesh cells in order to improve the stability and the calculation speed. However, this requirement is a real challenge for complex formwork geometries and rebar configurations. Further research should be performed to improve the stability of this combined numerical scheme when applied to an irregular mesh, like a tetrahedral mesh, with varying mesh density, which is the type of mesh typically used for complex geometries.
- The simulations with the porous zone analogy where the steel rebars were modelled implicitly showed very promising results. The time needed for pre-processing and computation was drastically reduced. However, determining the porous zone parameters is not straightforward. Further research should performed on finding mathematical models, like the one presented in chapter 6, which are able to determine these values for any rebar configuration.
- In chapter 6, the application of the new analytical model derived with the introduction of the hydraulic diameter revealed to be very fast and quite accurate for determining the wall pressures during the performed formwork base-filling processes. However, further research should performed to expand the use of this analytical model to the base-filling processes of more complex formwork geometries and rebar configurations. For complex geometries, the adequate determination of the hydraulic diameter is not obvious.
- Following the line of the newly derived analytical model for the flow losses and the resulting wall pressure, it would be very interesting to develop a similar simplified hydraulic network calculation concept as encountered in the design of hydraulic circuits with Newtonian fluids relying on a simple 1-D flow model with linearly distributed shear flow losses combined with additional flow losses due to bifurcations, sudden reductions or expansions of flow cross-sections, etc. The introduction of this concept would surely improve the practical application of the presented calculation models during the design of base-filling processes.
- In our base-filling experiments, the casting speed was very high compared to the casting speeds typically applied when filling a formwork form the top with CVC. As such, we could disregard the effect of thixotropy in our experiments. However, for longer casting times and/or the filling of larger formwork volumes, the effect of thixotropy and the related reduction of wall pressure cannot be disregarded. Therefore, it would be necessary to develop and implement a model for thixotropic structural build-up, where the dynamic evolution of the structural state parameter presented in chapter 2 would be modelled as a transported property.
- Finally, in order to determine if the application of the lubrication layer concept is required or not when implementing the wall boundary conditions, it would be useful to define a more adequate decision parameter than the proposed critical hydraulic parameter or critical Reynolds number.

Appendices

Appendix A: Calibration and transformation procedure for the Tattersal Mk-II rheometer

A. Conversion of measurement data into rheological properties

As mentioned in chapter 2, due to the rather complex geometry of the inner cylinder of the Tattersal Mk-II rheometer, no analytical formulas exist which allow to transform the measured torque *T* versus the rotational velocity *N* data into the fundamental rheological relation between shear stress τ and shear rate $\dot{\gamma}$.

Two different procedures can be followed in order to transform the measured *T* - *N* data into τ - $\dot{\gamma}$ data:

- Performing a rheometer calibration with for example oil and honey, and deriving a transformation procedure based on this calibration. This procedure has been worked out by Feys [A.1];
- Building a numerical model of the Tattersall Mk-II rheometer and performing CFD simulations, and as such deriving the necessary transformation equations by applying a numerical regression on the simulation results. This procedure has been worked out by Le et al. [A.2].

A.1 Calibration and transformation procedure of Feys [A.1]

A.1.1 Applied materials and reference rheometer

Both a very viscous oil (poly-iso-butene) and “white” honey have been applied as reference materials. The oil is a Newtonian liquid and the honey is shear-thinning, but for the shear rate range observed in pumping and formwork filling tests, the honey is behaving as a Bingham material with an apparent yield stress.

Both materials have been tested in the Tattersall Mk-II rheometer at different temperatures, resulting in different values of the viscosity and the yield stress. Small samples of both materials has also been measured using a cone and plate reference rheometer, where the rheological properties have been determined at the same set of temperatures.

The rheological properties of the oil were determined at three different temperatures by performing at each temperature three tests with each rheometer. For the honey, four different temperatures have been applied, with three tests per temperature in the cone and plate geometry and five tests per temperature in the Tattersall Mk-II rheometer.

A.1.2 Observations

The average of the results at each temperature for the oil, measured with the cone and plate rheometer, clearly indicated a Newtonian behaviour and a temperature dependent viscosity.

In the Tattersall Mk-II rheometer, the oil did not show a linear Newtonian behaviour. Whereas at high rotational velocities, the relationship between the torque *T* and the rotational velocity *N* was linear, at low rotational velocities and low torque values it was non-linear. Feys attributed this non-linear behaviour to the flow of oil between the blades of the inner cylinder.

Based on the measurements with the Tattersall Mk-II rheometer, a zone of non-linearity was defined by the following relationship:

$$T = 1 - \frac{N}{55} \tag{A.1}$$

The data in the zone of non-linearity obeyed the following Power-Law relationship:

$$T = A.N^{2.55} \tag{A.2}$$

where *T* is the measured torque (Nm) and *N* is measured rotational velocity (rev./min).

The results for the honey measured in the cone and plate rheometer revealed that both the yield stress and the plastic viscosity were increasing with decreasing temperature. In the Tattersall Mk-II rheometer, the data outside the zone of non-linearity showed a linear relationship.

For each curve at a certain temperature, a corresponding Newtonian curve, with equal inclination was determined. As such, the yield torque was defined as the difference in torque value between the measured curve and the corresponding Newtonian curve with the same inclination.

A.1.3 Transformation of data for Bingham materials

In order to transform data points expressed in torque and rotational velocity into shear stress and shear rate, the following steps (see Fig. A-1) must be applied in case of a Bingham material, which can be recognized by the linear relationship between torque and rotational velocity in a *T* - *N* diagram outside the zone of non-linearity (see Fig. A-1 a):

1. The yield torque is calculated following the procedure mentioned in section A.1.2 (see Fig. A-1 b).
2. The intersection of the extrapolated line outside the zone of non-linearity with the edge of this zone is calculated, corresponding to a value Ni. Inside the zone of non-linearity, a curve of the form T = T0' + A.N2.55 is fitted to the measured data points. On the extrapolated line from outside the zone of non-linearity, the N-value corresponding to T0' is defined as Na (see Fig. A-1 c-d).
3. All measured data points outside the zone of non-linearity are corrected by performing a horizontal translation towards the origin over a distance Na. The new N-values are described by N' = N - Na (see Fig. A-1 e).
4. All data points inside this zone of non-linearity are modified using the following transformation: N' = (Ni - Na).(N/Ni)2.55. As a result, all corrected data points inside the zone of non-linearity are situated on the extrapolated line of the data points outside this zone, in a T - N' diagram (see Fig. A-1 f). Logically, applying step 3 or step 4 on the data point at the intersection of the T - N diagram with the edge of the zone of non-linearity results in the same value for N'.
5. A new value for T0 in the T - N' diagram is obtained. The new line must be shifted vertically in order to match T0 with the yield torque obtained in step 1 (see Fig. A-1 g).

Applying the above procedure, the influence of the zone of non-linearity is eliminated. The new data has been compared to the results from the cone and plate rheometer and the following calibration constants were derived:

- The torque *T* (Nm) must be multiplied with 124.37 in order to obtain the shear stress τ (Pa).
- The rotational velocity *N* (rev./min) is multiplied with 0.1931 in order to obtain the shear rate (s^{-1}) (see Fig. A-1 h).

Problems could arise when not enough data points are available in order to determine the Power-Law relationship in the zone of non-linearity. If only one data point is available, the second data point is chosen to be the intersection of the extrapolated curve from outside the zone with the edge of the zone.

If no data points are in the zone of non-linearity, but there is an intersection, the intersection point is the only data point available, and the *A*-value is chosen based on a linear correlation between the inclination of the extrapolated line and other obtained *A*-values.

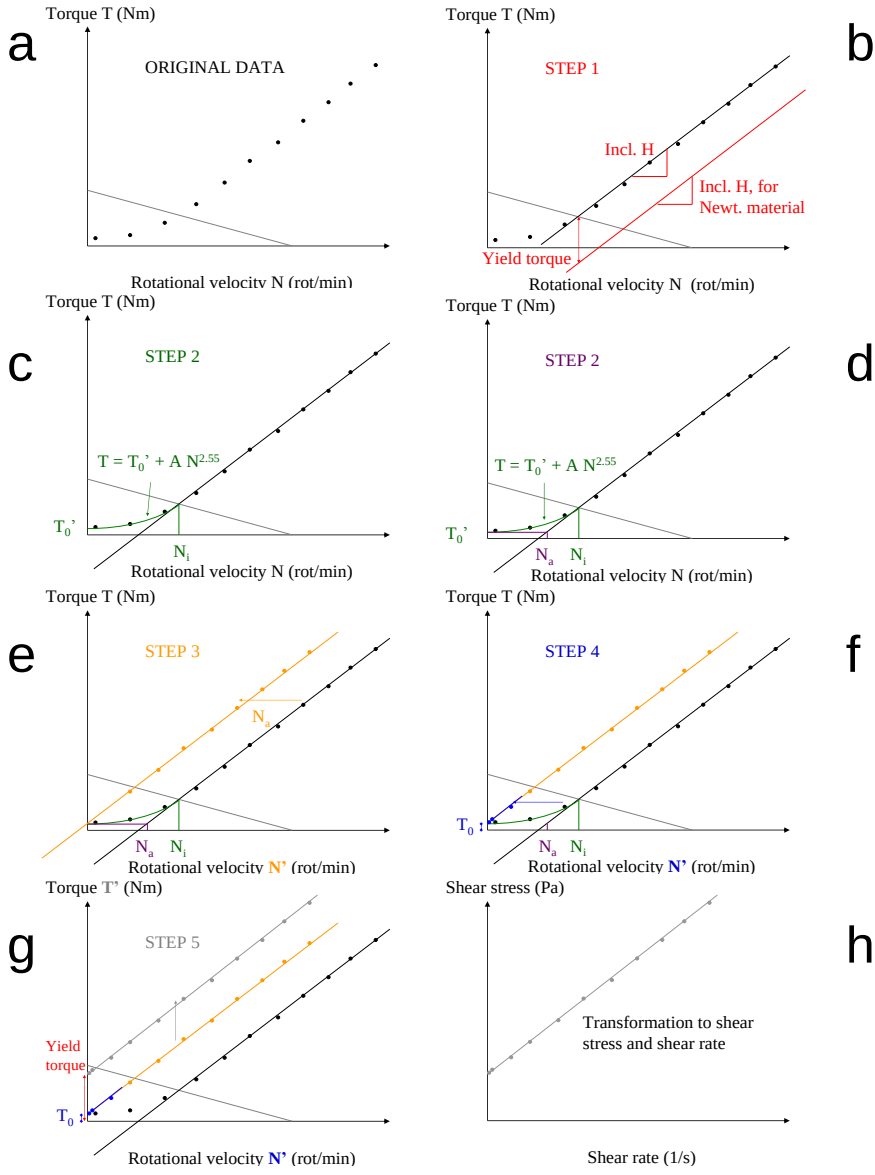

Fig. A-1: Transformation of measured *T* - *N* data into shear stress τ - shear rate $\dot{\gamma}$ data.

A.1.4 Transformation for non-Bingham materials

In case the relationship between the torque *T* and the rotational velocity *N* outside the zone of non-linearity is not linear, it is difficult to determine the extrapolated curve. Two additional steps need to be included in the transformation procedure in order to overcome this problem. From the raw *T* - *N* data, the best fitted straight line through the five data points at the lowest *N*-values is determined.

Although this induces a new error, in most cases, according to Feys this procedure seemed to be reasonable, except when the data showed a clear curvature, especially for very fluid concrete with a few data points near zero torque. In this case, some points need to be omitted in order to obtain a straight line.

This procedure is illustrated in Fig. A-2. N_a, the corresponding *N*-value with T_0', is determined using straight line defined above.

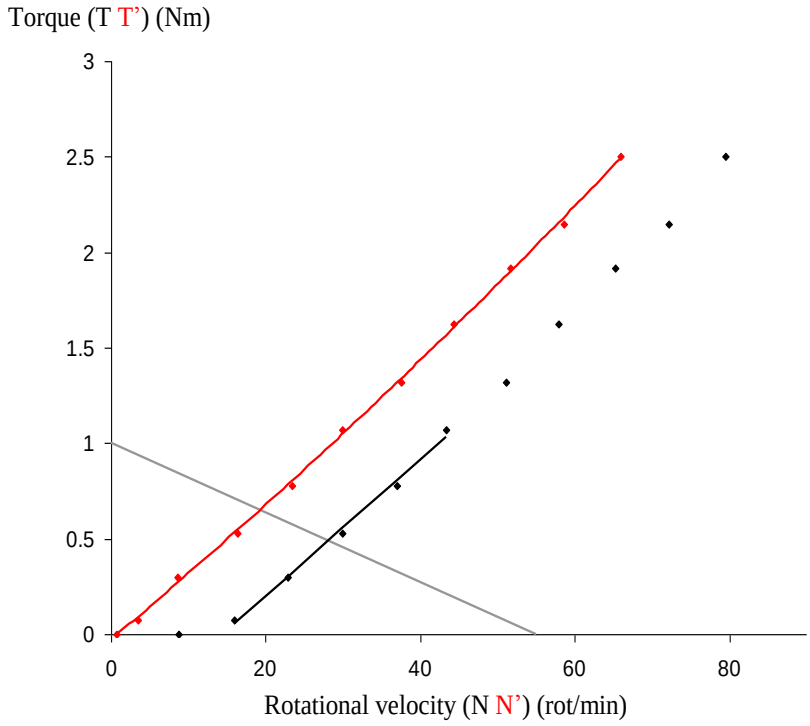

Fig. A-2: Transformation of data (black = original, red = obtained results after step 4) for a non-Bingham material.

A.2 Regression and transformation procedure of Le et al. [A.2, A.3]

A.2.1 General information

Ansys Fluent v.12.1 has been used for the performed numerical simulations of the Tattersall Mk-II rheometer. By default, Ansys Fluent solves the flow equations in a stationary reference frame. However, in order to accurately determine the flow around the complex geometry of the helical rotor of the rheometer, the sliding mesh technique has been used. This technique consists of dividing the domain into multiple cell zones with a defined interface between these cell zones, and then applying a rotational movement to the part containing the rotor of the rheometer. In case of an unsteady interaction between the stationary and moving parts, the sliding mesh technique is very powerful for accurately capturing the transient behaviour of the flow inside the modelled Tattersall Mk-II rheometer.

As also mentioned in chapter 6, the Herschel-Bulkley model has been modified in the Ansys Fluent software, in order to avoid the numerical discontinuity of the flow curve at zero shear rate. The following modified two-zone Herschel-Bulkley model has been used:

For $\dot{\gamma} \leq \dot{\gamma}_c$:

$$\eta = \tau_0 \frac{\left(2 - \dot{\gamma}/\dot{\gamma}_c\right)}{\dot{\gamma}_c} + k\left[(2-n) + (n-1)\frac{\dot{\gamma}}{\dot{\gamma}_c}\right] \tag{A.3}$$

For $\dot{\gamma} > \dot{\gamma}_c$:

$$\eta = \frac{\tau_0}{\dot{\gamma}} + k\left(\frac{\dot{\gamma}}{\dot{\gamma}_c}\right)^{n-1} \tag{A.4}$$

$$k = K.(\dot{\gamma}_c)^{n-1} \tag{A.5}$$

where τ is the shear stress (Pa), $\dot{\gamma}$ is the shear rate (s^{-1}), τ_0 is the yield stress (Pa), K is the consistency factor ($Pa.s^n$), k is the modified consistency factor ($Pa.s^{n/(n-1)}$), n is the consistency index (-), η is the apparent viscosity (= $\tau/\dot{\gamma}$) of the material (Pa.s) and $\dot{\gamma}_c$ is the critical shear rate (s^{-1}).

A.2.2 Regression plan

After completing 2700 simulations, the simulation results of the Tattersall Mk-II rheometer did reveal that the parameters G_{HB}, K_{HB} and m were all depending on τ_0, k and n, and vice versa. These relations were determined from the simulations results through numerical regression. The following equations resulted from this numerical regression:

$$K_{HB} = \frac{(Ak+B)e^{Ck}+(Dk+E)e^{Fk}}{e^{Ck}+e^{Fk}} \tag{A.6}$$

with:

$$A = \frac{A_1}{1+A_2 e^{A_3\tau_0}} + A_4$$

$$A_1 = A_{11}n + A_{12}$$
$$A_2 = A_{21}n + A_{22}$$
$$A_3 = A_{31}n + A_{32}$$
$$A_4 = A_{41}n + A_{42}$$
$$A_{ij} = \begin{bmatrix} 0.1553 & 0.1378 \\ -79147 & 1147.6 \\ 0.0182 & -0.0312 \\ 0.0933 & -0.0595 \end{bmatrix}$$

$$B = B_1 {\tau_0}^{B_2} + B_3$$

$$B_i = [-2.4979.10^{-6} \quad 1.8575 \quad -0.1287]$$

$$C = C_1(1 - e^{C_2\tau_0}) + C_3$$

$$C_1 = C_{11}n + C_{12}$$
$$C_2 = C_{21}e^{C_{22}\tau_0+C_{23}}$$
$$C_3 = C_{31}$$
$$C_{ij} = \begin{bmatrix} 0.0818 & -0.5190 & 0 \\ -0.1370 & -1.1451 & -2.2653 \\ 0.4467 & 0 & 0 \end{bmatrix}$$

$$D = D_1 {\tau_0}^{D_2} + D_3$$

$$D_1 = D_{11}(1 - e^{D_{12}n+D_{13}})$$
$$D_2 = D_{21}n + D_{22}$$
$$D_3 = D_{31}n^{D_{32}} + D_{33}$$
$$D_{ij} = \begin{bmatrix} 1.2970.10^{-15} & -20.5211 & -13.3869 \\ -2.8162 & 5.8250 & 0 \\ 0.00405 & 1.44042 & 0.00766 \end{bmatrix}$$

$$E = E_1 {\tau_0}^{E_2}$$

$$E_i = [5.9474.10^{-6} \quad 1.7684]$$

$$F = F_1 {\tau_0}^{F_2} + F_3$$

$$F_i = [5.6720 \quad -0.9727 \quad 0.0081]$$

and

$$G_{HB} = I {\tau_0}^{J} \tag{A.7}$$

with: $$I = (I_1 k + I_2)(1 - e^{I_3 k}) + I_4$$

$$I_1 = I_{11} n + I_{12}$$
$$I_2 = I_{21} (n-1)^{I_{22}} + I_{23}$$
$$I_3 = I_{31} n + I_{32}$$
$$I_4 = I_{41}$$
$$I_{ij} = \begin{bmatrix} 2.2622.10^{-5} & -7.8847.10^{-6} & 0 \\ 0.8231.10^{-2} & 1.4403 & 9.6420.10^{-2} \\ 0.2984.10^{-1} & -0.7410.10^{-1} & 0 \\ 0.0043 & 0 & 0 \end{bmatrix}$$

$$J = J_1 (1 - e^{J_2 k}) + 1$$

$$J_i = [-0.1745 \quad -0.5763.10^{-1}]$$

and

$$m = K {\tau_0}^{L} + M {\tau_0}^{O} + P + Q \tag{A.8}$$

$$K = e^{K_1 n + K_2}$$

$$K_i = [-3.8393 \quad 4.5578]$$

$$L = L_1 n + L_2$$

$$L_i = [0.2170 \quad -1.4221]$$

$$M = (M_1 k + M_2)(1 - e^{M_3 k})$$

$$M_1 = M_{11} n + M_{12}$$
$$M_2 = M_{21} n + M_{22}$$
$$M_3 = M_{31} n + M_{32}$$
$$M_{ij} = \begin{bmatrix} -0.1080.10^{-3} & 7.1349.10^{-5} \\ -0.6431 & -0.2857 \\ 0.0724 & -0.1239 \end{bmatrix}$$

$$O = O_1 k^{O_2} + O_3$$

$$O_1 = O_{11} n + O_{12}$$
$$O_2 = O_{21} n + O_{22}$$
$$O_3 = O_{31} n + O_{32}$$

$$O_{ij} = \begin{bmatrix} -48.8135 & 119.03964 \\ 0.3627.10^{-2} & -0.3874.10^{-3} \\ 48.4857 & -120.2906 \end{bmatrix}$$

$$P = n + P_1$$

$$P_i = [0.0142]$$

$$Q = Q_1\tau_0$$

$$Q_i = [0.00075]$$

where G_{HB} is the yield torque (Nm), K_{HB} is the factor of the power term (Nm.s^m) and m is the power index (-).

A.3 References

[A.1] Feys D., “Interactions between Rheological Properties and Pumping of Self-Compacting Concrete”, Ph-D dissertation, Ghent University, Ghent (2009).

[A.2] Le H.D., Vierendeels J., Tichko S., Troch P., Kadri E.H., Aggoun S., De Schutter G., “Computational fluid dynamics calibration of Tattersall MK-II type rheometer for concrete”, Applied Rheology **23**, (2013), 12 pages.

[A.3] Le H.D., “Etude de l'effet de la couche limite sur les profils de vitesses du béton pompé”, Ph-D dissertation, Université de Cergy-Pontoise, Cergy-Pontoise (2014).

Appendix B: Fresh concrete measurement data of the formwork filling experiments

B. Fresh concrete measurement data

During the formwork filling experiments with SCC being performed at the MLCR of Ghent University, several measurement campaigns have been carried out in order to provide experimental data for the validation of the numerical models of the filling processes.

During both series of casting experiments, the following properties were measured:

- Several characteristic properties of the selected SCC mixture in the fresh state, by performing the standard fresh concrete tests, as described in chapter 5 and in [B.1, B.2];
- Rheological properties of the selected SCC mixture in the fresh state, using a rheometer, as described in chapter 5 and in [B.3, B.4];
- Formwork wall pressure at relevant positions, using electronic pressure sensors and in-house developed pressure measurement units (see also chapter 5 and [B.3, B.4]).

Additionally, a visual inspection of the resulting homogeneity of the two SCC mixtures of the second series of formwork filling tests has been carried out on drilled samples of the cast columns. This was done in order to assess the cast quality.

B.1 First series of formwork filling tests [B.3]

B.1.1 Fresh properties of the selected SCC obtained through the standard concrete tests

A ready-mix company supplied the SCC used in the first series of formwork filling processes. Table B-1 lists the type and amount of ingredients of the delivered SCC. Although the SCC mixture design was based on a grading curve with a maximum aggregate size of 14 mm, some aggregates with a size of 20 mm were observed.

The water-to-cement ratio, W/C, is 0.53 and the water-to-powder ratio, W/P, is 0.32.

The standard tests and the rheometer measurements were performed on the chosen SCC mixture at three different moments during the filling tests:

- When the concrete mixing truck arrived at the Magnel Laboratory, before the start of the first filling test - time t = 0 min - sample n° 1;
- After filling the first wall formwork (wall type A) - time t = 16 min - sample n° 2;
- After filling the last column formwork (column type B) - time t = 47 min - sample n° 3.

Table B-1: SCC mixture design per m³.

Ingredient	Comments	Quantity	Units
Sand 0/4	Grain size between 0 mm and 4 mm	805	kg/m³
Limestone aggregates 2/7	Aggregate size between 2 mm and 7 mm	450	kg/m³
Limestone aggregates 7/14	Aggregate size between 7 mm and 14 mm	265	kg/m³
Cement type C I 52.5 N	Portland cement	100	kg/m³
Cement type C III/A 42.5 LA	Blast furnace cement - Low Alkaline	265	kg/m³
Calcitec	Limestone filler	235	kg/m³
Rheomatrix	Viscosity modifying Agent (VMA)	0.5	kg/m³
Glenium 27	Polycarboxylether (PCE) type superplasticiser	7.2	l/m³
Water	-	193	l/m³

The results from the performed standard concrete tests are summarised in Table B-2.

Table B-2: Results from the standard tests.

SCC sample n° 1		SCC sample n° 2		SCC sample n° 3	
Density [kg/m³]	2315	Density [kg/m³]	2329	Density [kg/m³]	2298
Sieve stability [%]	12.8	Sieve stability [%]	18.3	Sieve stability [%]	17.6
L-box ratio [-]	0.97	L-box ratio [-]	1.00	L-box ratio [-]	0.94
Slump flow [mm]	820	Slump flow [mm]	935	Slump flow [mm]	830
V-funnel time [s]	4.9	V-funnel time [s]	3.3	V-funnel time [s]	4.6
Air content [%]	3.5	Air content [%]	4.2	Air content [%]	3.5

The results from the standard tests indicate that the delivered SCC mixture was very fluid, which was also confirmed by the measurements being performed with the Tattersall Mk-II rheometer.

Sample n° 2 was extracted from the top of wall type A and consisted mainly of cement paste with a small amount of coarse aggregates, indicating the occurrence of segregation during the filling process.

The measurement results of the first and the last sample revealed that the rheology of the delivered SCC remained quite constant during the filling tests.

B.1.2 Rheological properties of the selected SCC through rheometry

Only the rheological measurements of sample n° 1 and sample n° 3 were processed further, because sample n° 2 was not representative for the fresh concrete batch due to segregation occurring at the top of the formwork of wall type A.

Fig. B-1 and Fig. B-2 show the measured torque *T* and the measured rotational speed *N* for sample n° 1 and sample n° 3 respectively.

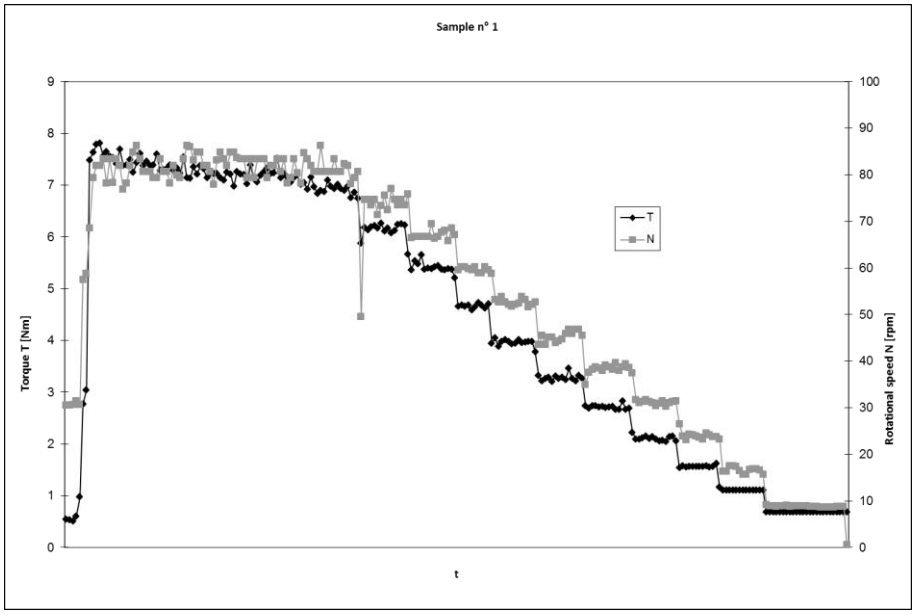

Fig. B-1: Measured torque and rotational speed of sample n° 1.

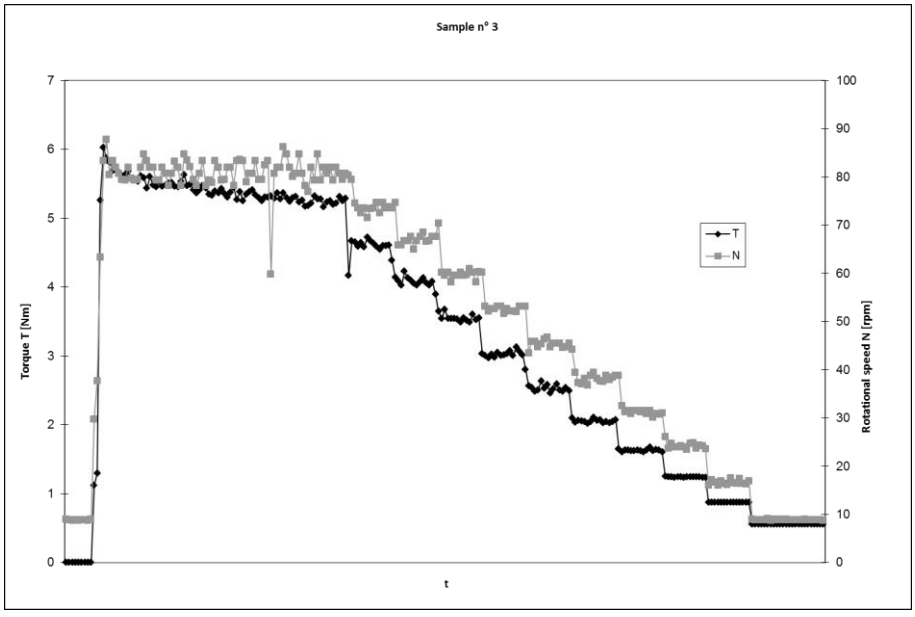

Fig. B-2: Measured torque and rotational speed of sample n° 3.

After processing the equilibrium data points and converting the rotational speed from rpm to rad/s, the following torque-rotational speed graphs were obtained, which allowed to calculate, through curve-fitting, the rheometer parameters G_{HB}, K_{HB} and m presented in Eq. (4.8) of chapter 4.

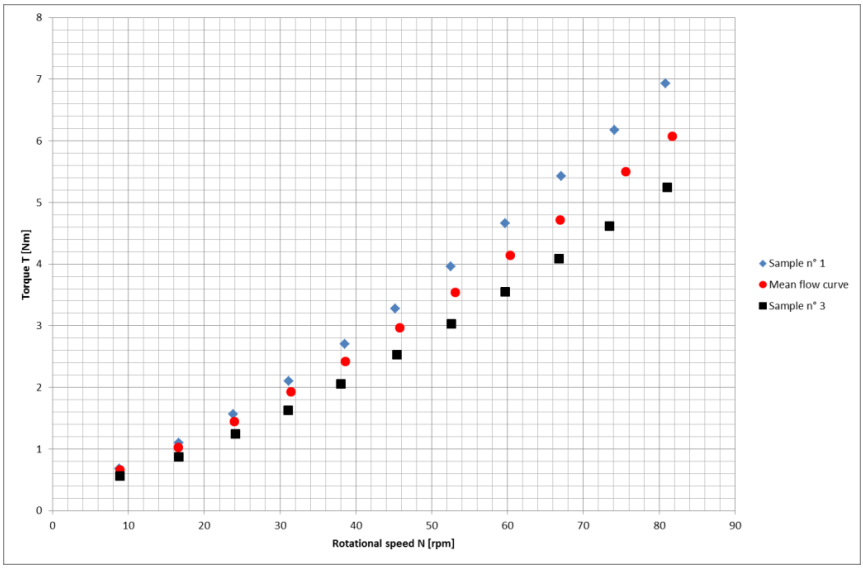

Fig. B-3: Processed T - N data of sample n° 1 and sample n° 3.

Once these rheometer parameters were determined for both samples, the numerical regression procedure of Le et al. presented in section A.2.2 of appendix A was applied in order to determine the modified two-zone Herschel-Bulkley parameters τ_o, k and n, being presented in section A.2.1 of appendix A. The calibration and conversion procedure of Feys (see section A.1 of appendix A) has not been applied during this research, because it was not suited for very fluid SCC. The rheometer parameters and the resulting modified two-zone Herschel-Bulkley parameters are summarised in Table B-3.

Table B-3: Summary of the resulting rheometer and Herschel-Bulkley parameters.

Sample:	G_{HB} [Nm]	K_{HB} [Nm.s^m]	m [-]	τ_0 [Pa]	k [Pa.s$^{n/(n-1)}$]	n [-]
Sample n° 1	0.39	0.326	1.404	10.6	17.7	1.385
Sample n° 3	0.332	0.252	1.389	9.9	14.4	1.36
Average	0.387	0.301	1.369	10.3	17.7	1.35

The modified two-zone Herschel-Bulkley parameters of the average flow curve were used in the simulations of the first series of formwork filling test, as described in chapter 6.

B.1.3 Measurement of formwork wall pressures

The formwork pressure was measured at several positions near the base of the formworks, where the maximum pressure on the formwork walls was expected. Two types of pressure measurements devices were used; manometers and electronic pressure transducers. The manometers were fixed on an intermediate water chamber, sealed with a rubber membrane, and flush mounted on the formwork. The electronic pressure transducers were flush mounted on the formworks, without the intermediate water chamber configuration. Fig. B-4 shows the very simple in-house design of the pressure measurement system with the intermediate water chamber, as well as the hydraulic testing equipment, which was used for the calibration of these pressure measurement units. The pressure measurement devices with the manometer and the intermediate water chamber were developed at the LfH of Ghent University.

Fig. B-4: In-house developed pressure measurement system.

The locations of the pressure measurements (cross hared squares) for the walls and for the columns are shown on Fig. B-5. The heights above the base at which these measurements were mounted on the different formworks are mentioned in Table B-4.

Table B-4: Mounting height of the pressure measurement systems.

Formwork	Type	Location	Height [m]
Column A	Manometer + water chamber	Above the inlet	0.385
Column B	Manometer + water chamber	Above the inlet	0.385
Wall A	Electronic pressure sensor	Above the inlet (position 1)	0.4
	Manometer + water chamber	Position 2	0.41
	Manometer + water chamber	Position 3	0.41
	Electronic pressure sensor	Position 4	0.08
Wall B	Manometer + water chamber	Above the inlet (position 1)	0.35
	Manometer + water chamber	Position 2	0.12
	Manometer + water chamber	Position 3	0.08

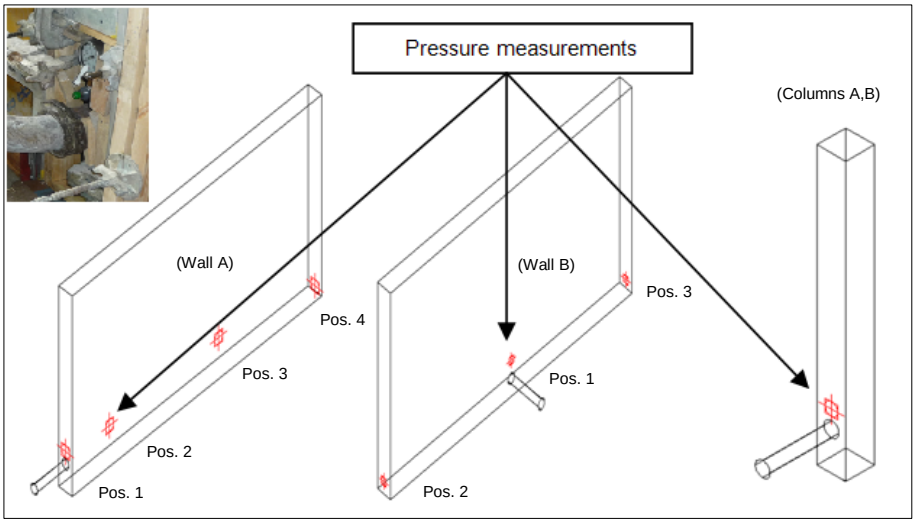

Fig. B-5: Connections of the SCC inlet for the walls and for the columns.

Unfortunately, several of the in-house designed pressure measurement units were damaged during the performed filling processes.

The wall pressures recorded by the non-damaged pressure measurement devices are presented in Fig. B-6 up to Fig. B-12.

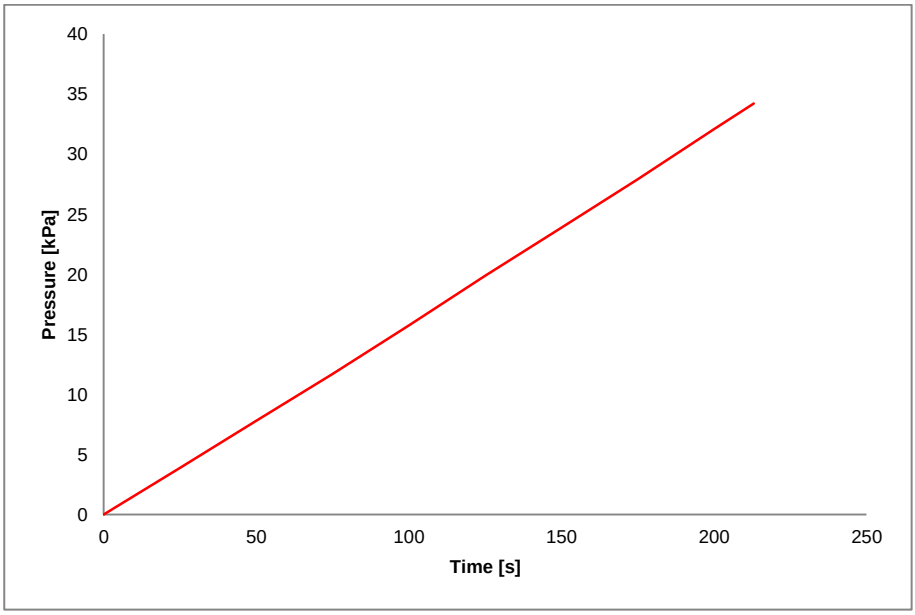

Fig. B-6: Wall pressure at the electronic pressure transducer above the inlet of wall type A - position 1.

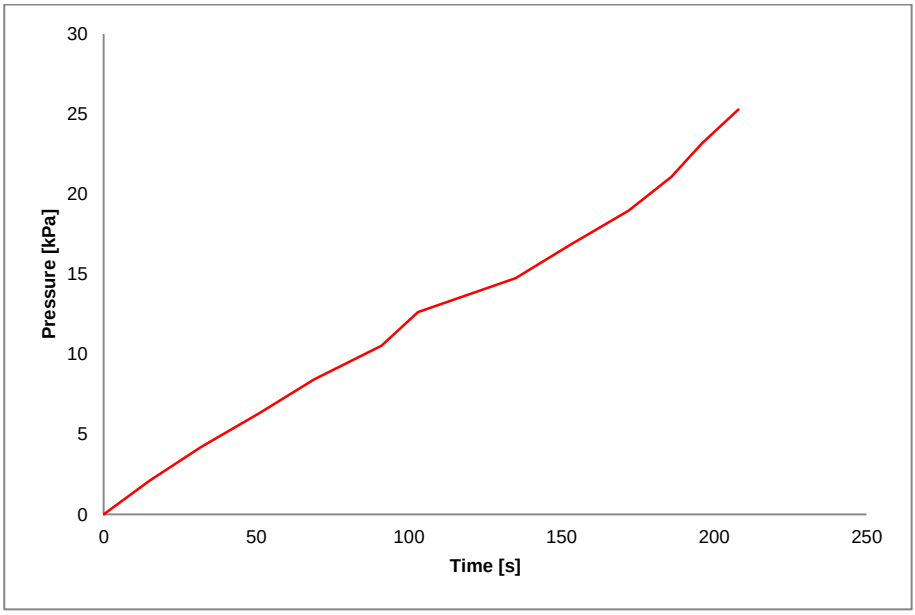

Fig. B-7: Wall pressure at the manometer of wall type A - position 2.

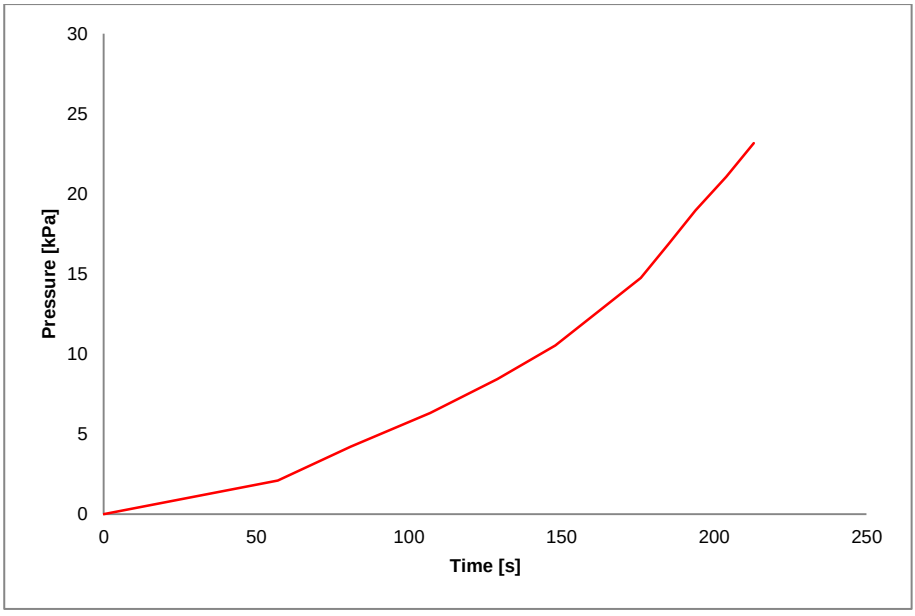

Fig. B-8: Wall pressure at the manometer of wall type A - position 3.

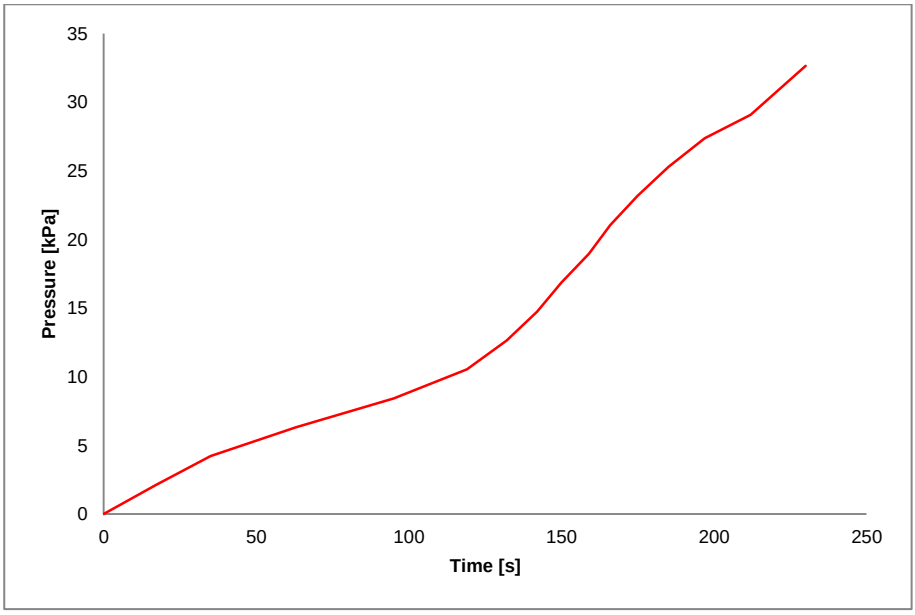

Fig. B-9: Wall pressure at the manometer above the inlet of wall type B - position 1.

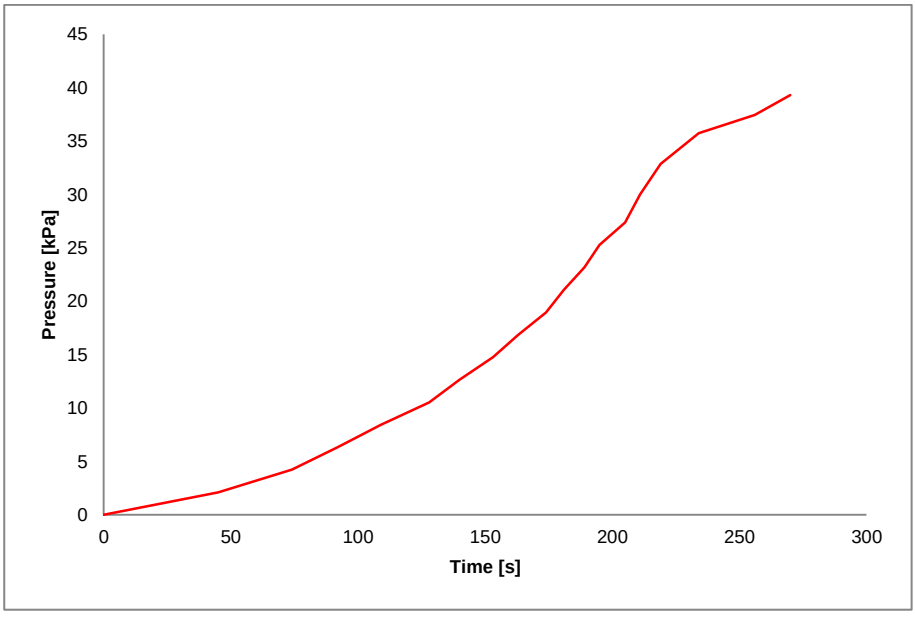

Fig. B-10: Wall pressure at the manometer of wall type B - position 2.

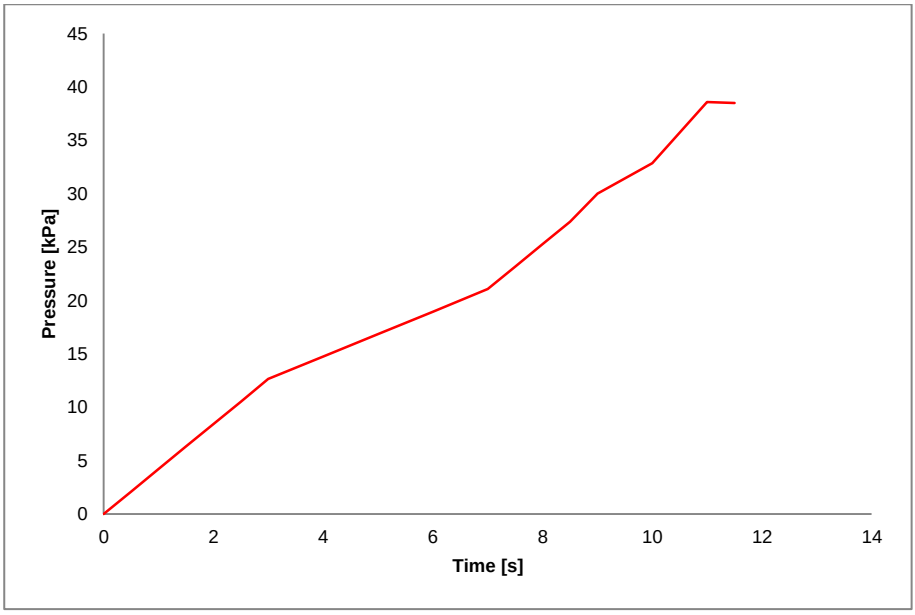

Fig. B-11: Wall pressure at the manometer above the inlet of column type A.

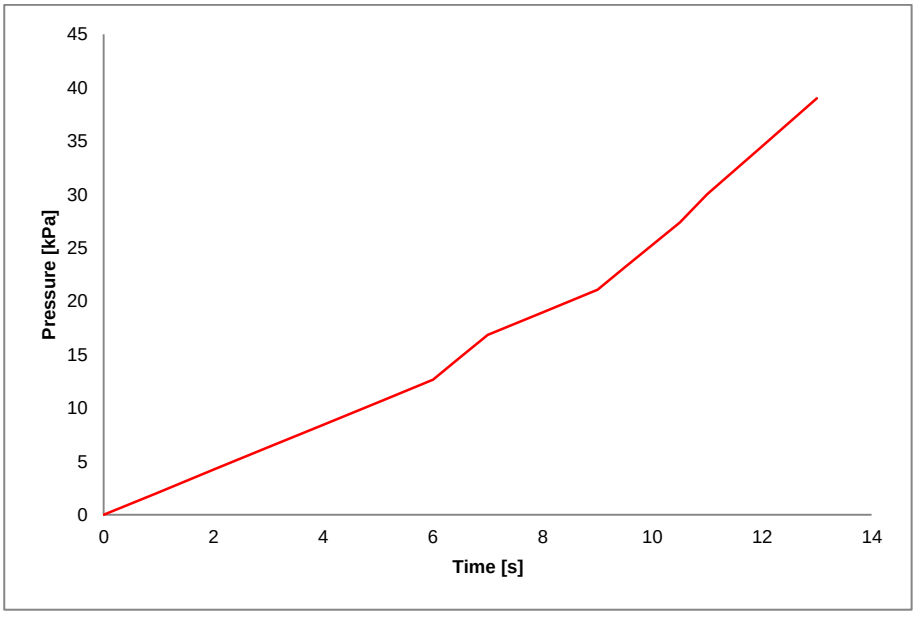

Fig. B-12: Wall pressure at the manometer above the inlet of column type B.

B.2 Second series of formwork filling tests [B.4]

B.2.1 Fresh properties of the selected SCC performing the standard concrete tests

The second series of formwork filling tests were performed with two SCC mixtures on two separate days. Again a ready-mix company supplied both SCC's. A low viscosity SCC was used for the filling tests on the first day, while a high viscosity SCC was used for the casting tests on the second day. Table B-5 lists the selected types and the amounts of the ingredients of both SCC mixtures.

Table B-5: SCC mixture per m^3.

SCC type:			**Low viscosity SCC**	**High viscosity SCC**
Ingredient	**Comments**	**Units**	**Quantity**	**Quantity**
Sand 0/5	Grain size between 0 - 5 mm	kg/m^3	848	895
Limestone aggregates 2/6.3	Aggregate size between 2 - 6.3 mm	kg/m^3	695	725
Cement type C III/A 42.5 LA	Blast furnace cement - Low Alkaline	kg/m^3	360	300
Calcitec	Limestone filler	kg/m^3	240	300
Glenium 27	Polycarboxylether (PCE) type super plasticiser	l/m^3	6.75	10.45
Water	-	l/m^3	190	160
Composition ratios:			W/C = 0.53 W/P = 0.32	W/C = 0.53 W/P = 0.27

The standard fresh SCC tests (slump flow, V-funnel, L-box, sieve stability, air content) and the rheometer measurements were performed with the low viscosity SCC at three different moments during the formwork filling tests:

- When the concrete mixing truck arrived at the MLCR - time t = 0 min - SCC sample n° 1;
- Just before filling the first column - time t = 38 min - SCC sample n° 2;
- Immediately after filling the last column formwork - time t = 82 min - SCC sample n° 3.

On the second testing day, the fresh concrete tests and rheometer measurements were performed with the high viscosity SCC at the beginning (time t = 0 min - SCC sample n° 4) and at the end (time t = 35 min - SCC sample n° 5) of the filling tests. The results of all the fresh SCC tests are summarized in Table B-6.

These fresh concrete test results show that the proposed SCC mixtures are in accordance with the recommendations stated in [B.1] and [B.2] for obtaining a good quality low and a high viscosity SCC. A visual inspection of the resulting homogeneity of the two SCC mixtures after the filling processes has been done on drilled samples of the cast columns. These visual inspection results also confirm the obtained high quality. They are reported in section B.2.4.

Table B-6: Results from the fresh concrete tests performed on both SCC mixtures.

SCC type:	**Low viscosity SCC**			**High viscosity SCC**	
Property	**SCC sample n° 1**	**SCC sample n° 2**	**SCC sample n° 3**	**SCC sample n° 4**	**SCC sample n° 5**
Density [kg/m³]	2250	2300	2269	2350	2319
Sieve stability [%]	4.3	3.7	4.5	0.6	1.2
L-box ratio [-]	0.99	0.89	0.80	0.79	0.83
Slump flow [mm]	720	705	678	655	658
V-funnel time [s]	7.3	5.9	9.7	15.9	15.9
Air content [%]	5.5	3.0	4.4	3.5	4.3

B.2.2 Rheological properties of the selected SCC through rheometry

The rheological properties of the SCC mixtures selected for the second series of base-filling tests were obtained from the BML Contec-Viscometer 5 measurements. The resulting flow curves are shown in Fig. B-13 up to Fig. B-17.

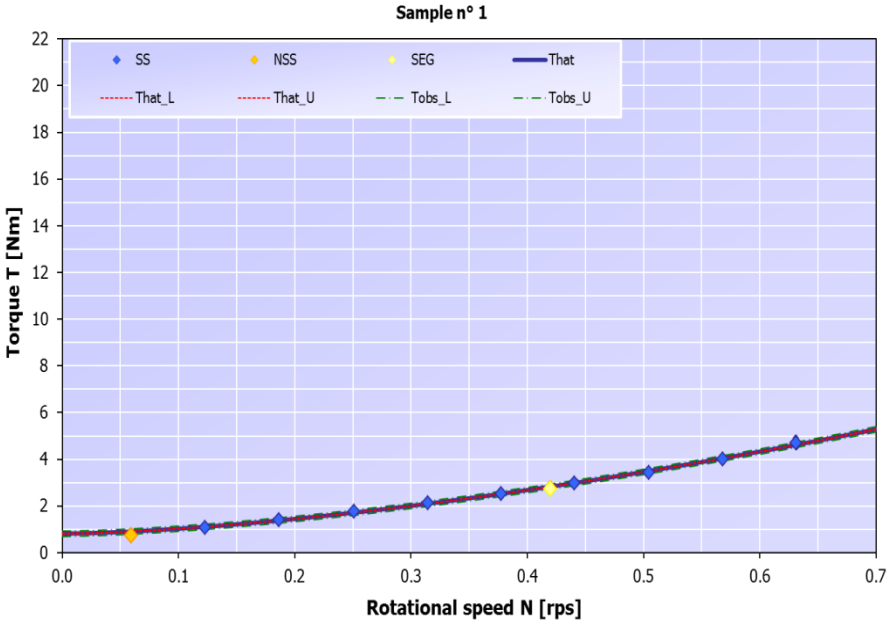

Fig. B-13: Measured torque and rotational speed of sample n° 1.

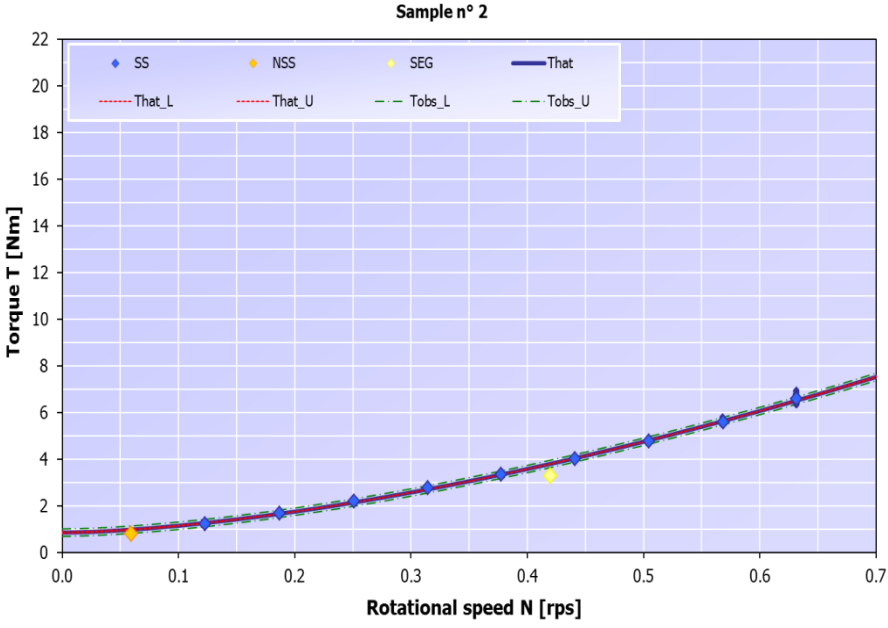

Fig. B-14: Measured torque and rotational speed of sample n° 2.

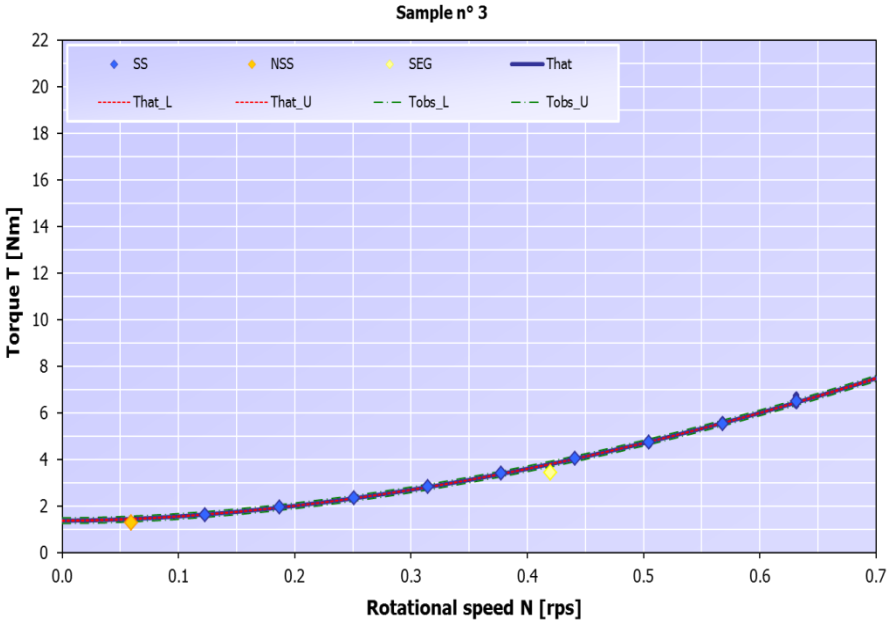

Fig. B-15: Measured torque and rotational speed of sample n° 3.

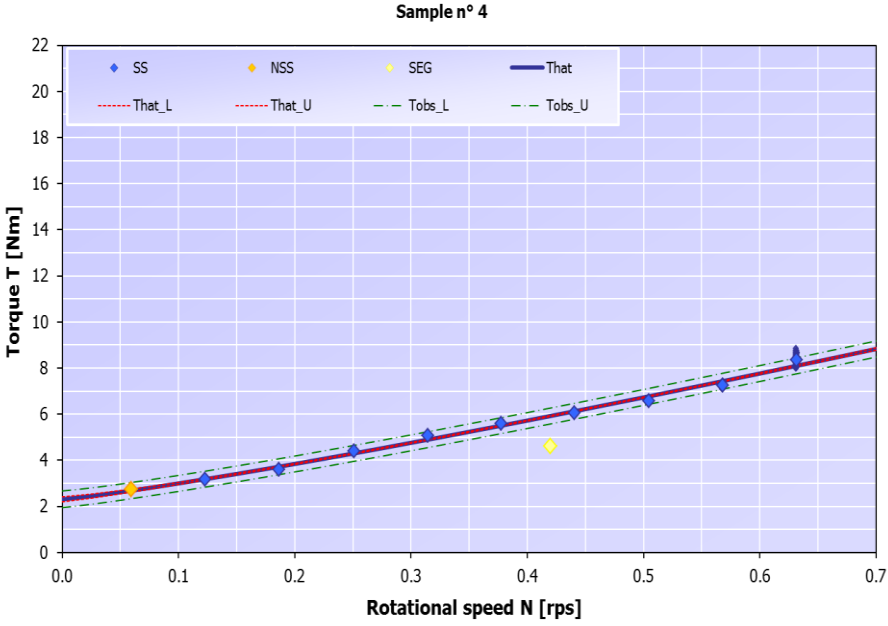

Fig. B-16: Measured torque and rotational speed of sample n° 4.

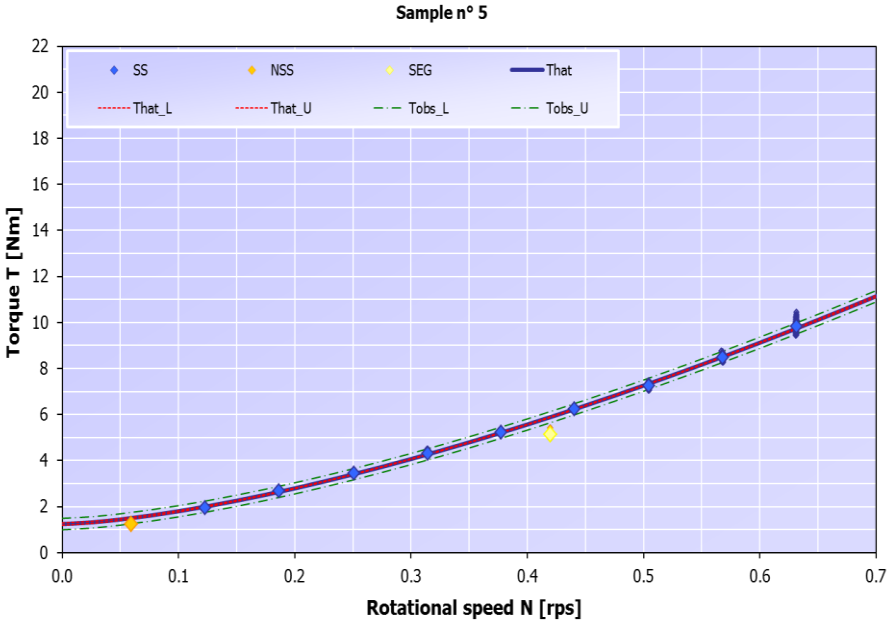

Fig. B-17: Measured torque and rotational speed of sample n° 5.

The resulting Herschel-Bulkley parameters (from the original model, not the modified two-zone model implement in Ansys Fluent) are summarized in Table B-7. They were calculated using Eq. (2.30) - (2.32), presented in chapter 2.

Table B-7: Fresh properties of the SCC used in the tests.

Mix design:	**Low viscosity SCC mix**			**High viscosity SCC mix**	
Property:	**SCC sample n° 1**	**SCC sample n° 2**	**SCC sample n° 3**	**SCC sample n° 4**	**SCC sample n° 5**
Yield stress τ_0 [Pa]	73.05	76.73	123.75	207.7	111.93
Consistency index n [-]	1.56	1.6	1.8	1.16	1.48
Consistency factor K [Pa.s^n]	8.48	11.45	6.29	33.63	22.81
Filling simulation (see Ch. 20 - 21)	I-beam	Column 1 Column 2	Column 3 Column 4	Column 7 Column 8	Column 5 Column 6

The choice of the set of material properties for the performed simulations is related to the filling sequence in time of the casting tests.

B.2.3 Measurement of formwork wall pressures

The evolution of the formwork wall pressure during the filling of the columns was recorded at three different positions: at the base of the formwork, at 1 m from the base and at 2 m from the base. Fig. B-18 shows the locations of the pressure measurements for the columns. Fig. B-19 and Fig. B-20 show the two types of electronic pressure sensors that were used for measuring and monitoring the formwork pressures during the column casts. These pressure measurement devices were provided by the Belgian Building Research Institute (BBRI).

The pressure sensors were calibrated with a very accurate hydraulic calibration unit. The pressure sensors of type 1 were mounted at the base of the columns, whereas the pressure sensors of type 2 were flush mounted on the walls of the formworks at 1 m and 2 m above the base.

The evolution in time of the formwork wall pressure at these three pressure sensor locations is represented in Fig. B-21 up to Fig. B-28 for each of the eight filled column formworks.

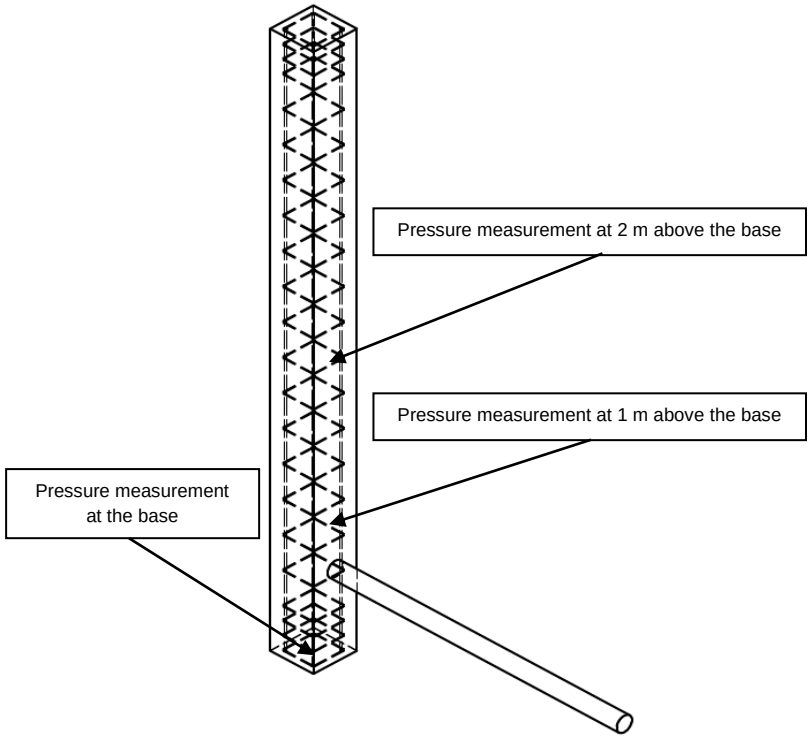

Fig. B-18: Pressure measurement locations of the columns.

Fig. B-19: Electronic pressure sensor type 1.

Fig. B-20: Electronic pressure sensor type 2.

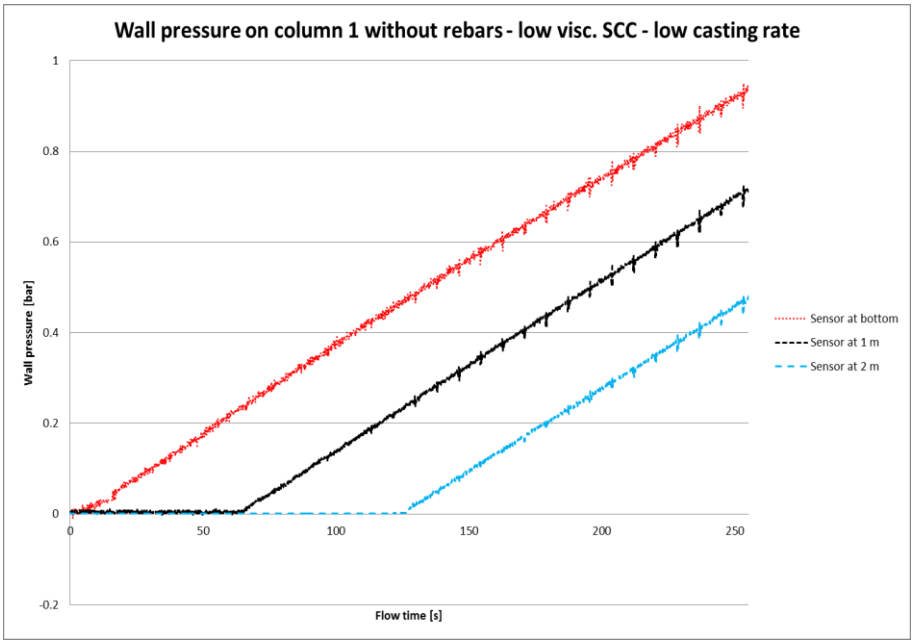

Fig. B-21: Measured wall pressures of column 1.

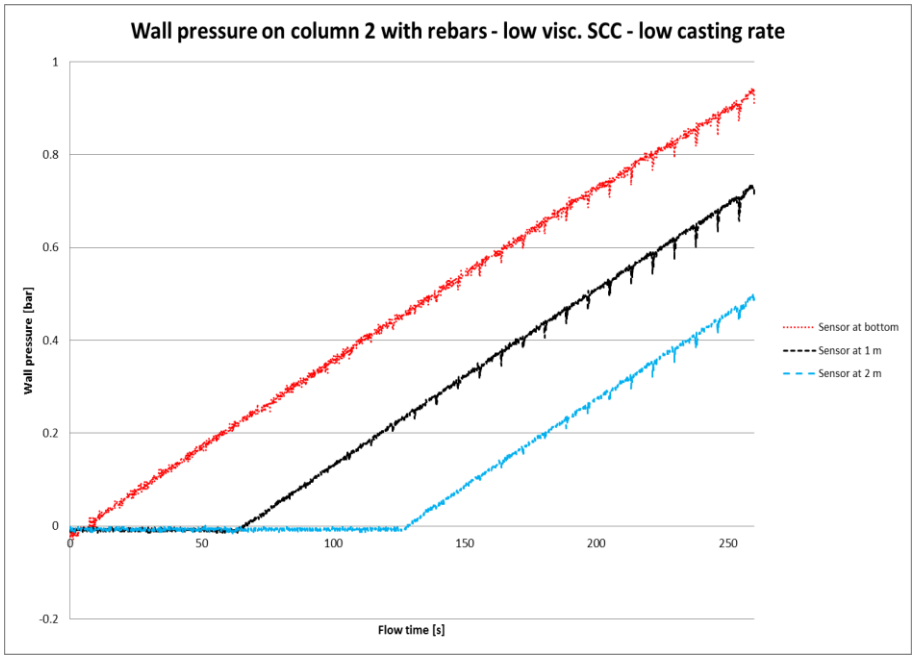

Fig. B-22: Measured wall pressures of column 2.

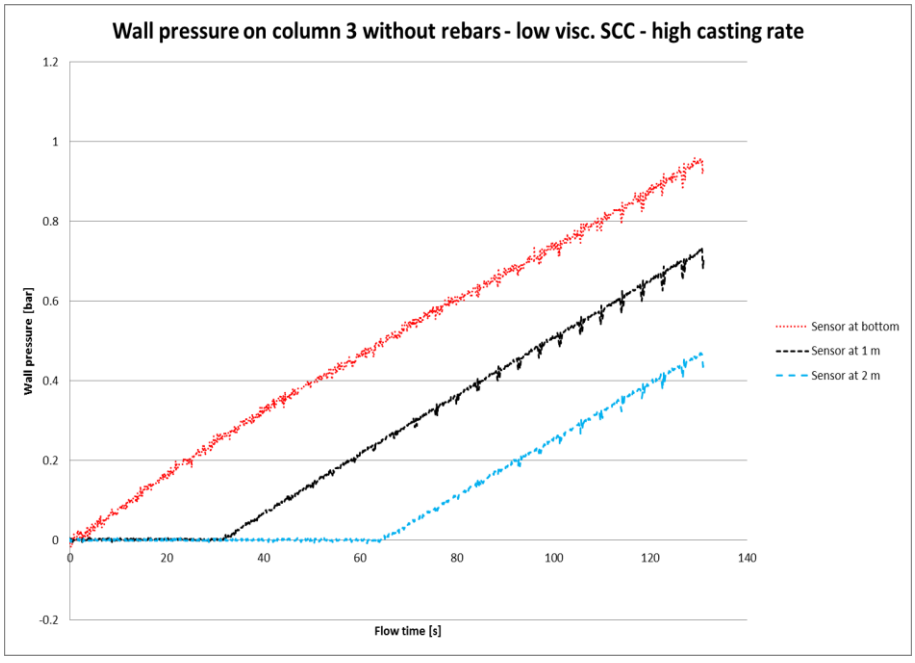

Fig. B-23: Measured wall pressures of column 3.

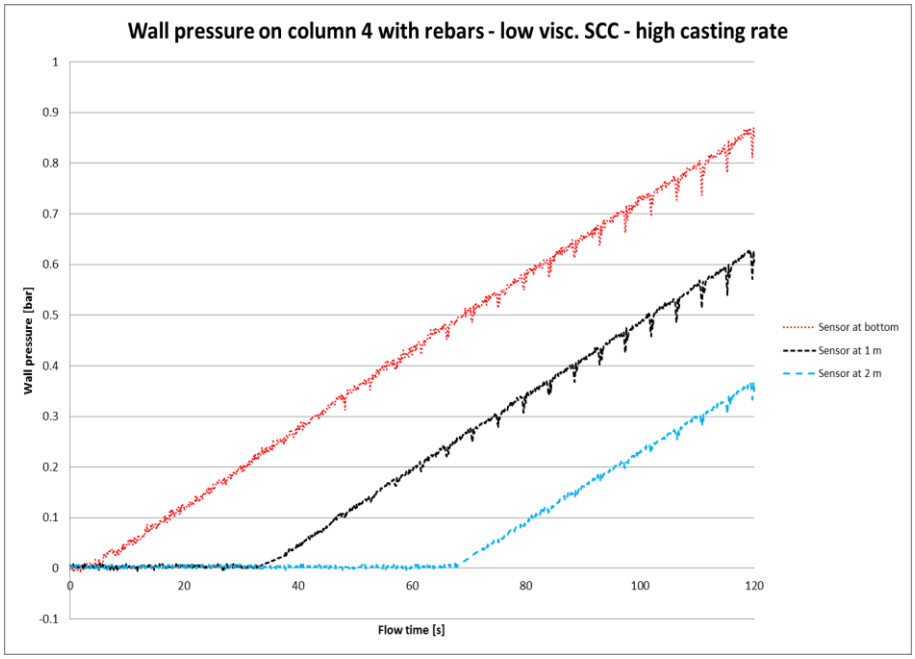

Fig. B-24: Measured wall pressures of column 4.

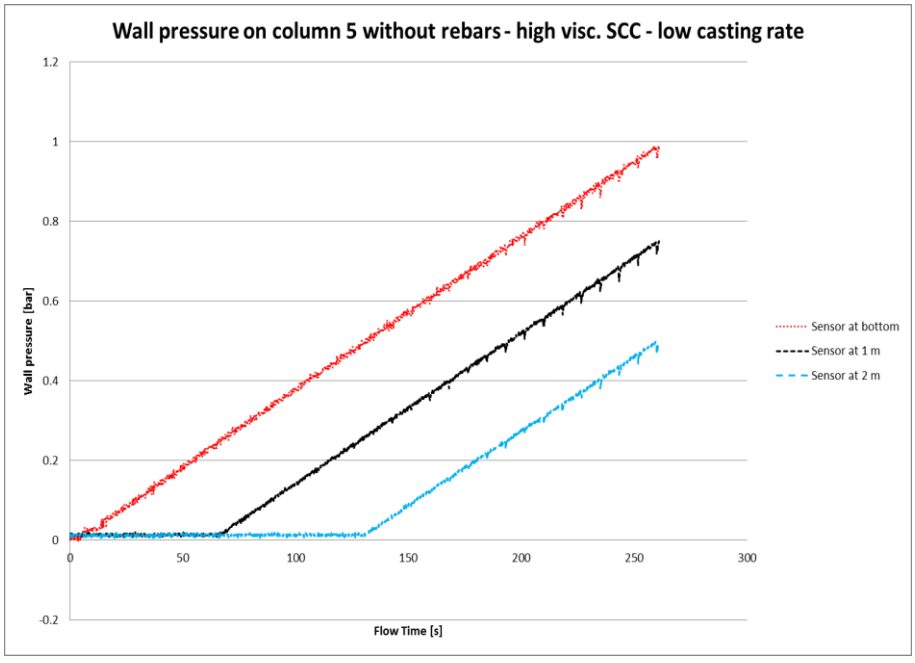

Fig. B-25: Measured wall pressures of column 5.

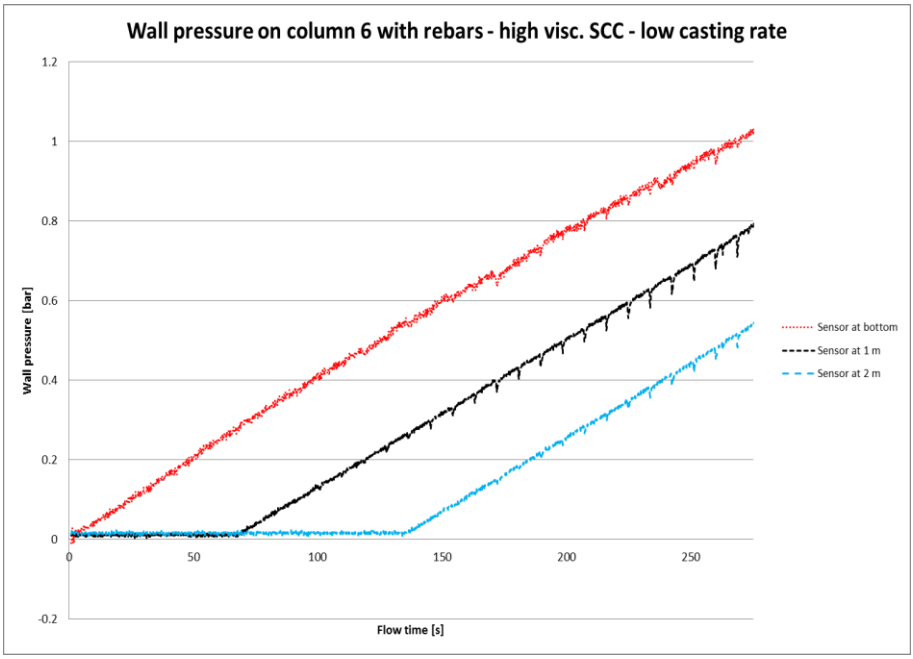

Fig. B-26: Measured wall pressures of column 6.

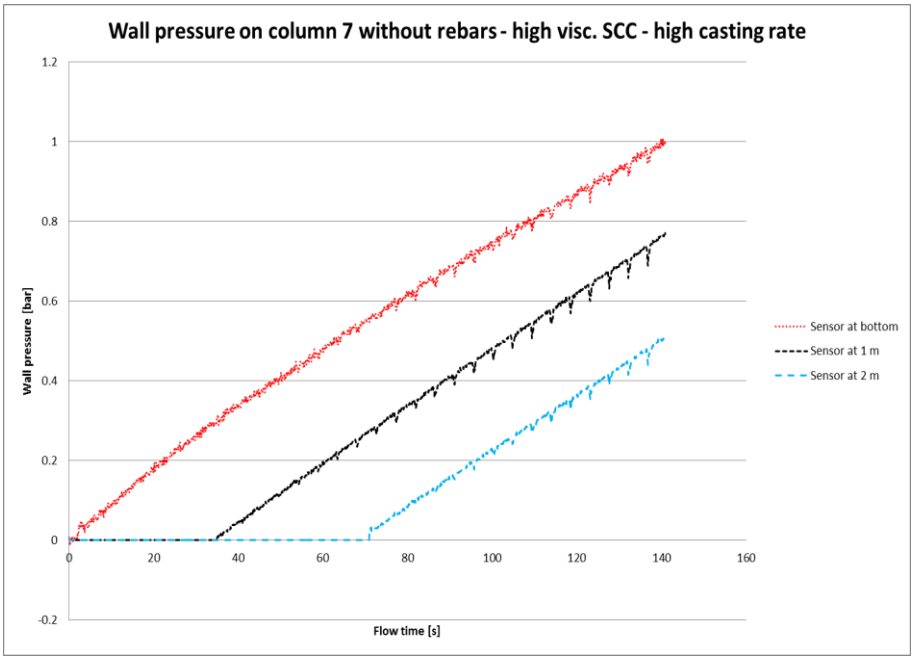

Fig. B-27: Measured wall pressures of column 7.

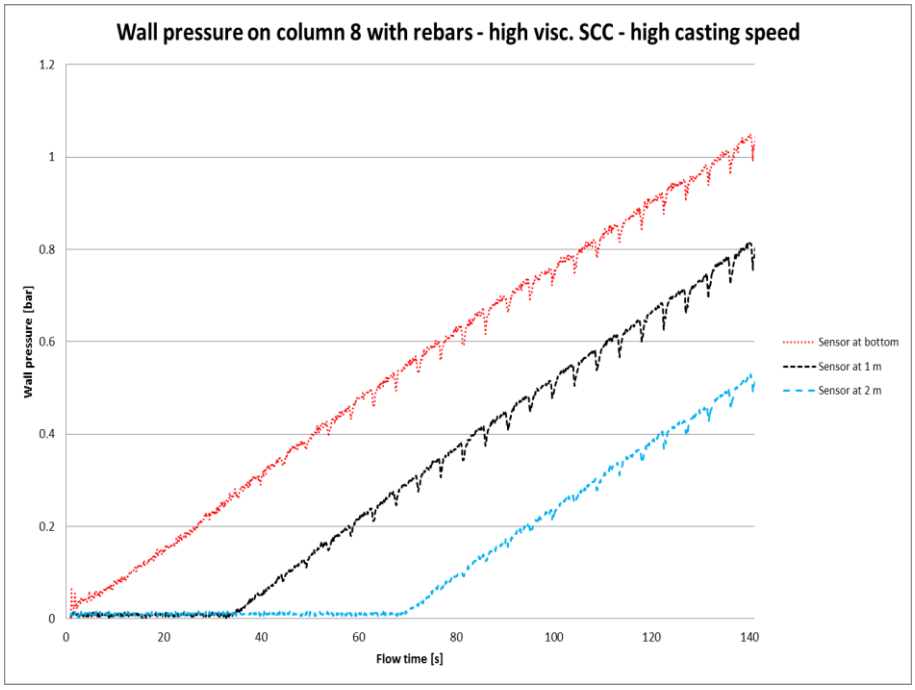

Fig. B-28: Measured wall pressures of column 8.

B.2.4 Visual inspection of the cast quality

A visual inspection was performed on drilled samples, taken at five equidistant locations along the height of the cast columns. Sample n° 1 is positioned near the bottom of each column, whereas sample n° 5 is positioned near the top of each column.

The results of the performed visual inspections (polished surfaces of the drilled samples) are summarized in Table B-8.

Table B-8: Results of the visual inspection performed on drilled samples of the eight cast columns.

	Column 1 - low viscosity SCC - low casting rate - no rebars	Column 2 - low viscosity SCC - low casting rate - with rebars
Position 1		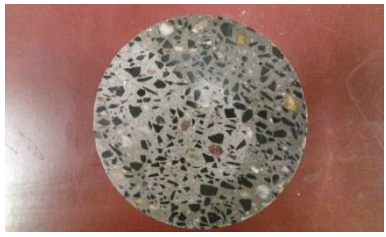
Position 2		
Position 3		
Position 4		
Position 5		

	Column 3 - low viscosity SCC - high casting rate - no rebars	Column 4 - low viscosity SCC - high casting rate - with rebars
Position 1		
Position 2		
Position 3		
Position 4		
Position 5		

	Column 5 - high viscosity SCC - low casting rate - no rebars	Column 6 - high viscosity SCC - low casting rate - with rebars
Position 1		
Position 2		
Position 3		
Position 4		
Position 5		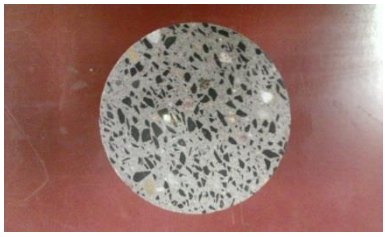

	Column 7 - high viscosity SCC - high casting rate - no rebars	Column 8 - high viscosity SCC - high casting rate - with rebars
Position 1		
Position 2		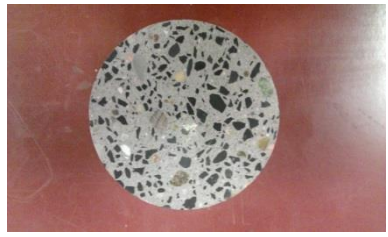
Position 3		
Position 4		
Position 5		

All the above sample pictures showed an extremely good resulting homogeneity of two SCC mixtures after the performed filling processes. No segregation can be observed. This is quite remarkable when taking into account the very high casting rates used in the base filling processes, compared to the casting rates normally used for casting CVC applying the top filling procedure.

B.3 References

[B.1] De Schutter G., Bartos P., Domone P., Gibbs J., “Self-Compacting Concrete”, Whittles Publishing, Caithness (2008), 296 pages.

[B.2] EFNARC European Project, “The European Guidelines for Self-Compacting Concrete: Specification, Production and Use”, EFNARC, (2005), 68 pages.

[B.3] Tichko S., Van De Maele J., Vanmassenhove N., De Schutter G., Vierendeels J., Verhoeven R., Troch P., “Numerical simulation of formwork pressure while pumping self-compacting concrete bottom-up”, Eng. Struct., vol. **70**, (2014), pp. 218-233.

[B.4] Tichko S., De Schutter G., Troch P., Vierendeels J., Verhoeven R., Lesage K., Cauberg N., “Influence of the viscosity of self-compacting concrete and the presence of rebars on the formwork pressure while filling bottom-up”, Eng. Struct., vol. **101**, (2015), pp. 698-714.